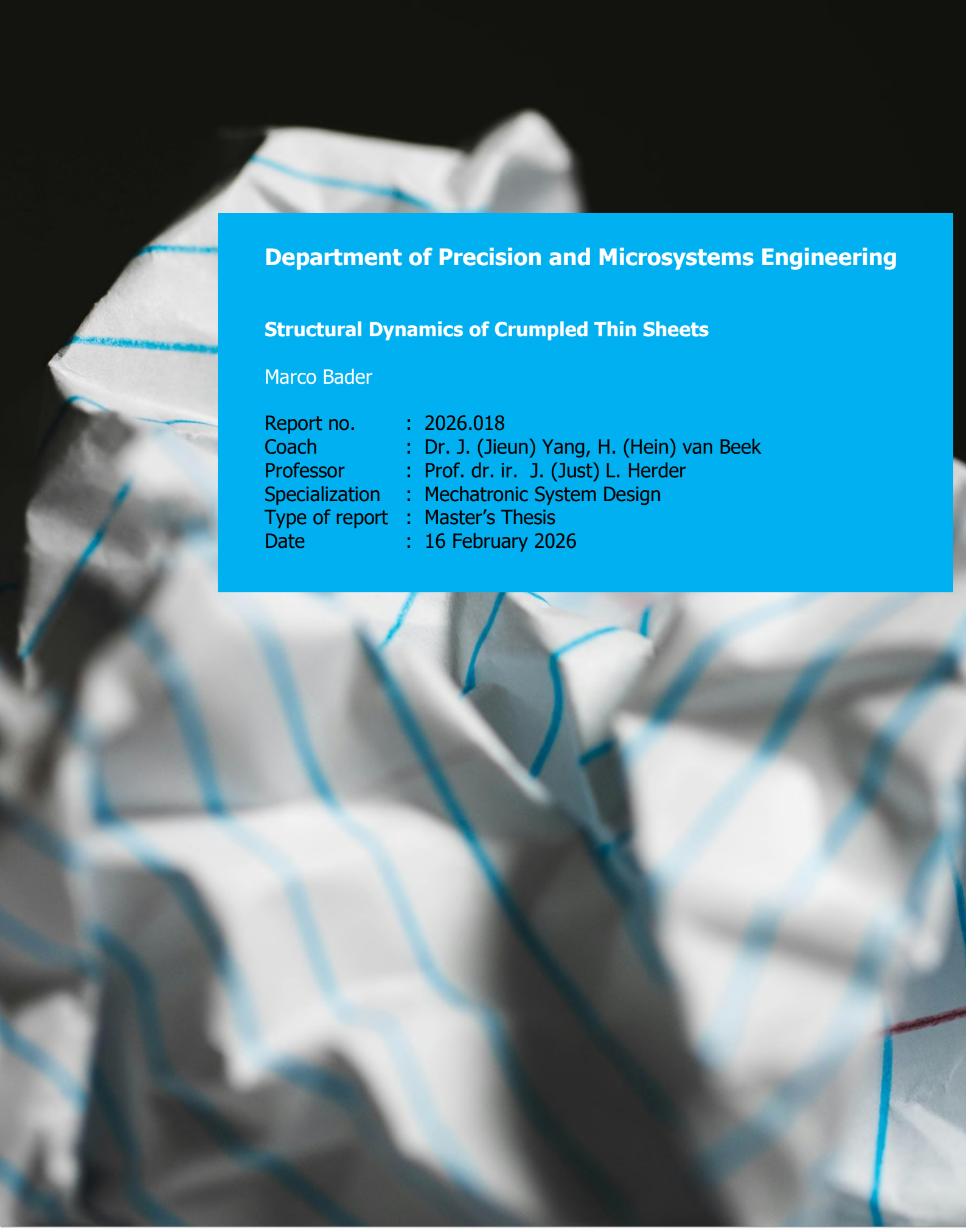

Department of Precision and Microsystems Engineering

Structural Dynamics of Crumpled Thin Sheets

Marco Bader

Report no. : 2026.018
Coach : Dr. J. (Jieun) Yang, H. (Hein) van Beek
Professor : Prof. dr. ir. J. (Just) L. Herder
Specialization : Mechatronic System Design
Type of report : Master's Thesis
Date : 16 February 2026

Structural Dynamics of Crumpled Thin Sheets

Beyond Wrinkling: A Numerical and Experimental Study

by

Marco Bader

to obtain the degree of Master of Science

at the Delft University of Technology,

to be defended publicly on Friday February 27, 2026 at 10:30 AM.

Student number:	5412110	
Project duration:	September 2, 2024 – February 27, 2026	
Thesis committee:	Prof. dr. ir. J. (Just) L. Herder	TU Delft, supervisor
	Dr. J. (Jieun) Yang	TU Delft, supervisor
	H. (Hein) van Beek	ASML, company supervisor
	Dr. ir. G. (Giuseppe) Radaelli	TU Delft
	P. (Pierre) C.J. Hoogenboom	TU Delft

This thesis is confidential and cannot be made public until February 27, 2028.

Cover:	Crumpled Paper by S. Forest under Unsplash License [1]
Style:	TU Delft Report Style, with modifications by Daan Zwaneveld

An electronic version of this thesis is available at http://repository.tudelft.nl/.

TU Delft

Preface

This thesis represents the culmination of a valuable partnership between Delft University of Technology and ASML, as well as my own academic journey. Following the completion of the first year of the Master's program in High-Tech Engineering, I was enthusiastic about the prospect of deepening my understanding of the high-tech sector during my graduation project. Given my expertise in dynamics and mechatronics, I could not have envisioned a more suitable partner than ASML, the epicentre of the Dutch mechatronics industry.

My first interaction with Hein van Beek, a system architect from the Dynamic Links team within Mechatronics Development & Engineering at ASML, was immediately a positive experience. He presented me with the rather unusual case study of the foil bellow, a problem which had long been shelved within ASML. However, now the time had finally come to take a closer and more rigorous look.

Once I decided to take on the assignment, I began searching for a supervisor at TU Delft. This was the moment I encountered Jieun Yang, who possessed faith in both the project and me and motivated me to generate and refine my initial project proposal. Shortly thereafter, Just Herder joined as a second supervisor, offering additional support through his extensive experience in guiding graduation projects.

As soon as the project officially started, I moved from Delft to Eindhoven so I could work on-site in ASML's vast facilities. There, I explored large parts of the lithography machine factory, giving me a much clearer sense of the industrial context of my work. I also established a new life in Eindhoven by becoming a member of the local student tennis association Fellenoord. Towards the conclusion of the year, I even coordinated the annual open tournament, which yielded numerous fun anecdotes.

Over the course of the year, a multitude of ASML colleagues generously shared their expertise and advice with me. Jeroen van Diermen deserves special recognition for his assistance in the development of my measurement system. I am also grateful to my fellow intern, Mouhriz Boulghalgh, for his willingness to engage in discussions about our work, exchange ideas, and learn from one another. In addition, I engaged in thought-provoking discussions with Hugo Verhelst, a post-doctoral researcher from Delft who provided me with valuable insights into the field of isogeometric structural analysis and the life of a researcher.

Of course, I would like to express my sincere gratitude to my three supervisors: Hein van Beek, Jieun Yang, and Just Herder for their unwavering support, constructive criticism, and insightful inquiries.
Finally, I want to thank my family and friends for always being willing to listen to me babble on about my work and future.

Marco Bader
Delft, February 2026

Summary

This thesis investigates crumpled thin-sheet bellows as a more compliant alternative to traditional corrugated bellows in vibrationally isolated mechatronic systems (ASML lithography machines). While conventional bellows rely on carefully engineered corrugations, the crumpled foil bellows studied here achieve compliance through an irregular, crumpled morphology, making their dynamic stiffness and vibrational transmissibility difficult to predict. The first part of the thesis is a stand-alone literature review into the diverse approaches employed to model wrinkled and crumpled thin sheets, with their structural dynamics of particular interest. The second part presents original research in which realistic crumpled bellow geometries are generated using explicit non-linear simulations via the dynamic relaxation method, and subsequently dynamically analysed using Hintz–Herting modal reduction. In this way, the static and frequency-dependent emergent stiffness can be extracted and examined as functions of compaction ratio and foil thickness. Experimental measurements of dynamic stiffness are used to validate the numerical trends and to identify the limitations of linearised models for these systems.

Contents

Nomenclature

Abbreviation	Definition
ALM	Arc-length method
BF	Base-frame
CAD	Computer aided design
CMS	Component-mode synthesis
DEA	Discrete element analysis
DoF	Degree-of-freedom
DRM	Dynamic relaxation method
FEA	Finite element analysis
IGA	Iso-geometric analysis
IMP	Iterative membrane properties
KL	Kirchhoff-Love
MAC	Modal assurance criterion
MF	Metrology-frame
NR	Newton-Raphson
PPMM	Penalty parameter modified material
TFT	Tension-field theory

1 Introduction

Crumpling is a ubiquitous physical phenomenon that occurs across a wide range of length scales, from the folding of proteins and the formation of flower buds to the buckling of Earth's tectonic plates [2]. In everyday life, it is perhaps most familiar in the wrinkling of fabrics: anyone who has worn a freshly ironed shirt knows how easily unwanted creases can form. In many engineering applications such imperfections are similarly undesirable; for example, wrinkles and creases in deployable space structures such as solar sails may lead to decreased thrust force and control difficulties [3].

Despite this traditionally negative perception, crumpling has recently attracted attention as a potential design principle rather than a defect. In particular, it has emerged within the broader field of *mechanical metamaterials*: engineered structures whose effective mechanical properties arise primarily from geometry and architecture rather than chemical composition [2, 4]. However, while conventional metamaterials are typically constructed from carefully designed periodic structures, crumpled sheets form a highly irregular and disordered network of ridges, vertices, and self-contacts. Yet, this complex structural disorder can also give rise to rich emergent behaviour, including low density, high compression resistance, and strong shock and energy absorption [2, 4–6]. Because crumpling can be induced through simple mechanical processing, it offers a potentially scalable and cost-effective route toward *disordered* metamaterials with tuneable properties. Early applications include crumpled graphene for micro-scale strain and pressure sensing [7], crumpled metallic foils as lightweight alternatives to solid foams in sandwich structures [8], and controlled crumpling approaches for porous biomaterial implants [9].

In this thesis, crumpling is investigated not as a defect nor as a metamaterial design strategy, but as a functional mechanism for a novel use in engineering: enabling ultra-flexible mechanical links in high-precision mechatronic systems.

1.1. Industrial context

With the advent of the information age and the recent rise of artificial intelligence, the global demand for high-performance computer chips is set to ascend to new levels [10, 11]. A crucial step in producing such chips is optical lithography, performed by the lithography machines developed by the Dutch company ASML. Their state-of-the-art extreme ultra-violet lithography systems are capable of patterning extremely small circuits onto silicon wafers with sub-13 nanometer resolution [12]. This is achieved through an exceptionally complex combination of optics, high-precision mechatronic systems, thermal control, vacuum technology, and advanced metrology [13]. For these machines, precision is paramount; even the slightest vibrations [14, 15] or microscopic contamination [16] can compromise imaging quality and reduce wafer yield.

Achieving this unprecedented level of precision requires machines that are increasingly large, more sophisticated, and correspondingly more expensive to manufacture. To keep the cost per chip economically viable, lithography systems must not only be accurate but also deliver high throughput. The wafer stage must therefore accelerate and decelerate at very high rates in order to expose wafers quickly,

up to 5 g $\simeq$ 50 m/s^2 [17]. These rapid motions inevitably generate mechanical vibrations, which in turn can degrade patterning accuracy. As a result, a substantial portion of the machine is dedicated to vibration isolation, both for damping vibrations from internal sources such as moving stages, but also for minimizing the influence of external disturbances such as mild seismic activity [14].

To achieve this, sensitive optical modules are suspended on large air-spring isolation systems [14]. These air mounts are designed to drastically reduce transmissibility, the extent to which vibrations in one part of the machine propagate into another. In this architectural view, the machine is conceptually divided into two domains: a grounded base frame that carries the high-acceleration wafer stage, and the isolated frame consisting of the high-precision optical modules, see Figure 1.1.

Despite this separation, the isolated frame still requires power, cooling water, vacuum lines, and high-bandwidth data connections. These utilities must be routed between the two frames, typically through a network of cables, hoses, and tubes. Each of these elements, however necessary, provides an additional mechanical connection (Figure 1.1), a parallel path through which vibrations can bypass the air mount isolators. Consequently, considerable effort is invested in designing these so-called *dynamic links* [18] to be as compliant as possible, thereby minimizing mechanical transmissibility.

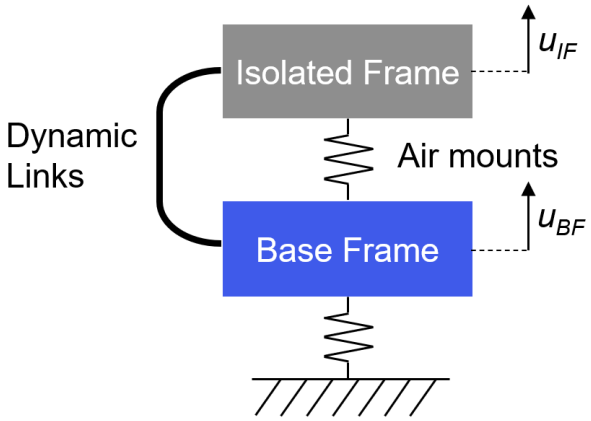

Figure 1.1: A high-level architectural view of a lithography machine. A grounded base frame is vibrated by slight seismic activity from the ground, but also by reaction forces associated with the fast accelerations of the wafer stage located in it. All high-precision optical components are separated from the base frame by a vibration isolation system based on air mounts, optimized for low mechanical transmissibility of vibrations. However, necessary dynamic links form a parasitic connection parallel to these air mounts and thereby compromise isolation performance.

1.2. Dynamic links

In the literature on vibration isolation, system performance is commonly expressed in terms of transmissibility, defined as the ratio between the vibration amplitude of the isolated mass and that of the source, as a function of frequency [19]:

$$T(f) = u_{IF}/u_{BF} \tag{1.1}$$

with u_{IF} and u_{BF} the displacements of the isolated and base frames, see Figure 1.1. While transmissibility is a useful measure at the system level, it becomes difficult to interpret when multiple compliant connections are present in series or in parallel. For this reason, module-level evaluation focuses on the dynamic stiffness of specific dynamic links, defined as the frequency-dependent relationship between reaction forces and relative displacements [19]:

$$k_{dyn}(f) = F_{IF}/|u_{IF} - u_{BF}| \tag{1.2}$$

with F_{IF} the disturbing force on the isolated frame due to a relative displacement between frames. Unlike transmissibility, the dynamic stiffness per component can be directly compared and added together.

For an ideal isolation system with constant stiffness, the transmissibility decreases rapidly once the excitation frequency lies well above the (damped) resonance, see the illustrative measurements in Figure 1.2. This reduction follows a characteristic −2 slope in log-log space, corresponding to 10^{-2} reduction in transmitted vibration per decade increase in frequency [20]. Real air mounts, however, do not maintain a constant stiffness: above a certain frequency their stiffness rises due to decoupling caused by structural resonances and acoustics [21]. This causes the total transmissibility to deviate from the ideal −2 slope and instead saturate to a plateau at high frequencies.

This saturation becomes even more pronounced when dynamic links are included; although such links are designed to be highly compliant in the static (zero-frequency) limit, their stiffness also increases with a nearly +2 slope due to their internal dynamics [19]. However, the first resonances and thus the rise in stiffness typically occur at lower frequencies than for the air mounts. Consequently, at higher frequencies the dynamic links may become a substantial source of stiffness compared to the isolator. This pushes the system further away from the ideal transmissibility behaviour and reduces the achievable isolation performance. These considerations highlight the importance of not only minimising the static stiffness of dynamic links, but also understanding and controlling their full frequency-dependent dynamic stiffness.

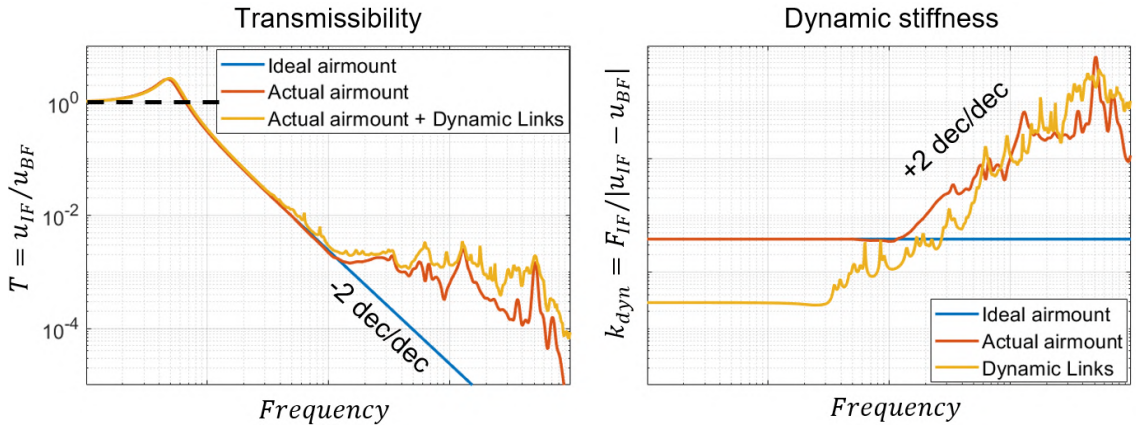

Figure 1.2: Typical behaviour of transmissibility and dynamic stiffness for three cases: an ideal air mount, a real air mount, and a real air mount including the effect of dynamic links. The ideal isolator of constant static stiffness exhibits the characteristic −2 slope in transmissibility, leading to a rapid decay above resonance [20]. In contrast, real systems show a plateau in transmissibility at higher frequencies due to the stiffening in the dynamic regime [19]. At sufficiently high frequencies, the dynamic links become substantial contributions to the stiffness compared to the air mounts since their stiffness rise begins earlier, thereby further degrading the achievable isolation performance.

One method to characterize the contribution of a specific link is to remove or replace components inside the machine and measure the resulting change in total transmissibility [19]. From these system-level measurements, using estimations for the mass and inertia properties, the corresponding forces are inferred. However, this indirect approach is cumbersome, sensitive to assumptions, and difficult to interpret as the effects of multiple links may overlap. Moreover, physically removing and reinstalling components is time-consuming and costly, especially given that many links are deeply embedded in the machine architecture.

For these reasons ASML invests heavily in the direct measurement of dynamic stiffness using dedicated experimental setups, capable of applying controlled vibrations and measuring the resulting forces to obtain their transfer functions [19]. At the same time, significant effort is directed toward developing robust finite-element-based modelling strategies for predicting dynamic stiffness. Such simulation tools enable rapid design iterations and optimization without the need for repeated physical prototyping.

1.3. Problem statement: foil bellows

The dynamic link investigated in this work is a particularly unconventional one; whereas most dynamic links in the machine consist of hoses or tubes with well-defined and tightly controlled geometries, the component studied here is a randomly crumpled foil bellow, as shown in Figure 1.3. In the lithography system, these bellows serve as vacuum barriers: they separate different vacuum regimes and prevent particles generated near the wafer stage from migrating toward the highly sensitive optical modules.

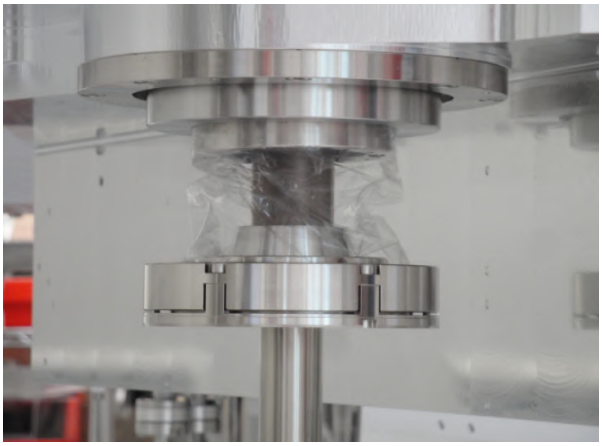

Figure 1.3: A transparent, crumpled thin-foil bellow that is used in ASML lithography machines to separate vacuum regimes. It also forms a mechanical dynamic link between the base and isolated frames. The crumpled nature of the foil allows for a relatively simple method of manufacturing a highly compliant structure.

Due to the specifics of the system architecture, each bellow also forms a mechanical connection between the base and isolated frame, thereby contributing a parasitic stiffness. As with other dynamic links, these parts must thus be designed to be as compliant as possible within the available working volume. While cylindrical bellows are not uncommon in ASML systems, most are made from metal or rubber and feature a well-engineered corrugated geometry to achieve the required compliance, see Figure 1.4. The foil bellows considered here are fundamentally different: because no significant pressure differential exists between the vacuum regimes, the structure does not need to withstand large loads. This makes it attractive to use a thin polymer foil and rely on crumpling to introduce flexibility, with the crumpling ridges acting as hinge-like features similar to those in corrugated bellows. The effective stiffness is thus primarily governed by the emergent ridge network created by crumpling, rather than by a precisely engineered periodic geometry.

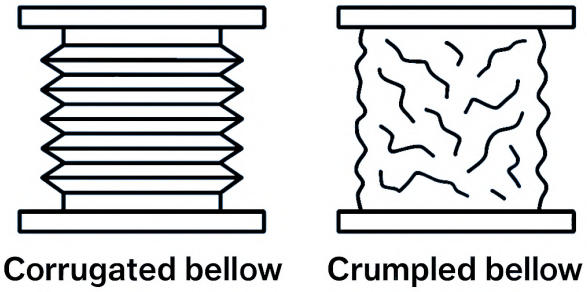

Figure 1.4: Schematic comparison between engineered corrugation ridges and disordered crumpled morphologies as routes to compliant dynamic links.

However, the apparent simplicity of 'crumpling to induce compliance' hides a fundamental knowledge gap: the frequency-dependent dynamic stiffness of such a foil bellow, its key performance metric, is not well-understood. Unlike engineered corrugations, a crumpled bellow does not have a prescribed geometry that can be directly related to stiffness: its response emerges from a stochastic ridge network whose morphology is shaped by manufacturing history and boundary conditions.

From an industrial perspective, several practical design drivers motivate a systematic investigation. Current foil bellows are manufactured from ultra-clean fluoropolymer films (PFA), which offer excellent vacuum compatibility and flexibility [22]. However, increasing industrial and regulatory pressure to phase out PFAS-type materials necessitates a transition toward alternative polymers [23]. Many candidate replacements with similar vacuum stability are substantially stiffer than PFA, directly affecting the dynamic stiffness of the link.

Foil thickness plays a critical role in vacuum robustness, as sharp folds generated during crumpling may lead to pinhole formation when the foil is too thin (see Figure 1.5). The degree of crumpling likewise constitutes more than a manufacturing choice: it acts as a design variable that can further increase the likelihood of pinholes, while also promoting geometric shortcuts—unintended contacts between the foil and itself or surrounding hardware. Such contacts may introduce frictional constraints that add parasitic stiffness to the system. These considerations illustrate that there exists a practical limit to the permissible degree of crumpling, which naturally leads to the central question: *how do the static and dynamic stiffness of a crumpled foil bellow depend on foil thickness and the degree of crumpling?*

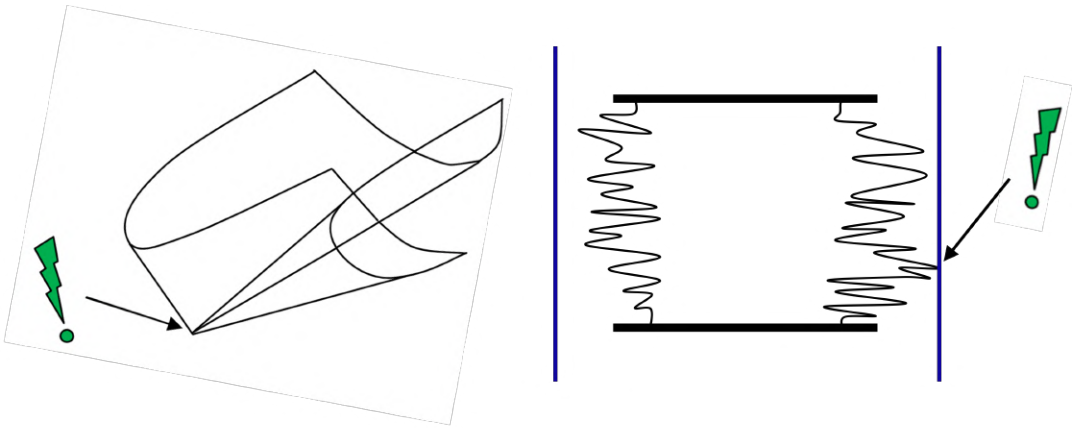

Figure 1.5: At high degrees of crumpling, sharp vertices in the sheet may promote pinhole formation if the foil is too thin, thereby compromising vacuum robustness (left). Similarly, excessive overlength increases the risk of mechanical shortcuts between the foil and itself or surrounding machine components (shown in blue), where frictional contact may introduce additional parasitic stiffness (right).

Answering such questions is challenging because analytical understanding of strongly crumpled structures remains limited. Classical buckling theory is highly successful near the onset of instability, where deformations remain sufficiently small for linearised assumptions and mode superposition to hold [24]. In this regime, buckling often manifests as *wrinkling*: small, periodic undulations that are homogeneously distributed over the surface [25]. Yamaki [24] provides extensive analytical and experimental results for various loading conditions of cylindrical shells, illustrating how post-buckled wrinkled morphologies can be predicted under ideal conditions, see Figure 1.6. However, these frameworks are still limited to idealized geometries and weakly post-buckled states; they do not encompass the ridge-dominated, highly non-linear morphologies that are pertinent to crumpled bellows. Although studies have investigated intentionally crumpled structures for crashworthy automotive components [26, 27], they frequently only concentrate on reaction forces and plastic energy absorption rather than the structural characteristics of the *resulting* system.

A further obstacle is the inherently stochastic nature of crumpling. Even under nominally identical conditions, small perturbations can lead to different ridge networks and therefore different stiffnesses. For design purposes, quantities such as static and dynamic stiffness must therefore be characterised not only as functions of design parameters, but also statistically across many realisations. This requirement for repeated sampling places a heavy burden on conventional finite-element workflows: strongly buckled morphologies are numerically unstable, often leading to convergence difficulties and long runtimes [28]. For instance, a preliminary simulation that was previously carried out in ANSYS Structural Mechanics, using 12 threads on ASML's internal computation cluster, produced runtimes of $\sim$2.5 hours for a single run. This demonstrates the inadequacy of conventional approaches for large parameter studies and subsequent design optimization.

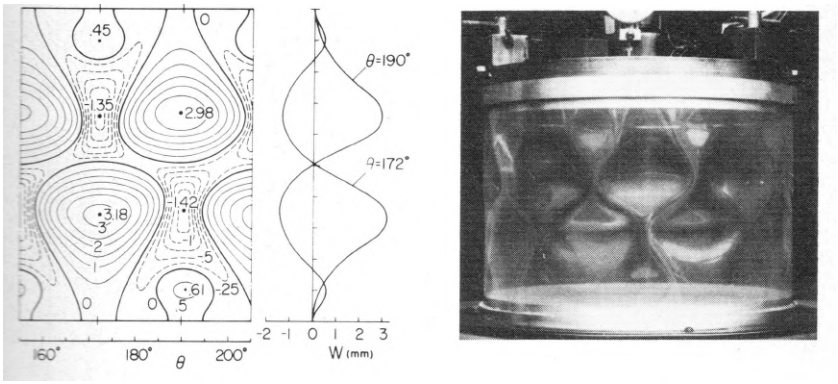

Figure 1.6: Example of analytical predictions and experiments of linearly buckling cylindrical shells. The predicted periodic wrinkle pattern is reproduced experimentally under near-ideal conditions [24]. However, this weakly post-buckled regime is fundamentally different from the irregular, ridge-dominated morphologies that arise at higher degrees of compaction [25].

1.4. Research objective

The overarching aim of this work is therefore to develop the numerical methodologies needed to study the static and dynamic stiffness of crumpled structures in a systematic, robust, and computationally efficient manner. This includes creating reliable approaches for generating crumpled morphologies, modelling their dynamic behaviour across relevant frequency ranges, and validating these models experimentally. Taken together, these efforts seek to establish a foundation for understanding how crumples govern stiffness and how this knowledge may be used to design flexible dynamic links.

These aforementioned goals may be summarised as follows:

1. **Define the scientific context and research gap** by critically reviewing the structural mechanics and dynamics of buckled thin sheets, and examining relevant existing numerical approaches to wrinkling and crumpling.
2. **Formulate a repeatable modelling framework** that enables robust generation of crumpled morphologies and extraction of static and dynamic stiffness within practical computational cost.
3. **Characterise parameter dependence and variability** of emergent stiffness by determining how static and dynamic stiffness change with sheet thickness and degree of crumpling.
4. **Develop an experimental methodology** for direct measurement of dynamic stiffness for highly compliant crumpled structures.
5. **Compare and validate** numerical and experimental results, and interpret the observed trends using physical insight into the mechanics of crumpled thin sheets.

1.5. Thesis outline

The thesis is structured in three parts.

The first part comprises a self-contained literature review, written in the format of an independent scientific paper. It surveys experimental, theoretical, and computational studies on thin-sheet mechanics, with particular emphasis on post-buckling behaviour and its implications for structural dynamics. The review concludes by formulating a generalised computational workflow that integrates the key methodologies required to simulate and analyse buckled geometries in a dynamic setting.

The second part presents the research study, likewise structured as an independent paper. It investigates variations of a crumpled cylindrical shell inspired by the foil bellow case study. The proposed workflow is applied to generate and analyse crumpled morphologies, enabling a statistical evaluation of static and dynamic stiffness across a range of sheet thicknesses and compaction ratios.

The thesis concludes with an integrated discussion of the main findings, outlining key limitations and directions for future research. Supplementary technical details, modelling procedures, and additional results are provided in the Appendices to ensure transparency and reproducibility.

2

Structural Dynamic Simulation of Post-Buckled Thin Sheets: a Review

This chapter contains the stand-alone literature review paper supporting the present research. It examines prior experimental, theoretical, and computational studies on wrinkling and crumpling of thin sheets, with emphasis on their relevance to structural dynamics and statistical analysis. The review identifies the key knowledge gaps, modelling challenges, and methodological limitations that motivate the research contributions developed in the remainder of this thesis.

The discussed topics include:

- Experimental behaviour observed for thin-sheet buckling
  - Wrinkle-to-crumple transition
  - Structural dynamics of wrinkling
- Computational challenges particular to thin-sheet buckling
  - Under-constrained buckling
  - Small features
  - Elasto-plasticity
  - (Self-)avoidance
- Discretization methods and their relevant properties
  - Finite element analysis
  - Isogeometric analysis
  - Tension field theory
  - Discrete element analysis
- Solution procedures
  - Initial pertubation
  - Dynamic relaxation method
  - Arc-length method
  - Modal reduction
  - Uncertainty analysis
- Generalised computational workflow illustrating all relevant methodologies and their limitations

Structural Dynamic Simulation of Post-Buckled Thin Sheets: a Review

Marco Bader[a]

[a]*Department of Precision and Microsystems Engineering, Faculty of Mechanical Engineering, Delft University of Technology, the Netherlands*

Abstract

We present a comprehensive review of the diverse approaches employed to model wrinkled and crumpled thin sheets, with their structural dynamics of particular interest. To get better acquainted with the problem at hand, the experimental behaviour of such sheets is discussed and the common computational challenges are presented. Notably, buckled thin sheets have been modelled using various spatial discretizations besides traditional finite element analysis, such as isogeometric analysis, tension field theory and discrete element analysis. Advanced solution procedures for buckled sheets are also examined, such as initial perturbations, dynamic relaxation, arc-length methods, modal reduction and sensitivity analysis. A general flowchart with discussion is outlined to assist the reader in traversing all these options in methods and pinpoint which are especially relevant to the user's application.

Keywords: post-buckled thin sheets, wrinkling, crumpling, isogeometric analysis, tension field theory, dynamic relaxation, arc-length methods

1. Introduction

The crumpling of a sheet of paper is an everyday phenomenon that vividly illustrates the complex post-buckling behaviour of soft thin structures. Beyond the household scale, similar instabilities emerge in flower buds, the Earth's crust, and DNA packing, all of which reveal the intricate patterns that can form through wrinkling and crumpling [1]. Until recently, engineers have often regarded these features as nuisances that negatively impact their finely designed systems. For instance, wrinkles and creases in solar sails may lead to decreased thrust force and control difficulties [1].

However, compacted crumpled sheets have also been shown to exhibit rich mechanical properties such as high energy absorption, enhanced compression resistance, and a tuneable porosity [2–4]. Together with their low weight and ease of manufacturing, these special qualities have spurred research into so-called *disordered* metamaterials [4] across a wide range of industries. Early applications include crumpled graphene for micro-scale strain and pressure sensing [5], crumpled metallic foils as lightweight alternatives to solid foams in sandwich structures [6], and controlled crumpling approaches for porous biomaterial implants [7].

Another engineering context that may show promise is where thin buckled sheets are employed to realise highly compliant joints or seals. For example, corrugated bellows common to vacuum applications illustrate how deliberately engineered ridge networks can produce flexible links with low vibrational transmissibility [8], see Figure 1. Likewise, purposefully buckled or even completely crumpled sheets might provide a simpler and more economical path to multi-directional compliance.

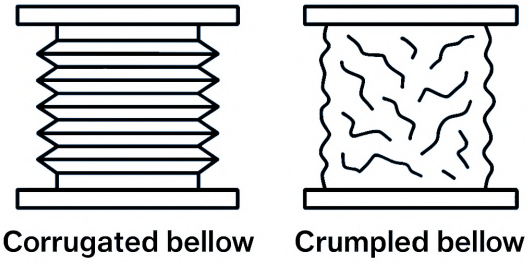

Figure 1: Schematic comparison between engineered corrugation networks and stochastic crumpled morphologies as routes to compliant thin-sheet mechanical links.

Realising this promise in design practice is hindered by the fact that the structural mechanics and dynamics of crumpled morphologies are still poorly understood. Analytical post-buckling theory is typically restricted to idealised situations close to the critical load, where deformations remain in a linearised and periodically wrinkled regime [9].

In contrast, crumpling represents the non-linear and irregular evolution of wrinkling [10]. For this regime there is no broadly applicable analytical framework. Moreover, the morphology is highly sensitive to initial imperfections and loading history, such that stochastic variability between realisations is intrinsic and many samples are needed to extract statistically meaningful trends. For engineering purposes, where one often wishes to explore parameter spaces, quantify uncertainty, and ultimately optimise designs, efficient and robust modelling strategies are therefore essential.

However, the strongly non-linear and path-dependent nature of buckled thin-sheet systems poses substantial computational challenges [11]. Even in the wrinkling regime, numerical models can rapidly lead to ill-conditioned system matrices and convergence problems, making conventional finite element approaches unstable or prohibitively expensive. Although a wide range of techniques has been proposed to address these issues [12], the literature still lacks a coherent overview that connects these computational developments to the specific task of dynamic analysis of crumpled flexible mechanical links.

To address this gap, this work aims to review how various modelling strategies can support structural-dynamic analysis for buckled thin-sheet structures. First, relevant experimental insights into the wrinkle-to-crumple transition and the dynamic behaviour of wrinkling are examined. Subsequently, common computational challenges along with the advantages of alternative spatial discretisations and advanced solution procedures are discussed. Finally, these methods are synthesised into a generalised workflow for the systematic, efficient and robust (dynamic) analysis of post-buckled thin-sheet structures.

2. Review method

Literature on the modelling of wrinkled and crumpled thin sheets was collected from the Scopus and Google Scholar databases using an iterative search strategy. A preliminary broad search was conducted using the following keyword combination:

```
("sheet" OR "membrane" OR "foil") AND
("wrinkl*" OR "crumpl*") AND ("simulat*" OR
"model*") AND NOT "bio*"
```

To efficiently screen the large number of resulting references, the AI-assisted systematic review tool *ASReview* [13] was employed. Relevant publications were first identified on the basis of their abstracts, and these labels were then used to train an active-learning model to prioritise similar documents. This procedure was repeated three times on slightly different datasets, each derived from modified search queries targeting specific subtopics, with approximately 50 references manually labelled for each run. The tool proved effective in identifying additional papers closely related to the initially selected works. However, its recommendations tended to focus on relatively narrow thematic clusters, limiting its usefulness for mapping the broader landscape of modelling approaches.

To complement this, for several key publications the web-based tool *Connected Papers* [14] was used to generate citation-based network graphs of closely related prior and derivative works. In combination with manual forward- and backward-citation tracking from these networks, this approach was found to provide a more comprehensive overview of the literature on the topic.

3. Experimental behaviour

To evaluate the accuracy and suitability of different modelling approaches, it is deemed necessary to understand the expected mechanical and dynamic behaviour of wrinkled and crumpled structures. This section therefore briefly reviews the wrinkle-to-crumple transition and its implications for structural dynamics.

3.1. Wrinkle-to-crumple transition

The formation of wrinkles, crumples, folds, and creases is a fundamental response of thin-sheet structures subjected to compressive stresses. Such stresses can arise in a wide variety of loading and geometric configurations, including sheared, stretched, pressurised, or inflated systems. Because the terminology used for these surface instabilities is not entirely standardised, the following discussion adopts pragmatic working definitions that are consistent with the cited literature.

Thin sheets are comparatively stiff in in-plane compression, and therefore tend to relieve compressive stresses by buckling out-of-plane, ultimately minimizing energy by trading membrane energy for bending energy. *Wrinkles* provide an effective mechanism for this relaxation: they are small-wavelength undulations that typically form in a spatially homogeneous manner around a slightly sheared or compressed region. Wrinkling usually remains within the elastic regime and is therefore largely reversible once the compressive load is removed. [1, 10]

When geometric confinement is increased, Timounay et al. [10] showed that *crumples* arise as the generic evolution of wrinkles. A small number of smooth wrinkles sharpen into stress-focusing ridges and vertices, while other wrinkles disappear, see Figure 2. In this process, Gaussian curvature and material stress are reduced over most of the sheet, with stresses and (optionally plastic) deformations becoming highly localised near the edges of individual crumples.

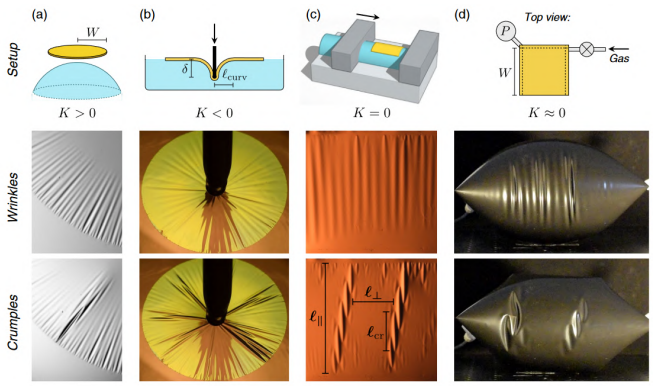

Figure 2: Wrinkle-to-crumple transition in a wide range of systems. The formation of stress-localising crumples from homogeneous wrinkles is a generic response to increasing confinement and compressive stress [10].

Folds can likewise be viewed as a further evolution of wrinkling, characterised by localised, deep surface valleys. In the extreme, *creases* are formed, characterized by self-contact and extremely sharp ridges. Although these terms are sometimes used interchangeably with crumples, the terms folds and creases are more commonly employed in the context of stiff films bonded to soft substrates or floating on liquids [11]. Various studies have attempted to predict which type of instability (wrinkling, folding, creasing, or crumpling) will emerge based on generalised system properties, with the aim of characterising the wrinkle-to-crumple transition. [10, 15]

Various variables can affect the evolution from a wrinkled to a crumpled structure. For example, the loading rate influences the ratio of elastic to plastic deformation [2]; as a fast deformation does not allow for much material relaxation, the resulting structure is more randomly folded (high entropy) with sharper plastic ridges [2]. Furthermore, for highly compacted crumpled sheets the *packing density* reaches a limit where the network of self-contact and interlocking stiffens the system, despite the fact that a significant part of the structure is still air [2]. In various situations, there exists a power-law correlation between the compaction force and this final packing density. Finally, the elasto-plastic behaviour of materials can vary; aluminium sheets are one example of a system that can be readily plastically creased [2, 4].

3.2. Structural dynamics of wrinkling

Although not available for crumpled structures, several experiments have been performed on the vibrational behaviour of wrinkled membranes compared to their unwrinkled state.

Photogrammetry is a method where multiple high-resolution cameras are used to triangulate a 3-dimensional map of a system's wrinkled configuration. These measurements have been used to compare computational findings with experimental data [16–18]. If one is also interested in the modified dynamics caused by wrinkling, *Doppler-interferometry* can be used. These studies make use of scanning laser vibrometers to capture the displacements of many points on the surface, utilising the fast Fourier transform to calculate a collection of mode shapes with corresponding eigenfrequencies [1, 19].

In general, wrinkles have been found to greatly influence the dynamics of systems in a variety of situations [16, 20]. One often encounters new low-frequency mode shapes with strong undulations localised to the wrinkled region, albeit with low modal mass. The global mode shapes with high modal mass, also present in the unwrinkled configuration, are affected as well. Depending on the interaction of a particular mode with the wrinkled region, the eigenfrequencies found are often several percent lower. This is commonly explained via the lower stiffness associated with the bent wrinkled structures [16, 20].

As performing experiments in a perfect vacuum environment is a difficult task, one should be aware of the effects the surrounding air can have on the vibrational behaviour of membranes. Kukathasan and Pellegrino [21] found that there exists a coupling between a *non-wrinkled* membrane and the surrounding layer of air, with the thickness of this layer dependent on the mode number. The air acts as an additional non-structural mass term which causes the eigenfrequencies to decrease and mode shapes to change. As more air mass is in play for the lower frequency modes, this effect is less pronounced at higher frequencies. The results found for their in-air model were subsequently backed-up by experimental data. In a follow-up study using the same in-air computational procedure on a *wrinkled* membrane, Kukathasan and Pellegrino [19] found the same decrease in eigenfrequencies. Also notable is that the vacuum modes with small modal mass, where only the wrinkles vibrate, were removed by the added mass of air.

Puzzled by the high modal damping values (3-10%) found by another experiment on a wrinkled sun-shield [22], Kukathasan and Pellegrino [19] also searched for other sources of damping besides material damping. They indeed found non-linear behaviour at larger shaker excitations where the apparent damping would increase. This was found to be caused by energy scattering into the excitation of harmonic modes at multiples of the actuation frequency. This hardening non-linearity would lead to an increased apparent damping of the system with increasing excitation amplitudes.

Hossain et al. [1] observed the dynamics of a systematically creased tensioned membrane. Here the change in eigenfrequencies compared to the pristine configuration depended on the mode and number of creases. It was argued that the mode dependence relied on the specific interaction of the crease with that mode, a feature that is also seen with wrinkles. Some modes of vibration may stretch the crease, decreasing the stiffness and thus decreasing the eigenfrequency. Other modes may bend the crease, leading to the opposite reaction.

In another study a wrinkled inflated arch was subjected to a transverse tip load by Wang et al. [20] under various internal pressures. They found the wrinkling characteristics to be sensitive to this inflation pressure, which in turn had an effect on the vibrational behaviour. As expected, for pressures leading to more wrinkling a larger decrease in eigenfrequencies was found, especially for mode shapes interacting with the wrinkled regions.

In conclusion, it may be assumed that wrinkles in any structure will have a considerable effect on the resulting mode shapes and eigenfrequencies. Although highly dependent on the system and wrinkling configuration, the reduced stiffness due to the created undulations tends to decrease the eigenfrequencies of the global modes. Unfortunately, little is known regarding the dynamics of crumpled structures, or how these buckling instabilities affect vibrational transmissibility.

4. Computational challenges

The static and dynamic simulation of post-buckled thin structures poses some particular challenges compared to stiff solids. The most pressing computational obstacles often discussed in the literature are listed, roughly in order of priority.

1. **Under-constrained buckling**
   For highly under-constrained buckling structures the solution path often becomes unstable. These systems show an extreme amount of bifurcation points associated with the many configurations in which the sheet can buckle. Each of these bifurcations marks an instability leading to a (near-)singular stiffness matrix [23]. Traditional computational methods aim to iteratively converge to the equilibrium solution of a system by implicitly solving the static or dynamic system of equations. For (geometrically) non-linear systems, these Newton-Raphson (NR) type integration schemes base their search direction on the locally linearised system stiffness matrix. By taking the inverse of this stiffness matrix, the appropriate step in the solution space can be found. However, with the use of implicit schemes this near-singular stiffness matrix can lead to instability and slow convergence. Therefore, measures must be taken to better condition the stiffness matrix, while also carefully traversing the sudden snap-throughs and snap-backs present at the bifurcation into buckling [24, 25].

2. **Small features**
   As the average size of wrinkles and crumples gets smaller with lower bending stiffness, the number of wrinkles in thin sheets can quickly become substantial. The mesh density needed to correctly capture the intricate out-of-plane geometry is roughly inversely proportional to the expected size of the wrinkles [24]. This decrease in element size will subsequently lead to an increase in computational time, even if the global out-of-plane behaviour may not be overly complicated. Therefore, measures which can lessen the need for high element densities are often sought after.

3. **Elasto-plasticity**
   The formation of folds and creases can lead to the need to consider material plasticity effects. In ridges with extreme bending, plastic deformation may relieve some bending stress by plastic yielding, leading to a softer response. The simulation of highly elasto-plastic materials such as aluminium sheets would benefit from such a non-linear material model [2]. However, it should be noted that the intended use case of the present study does not concern this extreme degree of compaction and will therefore not focus on the particular implementations of elasto-plastic materials models as seen in literature.

4. **(Self-)avoidance**
   For highly compacted crumpled structures, the self-contact of a sheet with its other faces starts to play a larger role. The physical fact that a crumpled sheet should never intersect itself is often coined *self-avoidance* in computational mechanics [4, 26, 27]. However, the computational cost to make sure these laws are respected is often substantial. Therefore, in many cases *phantom* sheets are considered where collision is neglected entirely. Nevertheless, one should make sure to mind the effects of collision of a sheet with itself or other objects, as the introduction of (self-)avoidance has shown to affect the number and length of crumpling ridges predicted [2]. Again, as the case study relevant to the present study does not entail this extreme degree of compaction, collision detection methods will also not be covered elaborately.

5. Discretization methods

The first step in the creation of any computational model is to decide on the appropriate spatial discretization method. Various techniques allow complex geometries to be segmented into smaller elements, making their collection easier to solve. The most familiar method to most engineers will be shell-based finite element analysis, but other recent methods have shown their capability in the modelling of thin sheets. Examples include spline-based isogeometric analysis, membrane-based tension field theory, and particle-based discrete element analysis. These specialised methods will be explained and compared to finite element analysis based on their characteristics relevant to the (dynamic) simulation of buckled thin sheets.

5.1. Finite element analysis

Finite element analysis (FEA) is the most traditional method for the simulation of all types of mechanical problems. Typically, buckling thin sheets are modelled using shell formulation capable of six degrees-of-freedom (DoF) in order to consider large displacements and rotations [28]. The static equilibrium can then be solved using geometrically non-linear iterative solvers, available in numerous commercial finite element software. Linearised modal analyses can be performed on the resulting buckled geometry and system matrices to obtain dynamic insights. For the purposes of this review, FEA will be used as a benchmark to compare the other discretization methods in this section to. Also, it should be assumed that referenced studies showcasing advanced solution procedures in section 6 make use of FEA unless otherwise stated.

5.2. *Isogeometric analysis*

In a landmark 2005 paper by Hughes et al. [29], the framework of isogeometric analysis (IGA) was proposed to bridge the gap between computer-aided design (CAD) and traditional FEA software. As is customary in CAD software, the geometry of a body in IGA is represented using *non-uniform rational B-splines* (NURBs), defined by control points [30]. This method eliminates the time needed to convert a spline-based CAD geometry to a Lagrangian node-based discretised mesh suitable for FEA. However, in practice analysis-aware geometric modelling of the part is needed to create so-called *watertight* models [31], as the boolean operations and trimming often used in CAD cannot be used directly. One needs to create the model out of several topologically rectangular *patches*, stitched together with non-smooth connections. This fact introduces the need for some additional precaution during design to make sure non-symmetric stitches do not influence results.

In many aspects, the goal of simulation stays the same as in traditional FEA: minimizing the residual between internal and external forces, but now with the solution represented as a vector of spline control-points instead of nodal displacements. As the spatial discretization is in principle decoupled from a solution procedure, the techniques of section 6 are also applicable here. Because IGA is still in its infancy compared to FEA, the preference of one method over the other is a highly debated topic between researchers. However, the spline-based structure does incur some unique advantages relevant to the simulation of thin sheets in particular.

The first difference to FEA is the allowance for simulation using exact geometries. As portrayed in Figure 3, a geometry does not suffer from discretisation errors when build using NURBs, with smooth splines connecting the geometry between *knots*. As there is no need to approximate the geometry using line-elements between nodes, performance improvements may be applicable when considering fine structures. In his introductory paper Hughes et al. [29] already notes the analysis of thin shells in particular as a field notoriously sensitive to geometric imperfection.

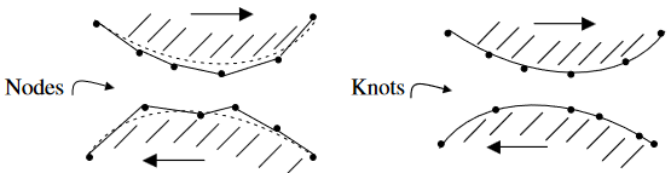

Figure 3: Approximated node-based finite element geometry (left) and exact knot-based isogeometric geometry (right). [29]

To test this notion Oesterle et al. [32] performed a buckling analysis on an axially compressed thin-shell cylinder. It was found that the correct analytical buckling mode shape was obtained using far less total DoFs using IGA compared to various FEA shell representations. For example, for the buckling cylinder the analytically predicted first buckling mode was reproduced using a mesh with one to two orders of magnitude less DoFs compared to the FEA representations. The effect seemed particularly pronounced if numerous critical buckling bifurcations appeared within a small range of load levels.

However, an accompanying analysis was performed [32] to artificially add the geometric imperfections back into the IGA model. By matching the size of the non-smooth topologically rectangular patches in IGA to the element sizes in FEA, the same approximated discretization was obtained. Interestingly, this did not seem to change the results much and the researchers concluded that the geometric exactness of IGA is not the driving force behind the apparent reduction in the required DoFs.

The second advantage of IGA may provide us the explanation for IGA's faster mesh convergence: two strategies to reach convergence in FEA are *h*-refinement, simply increasing the density of the discretized elements, and *p*-refinement, increasing the polynomial order of the basis function of elements. Using *p*-refinement allows for the representation of more complex solution fields using the same number of elements. However, in FEA the polynomial basis function will always only maintain C^0 continuity across element boundaries. A fundamentally new refinement method introduced in IGA allows the user to also increase the order of continuity between elements, at least within patches. These splines with additional smoothness due to *k*-refinement [29, 31, 32] are intuitively appealing for situations in which solutions are very smooth, such as vibrations of structures and wrinkled thin shells. This would subsequently lead to high accuracy per DoF for these applications. Another advantage of *k*-refinement is the possibility to eliminate *optical branches* in the eigenfrequency spectrum for modal analysis. These optical branches are fundamentally inaccurate spikes and outliers of eigenvalues apparent in the second half of the frequency spectrum, seen due to a side-effect of FEA's C^0 continuity [31, 33, 34].

Another benefit for thin sheets in particular is the straightforward implementation of the Kirchhoff-Love (KL) shell theory. Due to the spline's C^1 or higher continuity the curvature of the surface can be used directly to model the bending stiffness, without the need to calculate separate rotational degrees of freedom like in FEA. These KL-shells do also not suffer from the same membrane locking effect as pure displacement shell formulations due to their inter-element continuity, preventing underestimations of deformations and stress oscillations for small-thickness elements [35].

Of course, the use of IGA over FEA also carries multiple downsides. Perhaps the most pressing one is the relatively limited software available as compared to the numerous elaborate FEA packages. Nevertheless, IGA has been implemented in open-source packages such as *G+Smo* [36] or as experimental features in larger FEA software, namely *ANSYS LS-Dyna* [37] or *Altair Radioss* [38]. Performance improvements are also certainly not guaranteed, as the higher degree of conti-

nuity between elements leads to larger overlap between basis functions and thus system matrices with increased bandwidth [31]. Despite k-refinement generally allowing for reduced mesh sizes, the actual improvement in computational time highly depends on the geometry and analysis-type [39] and is not yet well-understood. For example, Li et al. [37] found FEA to be faster in principle in the case of a compressed solid cylinder, but IGA did scale better on a higher number of computational cores. Still, thin shells are considered one of the more interesting applications due to the natural implementation of Kirchhoff-Love shell theory and the smooth nature of buckling shell problems.

5.3. Tension field theory

Tension field theory (TFT) is a wrinkling approximation method often used for gossamer (extremely thin) structures in aeronautical applications, such as deployable antennas, solar sails and sun-shields [12]. First proposed by Wagner [40] in 1931 for the analysis of sheet metal girders, the theory assumes the creation of a *tension field* for membranes under shear stresses. Here, a membrane is defined as a sheet of infinitesimal thickness and therefore negligible bending stiffness. Wrinkling will therefore always be preferred to compression, leading to a structure with no compressive stresses and uni-axial tension along the wrinkle lines. Tension field theory refers to the collection of methods to replicate this behaviour by removing compressive stresses without modelling the small features of the complicated wrinkled geometry explicitly, focussing on the resulting average plane strains. [41]

The rich history of TFT begins with various analytical formulations such as the *variable Poisson's ratio* method introduced by Stein and Hedgepeth [42]. Here, the compressive stresses are released by allowing for the over-contraction of wrinkled parts of the membrane via a variable Poisson-ratio. Another influential contribution by Pipkin and Allen [43] formulated wrinkling as an energy-minimization problem: by introducing the *relaxed strain energy density* the membrane was allowed to perform a 'free' zero-energy contraction along the compression direction.

With the advent of FEA, Roddeman et al. [44] were the first to implement TFT in simulation using a modified deformation gradient tensor and membrane-elements. In order to numerically predict which elements these wrinkling modifications should be applied to, a new procedure was introduced: occasionally referred to as the *iterative membrane properties* (IMP) procedure [19], the general goal is to iteratively determine which regions of the membrane should be wrinkled via a *wrinkling criterion*, and subsequently applying a *wrinkling model* to that region. A wrinkling criterion often determines if an element should be considered to be in a taut, wrinkled or slack state based on the in-plane stresses and strains found in the previous iteration. The most accepted method looks at the major and minor principal stresses and strains, the so-called mixed (stress-strain) criterion [44, 45]:

- **Taut** ($\sigma_{min} > 0$)
  Bi-axial tension: use standard membrane element stiffness matrix.
- **Wrinkled** ($\sigma_{min} \leq 0$ and $\epsilon_{max} > 0$)
  Uni-axial tension: apply wrinkling model to modify membrane element stiffness matrix such that compressive stresses are removed, resulting in zero stiffness in the compression direction.
- **Slack** ($\epsilon_{max} \leq 0$)
  Bi-axial compression: set membrane element stiffness matrix to zero, allowing for a zero stiffness contraction as needed.

Various formulations of a wrinkling model have been implemented, such as the use of a variable Poisson's ratio or modified deformation gradient. However, most of these methods have been proven to be (mostly) mathematically equivalent by Miyazaki [46]. Alternatives to IMP methods have also been created, for example by the minimization of compression using a *penalty parameter modified material* (PPMM) method [47] or via energy-minimization using Pipkin's relaxed strain energy density model [45]. The most appropriate method often depends on the available software, as many implementations use custom user subroutines in FEA packages such as *ABAQUS* or *ANSYS*. TFT has even been demonstrated by Verhelst [31] using isogeometric analysis in G+Smo, see Figure 4. In this figure it can be seen that the general outline of a stretched and twisted thin cylinder is preserved in the TFT-approximation by predicting taut and wrinkled regions. The most important unifying feature of any wrinkling model is that the stress in the principal direction of compression, normal to the wrinkle lines, vanishes by allowing a zero-stiffness contraction.

Figure 4: Stretched and twisted thin cylinder using Neo-Hookean material in isogeometric analysis [31]. Left figure shows the full Kirchhoff-Love shell model, while the right figure shows a wrinkle approximation based on tension-field theory. The black regions denote taut sections, while grey denotes a wrinkled region where a wrinkling model is defined based on Roddeman et al. [44]. While the shape of wrinkles is not calculated using the approximation, it should be noted that the general outline of the right structure is consistent with the left case.

Some advanced techniques have been devised to help numerical stability for the use of TFT. Rossi et al. [24] use a variable penalty factor to smoothen the transition between states, such that the system does not land in a slowly converging loop by constantly switching states. Liu et al. [48] also use penalty factors in a PPMM method to allow the system to exhibit small but non-zero compressive stresses, such that the non-singularity of the stiffness matrix is retained. Miyazaki [46] notes that this also leads to a better model for a finite thickness physical sheet, as the small compressive stresses capture the real irreversible deformation around wrinkles

as they depend on the deformation path. Taylor et al. [49] decide to skip the inversion of the stiffness matrix entirely by using a dynamic relaxation procedure, to be discussed in section 6, combined with Pipkin's relaxed strain energy density.

In general, TFT has been found to be an effective alternative to full shell-based membrane models. As there is no need to pick mesh sizes small enough to model the individual small-wavelength wrinkles, significant reductions in computational effort can be achieved. Many examples have proven to provide average plane strains consistent with shell-based FEA while using only a fraction of the mesh fidelity, particularly in systems with pre-tensioned or inflated membranes [41, 44]. For example, Rossi et al. [24] showcase that the application of TFT can provide the same results for an inflated airbag as full shell simulation using only 236 instead of 4802 elements. However, it should be noted that TFT is only applicable to very thin sheets and provides us no information on the actual amplitude, wavelength, or distribution of wrinkles. Nevertheless, efforts have been made by Iwasa [17] to compare 3D photogrammetry of a wrinkled membrane to computational results to find the relation between predicted plane shrinkage and wrinkle size.

While most research into TFT focuses on the static solution of wrinkled structures, attention has been devoted into expanding these models into structural dynamics. Comparing wrinkled membrane configurations analysed with and without a TFT algorithm, Hossain et al. [47] found that the application of TFT does indeed influence the resulting eigenfrequencies found. For the shell simulation, the appearance of wrinkles decreases the eigenfrequencies compared to the unwrinkled model. With the TFT algorithm then applied eigenfrequencies increase slightly, attributed to the change in geometric stiffness due to the minimization of compressive stresses. It should be noted that this behaviour is dependent on the particular vibrational mode, as not all modes share the same modal participation factor in the wrinkled region. Hossain et al. [1] used a PPMM wrinkling model, along with a local non-linear material model to model creases, to numerically study the modal dynamics of the creased system mentioned in section 3. They found satisfactory eigenfrequencies within 10% margin of error for both the single- and double-crease case.

Another study by Johnston and Brodeur [50] found less clear correlations. Here a shell-based, TFT-based and physical scale-model of a sun-shield were compared on their vibrational modes. While the eigenfrequencies of the dominant mode were similar, the two computational models differed significantly in the total number of modes, modes shapes and effective masses. More discrepancies were found comparing with the physical model, such as the appearance of more slack regions and asymmetries than predicted in the numerical studies. As the slack regions carry no internal stresses and behave like rigid material, their deformation is highly influenced by the deformation of nearby wrinkles. TFT is often found to have difficulty replicating these slack surfaces, as the wrinkles themselves cannot be simulated [17].

5.4. Discrete element analysis

Due to an emerging interest in the use of highly compacted sheets as a new type of metamaterial [2–4], modelling techniques traditionally used in the field of computer graphics are being adapted to analysis in mechanics. The overarching strategy of discrete element analysis (DEA), also referred to as 3D mass-spring systems [51], is to model a sheet as a collection of mass particles with spring-dampers connecting them to each-other.

Similarly to the simulation of cloth in computer animation or atomic structures in molecular dynamics, a thin sheet can be discretised into a collection of small masses. These particles, often point-masses or rigid triangles, connect to their neighbours via virtual springs and dampers. Andrejevic and Rycroft [27] performed such a simulation of an elasto-plastic thin sheet using a discretization of point-mass nodes, see Figure 5. By translating traditional elasticity models from continuum to discrete strain energy densities, the appropriate parameters can be found for the in-plane spring-dampers connecting these nodes. Bending stiffness was applied using a penalty function on the misalignment of the normal vectors of adjacent triangles, again aiming to imitate continuum bending rigidity. Plasticity can be replicated by adding a constant value to this bending penalty function to specify a non-flat shape as the resting angle.

Contact-detection and self-avoidance is a particularly well-developed subject in computer animation for fabrics and cloth. The detection method used by Andrejevic and Rycroft [27] assigns all nodes into blocks. During simulation all nodes in the blocks within the local search space of a particular node are checked for possible contact. If contact is detected, one method is to correct the position and velocity of the interacting nodes according to conservation of momentum. However, this method can become problematic if multiple contacts are present at once, as considering one contact may cause further self-intersection. Another method relies on penalty functions to separate the particles with stiff local springs, which proved more robust for the researcher's purpose.

Andrejevic and Rycroft [27] note the disparity in time scales between the slower large-scale deformations as opposed to the sudden localised buckling and snap-through events. They implemented a hybrid integration scheme to adaptively switch between an implicit quasi-static formulation and a fully explicit dynamic formulation. In the quasi-static formulation accelerations of nodes are approximated to zero, and the subsequent differential-algebraic system of equations is implicitly solved via a version of Newton's method. If large changes in local velocity are detected, for example during rearrangement of ridges and vertices by buckling or during abrupt self-contact, the solver switches to the fully dynamic formulation. The buckling is now explicitly solved

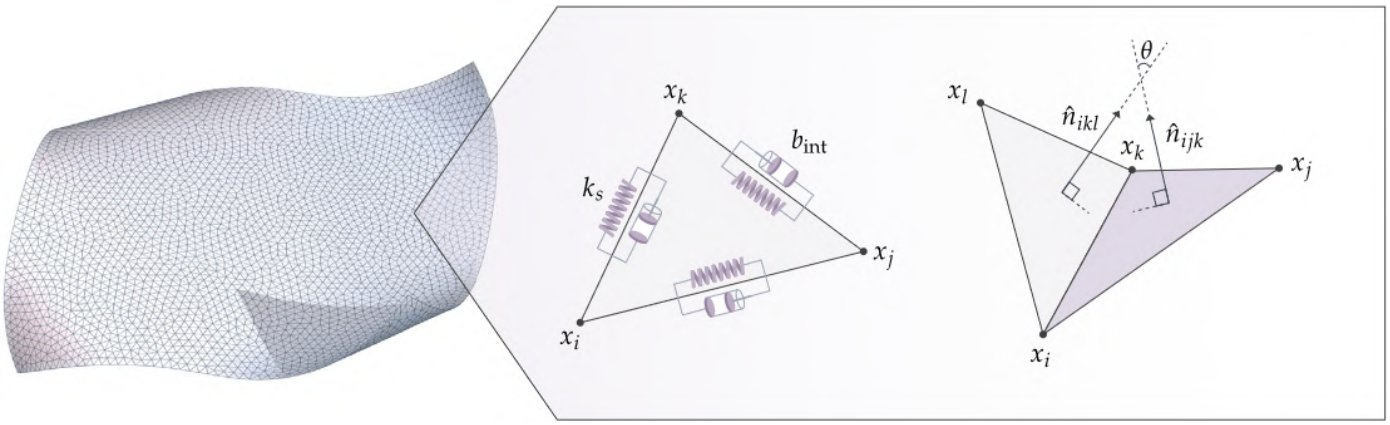

Figure 5: Microscopic model of a discretised sheet defined by point-masses in discrete element analysis [27]. In-plane stretching is governed by spring-dampers between neighbouring nodes. Bending stiffness is defined via a penalty factor on the misalignment of normal vectors between adjacent triangles.

using a Runge-Kutta integration method with adaptive step-control. Using this method the researchers were successful in the simulation of highly compacted sheets, finding the same logarithmic crease length growth as found in experiments [2, 4].

A common concern in DEA literature on stiff thin sheets is the issue of *bending locking* [52]. As bending can only occur along the vertices of adjacent triangles, sharp bends not perfectly aligned with these directions can only be achieved via the bending of multiple other ridges. When using a coarser mesh this fact leads to an artificial stiffness to bending and unrealistic bending behaviour. Narain et al. [52] used an adaptive re-meshing procedure to iteratively refine their triangle-based discretization to create edges aligning with bending. For stiff thin shells they found that jittering would occur when simply refining the mesh by splitting the existing triangles. For this reason, a dynamic projection method was introduced to interpolate node forces instead of node positions, such that the dynamic equilibrium before and after re-meshing is preserved. The researchers found adaptive re-meshing to be an effective way to reduce mesh density while being able to resolve fine features and large flat regions simultaneously.

Another way to prevent bending locking is by simply decreasing the stiffness of the bending springs (penalty factors). However, this would make the material appear softer than may be desired. Jin et al. [53] replaced the equality constraint on the triangle edge lengths with an inequality constraint to allow some element compression, such that this slight compression can function as a surrogate model for bending modes that would otherwise not be representable by the mesh. The inequality constraint was implemented using a penalty function (barrier method) and an optimization algorithm using Newton steps and line searches to solve for the equilibrium shape. This is an example of how form-finding problems in DEA are often formulated as optimization problems, with an energy function consisting of bending energies and penalty parameters to be minimized [54].

The discretised nature of DEA leaves one major drawback: many concepts found in continuous models that are often used in dynamic analyses are absent. Lacking any form of traditional system matrices, the inability to perform eigenvalue analysis rules out any modal and harmonic analyses. This only leaves explicit time-domain simulation to be used for structural dynamics. Due to the need for minuscule time-steps at higher frequencies, this would be costly to simulate and has not been attempted to the best of the author's knowledge. Common tools in computer graphics are also not designed for strict accuracy in the prediction of stresses and strains, as they are mainly designed for efficiency and visual realism. Only more recent studies provide any basic comparison to FEA in mechanical accuracy on simple problems [51]. Due to these two factors, DEA is not (yet) considered a complete tool for the structural dynamic analysis of thin sheets, and will be subsequently disregarded in following discussion.

6. Solution procedures

When a spatial discretization method and other model definitions have been established, the residual between external and internal forces can be calculated. Regardless of the discretization used, this residual and the corresponding solution vector can be used in a generalized non-linear solution procedure in order to integrate the residual to zero and find equilibrium. In this section, the most commonly used advanced numerical solution procedures relevant to buckled thin sheets will be covered, namely the introduction of initial perturbations, dynamic relaxation, arc-length methods, modal reduction and sensitivity analysis.

6.1. Initial perturbation

Initial perturbations are often applied to sheets in order to nudge the element nodes from their *perfect* initial condition, such that the initiation of buckling becomes easier. Without these perturbations, the structure would not prefer any one way to buckle and would slowly approach a buckling bifurcation with increasing load [55]. These buckling bifurcations are associated with singularities in the system stiffness matrix, which in turn contribute to stability problems for traditional implicit solvers. By applying small perturbations the perfect bifurcations can be smoothed and thus more easily passed without full singularities forming [55].

In general two methods exist to apply initial perturbations. The pseudo-random *direct turbulence* method uses randomly assigned force perturbations on the nodes, setting the net force on the total body equal to zero in order not to influence the system behaviour [16, 56]. A more commonly used method is to perform a linear buckling analysis on the initial configuration in order to calculate the first (few) buckling mode(s) [57, 58]. This *scaled buckling modes* method uses a scaled superposition of these modes to subsequently perturb the nodes. This buckling mode version of perturbation would theoretically cause the structure to buckle via the 'ideal' buckling path and is therefore repeatable. However, one could argue that the turbulence method is more accurate to the imperfect systems we find in reality, and could also be made repeatable by starting the random number generator with a consistent seed. In either case, the perturbations are removed shortly after the initial buckling in order not to influence the final result by too much. Liu and Cai [57] suggest a perturbation of 1%-100% of the membrane thickness as a middle-ground for not making the initial stage of buckling too slow while not influencing results.

6.2. Dynamic relaxation method

The dynamic relaxation method (DRM) is an explicit iterative algorithm for the static analysis of structures. The method avoids the calculation of a near-singular stiffness matrix by the use of an explicit scheme. First given this name by Day [59], the static solution is considered as the limit or steady-state part to the transient response of the system. To illustrate this, the static solution can be written as the solution of the system of differential equations

$$\mathbf{f}(\mathbf{u}, \dot{\mathbf{u}}) = \mathbf{p}, \tag{1}$$

with $\mathbf{f}$ being a generally non-linear vector function representing the internal forces, dependent on the nodal displacements $\mathbf{u}$ and its time derivative $\dot{\mathbf{u}}$, and $\mathbf{p}$ being the external forces. Note that Equation 1 can be written in a linear form where the left-hand side is converted to a product between the stiffness matrix K and displacement vector $\mathbf{u}$, to be solved algebraically. However, in the general non-linear case the solution can be iteratively solved for by integrating the solution via an implicit Newton-Raphson (NR) type method using the inverse of the locally linearized stiffness matrix K [60].

Alternatively, in DRM the equation is expanded by turning it into the damped dynamic equation

$$\mathrm{M'}\ddot{\mathbf{u}} + \mathrm{C'}\dot{\mathbf{u}} + \mathbf{f}(\mathbf{u}, \dot{\mathbf{u}}) = \mathbf{p}, \tag{2}$$

with M' and C' respectively the fictitious mass and damping matrices. This is a problem in the *pseudo-time* domain, which can be integrated using central finite difference methods [55, 60].

Note that in the absence of any nodal velocities $\dot{\mathbf{u}}$ or accelerations $\ddot{\mathbf{u}}$, Equation 2 reduces into the same form as Equation 1. Thus it can be seen that the static solution may indeed be regarded as the limit of the damped dynamic response. As the fictitious mass and damping matrices play no role in this final solution, they can be artificially chosen based on heuristic rules with the purpose of a fast but stable convergence. While various methods to construct the mass matrix exist, a popular way introduced by Underwood [61] is to choose a diagonal mass matrix based on Gershgorin's circle theorem. The diagonal mass elements are based on the corresponding entries in the effective stiffness matrix, and may be updated multiple times during iteration via the equation

$$m_i = \frac{\lambda \Delta t'^2}{2} \sum_j |\mathrm{K}_{ij}|, \tag{3}$$

where m_i is the mass at node i, $\Delta t'$ is the fictitious time-step and λ an adjustable parameter used to improve stability. The sum is taken over the absolute entries of the local tangent stiffness matrix in all Cartesian directions j. The use of (a version of) Gershgorin's theorem ensures an optimum ratio between the minimum and maximum eigenfrequencies of the system [58, 62, 63].

For the fastest convergence possible, the fictitious damping term should lead to a perfectly damped system. In practice, *viscous* damping like in Equation 2 is usually avoided as a trial analysis is needed to estimate the lowest eigenvalue via Rayleigh's principle [62]. Instead, *kinetic* damping is regularly used [58, 60, 64]: setting C' = 0 in Equation 2, the damping behaviour is instead artificially replicated by studying the systems total potential and kinetic energies. For a conservative mechanical system, these two energy types alternate in their magnitudes. When the kinetic energy is at its maximum, the potential energy will be at its minimum, with this minimum corresponding to the state most resembling equilibrium. When using kinetic damping, the geometry of the system is frozen at this peak of kinetic energy. By constantly resetting the velocities to zero and restarting dynamic simulation from this frozen geometry, a simple yet efficient artificial damping behaviour is introduced, see Figure 6 [65].

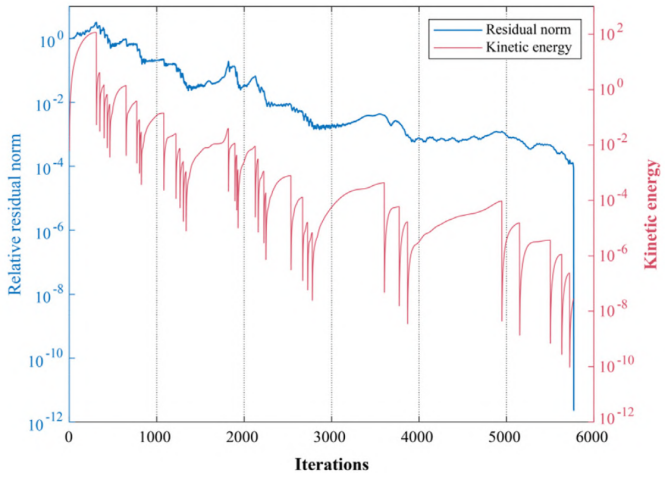

Figure 6: Typical histories of relative residual norm and kinetic energy of a system with kinetic damping. At every peak in kinetic energy the nodal velocities are reset to zero, leading to a damping effect without the need for viscous terms. The residual norm can be seen to decrease, with a sharp decline when the dynamic relaxation scheme switches to implicit Newton-Raphson integration in its final iterations [65].

DRM is particularly well suited to buckled thin sheets, as there is no need for an inversion of the often near-singular stiffness matrix due to its explicit nature. Since all quantities can be treated as vectors, the DRM is easily programmable and has low storage requirements, while also being ideal for systems with highly non-linear geometric and material behaviour [25].

Lee and Youn [63] successfully used viscously damped DRM together with a TFT-based discretization to simulate a twisted annulus and an inflated airbag. These results were used as benchmarks by Nakashino et al. [65] for their expanded model based on IGA and kinetic damping. Interestingly, both studies also perform some implicit NR-integration after their DRM procedure to make the final steps towards equilibrium, see Figure 6. This showcases the effectiveness of using DRM for the general form-finding for buckled structures, which may be combined with implicit solvers for the final steps to reach greater precision.

6.3. *Arc-length method*

Incremental NR-procedures are often adopted for problems with highly non-linear boundary conditions which lead to large forces and deformations. In these quasi-static methods the forces or displacements are slowly increased from zero to their final value, while equilibrium is continuously calculated. Depending on the independent variable in these procedures this procedure is respectively referred to as *load-controlled* or *displacement-controlled* time-stepping. For post-buckling analysis in particular these methods are essential to traverse the highly non-linear and unstable behaviour near buckling bifurcations, and thus also of importance to the simulation of crumpled sheets.

Buckling bifurcations lead to the creation of multiple stable and unstable branches. Referring to Figure 7 [66], this fact may lead to one of the most difficult issues for either load-control or displacement-control to solve: the creation of each additional wrinkle or crumple corresponds to a bifurcation where localised *snap-through* (BD in Figure 7) or *snap-back* (GI in Figure 7) may occur. the buckling path is illustrated as a non-linear relation between loading and displacement. It can be observed that the stable branch after a bifurcation point may lead to a (temporary) reduction in either load or displacement. Load-control and displacement-control cannot handle these bifurcations effectively and will suddenly snap to another part of the branch, or even not find any continuation at all [67]. It should be noted that Figure 7 is only a 2D simplification of the multidimensional load-deflection space.

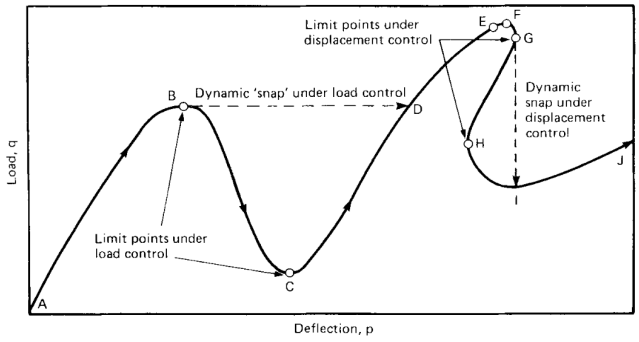

Figure 7: Buckling path plotted as non-linear function of load and displacement [66]. Snap-through (line BD) and snap-back (line GI) events can cause large jumps in the solution for traditional load-controlled or displacement-controlled time-stepping.

The solution for this problem is to combine the two paradigms of load-control and displacement-control in so-called *arc-length methods* (ALM). The main two methods were introduced by Riks [68] and Crisfield [67], both based on the addition of a constraint on the displacement and load increments to stay inside a defined hypersphere of certain arc-length [69]. For both methods a prediction step of this arc-length is taken tangent to the current position on the buckling path, see point A in Figure 8. From this predicted solution (B in Figure 8) the Riks method defines a hyper-plane (BC in Figure 8) normal to the prediction tangent, to be traversed via NR-iterations. Alternatively, Crisfield's method constrains the NR-iterations to the hyper-sphere (BD in Figure 8) or the hyper-cylinder tangent to the loading parameter (BE in Figure 8).

The Crisfield method is considered to be somewhat more robust, but for ever more non-linear buckling paths, a related but less popular method based on the *normal flow* algorithm could also be considered [69]. Here, the NR-iterations are forced along a path normal to the so-called Davidenko flow curves. These curves can be seen as the contour curves of constant perturbation ($\mathbf{f}(\lambda, d) = \delta$), positioned along the solution curve ($\mathbf{f}(\lambda, d) = 0$). This ensures the fasted possible path from the prediction point to the actual buckling path.

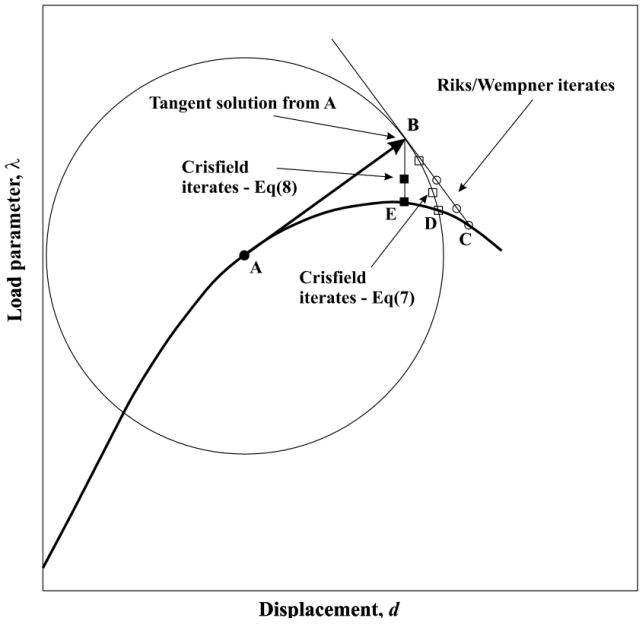

Figure 8: Arc-length method based on Riks' [68] and Crisfield's [67] methods. A prediction increment of certain arc-length is taken along the buckling path tangent. From there Newton-Raphson iterations are taken to find the real equilibrium point on the buckling path, either by walking normal to the prediction tangent (Riks) or along the hypersphere defined by the arc-length (Crisfield). [69]

In most cases DRM and ALM are used as two alternative methods for solving highly non-linear systems. For example, the analysis by Liu and Cai [57] shows ALM to come to a similar result as DRM for a tensioned membrane. However, Lee et al. [64] demonstrated an explicit ALM using dynamic relaxation with kinetic damping. Here, the representation of the external forces $\mathbf{p}$ in Equation 2 is expanded using an incrementally increasing loading parameter $\lambda^{t+\Delta t}\mathbf{p}_0$ (note that C'= 0 as kinetic damping is used). The loading parameters $\lambda^{t+\Delta t}$ can be subsequently constrained via Crisfield's hyper-cylindrical arc-length constraint. A *total displacement* constraint was also tested, where the arc-length is calculated centred around the initial configuration instead of the current configuration. Here, step increments are not taken tangent to the current position on the buckling curve, but in the direction through the origin to the current position. For both methods the researchers found good agreement with non-linear verification examples, although direct comparison to traditional implicit NR-methods in efficiency is lacking.

Verhelst et al. [23] used ALM to simulate a simple buckling beam via an isogeometric representation in *G+Smo*, but now without using initial perturbations. The ALM allowed for a slow approach near to the bifurcation point. At a small distance from this limit point the first buckling mode was extracted and applied to the system as a perturbation. In this way, it was made possible to skip past the bifurcation and safely switch to the buckling branch past it, without needing 'random' initial perturbations which could influence results.

6.4. Modal reduction

Assuming one has been able to calculate the static crumpled configuration of a thin sheet using one of the aforementioned procedures, various methods exist to get information on the dynamic behaviour. Traditionally, these structural dynamic problems are tackled via frequency domain representations, namely modal analysis [70]. By solving an eigenvalue problem for the mass and stiffness matrices, one quickly finds the relevant eigenmodes and natural frequencies of vibration.

For large interconnected mechanical systems engineers are often interested in the combined dynamics of a large number of subsystems. As modal analyses of the whole system are too large and complex, *dynamic substructuring* (DS) is often applied to compartmentalize the problem [70, 71]. DS aims to decompose a large structure into subcomponents and calculate the dynamics behaviour on component-basis, to be combined later. This recombination may be performed using *frequency-based substructuring* (FSB), which also allows for integration of simulated and experimental data in the form of frequency response functions. However, recombination via *component-mode synthesis* (CMS) in the modal domain proves more flexible and allows for the extraction of mode shapes and time-domain behaviour. Here, *modal reduction* is used to rewrite the equations of motion of a simulated component into a basis of modal vectors [71, 72]. By only considering modes up to a frequency of interest, the full set of physical coordinates can be reduced to a smaller set of generalised coordinates. Examples of popular methods to perform this matrix projection into reduced modal coordinates are the Guyan, Craig-Bampton and Hintz-Herting techniques [71], which differ in how they handle the interfaces and reactions between different components [70, 71].

It should be noted that standard modal analysis and CMS assume linear system behaviour, and will thus be inaccurate for non-linear material behaviour, self-contact, or large vibrations with dynamic buckling [71]. To address the problem for large vibrations, Weeger [34] proposed a nonlinear vibration analysis based on the harmonic balancing method, in which the equations of motion are approximated in the frequency domain using Fourier expansions. However, this approach significantly increases the system size and computational cost. To make the method feasible, a nonlinear-compatible model reduction is required. Weeger [34] introduces a reduction based on *modal derivatives*, which extends the linear modal basis to account for nonlinear deformation effects. This approach enables accurate prediction of nonlinear frequency responses while keeping the computational effort manageable.

6.5. *Uncertainty analysis*

Noting a lack of insight into uncertainty effects associated with system imperfections, Luo et al. [73] performed experiments and simulations to establish the sensitivity of wrinkling amplitude to the non-uniformity of thickness for a stretched Kapton film. Twelve sheets of varying thicknesses were examined, and a substantial spread was found in the location of wrinkles and the extremes in wrinkling amplitudes, see Figure 9. Interestingly, post-buckling simulations of 'perfect' membranes with uniform nominal thickness were consistently found to show less wrinkling than experiment would suggest, indicating the important role uncertain initial conditions play in the initiation of buckling.

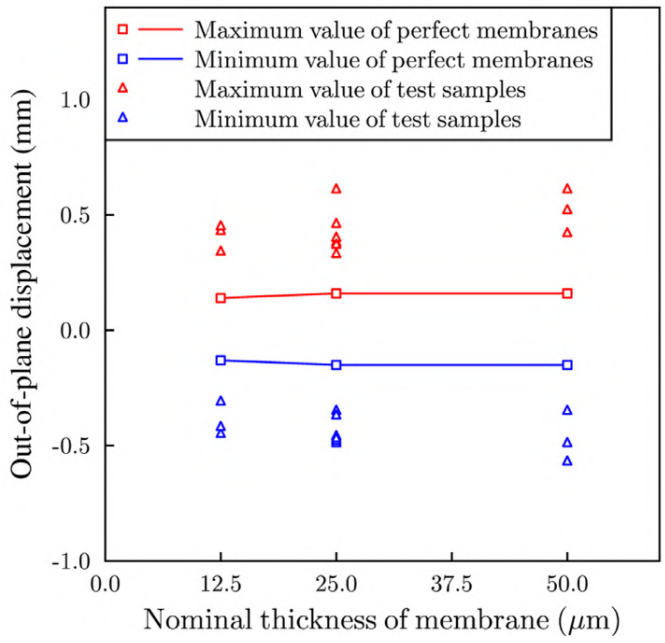

Figure 9: Maximum and minimum out-of-plane wrinkling amplitudes of stretched Kapton membranes from test samples and perfect simulated membranes with uniform nominal thickness [73]. The imperfect test samples consistently showed larger wrinkles than simulation would suggest. The spread between experimental values indicates the importance of accounting for imperfections in experiment.

As experimental data will always be limited by sample size, Luo et al. [73] set out to perform a probabilistic computational analysis of the problem. It should be noted that for most applications it is difficult to get an exact measure of the non-uniform thickness profile, therefore an uncertain field model with *bounded-field* description was used based on the nominal thickness and tolerance provided by the manufacturer. A probabilistic function determined a continuous thickness field within the aforementioned bounds, utilising a spatial correlation parameter to determine smoothness. The resulting total out-of-plane displacement was calculated for numerous models in order to construct a surrogate model to predict input-output behaviour. The initial sampling points were determined via orthogonal-maximin Latin hypercube design, with subsequent sampling points efficiently added to maximise the expected value of a so-called improvement function. The method was able to efficiently compute the expected upper and lower bounds for the total out-of-plane displacement for an increasing thickness tolerance bound, see Figure 10. These bounds were proven to be consistent with the results from 10,000 Monte Carlo realisations.

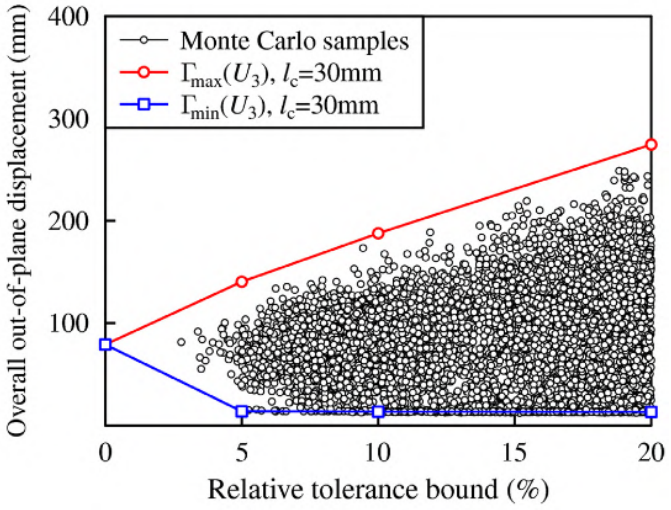

Figure 10: Relationship between overall out-of-plane displacement and relative tolerance bound for rectangular Kapton membrane simulations. The spread for 10,000 Monte Carlo realizations is shown to be consistent with the predictions for the upper (Γ_{max}) and lower (Γ_{min}) bounds made by a trained surrogate model. [73]

A generalization of the uncertainty analysis procedure was presented by Vu-Bac et al. [74] in the form of a *MATLAB* toolbox. The unified framework can be used to generate random samples, build surrogate models to approximate the real system, and perform sensitivity analysis. Again, sampling is performed via the Latin hypercube method in order to get a representative variety of data-points. Surrogate models can be trained via multi-variable polynomial regression, taking overfitting in mind by using cross-validation to assess the validity of the model by performing a priori predictions for a subset of the training data. The surrogate model can then be used to estimate the sensitivity indices of the model with correlated parameters, allowing for a variance-based sensitivity estimation for interdependent variables.

7. Discussion

A great variety of techniques to model the mechanics and dynamics of buckling thin sheets has been presented. We have developed a generalised flowchart to help the reader navigate the relevant choices for themselves, see Figure 11. Many alternative techniques are possible for the discretisation method, material model, perturbation method and the specifics of the post-buckling solver. The aim is to guide the user in finding a suitable collection of methods for their application, discussing (dis)advantages of the different options along the way.

7.1. Preprocessing

As concluded in section 5, DEA is out of the question for structural dynamics due to the impossibility for eigenvalue analysis, and thus the competition falls between FEA and IGA. IGA has proven to have high accuracy per DoF, particularly for thin sheets. The higher degree of continuity associated with the spline-based meshes allow for fast k-refinement, while also making KL-shells easily implementable. Another advantage is the subsequent lack of inaccurate optical branches in the eigenfrequency analysis, relevant to the structural dynamics. However, the efficiency improvements of IGA are not yet well-understood and may depend on the use-case. Along with the relative lack of available software negatively impacting the ease-of-use, FEA is still the best option for most engineering proposes. However, IGA is a quickly developing field which may be of interest to certain specialised applications.

Regardless of the spatial discretization, a TFT algorithm may be used to greatly reduce mesh density. However, it should be noted that TFT can only be applied to small-deformation elastic wrinkling, and not crumpling. Furthermore, TFT may only be applicable in situations of shearing, stretching and inflation, as the slack regions present in compression cannot

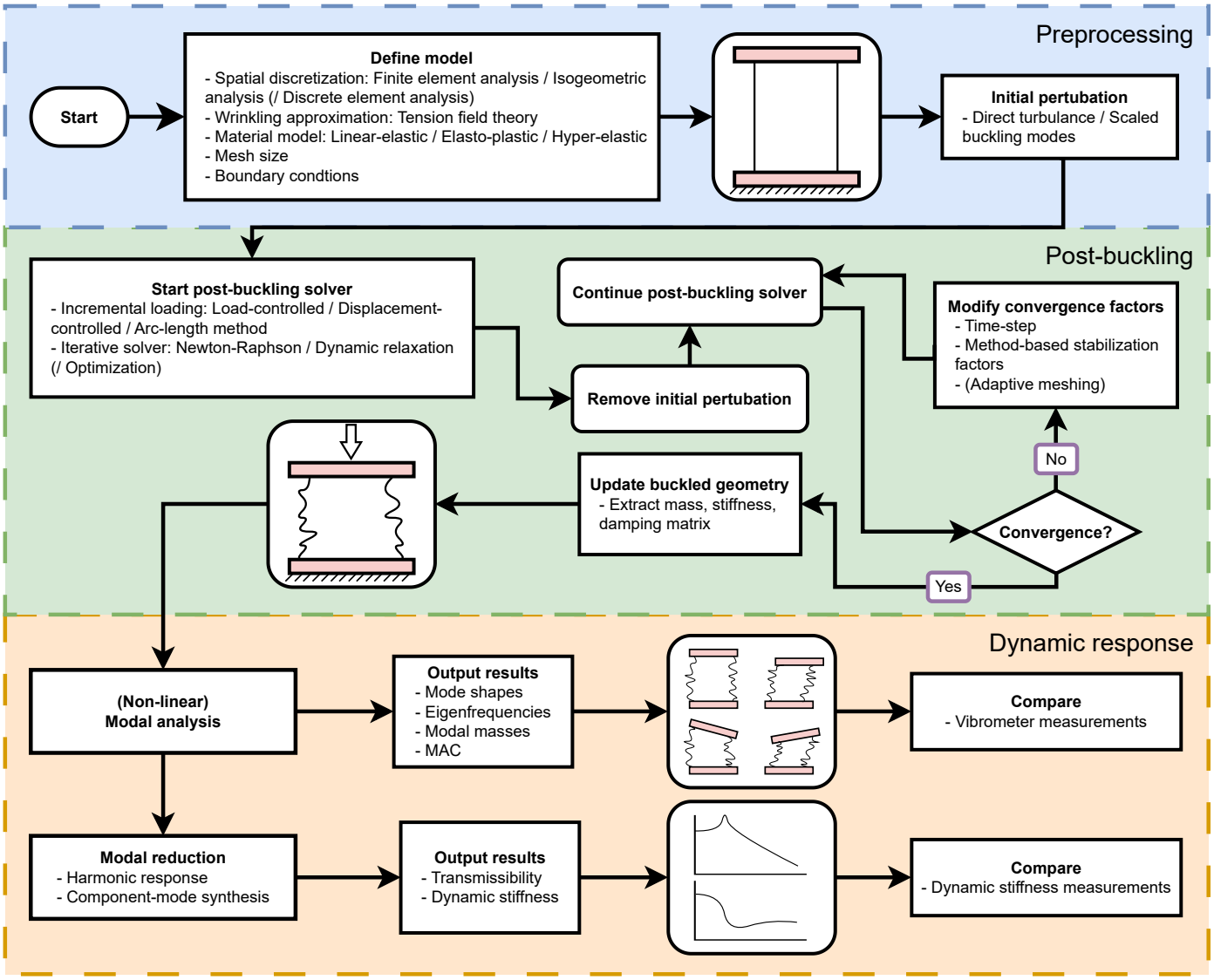

Figure 11: Flowchart for a general structural dynamic analysis of buckled thin sheets structures, developed with the aim to help the reader traverse the diverse options in numerical methods. Sketches indicate the stage in the simulation process, inspired by the cylindrical bellow case study mentioned in the section 1.

be captured accurately. Another disadvantage is the lack of information on the wrinkling geometry itself, which may also negatively impact the accuracy of subsequent modal analysis.

Materials models have not been covered explicitly in this review. However, it should be noted that non-linear material models may be needed in case of extreme compaction (elasto-plastic) or stretching (hyper-elastic).

Regarding initial perturbations, scaled buckling modes may be used to induce the preferred way of buckling for a certain 'perfect' structure. However, in practice no structure is perfect and a more easily implemented random direct turbulence perturbation is probably sufficient. To make results repeatable a consistent seed can be used for the random number generator. It may also be interesting to perform sensitivity analysis on this random perturbation to establish how much we expect experimental data to differ between tests.

7.2. Post-buckling solver

For the non-linear post-buckling solver there exist multiple ways to increment the loading for large deformations. In problems with snap-through and snap-back buckling, load-controlled and displacement-controlled time-stepping may become unstable. ALM offers a combination of the two to create a more stable method, ensuring that the buckling path is not lost at bifurcation points, at the cost of more complicated implementation.

Dynamic relaxation is also a useful method to ensure stability despite the near-singular stiffness matrices found in buckling. DRM with kinetic damping is easily implemented via vector-representations and convergence can be intuitively understood. However, convergence may still not be as fast as the quadratic convergence of implicit Newton-Raphson integration. For this reason some NR-iterations are preferred after a DRM procedure to make the last steps toward equilibrium. As modal analysis requires the calculations of the system matrices either way, the implementation of implicit NR-integration should not incur much more effort.

After a few iterations of the non-linear solver the initial perturbations should be removed in order to not influence the final results. If convergence cannot be reached after more iterations, the relevant convergence factors may be modified. Besides simply reducing the time-step, specific methods allow for the adjustment of their stabilization factors. Examples include the fictitious mass matrix and kinetic damping criteria in DRM, the arc-length in ALM, or the compression-minimizing penalty factors in TFT. Adaptive meshing could also be considered in order to more finely describe the mesh around crumple lines, although thus far such methods have only been tested in DEA.

7.3. Dynamic response

After the static post-buckling form-finding problem has been solved, the buckled geometry can be updated and the system matrices extracted. Mode shapes, eigenfrequencies and modal masses can be calculated by solving the eigenvalue problem on the updated mass and stiffness matrices. As most engineering problems consider small-amplitude vibrations, non-linear modal analysis is not required. A *modal assurance criterion* (MAC) may be used to know what mode shapes to compare between slightly different simulation by computing their correlation in displacement [72]. Mode shapes and eigenfrequencies may also be checked against vibrometer measurements, allowing for the verification and improvement of the modelling method. In the same vein, modal reduction using component-mode synthesis may be used to calculate the harmonic response for vibrational transmissibility between specified interface nodes. The resulting transmissibility or dynamic stiffness frequency response may again be compared against measurements.

Depending on the perceived spread between measurement results, it may be of interest to perform uncertainty analysis on the problem by building a surrogate model. Many variables are expected to impact buckling behaviour, such as sheet dimensions, non-uniform thicknesses or the random initial perturbations.

8. Conclusion

We have presented a generalised framework for the dynamic simulation of buckled thin sheets, highlighting a range of methods found in the literature. Both advanced discretization and solver techniques are addressed, including comparisons between isogeometric and discrete element analysis versus traditional finite element approaches. Tension field theory is discussed as an effective tool for reducing mesh size, though it must be applied with care. To handle the near-singular stiffness matrices typical of buckled systems, advanced iterative solvers such as dynamic relaxation and the arc-length method are considered. Finally, we propose performing dynamic analysis of buckled sheets through modal reduction, complemented by uncertainty analysis methods to improve the predictive reliability of these complex systems.

References

[1] N. Hossain, K. Woo, C. Jenkins, Dynamic Response of Systematically Creased Membranes, in: 48th AIAA/ASME/ASCE/AHS/ASC Structures, Structural Dynamics, and Materials Conference, American Institute of Aeronautics and Astronautics, 2007. doi:10.2514/6.2007-1806.

[2] M. C. Fokker, S. Janbaz, A. A. Zadpoor, Crumpling of thin sheets as a basis for creating mechanical metamaterials, RSC Advances 9 (2019) 5174. doi:10.1039/c8ra07565d.

[3] J. Kwon, O. Bouaziz, H. S. Kim, Y. Estrin, Finite Element Modeling of Crumpling of Metallic Thin Foil, Advanced Engineering Materials 25 (2023) 2300063. doi:10.1002/adem.202300063.

[4] G. Giménez-Ribes, M. Motaghian, E. van der Linden, M. Habibi, Crumpled structures as robust disordered mechanical metamaterials, Materials & Design 232 (2023) 112159. doi:10.1016/j.matdes.2023.112159.

[5] S. Kundu, R. Sriramdas, K. R. Amin, A. Bid, R. Pratap, N. Ravishankar, Crumpled sheets of reduced graphene oxide as a highly sensitive, robust and versatile strain/pressure sensor, Nanoscale 9 (2017) 9581–9588. doi:10.1039/C7NR02415K.

[6] O. Bouaziz, R. Bouafif, R. Massion, Sandwich materials with a crumpled aluminium core, Metallurgical Research & Technology 118 (2021) 320. doi:10.1051/metal/2021014.

[7] M. Ganjian, S. Janbaz, T. van Manen, N. Tümer, K. Modaresifar, M. Minneboo, L. E. Fratila-Apachitei, A. A. Zadpoor, Controlled metal crumpling as an alternative to folding for the fabrication of nanopatterned meta-biomaterials, Materials & Design 220 (2022) 110844. doi:10.1016/j.matdes.2022.110844.

[8] C. A. Maas, B. Thibault, New Generation of Flexible Elastomer Exhaust Decouplers: LINKEO™ System, Technical Report 2005-01-1153, SAE Technical Paper, 2005. doi:10.4271/2005-01-1153.

[9] N. Yamaki, Elastic Stability of Circular Cylindrical Shells, North-Holland Series in Applied Mathematics and Mechanics; Vol. 27, North-Holland, Amsterdam, 1984.

[10] Y. Timounay, R. De, J. L. Stelzel, Z. S. Schrecengost, M. M. Ripp, J. D. Paulsen, Crumples as a Generic Stress-Focusing Instability in Confined Sheets, Physical Review X 10 (2020) 021008. doi:10.1103/PhysRevX.10.021008.

[11] B. Li, Y.-P. Cao, X.-Q. Feng, H. Gao, Mechanics of morphological instabilities and surface wrinkling in soft materials: A review, Soft Matter 8 (2012) 5728–5745. doi:10.1039/C2SM00011C.

[12] A. Chandraul, M. V, S. Kumar, A review on dynamic analysis of membrane based space structures, Advances in Space Research 74 (2024) 740–763. doi:10.1016/j.asr.2024.03.082.

[13] ASReview - Active learning for Systematic Reviews, https://asreview.nl/, 2025.

[14] Connected Papers | Find and explore academic papers, https://www.connectedpapers.com/, 2025.

[15] H. King, R. D. Schroll, B. Davidovitch, N. Menon, Elastic sheet on a liquid drop reveals wrinkling and crumpling as distinct symmetry-breaking instabilities, Proceedings of the National Academy of Sciences 109 (2012) 9716–9720. doi:10.1073/pnas.1201201109.

[16] Y.-L. Li, M.-Y. Lu, H.-F. Tan, Y.-Q. Tan, A study on wrinkling characteristics and dynamic mechanical behavior of membrane, Acta Mechanica Sinica 28 (2012) 201–210. doi:10.1007/s10409-011-0512-2.

[17] T. Iwasa, Experimental verification on wrinkling behavior given by wrinkling analysis using the tension field theory, International Journal of Solids and Structures 136–137 (2018) 1–12. doi:10.1016/j.ijsolstr.2017.11.028.

[18] C. G. Wang, X. W. Du, H. F. Tan, X. D. He, A new computational method for wrinkling analysis of gossamer space structures, International Journal of Solids and Structures 46 (2009) 1516–1526. doi:10.1016/j.ijsolstr.2008.11.018.

[19] S. Kukathasan, S. Pellegrino, Nonlinear Vibration of Wrinkled Membranes, in: 44th AIAA/ASME/ASCE/AHS/ASC Structures, Structural Dynamics, and Materials Conference, Structures, Structural Dynamics, and Materials and Co-located Conferences, American Institute of Aeronautics and Astronautics, 2003. doi:10.2514/6.2003-1747.

[20] C. G. Wang, J. Xie, H. F. Tan, Vibration Simulations of a Wrinkled Membrane-Inflated Arch, Journal of Aerospace Engineering 27 (2014) 414–422. doi:10.1061/(ASCE)AS.1943-5525.0000260.

[21] S. Kukathasan, S. Pellegrino, Vibration of Prestressed Membrane Structures in Air, volume 2, 2002. doi:10.2514/6.2002-1368.

[22] S. Lienard, J. Johnston, B. Ross, Dynamic testing of a subscale sunshield for the Next Generation Space Telescope (NGST), 19th AIAA Applied Aerodynamics Conference (2001). doi:10.2514/6.2001-1268.

[23] H. M. Verhelst, M. Möller, J. H. D. Besten, F. J. Vermolen, M. L. Kaminski, Equilibrium Path Analysis Including Bifurcations with an Arc-Length Method Avoiding A Priori Perturbations, in: F. J. Vermolen, C. Vuik (Eds.), Numerical Mathematics and Advanced Applications ENUMATH 2019, Springer International Publishing, Cham, 2021, pp. 1109–1117. doi:10.1007/978-3-030-55874-1_110.

[24] R. Rossi, R. Vitaliani, E. Oñate, FE Analysis of membrane systems including wrinkling and coupling (2005). doi:10.1007/1-4020-3317-6_6.

[25] Haseganu, M. Eliza, Analytical Investigation of Tension Fields in Lightweight Membrane Structures, Ph.D. thesis, University of Alberta, 1994.

[26] T. Tallinen, J. A. Åström, J. Timonen, Discrete element simulations of crumpling of thin sheets, Computer Physics Communications 180 (2009) 512–516. doi:10.1016/j.cpc.2008.12.036.

[27] J. Andrejevic, C. H. Rycroft, Simulation of crumpled sheets via alternating quasistatic and dynamic representations, Journal of Computational Physics 471 (2022) 111607. doi:10.1016/j.jcp.2022.111607.

[28] W. Changguo, L. Yunliang, D. Xingwen, H. Xiaodong, S. Guozhi, Simulation Analysis of Vibration Characteristics of Wrinkled Membrane Space Structure, International Journal of Space Structures 22 (2007) 239–246. doi:10.1260/026635107783133825.

[29] T. J. R. Hughes, J. A. Cottrell, Y. Bazilevs, Isogeometric analysis: CAD, finite elements, NURBS, exact geometry and mesh refinement, Computer Methods in Applied Mechanics and Engineering 194 (2005) 4135–4195. doi:10.1016/j.cma.2004.10.008.

[30] R. Cardoso, O. Adetoro, D. Adan, Contact Modelling in Isogeometric Analysis: Application to Sheet Metal Forming Processes, Journal of Physics: Conference Series 734 (2016) 032123. doi:10.1088/1742-6596/734/3/032123.

[31] H. M. Verhelst, Isogeometric Analysis of Wrinkling (2024). doi:10.4233/0e4c3644-31a4-4157-983d-bd001d91b8ca.

[32] B. Oesterle, F. Geiger, D. Forster, M. Fröhlich, M. Bischoff, A study on the approximation power of NURBS and the significance of exact geometry in isogeometric pre-buckling analyses of shells, Computer Methods in Applied Mechanics and Engineering 397 (2022) 115144. doi:10.1016/j.cma.2022.115144.

[33] J. A. Cottrell, A. Reali, Y. Bazilevs, T. J. R. Hughes, Isogeometric analysis of structural vibrations, Computer Methods in Applied Mechanics and Engineering 195 (2006) 5257–5296. doi:10.1016/j.cma.2005.09.027.

[34] O. Weeger, Isogeometric Finite Element Analysis of Nonlinear Structural Vibrations, Ph.D. thesis, 2015.

[35] H. M. Verhelst, M. Möller, J. H. D. Besten, A Wrinkling Model for General Hyperelastic Materials based on Tension Field Theory, 2024. doi:10.48550/arXiv.2410.16990. arXiv:2410.16990.

[36] G+Smo, https://gismo.github.io/, 2025.

[37] L. Li, D. Benson, A. Nagy, M. Montanari, N. Petrinic, S. Hartmann, Recent Developments in Isogeometric Analysis with Solid Elements in LS-DYNA, in: 15th International LS-DYNA Users Conference, ANSYS, 2018.

[38] M. Occelli, T. Elguedj, S. Bouabdallah, L. Morançay, LR B-Splines implementation in the Altair RadiossTM solver for explicit dynamics IsoGeometric Analysis, Advances in Engineering Software 131 (2019) 166–185. doi:10.1016/j.advengsoft.2019.01.002.

[39] J. Bocko, P. Pleško, I. Delyová, P. Sivák, Comparison of Structural Analysis of Thin-Walled Structures Accomplished by Isogeometric Analysis and the Finite Element Method, Materials 15 (2022) 6516. doi:10.3390/ma15196516.

[40] H. Wagner, Flat sheet metal girders with very thin metal web. Part I : General theories and assumptions, 1931.

[41] C. Mseikeh, Wrinkling of Membranes, Plates, and Shells, Canadian Theses, McGill University Libraries, 1997.

[42] M. Stein, J. Hedgepeth, Analysis of partly wrinkled membranes, 1961.

[43] Pipkin, C. Allen, The Relaxed Energy Density for Isotropic Elastic Membranes, IMA Journal of Applied Mathematics 36 (1986) 85–99. doi:10.1093/imamat/36.1.85.

[44] D. G. Roddeman, J. Drukker, C. W. J. Oomens, J. D. Janssen, The Wrin-

kling of Thin Membranes: Part II—Numerical Analysis, Journal of Applied Mechanics 54 (1987) 888–892. doi:10.1115/1.3173134.
[45] X. F. Wang, Q. S. Yang, S.-s. Law, Wrinkled membrane element based on the wrinkling potential, International Journal of Solids and Structures 51 (2014) 3532–3548. doi:10.1016/j.ijsolstr.2014.06.004.
[46] Y. Miyazaki, Wrinkle/slack model and finite element dynamics of membrane, International Journal for Numerical Methods in Engineering 66 (2006) 1179–1209. doi:10.1002/nme.1588.
[47] A. Hossain, C. H. Jenkins, K. Woo, H. Igawa, Transverse Vibration Analysis for Partly Wrinkled Membranes, Journal of Spacecraft and Rockets 43 (2006) 626–637. doi:10.2514/1.11327.
[48] X. Liu, C. H. Jenkins, W. W. Schur, Large deflection analysis of pneumatic envelopes using a penalty parameter modified material model, Finite Elements in Analysis and Design 37 (2001) 233–251. doi:10.1016/S0168-874X(00)00040-8.
[49] M. Taylor, K. Bertoldi, D. J. Steigmann, Spatial resolution of wrinkle patterns in thin elastic sheets at finite strain, Journal of the Mechanics and Physics of Solids 62 (2014) 163–180. doi:10.1016/j.jmps.2013.09.024.
[50] J. Johnston, S. Brodeur, Finite Element Analysis of Wrinkled Membrane Structures for Sunshield Applications (2002).
[51] S. Tudruj, K. Kurec, J. Piechna, K. Kamieniecki, Mass-Spring System (MSS) 3D simulation of a thin flexible membrane with a new model of the elasticity parameters, Archive of Mechanical Engineering vol. 70 (2023) 199–218. doi:10.24425/ame.2023.144817.
[52] R. Narain, T. Pfaff, J. F. O'Brien, Folding and crumpling adaptive sheets, ACM Trans. Graph. 32 (2013) 51:1–51:8. doi:10.1145/2461912.2462010.
[53] N. Jin, W. Lu, Z. Geng, R. P. Fedkiw, Inequality cloth, in: Proceedings of the ACM SIGGRAPH / Eurographics Symposium on Computer Animation, SCA '17, Association for Computing Machinery, New York, NY, USA, 2017, pp. 1–10. doi:10.1145/3099564.3099568.
[54] J. Montes, B. Thomaszewski, S. Mudur, T. Popa, Computational design of skintight clothing, ACM Trans. Graph. 39 (2020) 105:105:1–105:105:12. doi:10.1145/3386569.3392477.
[55] Altair Engineering Inc., Altair Radioss User Documentation, Software Documentation Radioss 2025.1, 2025.
[56] A. Tessler, D. Sleight, J. Wang, Effective Modeling and Nonlinear Shell Analysis of Thin Membranes Exhibiting Structural Wrinkling, Journal of Spacecraft and Rockets - J SPACECRAFT ROCKET 42 (2005) 287–298. doi:10.2514/1.3915.
[57] X. Liu, G. Cai, Nonlinear dynamic analysis of wrinkled membrane structure, Engineering Computations 40 (2022) 41–61. doi:10.1108/EC-02-2022-0083.
[58] H. Le Meitour, G. Rio, H. Laurent, A. Lectez, P. Guigue, Analysis of wrinkled membrane structures using a Plane Stress projection procedure and the Dynamic Relaxation method, International Journal of Solids and Structures 208–209 (2021) 194–213. doi:10.1016/j.ijsolstr.2020.10.026.
[59] AS. Day, An introduction to dynamic relaxation, The engineer 219 (1965) 218–221.
[60] J. Rombouts, G. Lombaert, L. De Laet, M. Schevenels, On the equivalence of dynamic relaxation and the Newton-Raphson method, International Journal for Numerical Methods in Engineering 113 (2017). doi:10.1002/nme.5707.
[61] P. Underwood, Dynamic relaxation, Computational method for transient analysis, Elsevier (1983) 245–65.
[62] M. Rezaiee-Pajand, H. Estiri, Finding buckling points for nonlinear structures by dynamic relaxation scheme, Frontiers of Structural and Civil Engineering 14 (2020) 23–61. doi:10.1007/s11709-019-0549-z.
[63] E.-S. Lee, S.-K. Youn, Finite element analysis of wrinkling membrane structures with large deformations, Finite Elements in Analysis and Design 42 (2006) 780–791. doi:10.1016/j.finel.2006.01.004.
[64] K. Lee, S. Han., T. Park, A simple explicit arc-length method using the dynamic relaxation method with kinetic damping, Computers & Structures 89 (2011) 216–233. doi:10.1016/j.compstruc.2010.09.006.
[65] K. Nakashino, A. Nordmark, A. Eriksson, Geometrically nonlinear isogeometric analysis of a partly wrinkled membrane structure, Computers & Structures 239 (2020) 106302. doi:10.1016/j.compstruc.2020.106302.
[66] M. A. Crisfield, Snap-through and snap-back response in concrete structures and the dangers of under-integration, International Journal for Numerical Methods in Engineering 22 (1986) 751–767. doi:10.1002/nme.1620220314.
[67] M. A. Crisfield, A fast incremental/iterative solution procedure that handles "snap-through", Computers & Structures 13 (1981) 55–62. doi:10.1016/0045-7949(81)90108-5.
[68] E. Riks, An incremental approach to the solution of snapping and buckling problems, International Journal of Solids and Structures 15 (1979) 529–551. doi:10.1016/0020-7683(79)90081-7.
[69] S. A. Ragon, Z. Gürdal, L. T. Watson, A comparison of three algorithms for tracing nonlinear equilibrium paths of structural systems, International Journal of Solids and Structures 39 (2002) 689–698. doi:10.1016/S0020-7683(01)00195-0.
[70] D. Rixen, S. Voormeeren, General Framework for Dynamic Substructuring: History, Review, and Classification of Techniques, Aiaa Journal - AIAA J 46 (2008) 1169–1181. doi:10.2514/1.33274.
[71] J. van Steen, Comparison of Model Order Reduction Techniques for Interface Dynamics, Master's thesis, Eindhoven University of Technology, Eindhoven, 2020.
[72] R. Wijnen, Validation and Improvement of a Dynamic Stiffness Measurement Setup, Master's thesis, Eindhoven University of Technology, 2019.
[73] Y. Luo, J. Xing, Z. Kang, J. Zhan, M. Li, Uncertainty of membrane wrinkling behaviors considering initial thickness imperfections, International Journal of Solids and Structures 191–192 (2020) 264–277. doi:10.1016/j.ijsolstr.2020.01.022.
[74] N. Vu-Bac, T. Lahmer, X. Zhuang, T. Rabczuk, A software framework for probabilistic sensitivity analysis for computationally expensive models, Advances in Engineering Software 100 (2016) 19–31. doi:10.1016/j.advengsoft.2016.06.005.

3

Numerical and experimental analysis of structural dynamics of crumpled cylindrical foils

This chapter presents a self-contained research paper that details the proposed numerical and experimental methodologies as applied to the foil bellow case study. It systematically describes the core methodological framework and reports the resulting findings.

The discussed topics include:

- Foil bellow case study definitions
- Numerical method
  - Model definitions
  - Post-buckling solver choices
  - Static stiffness calculation using a stress-removal technique
  - Dynamic stiffness calculation using modal reduction
- Experimental setup
- Results
  - Crumpling morphologies
  - General trends in static stiffness
  - Observed power-law relations
  - Variability assessment between realisations
  - Dynamic stiffness comparisons
- General interpretation of observed results

Numerical and experimental analysis of structural dynamics of crumpled cylindrical foils

Marco Bader[a]

[a]*Department of Precision and Microsystems Engineering, Faculty of Mechanical Engineering, Delft University of Technology, the Netherlands*

Abstract

We investigate the structural mechanics and dynamics of crumpled cylindrical foils as ultra-compliant links for mechatronic systems. A systematic and computationally efficient finite element framework is developed to quantify how sheet thickness and degree of crumpling govern the emergent static and dynamic stiffness. Realistic crumpled morphologies are generated using explicit dynamic relaxation in Radioss, after which stress removal and modal reduction are employed to extract stiffness behaviour for direct comparison with shaker experiments. The results reveal a clear morphological transition from periodic wrinkling to stress-focusing crumpled ridge network, accompanied by new power-law scaling laws of stiffness with thickness and crumpling degree. Variability between measurements increases at higher crumpling levels, reflecting the intrinsic stochastic nature of ridge formation. Remaining discrepancies between simulations and experiments expose the critical influence of non-linear effects, particularly plasticity and self-contact, underscoring the need to incorporate these mechanisms to achieve fully predictive models of crumpled structures.

Keywords:
post-buckled thin sheets, crumpling, crumpling morphology, structural dynamics, dynamic relaxation, dynamic stiffness

1. Introduction

Anyone who has ever put on a freshly ironed shirt or dress is familiar with the frustrations caused by unwanted wrinkles and crumples. Likewise, in engineering contexts such buckling instabilities can compromise the performance of carefully designed structures. For instance, in aerospace applications such as solar sails, wrinkles and creases can reduce thrust and complicate control [1]. From a structural dynamics perspective, wrinkles have been shown to significantly influence system behaviour by reducing local stiffness and eigenfrequencies [1–5].

These challenges have motivated the development of numerous analytical and numerical methods to better understand wrinkling phenomena. One prominent approach is tension field theory (TFT), in which compressive stresses are relieved by approximating out-of-plane wrinkling patterns by equivalent in-plane membrane shortening [1, 4, 6–20]. While traditionally implemented in finite element analysis (FEA) software, TFT has also been applied to isogeometric analysis (IGA), which represents geometry using continuous splines rather than nodal discretizations [15, 21–28]. This approach is particularly advantageous for wrinkled sheets, as the higher inter-element continuity allows complex curved geometries to be captured with fewer degrees-of-freedom (DoFs).

Despite these advances, thin-sheet buckling remains challenging to model due to the under-constrained nature of the instability, which can induce matrix inversion instabilities in implicit solvers. Arc-length methods (ALM) mitigate this by following highly non-linear deformation paths using combined load-displacement increments [29–34]. Alternatively, explicit dynamic relaxation can bypass matrix inversions altogether, computing the static buckled geometry as the long-term limit of a damped dynamic system [35–43].

Still, most studies to date focus on the periodically wrinkled regime. In contrast, crumpling represents a generic evolution of wrinkling [44], in which periodic undulations give way to a limited number of stress-focusing ridges. While full FEA or IGA becomes impractical for highly crumpled and compacted sheets, discrete element analysis (DEA) has been shown capable of simulating such structures efficiently [41, 45–49]. DEA constructs sheets as networks of discrete mass elements connected by springs and dampers, allowing efficient self-contact handling. However, these methods have primarily been developed for computer graphics and remain limited with respect to engineering-oriented structural mechanics and dynamics studies.

Despite these challenges, the study of crumpled sheets holds promise for novel engineering applications. One such application is the design of ultra-compliant mechanical links between vibrationally isolated frames in vacuum mechatronic systems. Instead of engineered corrugated pipes or bellows, crumpled sheets naturally form multiple ridges and creases that function as flexible hinges, see Figure 1. For these links, accurate prediction of frequency-dependent vibrational transmissibility or dynamic stiffness is critical, as internal dynamics can cause apparent stiffening at higher frequencies [50].

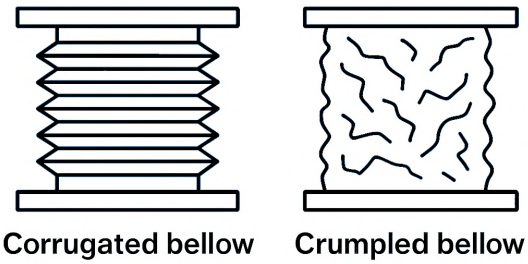

Figure 1: Comparison of engineered corrugation networks and stochastic crumpled morphologies as routes to compliant thin-sheet mechanical links.

However, to date literature on the structural dynamics of post-buckled sheets is limited to modal analyses in the wrinkled regime. Therefore, the present work aims to develop a systematic, robust, and computationally efficient numerical methodology for investigating the static and dynamic stiffness of crumpled structures. This involves generating crumpled morphologies, modelling their static and dynamic behaviour, and validating the models experimentally. Collectively, these efforts seek to establish a foundation for understanding how crumples govern emergent system stiffness, and ultimately leveraging this insight in the design of highly compliant mechanical links.

The remainder of this paper is organized as follows. Section 2 introduces the case study and outlines the numerical and experimental methodologies. Section 3 presents the results, first describing crumpling morphologies and then comparing simulated and experimental stiffness data, including emergent power-law scaling and variability trends. Section 4 discusses the implications and discrepancies between simulations and experiments. Finally, Section 5 summarizes the main contributions, with additional background provided in the Appendices.

2. Method

To demonstrate the feasibility of the proposed modelling approach a representative case study is employed, allowing direct validation of the numerical results against experimental measurements. The following sections first define the specifics of the case study, followed by a summary of the numerical and experimental methodologies.

2.1. Case study definitions

The present case study is motivated by a novel application of crumpling for the creation of flexible dynamic links in vacuum mechatronic systems [51]. Traditionally, corrugated bellows are used to connect vacuum regions requiring flexible joints, such as between two vibrationally isolated frames. These bellows illustrate how deliberately engineered ridge networks can provide compliant, low-transmissibility connections [52]. In an analogous manner, intentionally crumpled foils may offer a simpler and more cost-effective approach to achieving multi-directional compliance, provided their stiffness characteristics can be accurately predicted and controlled.

Figure 2 presents a schematic of the system under consideration. A cylindrical thin polymer sheet in its reference configuration (left) is axially crumpled and fixed between a top and bottom interface in the deformed configuration (right). In this study, the dynamic stiffness, defined as the frequency-dependent transfer function between a small excitation (< 1 mm) applied to the bottom interface and the resulting force on the top interface, is used to quantify vibrational transmissibility. The introduction of crumpling ridges is expected to substantially reduce the dynamic stiffness in all directions, as these ridges act as natural flexible hinges.

The degree of crumpling is characterized by the cylinder overlength, defined as the ratio between the axial height of the cylinder in the reference (h_{ref}) and deformed (h_{def}) configurations:

$$\text{Overlength} = \frac{h_{\text{ref}} - h_{\text{def}}}{h_{\text{def}}} \cdot 100\%. \tag{1}$$

In this study, overlength is varied by increasing h_{ref}. Additionally, multiple sheet thicknesses are considered: 50, 130, 250, and 500 µm. All other system parameters are held constant, with a cylinder diameter $D = 0.2$ m and deformed height $h_{\text{def}} = 0.13$ m. The sheet material is fluorinated ethylene propylene (FEP), with a density $\rho = 2150$ kg/m^3, elastic modulus $E = 650$ MPa, and Poissons ratio $\nu = 0.4$ [53].

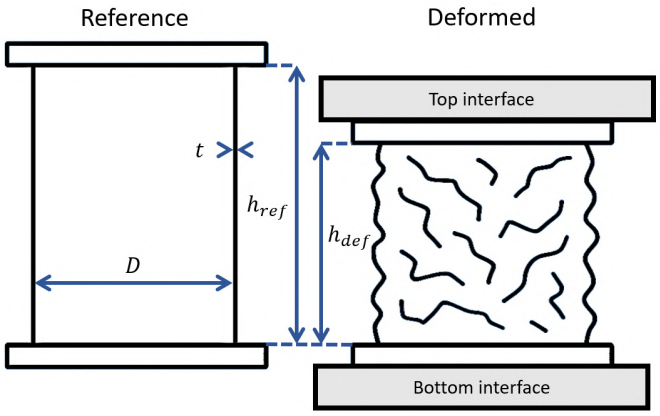

Figure 2: Case study: axially crumpled cylindrical foils as an alternative to corrugated bellow joints. The top interface is lowered towards the bottom interface to induce crumpling. Crumpling overlength is defined as the ratio between the axial heights of the reference (h_{ref}) and deformed (h_{def}) configurations. Overlength is varied via h_{ref}, together with sheet thickness t. Cylinder diameter D and deformed height h_{def} are kept constant across all tests.

2.2. Numerical method

A computational methodology was developed with an emphasis on efficiency and user-friendliness. The workflow is divided into four stages: (i) model definition, (ii) post-buckling simulation to generate crumpled geometries, and calculation of the (iii) static and (iv) dynamic responses. The key modeling decisions are outlined below, with additional details provided in Appendix A.

2.2.1. Model definition

Finite element analysis (FEA) remains the standard approach for structural mechanics and dynamics problems. However, for buckling thin shells the choice of discretisation method requires more careful consideration: discrete element analysis (DEA) and isogeometric analysis (IGA) offer potential advantages but also significant limitations in the present context.

DEA has been used successfully to simulate highly compacted sheets with plastic creasing and extensive self-contact [47]. However, existing DEA implementations are primarily developed for computer graphics and lack support for frequency-domain calculations due to their discretised nature [46]. IGA, by contrast, has already been applied to modal buckling of cylindrical shells [23] and typically requires fewer total DoFs than conventional FEA. Nevertheless, the resulting system matrices are considerably less sparse, which can offset computational gains [15]. Due to the limited availability of mature DEA and IGA software, a conventional finite-element approach was selected for this proof-of-concept study.

Drawing inspiration from automotive crashworthiness studies [54–56], two FEA solvers capable of handling highly geometrically nonlinear phenomena were considered: Ansys LS-Dyna and Altair Radioss. Radioss was selected for its clear input syntax, extensive documentation [57], and availability as the free stand-alone solver OpenRadioss, which benefits from an active user community and supporting tools [58].

Cylindrical shell models with five reference heights (h_{ref} = 0.135, 0.15, 0.17, 0.20, and 0.25 m) were created in Altair HyperMesh. Preliminary simulations and a mesh convergence study (Appendix A) determined that 5 mm square shell elements provided sufficient resolution for ridge formation. Following Radioss recommendations [57], the reduced-integration QEPH shell formulation (Quadrilateral Elasto-Plastic Physical Hourglass Control) was employed. This choice reduces computational cost and avoids shear locking compared with fully integrated elements, while the spurious zero-energy hourglass modes caused by the reduced integration are stabilised effectively.

Unlike traditional crashworthiness studies [54–56], where accurate plastic energy absorption and reaction forces play a central role, the present simulations aim solely to generate realistic crumpled geometries as quickly as possible. Consequently, linear-elastic material behaviour was adopted and self-contact was omitted, as the considered overlengths remain moderate.

Geometric imperfections were introduced using the `/RANDOM` keyword, superimposing Gaussian noise with an amplitude of 10 µm on the nodal coordinates. This is consistent with recommendations that imperfection amplitudes should range between 1% and 100% of the shell thickness [32]. To capture sensitivity to initial conditions, each thickness-overlength combination was simulated six times using reproducible random seeds.

2.2.2. Post-buckling simulation

The crumpling of thin cylinders is characterised by many local instabilities and snap-through events, which renders conventional incremental stepping procedures using implicit solvers fragile [16, 34, 42]. The implicit stepping can be improved by using an arc-length method to more closely follow the non-linear loading paths found in snap-through buckling. [29–31]. However, as for this work only the final crumpled morphology is of interest, the dynamic relaxation method (DRM) [35–40, 42] provides a more robust alternative: the desired static equilibrium is obtained as the long-time limit of a near-perfectly damped dynamic system, integrated explicitly in pseudo-time. This method is especially powerful for this form-finding application as it can easily deal with the under-constrained buckling present here, as there is no need to invert near-singular stiffness matrices in the explicit scheme.

Crumpling is induced by fixing all nodes at the bottom interface while imposing a downward displacement on the top interface. To minimize inertial effects and allow rapid convergence to steady state, the displacement follows a smooth sigmoid function over pseudo-time, producing small initial and final velocities and reducing high-frequency oscillations. Advanced mass scaling (`DT/AMS`) increases the stable time step without significantly affecting low-frequency response [57, 59, 60]. Additionally, adaptive viscous nodal damping (`/ADYREL`) [57] suppresses residual oscillations, yielding an effectively damped system.

Combined, these strategies allow efficient simulation of crumpling in under five minutes on a standard laptop. Further theoretical background and performance validation are provided in Appendix A.

2.2.3. Static response

To characterize the dependence of stiffness on overlength and thickness, an effective measure of axial and radial link stiffness is required. Direct tangent stiffness estimation from reaction forces ($k = \mathrm{d}F/\mathrm{d}z$) during crumpling is unreliable due to high-frequency fluctuations, sensitivity to loading rate and mass scaling, and local snap-through events, see Appendix A. Instead, a secant stiffness is computed by applying a known probing force F_{probe} = 100 N to the top interface and measuring the resulting displacement u_{probe} via a single linear-implicit step:

$$k_{\text{static}} = \frac{F_{\text{probe}}}{u_{\text{probe}}}. \tag{2}$$

This approach provides a global metric of morphology compliance, unaffected by transient dynamics.

However, if this probing force was applied with elastic stresses still present in the crumpled geometry, the cylinder would spring-back to its original shape, which would be indistinguishable from the deformation caused by the probing force. Thus, a key challenge was to remove stored elastic stresses post-deformation to establish a new crumpled but stress-free

reference geometry. As Radioss does not offer a function to automatically remove stresses in a single-run process, a novel stress-removal strategy was adopted using an elasto-plastic Johnson-Cook material law with strain-rate-dependent yield strength σ_y [57]:

$$\sigma_y = \sigma_{y,0}\left[1 + c\ln\left(\frac{\dot{\varepsilon}}{\dot{\varepsilon}_0}\right)\right], \tag{3}$$

where $\sigma_{y,0}$ is the base yield strength, c is a dimensionless strain-rate coefficient, and $\dot{\varepsilon}/\dot{\varepsilon}_0$ is the ratio between the local and reference strain rate. Parameters were artificially set ($\sigma_{y,0} = 1$ Pa, $c = 1 \times 10^6$, $\dot{\varepsilon}_0 = 1 \times 10^{-10}$ s^{-1}) to ensure linear-elastic behaviour during crumpling (high effective σ_y at non-zero $\dot{\varepsilon}$). At the end of the deformation, nodal velocities are frozen ($\dot{\varepsilon} \to 0$), collapsing σ_y to near-zero and plastically relaxing stresses while preserving geometry. While this method does not completely eliminate residual stresses, the equilibrium reached after unfreezing all nodes and relaxing is close to the desired crumpled shape.

To post-process the simulation results, the deformation u_{probe} resulting from the probing force is automatically acquired by extracting interface displacements from Radioss time-history files, converted to a Python dataframe using the OpenRadioss community library Vortex-Radioss [58].

2.2.4. *Dynamic response*

The dynamic behaviour of the crumpled foil is evaluated using a modal reduction approach to reduce computational cost while retaining essential interface dynamics. The full system is projected onto a basis of rigid-body and elastic eigenmodes up to 1000 Hz, following the Hintz-Herting methodology [50, 61]. This captures dynamic behaviour up to approximately 800 Hz without the need for computing the full system response, see Appendix A.

In practice, the crumpled geometry from Radioss is manually imported into an ANSYS modal analysis study. Interface nodes are rigidly connected to master nodes, and a free-free (no boundary conditions) modal analysis is performed. The resulting modes form the basis for the Hintz-Herting reduction, and the reduced-order model is exported using a proprietary user routine. In MATLAB, modal superposition using 5% modal damping is used to compute transfer functions from interface forces to displacements, which are then inverted to obtain the 6-DoF, frequency-dependent dynamic stiffness matrix [50].

This method captures the principal dynamic characteristics within the frequency range of interest but is limited to linearized behaviour and thus does not account for contact or prestress effects. Due to the high modal density of these compliant structures, generating the reduction basis is still computationally intensive. This underscores the advantage of the static secant stiffness calculation via stress-removal, which can be performed efficiently in a single Radioss run without repeated geometry export and import.

2.3. *Experimental method*

Experiments were performed using a 6-DoF dynamic stiffness measurement system originally developed for air-mount qualification and validated by Wijnen [50]. A schematic cross-section and photograph of the setup are shown in Figure 3. A specimen is clamped between a base frame (BF) and a metrology frame (MF). Vertical axial excitation (<1 mm amplitude) is applied to the BF using three in-phase piezoelectric stack actuators. Alternatively, radial excitation can be introduced via a horizontal shaker. The MF consists of a 500 kg mass that can be suspended using a preload bellow to apply gravitational preload. In this study, no preload was applied; the MF was lifted to float freely above its end stops.

Transmitted forces and moments are measured using three triaxial force sensors mounted on the MF. Interface motions of BF and MF are reconstructed from accelerometer arrays assuming rigid-body kinematics. Although the system measures all six force and moment components, the present study considers only axial (Z) and radial (X) forces and the corresponding relative displacements. Dynamic stiffness is defined in the frequency domain as the transfer function between relative displacement (MF-BF) and transmitted force at the MF.

Time signals were recorded at 50 kHz over 60 s intervals. Spectral estimation employed periodic block processing with 2 s blocks, Hanning windowing, and 50% overlap, yielding a frequency resolution of 0.5 Hz. Signal power and coherence functions were obtained from averaged spectra to verify data quality, see Appendix B and C. To maximize measurement coherence for highly compliant configurations (small thickness, large overlength), excitation was applied using two band-limited multi-sine signals (0-150 Hz and 100-500 Hz) instead of a single broadband coloured-noise signal as used by Wijnen [50]. Concentrating signal power within narrower frequency bands proved essential, as transmitted axial forces were small and easily masked by parasitic MF vibrations arising from shaker reaction paths, see Appendix B

For each combination of foil thickness and overlength, three independent measurements were conducted. Between repetitions, the sheet was manually perturbed to generate distinct crumpled geometries. This procedure enables quantification of both mean dynamic stiffness and variability arising from the stochastic crumpling process.

Static stiffness is extracted from the low-frequency region of the dynamic stiffness curves. However, for thin sheets with large overlength limited signal-to-noise ratios obscure a clear stiffness plateau. To obtain robust estimates, the dynamic stiffness is first smoothed using a symmetric moving-average filter (30 Hz bandwidth). Static stiffness is then defined as the mean smoothed stiffness between 1 and 10 Hz. This procedure provided the most consistent and physically representative values across all tested configurations and crumpling realizations, see Appendix B.

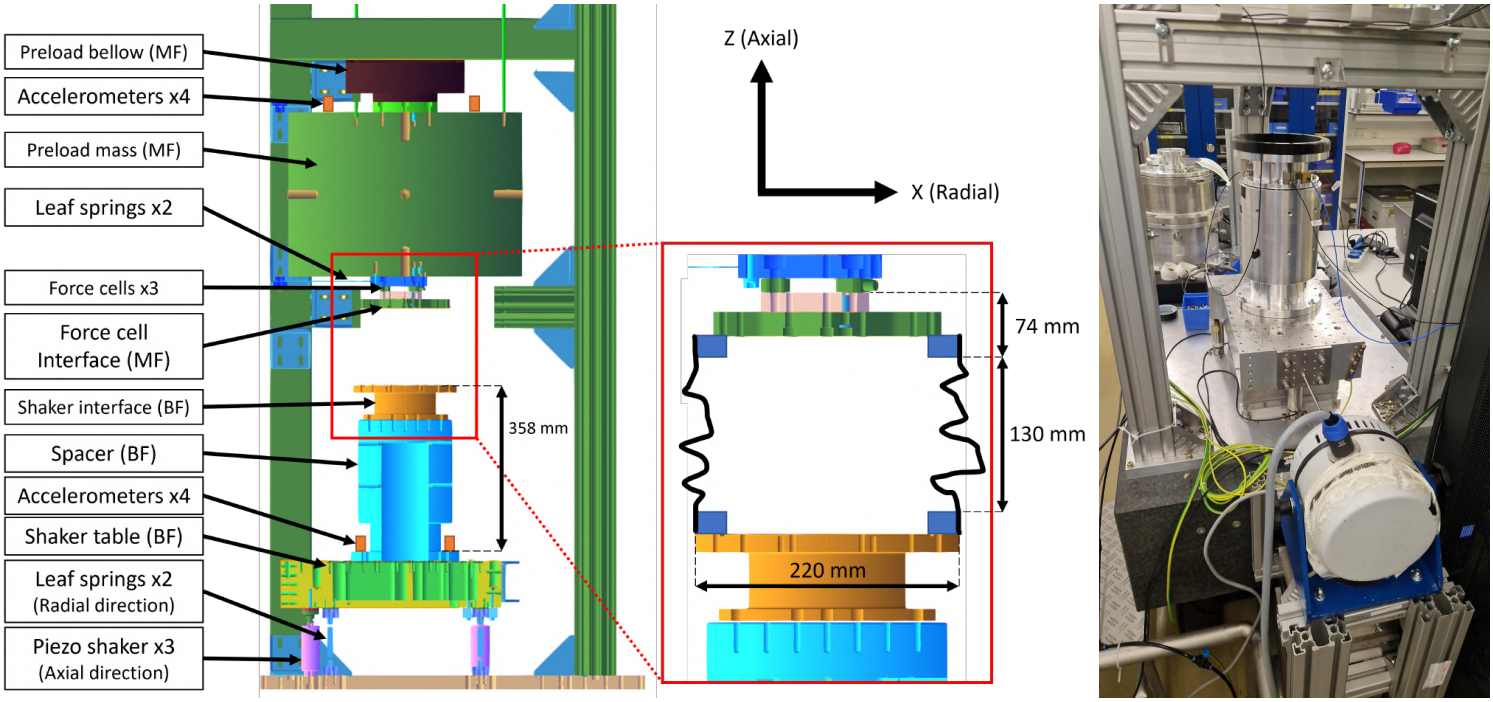

Figure 3: Schematic cross-section and photograph of the 6-DoF dynamic stiffness setup. The BF is excited using three vertical or one horizontal piezoelectric actuator(s). Three triaxial force sensors on the MF measure transmitted forces and moments, while accelerometers reconstruct BF and MF motions. The MF (500 kg) can apply gravitational preload via a preload bellow; no preload was used in this study.

3. Results

This section covers the results of the applied numerical and experimental methods, focusing on shared trends and discrepancies found in the crumpled morphologies and static and dynamic stiffnesses.

3.1. Crumpling morphology

Figure 4 compares simulated and experimental configurations for increasing overlength and thickness. While post-buckling states are inherently imperfection-sensitive and therefore not expected to match exactly between simulation and experiment, both approaches reveal the same underlying mechanical progression.

For small overlengths, the response is governed by classical shell buckling. The deformation field closely resembles the diamond-shaped modes predicted for cylindrical shells by Yamaki [62], indicating that the structure remains in a near-linear post-buckling regime. The surface pattern consists of spatially periodic wrinkles with well-defined wavelength and amplitude. Increasing thickness increases bending stiffness, which energetically penalizes curvature and therefore drives a coarsening of the wrinkle pattern: both wavelength and amplitude increase, consistent with established membrane bending scaling arguments [16].

As overlength increases, the deformation mechanism changes qualitatively. The structure transitions from distributed wrinkling to localized crumpling. Rather than maintaining a periodic mode, the shell minimizes its elastic energy by concentrating Gaussian curvature into sharp ridges and vertices, forming a network of stress-focusing ridges and vertices [44]. This localization reduces the energetically expensive bending over large areas by confining curvature to narrow regions. In this regime, a single characteristic wavelength is no longer meaningful. Instead, the morphology is defined by ridge density and ridge amplitude.

Again, thickness continues to act as the dominant mechanical control parameter. Higher bending stiffness suppresses fine-scale localization, resulting in fewer but more pronounced ridges. This reflects a stiffness-controlled length scale selection: as bending energy becomes more costly, the system favours larger structural features to balance membrane and bending contributions.

The experiments exhibit the same mechanics-driven transition from periodic wrinkling to ridge-dominated crumpling. Although boundary imperfections introduced by hose clamps reduce wrinkle regularity, the governing trend remains similar. In both simulation and experiment, increasing thickness leads to systematic coarsening of surface features, confirming that bending stiffness dictates the morphological length scale across regimes.

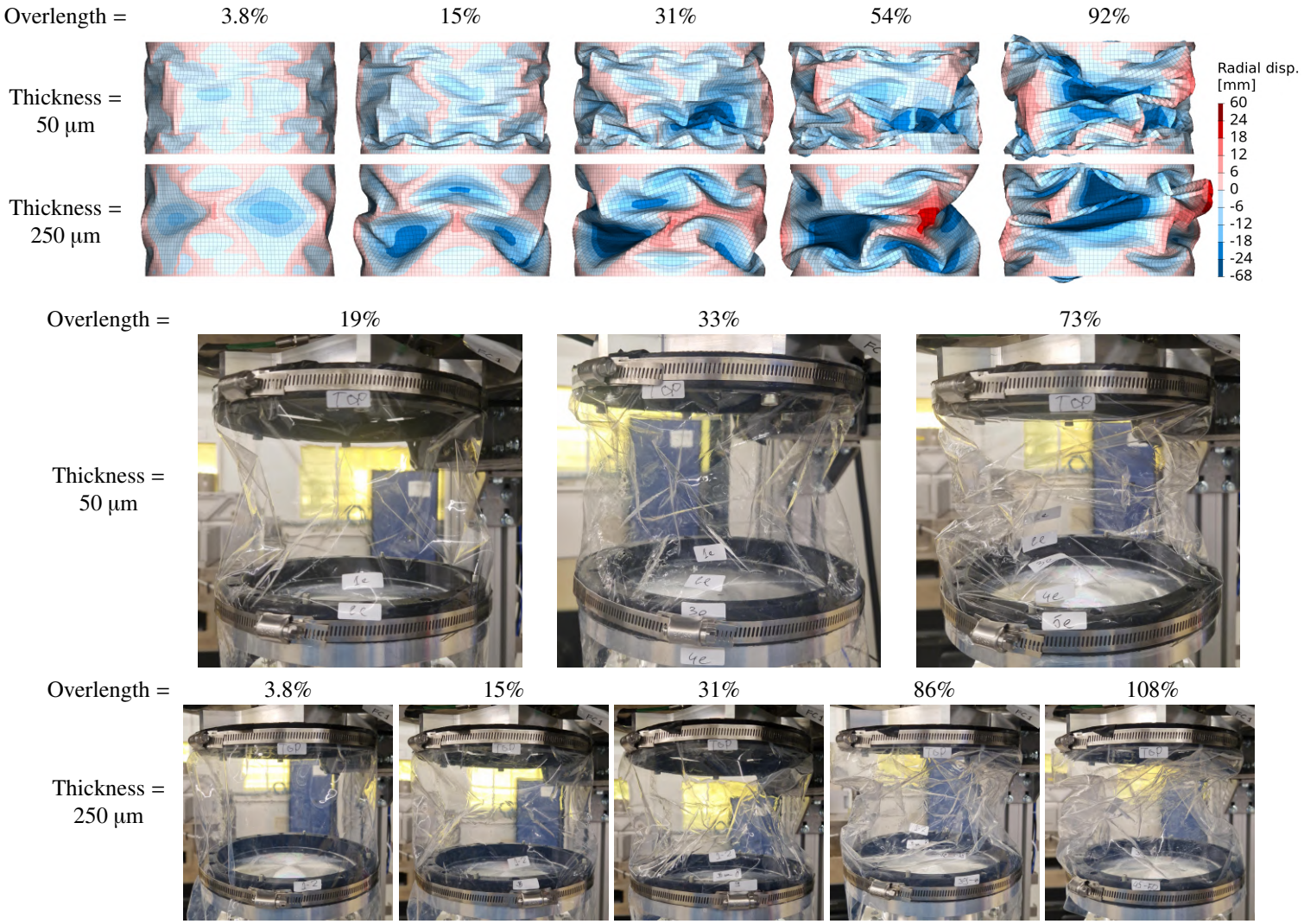

Figure 4: Simulated and experimental crumpled morphologies for increasing overlength and thickness. Simulations show radial displacement relative to the cylinder centreline (outward positive). The colour scale is limited to ±24 mm to enhance contrast between configurations; the full displacement range spans −68 mm to +60 mm.

3.2. *Static stiffness*

Figure 5 shows the evolution of the von Mises stress in a random element over pseudo-time, along with the axial height of five cylinders with different overlength. It can be seen that the cylinders are axially compressed to a final common height along a sigmoid function (0–0.8 s). Thereafter, all nodal velocities are frozen in order to remove stresses using non-physical plastic yielding (0.8 s), with a drop in von Mises stress as a result. With the sheet now relieved of most stresses, the cylinders are allowed to find a new (crumpled) equilibrium (0.8–1.0 s). Finally, a linear-implicit step is used (1.0–2.0 s) to apply a probing force F_{probe} on the top interface of each stress-free crumpled cylinder in axial or radial direction, with the magnitude of deformation u_{probe} indicating the effective stiffness k_{static} in that direction. As expected, the cylinders with largest overlength deform most and thus have the lowest stiffness.

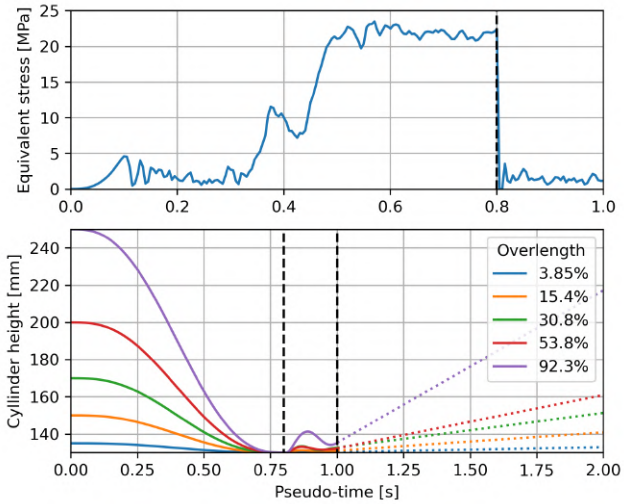

Figure 5: Evolution of von Mises stress and axial height for five cylinders with different overlengths, probed for effective stiffness in the axial direction.

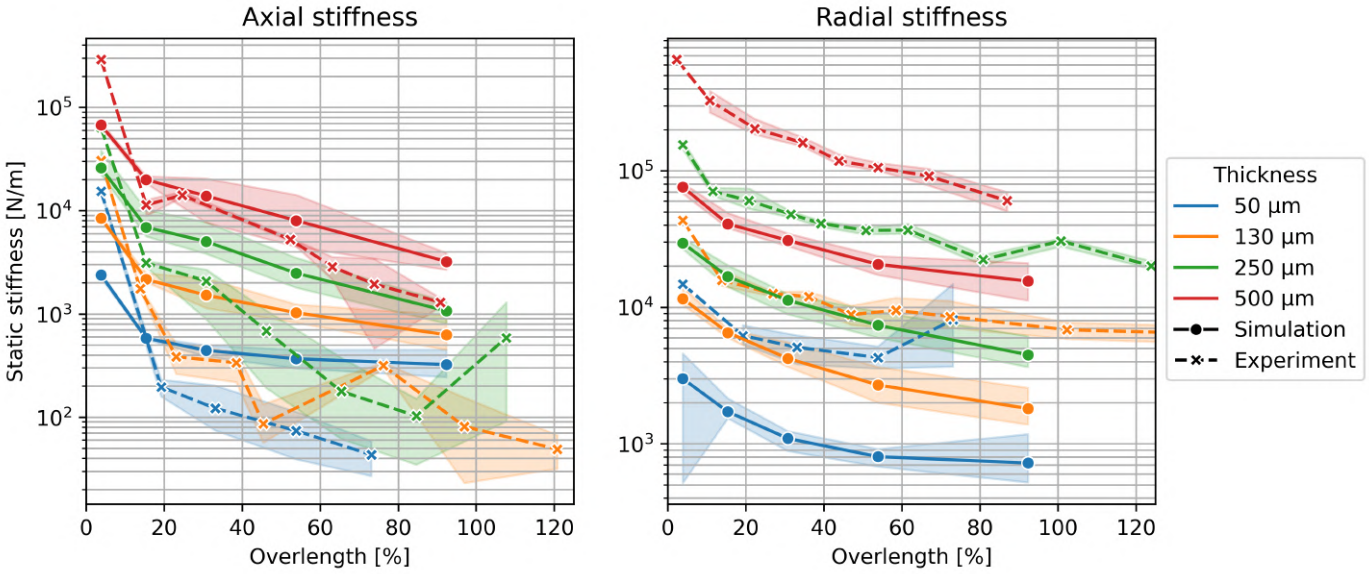

Figure 6: Simulated and experimental responses of axial and radial static stiffness as a function of overlength and thickness. For each configuration, the mean value of multiple realizations with different initial conditions is shown (six for simulations and three for measurements). Shaded regions indicate the absolute minimum and maximum bounds for each configuration.

Figure 6 presents the axial and radial static stiffness as a function of overlength, obtained from both simulation and experiment. For each thickness, the mean stiffness is shown together with shaded bands indicating the observed minimum and maximum values. Several systematic trends emerge: first, all configurations exhibit a fast exponential decay of stiffness with increasing overlength, indicating that even modest overlength already substantially diminishes the effective structural stiffness. Second, stiffness increases monotonically with thickness, reflecting the increased bending rigidity of the shell. Notably, the overall shape of the stiffness-overlength curves remains largely invariant across thicknesses, while their absolute magnitude shifts. This suggests that the effects of overlength and thickness act predominantly independently.

Despite the qualitative agreement in trends, clear quantitative discrepancies are observed between simulation and experiment. In particular, the experimentally measured axial stiffness exhibits a significantly steeper decay with overlength. This stronger sensitivity is not observed in the radial direction, where simulation and experiment display closer agreement, aside from a systematic offset in magnitude.

Motivated by the apparent independence of thickness and overlength effects (see Appendix C), the static stiffness k_{static} was modelled using a decoupled power-law relation,

$$k_{\text{static}} = \exp(\alpha) \cdot (\text{Overlength})^{\beta} \cdot (\text{Thickness})^{\gamma}, \tag{4}$$

with α, β, and γ as fitting parameters obtained using least-squares regression. To perform this fit, the model is linearized by taking the logarithm of both sides, yielding:

$$\ln(k_{\text{static}}) = \alpha + \beta \cdot \ln(\text{Overlength}) + \gamma \cdot \ln(\text{Thickness}). \tag{5}$$

This transformation ensures that relative variations are weighted uniformly across the data range, preventing configurations with large absolute stiffness values from dominating the fit.

The resulting parameters are summarized in Table 1. The high R^2-values indicate that the decoupled power-law relation captures the dominant trends in the data. The lowest coefficient of determination ($R^2 = 0.856$) corresponds to the experimental axial stiffness, consistent with its larger scatter and less smooth behaviour in Figure 6.

A marked discrepancy is observed in the overlength exponent β for axial stiffness: the experimentally obtained value ($\beta = -1.8$) is significantly more negative than the simulated value ($\beta = -0.85$), reflecting the steeper decay observed experimentally. In contrast, the radial stiffness exponents for overlength agree within uncertainty bounds, indicating consistent scaling behaviour between simulation and experiment in that direction.

The thickness exponent γ remains remarkably consistent across all cases ($1.4 \leq \gamma \leq 1.6$), suggesting that the influence of bending rigidity on stiffness follows a natural scaling law largely independent of loading direction.

Finally, systematic differences in absolute magnitude are reflected in the parameter α. For radial stiffness, where β and γ are nearly identical between simulation and experiment, the difference in α corresponds to a multiplicative factor of approximately $\exp(4.5 - 3.2) = 3.7$. It should be noted that the absolute value of α is unit-dependent and therefore does not carry independent physical meaning beyond this global scaling offset.

	Axial stiffness		Radial stiffness	
	Simulation	Experiment	Simulation	Experiment
R^2	0.960	0.856	0.963	0.939
α	3.5 ± 0.2	4.6 ± 0.8	3.2 ± 0.2	4.5 ± 0.3
β	-0.85 ± 0.03	-1.8 ± 0.1	-0.52 ± 0.02	-0.55 ± 0.04
γ	1.40 ± 0.04	1.6 ± 0.1	1.42 ± 0.03	1.48 ± 0.05

Table 1: Fitted parameters of the log-linear regression model in Equation 5, for axial and radial static stiffness. Reported uncertainties represent standard deviations obtained from the least-squares fit. The coefficient of determination R^2 quantifies the goodness of fit.

The variability of static stiffness measurements across repeated simulations and experiments is quantified in Figure 7 using the coefficient of variation (standard deviation normalized by the mean) for each overlength. As no systematic trend with sheet thickness was observed, data from all thicknesses are grouped together. It should be noted that the limited number of experimental repetitions renders the standard deviation sensitive to outliers, particularly at high overlength.

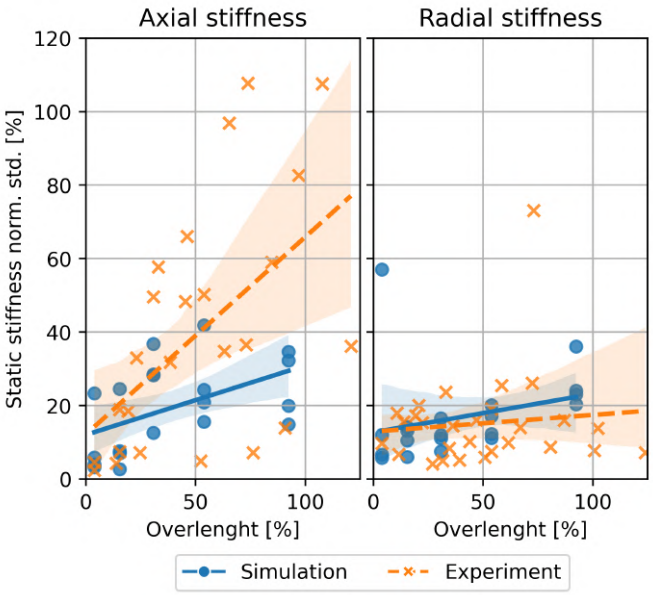

R^2-value	Axial stiffness	Radial stiffness
Simulation	0.305	0.079
Experiment	0.297	0.012

Figure 7: Scatter plot of normalised standard deviations (coefficient of variation) per overlength-thickness configuration, with all thicknesses grouped. A linear regression indicates the general trend, along with a shaded 95% confidence interval of the regression. The strength of correlation in the data is represented by R^2-values.

A weak positive correlation between stiffness variability and overlength is apparent for both axial and radial directions in simulations and experiments. This trend is consistent with the expected increase in morphological divergence at higher overlengths as cylinders transition from regular wrinkling patterns to irregular, stress-focused crumpled states. At minimal overlength, all realizations closely resemble the periodic diamond-shaped wrinkle pattern, yielding nearly identical stiffness values. With increasing overlength, deviations between realizations grow due to the amplification of local snap-through events and ridge localization, see Figure 8.

Experimental measurements display a more pronounced increase in variability compared to simulations, reflecting additional sources of uncertainty such as imperfect boundary conditions, clamping irregularities, and intrinsic noise of the measurement system. Moreover, low-stiffness configurations at high overlength approach the noise floor of the experimental setup, further enhancing relative variability.

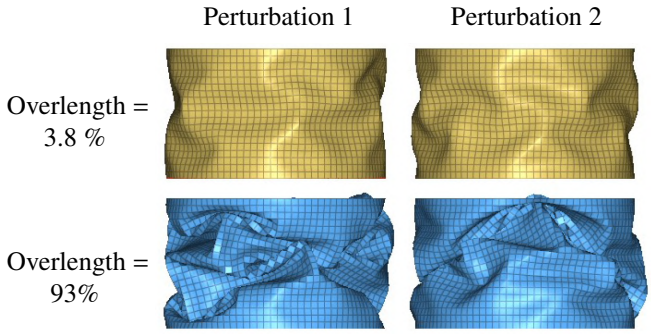

Figure 8: Comparison of crumpled morphologies for the same thickness (t = 500 µm) but different seeds for the initial perturbation.

3.3. *Dynamic stiffness*

The dynamic response of the crumpled cylinders, expressed as frequency–dependent dynamic stiffness, is shown in Figure 9. The shaded minimum-maximum bounds illustrate variability across different realizations, reflecting the pronounced sensitivity of resonance peak positions to small initial geometric perturbations which are amplified during crumpling. Background noise measurements, obtained without a bellow fixed between the interfaces, are also included to represent force cell disturbances caused by parasitic shaker vibrations propagating through the springsuspension of the metrology frame. These reference measurements indicate the effective noise floor of the setup and highlight the intrinsic challenge of testing ultra-compliant links. It should be noted that only a representative subset of configurations is presented here; the complete dataset, including coherence plots and additional realizations, is provided in Appendix C.

Simulated results exhibit the expected characteristics of flexible dynamic links. At low frequencies, the dynamic stiffness coincides with the static stiffness, forming a flat baseline that reflects quasi-static geometric compliance. The onset of the dynamic regime occurs at the first structural resonance, beyond which stiffness increases with frequency due to the cumulative contribution of multiple vibration modes. Configurations with lower static stiffness enter this dynamic regime at lower frequencies, as their reduced structural rigidity leads to lower natural frequencies. Consequently, the dynamic stiffness

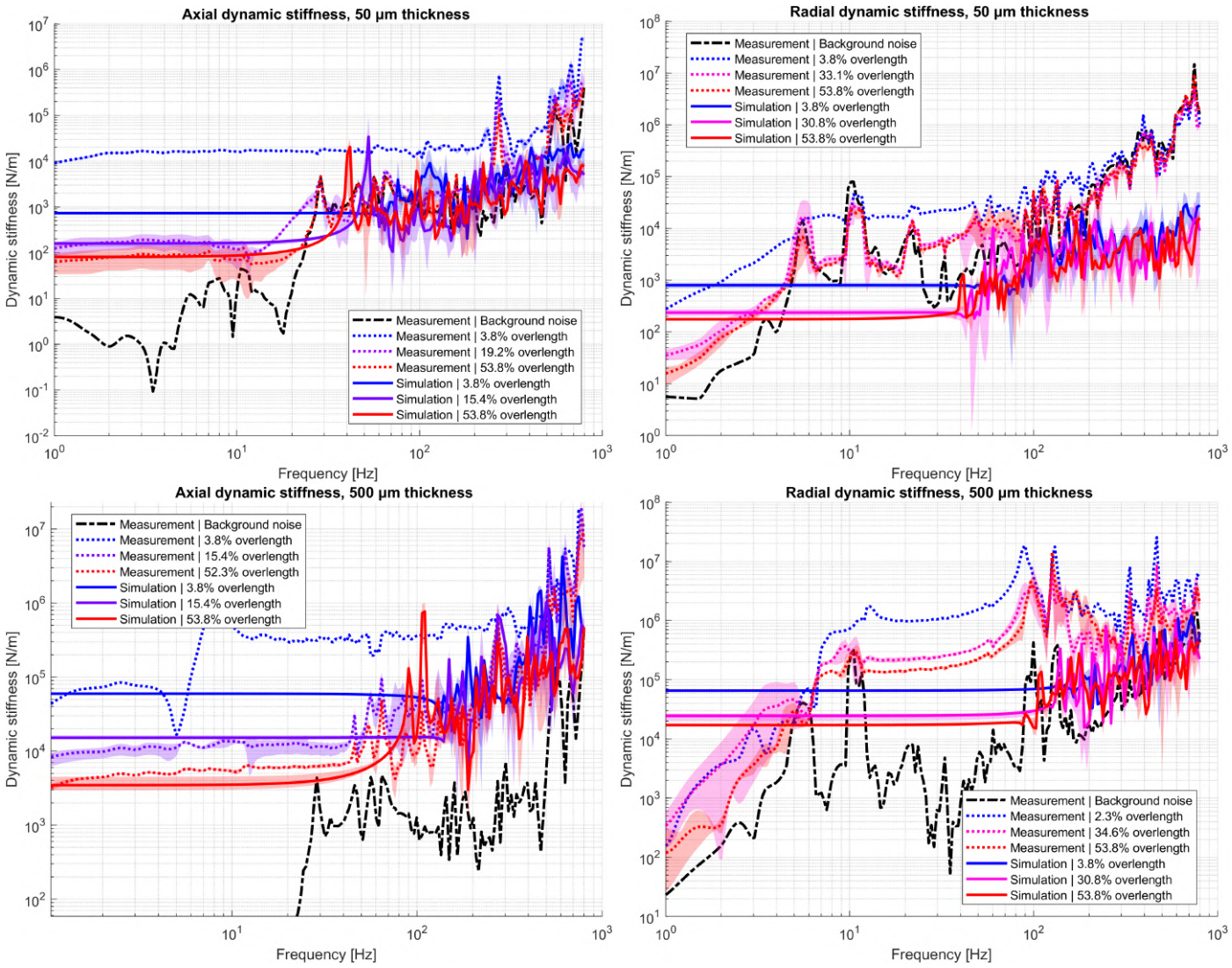

Figure 9: Dynamic stiffness transfer functions in axial and radial directions, for $t = 50$ µm and $t = 500$ µm and various overlengths. Shaded areas indicate minimum and maximum bounds between three realisations. Measurements without any specimen present are indicated as background noise, resulting from force cell disturbances due to reaction path vibrations.

curves progressively converge at higher frequencies. This convergence suggests that while static response is governed primarily by geometric factors such as ridge curvature and fold topology, the high-frequency behaviour becomes increasingly influenced by distributed mass participation, which is similar across configurations of equal thickness.

The exceptionally high modal density observed in all configurations is consistent with the presence of a hierarchical ridge network, in which local bending and folding elements introduce numerous low-mass, low-stiffness substructures. Each ridge segment effectively behaves as a local oscillator, weakly coupled to the global deformation field. The resulting dynamic behaviour is therefore not dominated by a few well-separated global modes, but rather emerges from the superposition of many interacting local modes spanning a broad frequency range. In such stochastic systems, small geometric variations shift individual resonance frequencies without fundamentally altering the overall response envelope. This underscores the importance of interpreting general stiffness trends rather than attempting peak-to-peak comparisons, which are inherently non-repeatable and of limited physical significance.

For experimental measurements, configurations with small thickness and high overlength are strongly influenced by background noise transmitted through the shaker reaction path. As specimen stiffness approaches the compliance of the measurement frame, their dynamics become increasingly coupled. While the low-frequency static region remains distinguishable, the onset of the dynamic regime is partially contaminated by setup resonances, reducing the reliability of individual peaks. These measurements must therefore be interpreted with caution, as some apparent resonances may originate from the measurement system rather than the specimen itself.

For thicker sheets, the signal-to-noise ratio improves significantly, and the transition from static to dynamic stiffness is more clearly resolved. In these cases, both simulations and experiments indicate that the dynamic regime begins around 100 Hz. Although resonance peaks shift in frequency with overlength and between realizations, their overall shape and spacing remain qualitatively similar, suggesting that the global deformation mechanisms of the crumpled cylinders are preserved despite geometric variability. Nevertheless, individual peaks remain difficult to isolate unequivocally from background contributions and should not be interpreted literally; instead, the global evolution of the dynamic stiffness envelope is of primary importance.

Overall, the dynamic behaviour of crumpled cylinders appears to be governed by a transition from geometry-dominated compliance at low frequencies to increasingly inertia-dominated response at higher frequencies, superimposed with a dense spectrum of locally activated ridge modes. This dual character explains both the sensitivity to initial crumpling configuration and the eventual convergence of stiffness curves in the dynamic regime. It also provides a consistent framework for interpreting discrepancies between experiment and simulation, particularly in directions where non-linear ridge mechanics or plastic deformation may enhance stiffness beyond that predicted by the current elastic numerical model.

4. Discussion

The results presented in this study demonstrate that crumpling fundamentally transforms both the static and dynamic stiffness of thin sheets. Increasing overlength initially produces a pronounced reduction in static stiffness, marking the transition from a membrane-dominated response to one governed by a sparse network of bending ridges and vertices. In this regime, load transfer is concentrated in a limited number of hinge–like features, allowing substantial compliance through localized bending. However, as overlength increases further, the stiffness reduction exhibits clear diminishing returns. Beyond moderate overlengths, the static stiffness approaches an apparent lower bound (see Appendix C), indicating that additional geometric complexity does not translate into proportional gains in compliance.

This saturation can be understood as a structural evolution of the crumpled network. As the configuration densifies, ridge-ridge interactions and self–contact become increasingly frequent [63]. The structure gradually transitions from a hinge-dominated system toward a contact–stabilized network with finite residual stiffness. In this regime, further crumpling may even induce local stiffening through mechanical shortcuts with other parts of the machine, such that direct frictional contacts bypass compliant bending ridges and provide unintended load transfer paths. The effective stiffness is therefore governed not only by geometric freedom, but also by contact topology.

These mechanisms introduce an important engineering trade-off. Larger overlengths (and small thicknesses) reduce quasi-static stiffness and may be attractive for designing ultra-compliant links. However, excessive crumpling increases the risk of pinhole formation due to extreme local curvature, as well as the likelihood of contact–induced stiffening and mechanical shortcuts. From a reliability perspective, highly densified configurations may therefore compromise structural integrity or long-term durability. The results suggest that stiffness reduction through crumpling is beneficial only within a finite window: beyond that window, gains in compliance are marginal.

Interestingly, a consistent anisotropy is observed between axial and radial loading directions in both static and dynamic responses. Axial stiffness is generally lower and exhibits greater variability, reflecting the dominant role of a limited number of ridge structures in accommodating axial deformation. Under axial loading, deformation energy is concentrated in a small subset of highly stressed ridges, rendering the global response sensitive to crumpling history and ridge orientation. Radial stiffness, by contrast, is distributed over a larger ensemble of circumferential load paths, resulting in a stiffer and more repeatable response. This directional dependence highlights that crumpled sheets cannot be described by a single effective stiffness parameter; rather, they exhibit intrinsically anisotropic and configuration–dependent behaviour.

The comparison between simulations and experiments further underscores the importance of material and contact nonlinearities. Although the numerical model captures the overall stiffness trends and the convergence behaviour in the dynamic regime, discrepancies in the axial response remain. The simulations do not fully reproduce the experimentally observed faster softening at large overlengths. A plausible explanation is the absence of material plasticity in the current model: Stress–focusing ridges with extreme curvature are likely to undergo local yielding, permanently weakening hinge stiffness. Incorporating plastic deformation in future models is therefore essential for quantitatively accurate prediction of crumpled-sheet mechanics.

In the dynamic domain, all configurations exhibit a transition from geometry-dominated compliance at low frequencies to inertia–dominated behaviour at higher frequencies, accompanied by a dense spectrum of locally compliant ridge modes. Importantly, the dynamic stiffness curves converge at higher frequencies, irrespective of overlength. This convergence indicates that increasing overlength primarily affects quasi-static compliance, while offering limited benefit for high–frequency dynamic isolation. From a design perspective, this suggests diminishing returns when selecting extreme overlength values: improvements in static flexibility do not proportionally enhance dynamic performance.

Taken together, these findings indicate that crumpling is a powerful but bounded strategy for stiffness reduction. An optimal crumpling state likely exists in which static compliance is significantly enhanced, dynamic behaviour remains predictable, and risks associated with self–contact, plastic damage, and pinhole formation are minimized. The combined static and dynamic characterization framework developed in this study provides a basis for identifying this balance and for guiding the engineering design of crumpled sheet structures as compliant dynamic links.

5. Conclusion

In this study, we have developed a systematic, robust, and computationally efficient numerical framework for analysing the static and dynamic stiffness of crumpled structures. Dynamic relaxation methods were used to quickly generate representative crumpled morphologies, while stress–removal techniques and modal reduction approaches were applied to extract the static and dynamic stiffness of these deformed configurations. The numerical results were validated against experimental measurements of dynamic stiffness, obtained using multi-sine shaker excitation to enhance the signal-to-noise ratio. From these analyses, new power-law relationships were identified to characterize the influence of crumpling on the emergent stiffness of the structures. Observed discrepancies in the scaling parameters highlight limitations of the current simulation workflow, particularly the absence of plasticity and self-contact effects, which should be addressed in future developments to improve predictive accuracy. However, this work still marks a strong foundation for the understanding of crumpling in the engineering context of structural mechanics and the design of ultra-flexible dynamic links.

References

[1] N. Hossain, K. Woo, C. Jenkins, Dynamic Response of Systematically Creased Membranes, in: 48th AIAA/ASME/ASCE/AHS/ASC Structures, Structural Dynamics, and Materials Conference, American Institute of Aeronautics and Astronautics, 2007. doi:10.2514/6.2007-1806.

[2] Y.-L. Li, M.-Y. Lu, H.-F. Tan, Y.-Q. Tan, A study on wrinkling characteristics and dynamic mechanical behavior of membrane, Acta Mechanica Sinica 28 (2012) 201–210. doi:10.1007/s10409-011-0512-2.

[3] C. G. Wang, J. Xie, H. F. Tan, Vibration Simulations of a Wrinkled Membrane-Inflated Arch, Journal of Aerospace Engineering 27 (2014) 414–422. doi:10.1061/(ASCE)AS.1943-5525.0000260.

[4] S. Kukathasan, S. Pellegrino, Nonlinear Vibration of Wrinkled Membranes, in: 44th AIAA/ASME/ASCE/AHS/ASC Structures, Structural Dynamics, and Materials Conference, Structures, Structural Dynamics, and Materials and Co-located Conferences, American Institute of Aeronautics and Astronautics, 2003. doi:10.2514/6.2003-1747.

[5] S. Lienard, J. Johnston, B. Ross, Dynamic testing of a subscale sunshield for the Next Generation Space Telescope (NGST), 19th AIAA Applied Aerodynamics Conference (2001). doi:10.2514/6.2001-1268.

[6] A. Chandraul, M. V, S. Kumar, A review on dynamic analysis of membrane based space structures, Advances in Space Research 74 (2024) 740–763. doi:10.1016/j.asr.2024.03.082.

[7] H. Wagner, Flat sheet metal girders with very thin metal web. Part I : General theories and assumptions, 1931.

[8] C. Mseikeh, Wrinkling of Membranes, Plates, and Shells, Canadian Theses, McGill University Libraries, 1997.

[9] M. Stein, J. Hedgepeth, Analysis of partly wrinkled membranes, 1961.

[10] Pipkin, C. Allen, The Relaxed Energy Density for Isotropic Elastic Membranes, IMA Journal of Applied Mathematics 36 (1986) 85–99. doi:10.1093/imamat/36.1.85.

[11] D. G. Roddeman, J. Drukker, C. W. J. Oomens, J. D. Janssen, The Wrinkling of Thin Membranes: Part II—Numerical Analysis, Journal of Applied Mechanics 54 (1987) 888–892. doi:10.1115/1.3173134.

[12] X. F. Wang, Q. S. Yang, S.-s. Law, Wrinkled membrane element based on the wrinkling potential, International Journal of Solids and Structures 51 (2014) 3532–3548. doi:10.1016/j.ijsolstr.2014.06.004.

[13] Y. Miyazaki, Wrinkle/slack model and finite element dynamics of membrane, International Journal for Numerical Methods in Engineering 66 (2006) 1179–1209. doi:10.1002/nme.1588.

[14] A. Hossain, C. H. Jenkins, K. Woo, H. Igawa, Transverse Vibration Analysis for Partly Wrinkled Membranes, Journal of Spacecraft and Rockets 43 (2006) 626–637. doi:10.2514/1.11327.

[15] H. M. Verhelst, Isogeometric Analysis of Wrinkling (2024). doi:10.4233/0e4c3644-31a4-4157-983d-bd001d91b8ca.

[16] R. Rossi, R. Vitaliani, E. Oñate, FE Analysis of membrane systems including wrinkling and coupling (2005). doi:10.1007/1-4020-3317-6_6.

[17] X. Liu, C. H. Jenkins, W. W. Schur, Large deflection analysis of pneumatic envelopes using a penalty parameter modified material model, Finite Elements in Analysis and Design 37 (2001) 233–251. doi:10.1016/S0168-874X(00)00040-8.

[18] M. Taylor, K. Bertoldi, D. J. Steigmann, Spatial resolution of wrinkle patterns in thin elastic sheets at finite strain, Journal of the Mechanics and Physics of Solids 62 (2014) 163–180. doi:10.1016/j.jmps.2013.09.024.

[19] J. Johnston, S. Brodeur, Finite Element Analysis of Wrinkled Membrane Structures for Sunshield Applications (2002).

[20] T. Iwasa, Experimental verification on wrinkling behavior given by wrinkling analysis using the tension field theory, International Journal of Solids and Structures 136–137 (2018) 1–12. doi:10.1016/j.ijsolstr.2017.11.028.

[21] T. J. R. Hughes, J. A. Cottrell, Y. Bazilevs, Isogeometric analysis: CAD, finite elements, NURBS, exact geometry and mesh refinement, Computer Methods in Applied Mechanics and Engineering 194 (2005) 4135–4195. doi:10.1016/j.cma.2004.10.008.

[22] R. Cardoso, O. Adetoro, D. Adan, Contact Modelling in Isogeometric Analysis: Application to Sheet Metal Forming Processes, Journal of Physics: Conference Series 734 (2016) 032123. doi:10.1088/1742-6596/734/3/032123.

[23] B. Oesterle, F. Geiger, D. Forster, M. Fröhlich, M. Bischoff, A study on the approximation power of NURBS and the significance of exact geometry in isogeometric pre-buckling analyses of shells, Computer Methods in Applied Mechanics and Engineering 397 (2022) 115144. doi:10.1016/j.cma.2022.115144.

[24] J. A. Cottrell, A. Reali, Y. Bazilevs, T. J. R. Hughes, Isogeometric analysis of structural vibrations, Computer Methods in Applied Mechanics and Engineering 195 (2006) 5257–5296. doi:10.1016/j.cma.2005.09.027.

[25] O. Weeger, Isogeometric Finite Element Analysis of Nonlinear Structural Vibrations, Ph.D. thesis, 2015.

[26] H. M. Verhelst, M. Möller, J. H. D. Besten, A Wrinkling Model for General Hyperelastic Materials based on Tension Field Theory, 2024. doi:10.48550/arXiv.2410.16990. arXiv:2410.16990.

[27] L. Li, D. Benson, A. Nagy, M. Montanari, N. Petrinic, S. Hartmann, Recent Developments in Isogeometric Analysis with Solid Elements in LS-DYNA, in: 15th International LS-DYNA Users Conference, ANSYS, 2018.

[28] J. Bocko, P. Pleško, I. Delyová, P. Sivák, Comparison of Structural Analysis of Thin-Walled Structures Accomplished by Isogeometric Analysis and the Finite Element Method, Materials 15 (2022) 6516. doi:10.3390/ma15196516.

[29] M. A. Crisfield, A fast incremental/iterative solution procedure that handles "snap-through", Computers & Structures 13 (1981) 55–62. doi:10.1016/0045-7949(81)90108-5.

[30] E. Riks, An incremental approach to the solution of snapping and buckling problems, International Journal of Solids and Structures 15 (1979) 529–551. doi:10.1016/0020-7683(79)90081-7.

[31] S. A. Ragon, Z. Gürdal, L. T. Watson, A comparison of three algorithms for tracing nonlinear equilibrium paths of structural systems, International Journal of Solids and Structures 39 (2002) 689–698. doi:10.1016/S0020-7683(01)00195-0.

[32] X. Liu, G. Cai, Nonlinear dynamic analysis of wrinkled membrane structure, Engineering Computations 40 (2022) 41–61. doi:10.1108/EC-02-2022-0083.

[33] K. Lee, S. Han., T. Park, A simple explicit arc-length method using the dynamic relaxation method with kinetic damping, Computers & Structures 89 (2011) 216–233. doi:10.1016/j.compstruc.2010.09.006.

[34] H. M. Verhelst, M. Möller, J. H. D. Besten, F. J. Vermolen, M. L. Kaminski, Equilibrium Path Analysis Including Bifurcations with an Arc-Length Method Avoiding A Priori Perturbations, in: F. J. Vermolen, C. Vuik (Eds.), Numerical Mathematics and Advanced Applications ENUMATH 2019, Springer International Publishing, Cham, 2021, pp. 1109–1117. doi:10.1007/978-3-030-55874-1_110.

[35] AS. Day, An introduction to dynamic relaxation, The engineer 219 (1965) 218–221.

[36] J. Rombouts, G. Lombaert, L. De Laet, M. Schevenels, On the equivalence of dynamic relaxation and the Newton-Raphson method, International Journal for Numerical Methods in Engineering 113 (2017). doi:10.1002/nme.5707.

[37] P. Underwood, Dynamic relaxation, Computational method for transient analysis, Elsevier (1983) 245–65.

[38] H. Le Meitour, G. Rio, H. Laurent, A. Lectez, P. Guigue, Analysis of wrinkled membrane structures using a Plane Stress projection procedure and the Dynamic Relaxation method, International Journal of Solids and Structures 208–209 (2021) 194–213. doi:10.1016/j.ijsolstr.2020.10.026.

[39] M. Rezaiee-Pajand, H. Estiri, Finding buckling points for nonlinear structures by dynamic relaxation scheme, Frontiers of Structural and Civil Engineering 14 (2020) 23–61. doi:10.1007/s11709-019-0549-z.

[40] E.-S. Lee, S.-K. Youn, Finite element analysis of wrinkling membrane structures with large deformations, Finite Elements in Analysis and Design 42 (2006) 780–791. doi:10.1016/j.finel.2006.01.004.

[41] J. Montes, B. Thomaszewski, S. Mudur, T. Popa, Computational design of skintight clothing, ACM Trans. Graph. 39 (2020) 105:105:1–105:105:12. doi:10.1145/3386569.3392477.

[42] Haseganu, M. Eliza, Analytical Investigation of Tension Fields in Lightweight Membrane Structures, Ph.D. thesis, University of Alberta, 1994.

[43] K. Nakashino, A. Nordmark, A. Eriksson, Geometrically nonlinear isogeometric analysis of a partly wrinkled membrane structure, Computers & Structures 239 (2020) 106302. doi:10.1016/j.compstruc.2020.106302.

[44] Y. Timounay, R. De, J. L. Stelzel, Z. S. Schrecengost, M. M. Ripp, J. D. Paulsen, Crumples as a Generic Stress-Focusing Instability in Confined Sheets, Physical Review X 10 (2020) 021008. doi:10.1103/PhysRevX.10.021008.

[45] J. Kwon, O. Bouaziz, H. S. Kim, Y. Estrin, Finite Element Modeling of Crumpling of Metallic Thin Foil, Advanced Engineering Materials 25 (2023) 2300063. doi:10.1002/adem.202300063.

[46] S. Tudruj, K. Kurec, J. Piechna, K. Kamieniecki, Mass-Spring System (MSS) 3D simulation of a thin flexible membrane with a new model of the elasticity parameters, Archive of Mechanical Engineering vol. 70 (2023) 199–218. doi:10.24425/ame.2023.144817.

[47] J. Andrejevic, C. H. Rycroft, Simulation of crumpled sheets via alternating quasistatic and dynamic representations, Journal of Computational Physics 471 (2022) 111607. doi:10.1016/j.jcp.2022.111607.

[48] R. Narain, T. Pfaff, J. F. O'Brien, Folding and crumpling adaptive sheets, ACM Trans. Graph. 32 (2013) 51:1–51:8. doi:10.1145/2461912.2462010.

[49] N. Jin, W. Lu, Z. Geng, R. P. Fedkiw, Inequality cloth, in: Proceedings of the ACM SIGGRAPH / Eurographics Symposium on Computer Animation, SCA '17, Association for Computing Machinery, New York, NY, USA, 2017, pp. 1–10. doi:10.1145/3099564.3099568.

[50] R. Wijnen, Validation and Improvement of a Dynamic Stiffness Measurement Setup, Master's thesis, Eindhoven University of Technology, 2019.

[51] M. Hoogerkamp, R. R. Waiboer, R. G. K. M. Aarts, Modeling of flexible non-linear dynamic links in Nano-Positioning Motion Systems, in: ECCOMAS Multibody Dynamics 2013, 1-4 July, 2013, University of Zagreb, Croatia, University of Zagreb, 2013, pp. 287–296.

[52] C. A. Maas, B. Thibault, New Generation of Flexible Elastomer Exhaust Decouplers: LINKEO System, Technical Report 2005-01-1153, SAE Technical Paper, 2005. doi:10.4271/2005-01-1153.

[53] Polyfluor Plastics B.V., Material Datasheet: FEP (Fluorinated Ethylene Propylene), Material Datasheet, Polyfluor Plastics B.V., 2026.

[54] A. Othman, A. Jailani, M. Hamzah, S. Applanaidu, Finite Element Modeling of Radial Corrugated Tubular Composite Structure under Axial Loading, 2012.

[55] A. Rossi, Z. Fawaz, K. Behdinan, Numerical simulation of the axial collapse of thin-walled polygonal section tubes, Thin-Walled Structures 43 (2005) 1646–1661. doi:10.1016/j.tws.2005.03.001.

[56] Z. Liu, W. Hao, J. Xie, J. Lu, R. Huang, Z. Wang, Axial-impact buckling modes and energy absorption properties of thin-walled corrugated tubes with sinusoidal patterns, Thin-Walled Structures 94 (2015) 410–423. doi:10.1016/j.tws.2015.05.002.

[57] Altair Engineering Inc., Altair Radioss User Documentation, Software Documentation Radioss 2025.1, 2025.

[58] Vortex CAE, Vortex-Radioss, Vortex Engineering Group Ltd, 9-9-25.

[59] DYNAmore GmbH, LS-DYNA User's Guide, https://www.dynasupport.com/tutorial/ls-dyna-users-guide, 2026.

[60] L. Morancay, G. Winkelmuller, Dynamic condensation and selective mass scaling in RADIOSS® Explicit (2009).

[61] J. van Steen, Comparison of Model Order Reduction Techniques for Interface Dynamics, Master's thesis, Eindhoven University of Technology, Eindhoven, 2020.

[62] N. Yamaki, Elastic Stability of Circular Cylindrical Shells, North-Holland Series in Applied Mathematics and Mechanics; Vol. 27, North-Holland, Amsterdam, 1984.

[63] M. C. Fokker, S. Janbaz, A. A. Zadpoor, Crumpling of thin sheets as a basis for creating mechanical metamaterials, RSC Advances 9 (2019) 5174. doi:10.1039/c8ra07565d.

4

Conclusions

4.1. Main contributions

In this work, we investigated the static and dynamic mechanical behaviour of crumpled thin-sheet bellows, motivated by their potential as ultra-compliant dynamic links for vibration isolation in vacuum mechatronic systems. The primary challenge addressed was the inherent geometric non-linearity and randomness of crumpled structures, which pose significant hurdles for both experimental characterization and numerical modelling.

Our key contributions include the development of a combined experimental-numerical framework to quantify axial and radial stiffness as functions of sheet thickness and overlength. Experimentally, we adapted an existing measurement setup to measure static and frequency-dependent dynamic stiffness, employing multi-sine excitation to concentrate signal power in targeted frequency bands despite low force levels. Although the dynamic regimes of the transfer functions exhibited significant contamination by background noise, the results revealed some clear correlations: static stiffness decreased with increasing overlength but showed diminishing returns, approaching a stable lower bound at high overlengths.

Numerically, we introduced an efficient and automatable explicit finite element approach using Altair Radioss to generate realistic crumpled morphologies, integrated with a novel stress-removal technique for single-run static stiffness evaluation. We further applied the Hintz-Herting modal reduction method in ANSYS to predict dynamic stiffness for select configurations. Simulations qualitatively replicated experimental trends, such as the convergence of dynamic stiffness between different overlengths in the dynamic regime. In general, trends and discrepancies between experiments and simulation were highlighted via the formulation of new power-law relations between stiffness, thickness and overlength.

Beyond methodological contributions, the thesis clarifies a fundamental design trade-off: increasing overlength is highly effective in reducing stiffness, particularly in the (axial) crumpling direction. However, excessive crumpling introduces diminishing returns and practical risks: extreme local curvature increases the likelihood of pinhole formation, dense self-contact may create unintended mechanical shortcuts, and dynamic stiffness converges irrespective of further geometric complexity. Crumpling is therefore a powerful but bounded stiffness-reduction mechanism. An optimal crumpling state likely exists in which compliance is maximized without sacrificing robustness, structural integrity, and dynamic predictability.

While general quantitative agreement between simulations and experiments remains limited, this study demonstrates that explicit modelling of crumpled geometries, combined with subsequent implicit (dynamic) analysis, provides a viable pathway for the study of such systems. The approach confirms that even relatively simple linear material models can capture the dominant stiffness trends, while also exposing their shortcomings such as the lack of plasticity or self-contact.

One conclusion is clear: crumpling may appear chaotic, but it is not beyond engineering control. Even within its geometric disorder, there is structure, and within that structure, there is design space.

4.2. Future work

The results of this thesis open several clear directions for further research aimed at improving predictive capability, computational efficiency, and experimental robustness.

Adaptive mesh refinement

Crumpled membranes concentrate curvature and strain in narrow ridges and folds, forcing uniformly fine meshes and high computational cost. Systematic implementation of adaptive mesh refinement would localize mesh resolution where needed while keeping the remainder coarse. Given that Altair Radioss already supports adaptive meshing [29], this represents a direct opportunity to significantly reduce computation time without sacrificing accuracy, as demonstrated in prior studies [30–34].

Further automation

The current simulation workflow involves multiple manual steps, including geometry generation, parameter variation, and post-processing of modal reduction results. Increased automation would improve both efficiency and reproducibility. In particular, scripting and programming in Altair HyperStudy could enable systematic, automated variation of model parameters. Furthermore, results generated in Radioss may be more easily transferred to Altair OptiStruct rather than ANSYS for the application of modal analyses, although additional scripting would be required to implement the subsequent modal reduction.

Alternatively, both explicit dynamic relaxation for crumpling and dynamic analysis via modal reduction could potentially be performed in ANSYS LS-DYNA [35]. While LS-DYNA offers a broader feature set, this comes at the cost of increased model complexity and a steeper learning curve. Initial experimentation with LS-DYNA via the ANSYS Workbench interface revealed limitations, such as restricted control over damping in dynamic relaxation. Recreating the full workflow would require LS-PrePost, which proved far less user-friendly than Altair pre- and post-processing tools.

Surrogate modelling

Exploring the full parameter space of crumpled foils is computationally expensive due to the high dimensionality of systems and highly non-linear system response. Following Luo et al. [36], Latin hypercube sampling could be used to efficiently generate representative configurations of key variables, such as foil thickness, overlength, cylinder diameter, and reference height. These samples could train surrogate models for capturing non-linear and interdependent effects of input parameters on static and dynamic stiffness. Existing frameworks, such as that of Vu-Bac et al. [37], could enable rapid evaluation of many parameter combinations, revealing trends, interactions, and sensitivities that would be impractical with full-scale parameter sweeps. Such surrogate-based approaches facilitate efficient design-space exploration and provide actionable insight into how geometric and material variability influence foil bellow performance.

Experimental modal analysis

A more in-depth understanding of crumpled structure dynamics could be achieved by directly examining their natural vibrational modes. In this work, modal analysis via modal reduction was employed to compute dynamic stiffness, but validation was limited to comparisons of emergent static and dynamic stiffness rather than individual eigenfrequencies or mode shapes.

Direct experimental identification of eigenmodes in crumpled membranes is challenging due to irregular geometry and limited sensor access. Nevertheless, studies on wrinkled and folded thin structures have demonstrated the feasibility of using laser-Doppler vibrometry to measure natural frequencies and mode shapes [3, 38]. Advanced vibrometer systems incorporating depth scanning could potentially be applied to crumpled membranes, providing insight into modal density, frequency spacing, and sensitivity to geometric perturbations. While exact correspondence of mode shapes between experiment and simulation is unlikely due to stochastic crumpling, comparisons of frequency spectra could serve as a meaningful validation metric.

Elasto-plasticity

The influence of plastic deformation in crumpled membranes warrants further investigation as it is suspected of increased weakening of bending ridges during axial deformations. The current stress-removal approach is incompatible with conventional plasticity models, preventing explicit capture of permanent deformations and their effect on stiffness evolution. Future work should explore methods to measure static stiffness without relying on custom material models, such as custom user routines for stress-removal. Incorporating plastic effects would be particularly relevant for understanding hysteresis and the quick weakening of axial stiffness at moderate overlengths.

Self-contact

Self-contact is a defining feature of highly compacted crumpled structures and significantly affects load transfer and stiffness saturation at extreme overlength, see appendix C. Radioss offers multiple contact formulations based on Lagrange multiplier or penalty method which should be systematically studied, informed by literature on crashworthiness [26, 27, 39] and approaches in discrete element analysis [5, 31, 40–43]. A study varying contact stiffness, friction, and contact density could clarify the role of self-contact in the experimentally observed transition from stiffness reduction to saturation.

Isogeometric analysis

While isogeometric analysis was not suitable for this study due to its relative immaturity compared to conventional finite element methods, literature suggests that buckled shell structures could benefit from spline-based modelling. IGA could reduce the number of degrees of freedom required to model complex geometries, potentially yielding substantial computational speed-ups. IGA is already being used in industry for automatic crash and crumpling simulations [33, 44], so it may also have benefits for the foil bellow case.

Foil bellow design

Although not the primary objective of this study, the acquired results provide several preliminary design insights for the foil bellow concept. As demonstrated in chapter 3, the axial stiffness increases very rapidly with overlength, indicating that only a moderate overlength (30-60%) is required to obtain a highly compliant link.

Furthermore, stiffness decreases strongly with decreasing sheet thickness. While thickness reduction is therefore an effective strategy for enhancing compliance, careful consideration must be given to manufacturability and durability. In particular, very thin sheets are more susceptible to pinhole formation and material damage at sharp folds introduced during the crumpling process. A balanced design must therefore account for both mechanical compliance and structural integrity.

Measurement setup

Finally, the experimental setup can be further improved. The measured dynamic stiffness coherence deteriorated above approximately 50 Hz, particularly for thin membranes with large overlengths. This reduced the reliability of the higher-frequency results and introduced uncertainty in the identification and interpretation of resonant behaviour.

The current setup was selected primarily based on availability and compatibility with the cylindrical geometry of the foil bellow. However, it was not specifically designed for ultra-compliant structures that generate extremely small force levels. For such low-stiffness systems, a purpose-built measurement configuration is essential to accurately capture the true dynamic behaviour.

It is suspected that part of the measurement noise originates from parasitic shaker reaction paths transmitted through the measurement frame. A redesigned setup with fully separated base and metrology frames would significantly reduce such disturbances. For example, mounting the shaker on one granite isolation table and the force measurement system on a second, mechanically decoupled granite isolation table (see Figure 4.1) would minimize force bypass and frame-coupling effects. In such a configuration, the large suspended preload mass could likely be omitted, enabling a simpler and mechanically cleaner force-cell interface frame.

In addition, constructing a setup suitable for in-vacuo experiments would allow direct investigation of the influence of surrounding air on the dynamic stiffness of the foil bellow. Although aerodynamic effects were not considered critical for the present experiments, studies by Kukathasan and Pellegrino [38, 45] indicate that fluid–structure interaction effects may become non-negligible for very thin, highly compliant sheets. Quantifying this influence would further strengthen the interpretation of dynamic stiffness measurements.

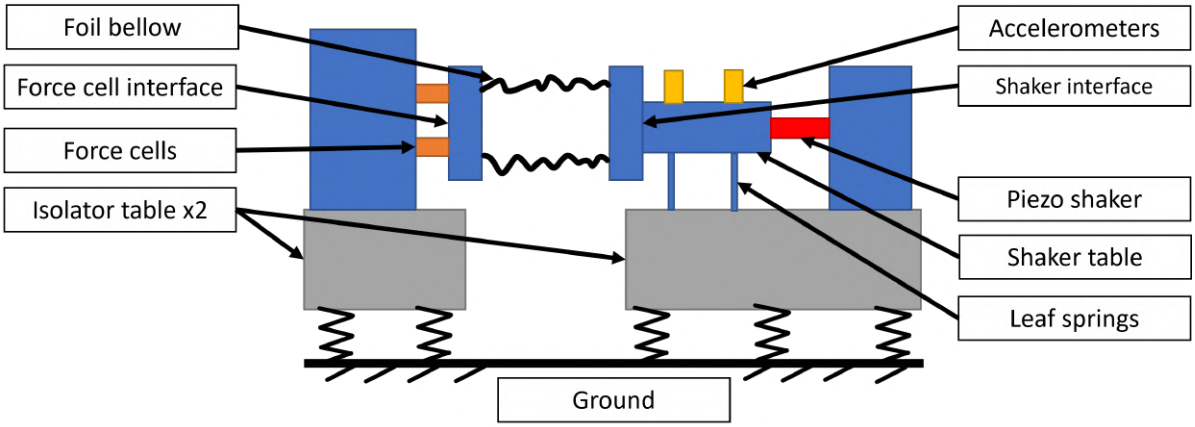

Figure 4.1: Schematic architecture of an improved measurement setup. The base and metrology frames are separated onto two (granite) vibration isolation tables to eliminate shaker reaction path disturbances affecting the force measurements.

References

[1] S. Forest. *Crumpled Paper*. Dec. 2018.

[2] M. C. Fokker, S. Janbaz, and A. A. Zadpoor. “Crumpling of Thin Sheets as a Basis for Creating Mechanical Metamaterials”. In: *RSC Advances* 9.9 (Nov. 2019), p. 5174. DOI: 10.1039/c8ra07565d. (Visited on 12/18/2024).

[3] N. Hossain, Kyeongsik Woo, and Christopher Jenkins. “Dynamic Response of Systematically Creased Membranes”. In: *48th AIAA/ASME/ASCE/AHS/ASC Structures, Structural Dynamics, and Materials Conference*. American Institute of Aeronautics and Astronautics, Apr. 2007. DOI: 10.2514/6.2007-1806. (Visited on 01/04/2025).

[4] Gerard Giménez-Ribes et al. “Crumpled Structures as Robust Disordered Mechanical Metamaterials”. In: *Materials & Design* 232 (Aug. 2023), p. 112159. ISSN: 0264-1275. DOI: 10.1016/j.matdes.2023.112159. (Visited on 12/15/2025).

[5] Jihye Kwon et al. “Finite Element Modeling of Crumpling of Metallic Thin Foil”. In: *Advanced Engineering Materials* 25.13 (2023), p. 2300063. ISSN: 1527-2648. DOI: 10.1002/adem.202300063. (Visited on 12/16/2024).

[6] Alex Lobkovsky et al. “Scaling Properties of Stretching Ridges in a Crumpled Elastic Sheet”. In: *Science* 270 (Dec. 1995), pp. 1482–1485. ISSN: 0036-8075. DOI: 10.1126/science.270.5241.1482. (Visited on 12/15/2025).

[7] Subhajit Kundu et al. “Crumpled Sheets of Reduced Graphene Oxide as a Highly Sensitive, Robust and Versatile Strain/Pressure Sensor”. In: *Nanoscale* 9.27 (July 2017), pp. 9581–9588. ISSN: 2040-3372. DOI: 10.1039/C7NR02415K. (Visited on 12/15/2025).

[8] Olivier Bouaziz, Rabeb Bouafif, and Roxanne Massion. “Sandwich Materials with a Crumpled Aluminium Core”. In: *Metallurgical Research & Technology* 118.3 (2021), p. 320. DOI: 10.1051/metal/2021014. (Visited on 12/15/2025).

[9] Mahya Ganjian et al. “Controlled Metal Crumpling as an Alternative to Folding for the Fabrication of Nanopatterned Meta-Biomaterials”. In: *Materials & Design* 220 (Aug. 2022), p. 110844. ISSN: 0264-1275. DOI: 10.1016/j.matdes.2022.110844. (Visited on 12/15/2025).

[10] Toby Sterling and Nathan Vifflin. “ASML’s Order Book Expected to Jump on AI Chip Boom”. In: *Reuters* (July 2024). (Visited on 12/15/2025).

[11] ASML Holding N.V. *2024 Annual Report*. Annual Report. Veldhoven, The Netherlands: ASML Holding N.V., Mar. 2025.

[12] ASML Holding N.V. *EUV Lithography Systems*. https://www.asml.com/en/products/euv-lithography-systems. (Visited on 12/15/2025).

[13] ASML Holding N.V. *Lithography Principles*. https://www.asml.com/en/technology/lithography-principles. (Visited on 12/15/2025).

[14] Boudewijn G. Sluijk et al. “Performance Results of a New Generation of 300-Mm Lithography Systems”. In: *Optical Microlithography XIV*. Vol. 4346. SPIE, Sept. 2001, pp. 544–557. DOI: 10.1117/12.435752. (Visited on 12/16/2025).

[15] Donis G. Flagello, Jan Mulkens, and Christian Wagner. “Optical Lithography into the Millennium: Sensitivity to Aberrations, Vibration, and Polarization”. In: *Optical Microlithography XIII*. Vol. 4000. July 2000, pp. 172–183. DOI: 10.1117/12.388983. (Visited on 12/16/2025).

[16] Rawan Semaan et al. “Imaging Effects of Particles on the Surface of EUV Mask and Wafer”. In: *39th European Mask and Lithography Conference (EMLC 2024)*. Vol. 13273. SPIE, 2024, pp. 30–48.

[17] ASML Holding N.V. *Mechanics & Mechatronics*. https://www.asml.com/en/technology/lithography-principles/mechanics-and-mechatronics. (Visited on 12/15/2025).

[18] M. Hoogerkamp, R. R. Waiboer, and Ronald G. K. M. Aarts. “Modeling of Flexible Non-Linear Dynamic Links in Nano-Positioning Motion Systems”. In: *ECCOMAS Multibody Dynamics 2013, 1-4 July, 2013, University of Zagreb, Croatia*. University of Zagreb, July 2013, pp. 287–296. (Visited on 12/16/2025).

[19] R.A.G. Wijnen. “Validation and Improvement of a Dynamic Stiffness Measurement Setup”. MA thesis. Eindhoven University of Technology, 2019.

[20] Arnaud Deraemaeker. *Dynamics of Structures*. Lecture Notes. Brussels, Belgium: Université libre de Bruxelles. (Visited on 12/16/2025).

[21] N. Gil-Negrete et al. “On the Dynamic Stiffness of Air Springs at Medium-High Frequencies”. In: *Proceedings of ISMA 2018 AND USD2018*. 2018, pp. 3567–3580.

[22] Aileen Crass. *What Is PFA and What Is It Used For?* Sept. 2021. (Visited on 12/17/2025).

[23] Semiconductor PFAS Consortium. *Background on Semiconductor Manufacturing and PFAS*. White Paper. Semiconductor Industry Association (SIA), May 2023.

[24] N. Yamaki. *Elastic Stability of Circular Cylindrical Shells*. North-Holland Series in Applied Mathematics and Mechanics; Vol. 27. Amsterdam: North-Holland, 1984. Chap. XIII, 558 p. : illustrations ; 23 cm. ISBN: 0-444-86857-7 978-0-444-86857-2.

[25] Yousra Timounay et al. “Crumples as a Generic Stress-Focusing Instability in Confined Sheets”. In: *Physical Review X* 10.2 (Apr. 2020), p. 021008. ISSN: 2160-3308. DOI: 10.1103/PhysRevX.10.021008. (Visited on 12/06/2024).

[26] Zhifang Liu et al. “Axial-Impact Buckling Modes and Energy Absorption Properties of Thin-Walled Corrugated Tubes with Sinusoidal Patterns”. In: *Thin-Walled Structures* 94 (Sept. 2015), pp. 410–423. ISSN: 0263-8231. DOI: 10.1016/j.tws.2015.05.002. (Visited on 04/29/2025).

[27] A. Rossi, Z. Fawaz, and K. Behdinan. “Numerical Simulation of the Axial Collapse of Thin-Walled Polygonal Section Tubes”. In: *Thin-Walled Structures* 43.10 (Oct. 2005), pp. 1646–1661. ISSN: 0263-8231. DOI: 10.1016/j.tws.2005.03.001. (Visited on 04/29/2025).

[28] H. M. Verhelst et al. “Equilibrium Path Analysis Including Bifurcations with an Arc-Length Method Avoiding A Priori Perturbations”. In: *Numerical Mathematics and Advanced Applications ENUMATH 2019*. Ed. by Fred J. Vermolen and Cornelis Vuik. Cham: Springer International Publishing, 2021, pp. 1109–1117. ISBN: 978-3-030-55874-1. DOI: 10.1007/978-3-030-55874-1_110.

[29] Altair Engineering Inc. *Altair Radioss User Documentation*. Software Documentation Radioss 2025.1. 2025.

[30] L Morancay and G Winkelmuller. “Dynamic Condensation and Selective Mass Scaling in RADIOSS® Explicit”. In: (2009).

[31] Rahul Narain, Tobias Pfaff, and James F. O’Brien. “Folding and Crumpling Adaptive Sheets”. In: *ACM Trans. Graph.* 32.4 (July 2013), 51:1–51:8. ISSN: 0730-0301. DOI: 10.1145/2461912.2462010. (Visited on 12/11/2024).

[32] H. M. Verhelst. “Isogeometric Analysis of Wrinkling”. In: (2024). DOI: 10.4233/0e4c3644-31a4-4157-983d-bd001d91b8ca. (Visited on 12/13/2024).

[33] T. J. R. Hughes, J. A. Cottrell, and Y. Bazilevs. “Isogeometric Analysis: CAD, Finite Elements, NURBS, Exact Geometry and Mesh Refinement”. In: *Computer Methods in Applied Mechanics and Engineering* 194.39 (Oct. 2005), pp. 4135–4195. ISSN: 0045-7825. DOI: 10.1016/j.cma.2004.10.008. (Visited on 12/17/2024).

[34] Hugo Verhelst. “Modelling Wrinkling Behaviour of Large Floating Thin Offshore Structures: An Application of Isogeometric Structural Analysis for Post-Buckling Analyses”. In: (2019).

[35] DYNAmore GmbH. *LS-DYNA User’s Guide*. https://www.dynasupport.com/tutorial/ls-dyna-users-guide. 2026. (Visited on 12/04/2025).

[36] Yangjun Luo et al. “Uncertainty of Membrane Wrinkling Behaviors Considering Initial Thickness Imperfections”. In: *International Journal of Solids and Structures* 191–192 (May 2020), pp. 264–277. ISSN: 0020-7683. DOI: 10.1016/j.ijsolstr.2020.01.022. (Visited on 02/18/2025).

[37] Nam Vu-Bac et al. “A Software Framework for Probabilistic Sensitivity Analysis for Computationally Expensive Models”. In: *Advances in Engineering Software* 100 (Oct. 2016), pp. 19–31. DOI: 10.1016/j.advengsoft.2016.06.005.

[38] S. Kukathasan and Sergio Pellegrino. “Nonlinear Vibration of Wrinkled Membranes”. In: *44th AIAA/ASME/ASCE/AHS/ASC Structures, Structural Dynamics, and Materials Conference*. Structures, Structural Dynamics, and Materials and Co-located Conferences. American Institute of Aeronautics and Astronautics, Apr. 2003. DOI: 10.2514/6.2003-1747. (Visited on 11/27/2024).

[39] Akbar Othman et al. *Finite Element Modeling of Radial Corrugated Tubular Composite Structure under Axial Loading*. Mar. 2012.

[40] Sylwester Tudruj et al. “Mass-Spring System (MSS) 3D Simulation of a Thin Flexible Membrane with a New Model of the Elasticity Parameters”. In: *Archive of Mechanical Engineering* vol. 70.No 2 (Apr. 2023), pp. 199–218. DOI: 10.24425/ame.2023.144817.

[41] Jovana Andrejevic and Chris H. Rycroft. “Simulation of Crumpled Sheets via Alternating Quasistatic and Dynamic Representations”. In: *Journal of Computational Physics* 471 (Dec. 2022), p. 111607. ISSN: 0021-9991. DOI: 10.1016/j.jcp.2022.111607. (Visited on 12/06/2024).

[42] Ning Jin et al. “Inequality Cloth”. In: *Proceedings of the ACM SIGGRAPH / Eurographics Symposium on Computer Animation*. SCA ’17. New York, NY, USA: Association for Computing Machinery, July 2017, pp. 1–10. ISBN: 978-1-4503-5091-4. DOI: 10.1145/3099564.3099568. (Visited on 01/27/2025).

[43] Juan Montes et al. “Computational Design of Skintight Clothing”. In: *ACM Trans. Graph.* 39.4 (Aug. 2020), 105:105:1–105:105:12. ISSN: 0730-0301. DOI: 10.1145/3386569.3392477. (Visited on 01/27/2025).

[44] H. M. Verhelst, M. Möller, and J. H. Den Besten. *A Wrinkling Model for General Hyperelastic Materials Based on Tension Field Theory*. Oct. 2024. DOI: 10.48550/arXiv.2410.16990. arXiv: 2410.16990 [cs, math]. (Visited on 12/13/2024).

[45] S. Kukathasan and Sergio Pellegrino. *Vibration of Prestressed Membrane Structures in Air*. Vol. 2. Apr. 2002. ISBN: 978-1-62410-117-5. DOI: 10.2514/6.2002-1368.

[46] Vortex CAE. *Vortex-Radioss*. Vortex Engineering Group Ltd. 9-9-25.

[47] Xiang Liu and G.P. Cai. “Nonlinear Dynamic Analysis of Wrinkled Membrane Structure”. In: *Engineering Computations* 40.1 (Jan. 2022), pp. 41–61. ISSN: 0264-4401. DOI: 10.1108/EC-02-2022-0083. (Visited on 11/25/2024).

[48] J.J. van Steen. “Comparison of Model Order Reduction Techniques for Interface Dynamics”. MA thesis. Eindhoven: Eindhoven University of Technology, Jan. 2020. (Visited on 11/27/2025).

A

Numerical method

This appendix documents additional details of the numerical implementation and support the modelling choices outlined in chapter 3. It focuses on the explicit dynamic relaxation strategy, the static stiffness extraction, the dynamic stiffness extraction, and validation studies.

For reference, all simulations were performed on a laptop equipped with an Intel(R) Core(TM) i7-9750H CPU @ 2.60 GHz and 16 GB of RAM. Radioss explicit analyses were executed using shared-memory parallelisation with 8 threads (command-line option `-nt 8`). Ansys modal analyses were executed on 6 threads.

A.1. Dynamic relaxation framework

In this work, static crumpled configurations are obtained using a dynamic relaxation approach in an explicit finite-element setting. The underlying static problem can be written schematically as [29]

$$\mathbf{f}(\mathbf{u}) = \mathbf{p}, \tag{A.1}$$

where $\mathbf{f}$ collects the internal forces and $\mathbf{p}$ the applied loads, and $\mathbf{u}$ representing the solution vector of nodal displacements. Instead of solving this highly non-linear equilibrium condition directly via load-stepping and Newton-Raphson iterations, DRM interprets the desired static state as the limit of a fictitious damped dynamic system in pseudo-time:

$$\mathbf{M}'\,\ddot{\mathbf{u}} + \mathbf{C}'\,\dot{\mathbf{u}} + \mathbf{f}(\mathbf{u}) = \mathbf{p}, \tag{A.2}$$

with artificial mass matrix $\mathbf{M}'$ and damping matrix $\mathbf{C}'$. These terms are chosen such that the structure oscillates around equilibrium and gradually settles into a static configuration. While $\mathbf{M}'$ and $\mathbf{C}'$ do not influence the final equilibrium (if convergence is reached), they strongly affect the admissible time step, the rate of convergence, and the robustness of the simulation.

In Radioss, this dynamic relaxation framework is realised by combining (advanced) mass scaling, which effectively controls the admissable time-step, with dedicated dynamic-relaxation damping models that suppress residual oscillations. The next subsections summarise the mass-scaling strategies used in this study and the damping options that were found to be robust for thin crumpling shells.

A.1.1. Mass-scaling strategies

For any explicit dynamic relaxation regime the absolute time-scale of the deformation is arbitrary, as only the final equilibrium state is of interest. Consequently, the total runtime is determined by the number of time-steps and the cost of each step, such that increasing the admissible time-step is crucial for accelerating the simulation.

In explicit integration the stable time step is limited by the Courant stability condition: the increment must be small enough that stress waves travelling through the material do not skip any elements between updates [29]. For a characteristic element length l_c and speed of sound c in the material, the critical time-step reads

$$\Delta t \leq \Delta t_{\text{Courant}} = \frac{l_c}{c} = l_c \sqrt{\frac{\rho}{E}}, \tag{A.3}$$

where ρ is the density and E the material Young's modulus. As a result, finer and more accurate meshes directly reduce the admissible time step and increase the number of required increments. However, for (quasi-)static problems the final equilibrium is not dependent on the mass of the system, only its stiffness. Therefore, explicit solvers such as Radioss and LS-Dyna offer several mass-scaling options to artificially increase density and thus the Courant time-step [29, 35].

In the traditional nodal mass-scaling scheme (`DT/NODA/CST`) [29], additional nodal mass is added in regions where the Courant time-step falls below a user-defined threshold Δt_{min}. This locally increases ρ and therefore relaxes the stability limit. However, the time step only grows with $\sqrt{\rho}$, so substantial mass must be added to achieve large gains in Δt. Beyond a certain point the artificial inertia dominates the dynamics and distorts the crumpling process.

In the present problem, this effect manifests as the cylindrical shell *lagging* behind the motion of the top rigid body when excessive nodal mass scaling is used: instead of crumpling, the shell folds globally due to its large inertia. A representative comparison is shown in Figure A.1, where a cylindrical quadrant is crumpled under four different mass-scaling strategies. Without mass scaling, over 2×10^5 time steps are required and runtime is prohibitive. With aggressive traditional nodal mass scaling, the number of time steps can be reduced by $\mathcal{O}(10^2)$. However, this corresponds to an effective mass increase of order $dM/M \approx 1.5 \times 10^5$, which leads to a folded rather than crumpled geometry as elements cannot follow the applied boundary conditions in time.

To circumvent this limitation, advanced (or selective [35]) mass scaling (`DT/AMS`) is employed. Rather than simply increasing the lumped masses on the diagonal of the mass matrix, this approach modifies the mass matrix $\mathbf{M}$ by adding off-diagonal terms that compensate the diagonal increase [29, 30].

$$\bar{\mathbf{M}} = \mathbf{M} + \alpha \mathbf{\Lambda} \text{ with } \lambda = \frac{m_e}{12} \begin{bmatrix} 3 & -1 & -1 & -1 \\ -1 & 3 & -1 & -1 \\ -1 & -1 & 3 & -1 \\ -1 & -1 & -1 & 3 \end{bmatrix} \tag{A.4}$$

where $\mathbf{M}$ and $\bar{\mathbf{M}}$ are the original and reformed mass matrices, α is the mass-scaling parameter, and the assembly $\mathbf{\Lambda}$ is created from the constant elementary matrices λ, here shown for a 4-node shell element with element mass m_e. In this way the total mass and translational kinetic energy of the system are preserved. Only the higher eigenfrequencies of the system are decreased, while affecting the lower frequencies as little as possible:

$$\bar{\omega}^2 = \omega^2 / (1 + \alpha \omega^2) \tag{A.5}$$

with ω and $\bar{\omega}$ the original and reformed eigenfrequencies.

Figure A.1 illustrates how advanced mass scaling can substantially reduce the required number of time steps while preserving the physical crumpling morphology. Because the mass matrix is no longer diagonal, however, the nodal accelerations cannot be updated explicitly in closed form and must instead be obtained iteratively, increasing the computational cost per time step and thereby offsetting part of the nominal runtime gain. In practice, a balance must therefore be found, typically by trial and error, where

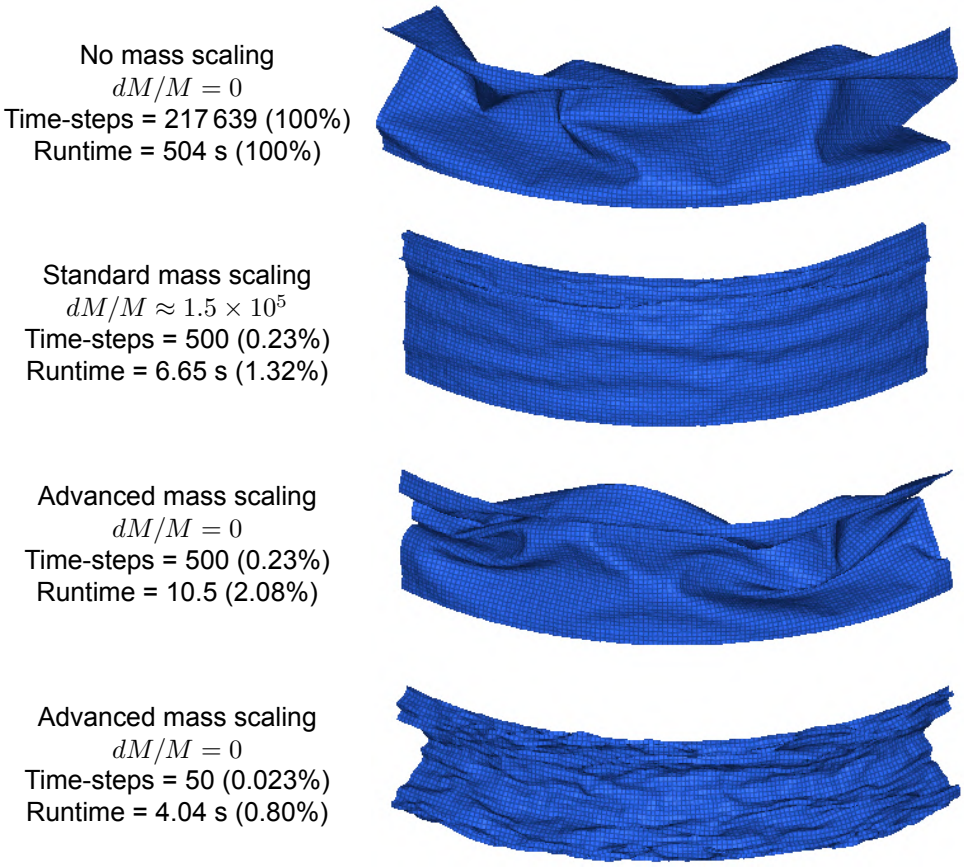

Figure A.1: Comparison between mass-scaling schemes for crumpling simulations of a cylindrical quadrant. The number of required time steps, and thus the computational effort, can be reduced drastically. However, achieving this degree of speed-up with standard nodal mass scaling requires an extreme amount of added mass ($dM/M \approx 1.5 \times 10^5$), which leads to the shell lagging behind the imposed motion and folding instead of crumpling. Advanced mass scaling preserves crumpling at comparable time steps by compensating the diagonal mass increase with off-diagonal terms, at the expense of a slightly higher cost per time step.

the reduction in time steps outweighs the additional cost of each step. Moreover, there is a physical limit to the admissible amount of mass scaling: for sufficiently large time steps the crumpled pattern starts to deviate visibly from the reference solution. The examples in Figure A.1 illustrate this trade-off between computational efficiency, geometric fidelity, and numerical robustness.

A sensitivity study on the allowable strength of mass-scaling for the cylinder case study is presented in section A.3.

A.1.2. Damping strategies

In dynamic relaxation only the final equilibrium state is of interest, so damping can be tailored to suppress transient oscillations and accelerate convergence. Radioss implements several DRM-oriented damping options, of which two were tested here, inspired by the conclusions of chapter 2:

- *Adaptive viscous nodal damping* (`/ADYREL`), which adds a damping matrix

$$\mathbf{C} = \frac{2\beta}{T}\,\mathbf{M} \tag{A.6}$$

  to the equations of motion, with β a dimensionless relaxation factor (typically $\beta \approx 1$) and T a characteristic period of the modes to be damped. In the adaptive version, T is updated throughout the simulation based on the evolving response, allowing the damping to remain effective as the structure softens and the spectrum shifts.
- *Kinetic damping* (`/KEREL`), an empirical scheme which repeatedly resets all nodal velocities to zero whenever the total kinetic energy reaches a local maximum. This method mimics critical damping without the need for explicitly forming a damping matrix.

For a simple benchmark problem from the Radioss reference manual involving the static settling of a simplified dummy structure [29], kinetic damping produced the shortest convergence time: the system decayed rapidly to equilibrium in a few oscillations without noticeable overshoot. However, when applied to the crumpling of thin cylindrical quadrants, significant differences emerged between thick and thin shells. Figure A.2 compares the final crumpled shapes for a thickness of 1000 µm and 100 µm, using either adaptive viscous damping or kinetic damping, without additional mass scaling.

For the thick shells, both schemes converged to similar geometries. For the thin shells, however, kinetic damping became unstable: localised oscillations amplified and led to mesh distortion and non-physical self-intersecting patterns, whereas the adaptive viscous scheme remained stable and produced a plausible crumpled pattern. In addition, kinetic damping is not recommended in combination with automatic mass scaling [29], which is essential for computational feasibility in the present study. For these reasons, adaptive viscous damping (`/ADYREL`) was adopted for all production runs due to its greater robustness, despite a slightly higher computational cost per time step.

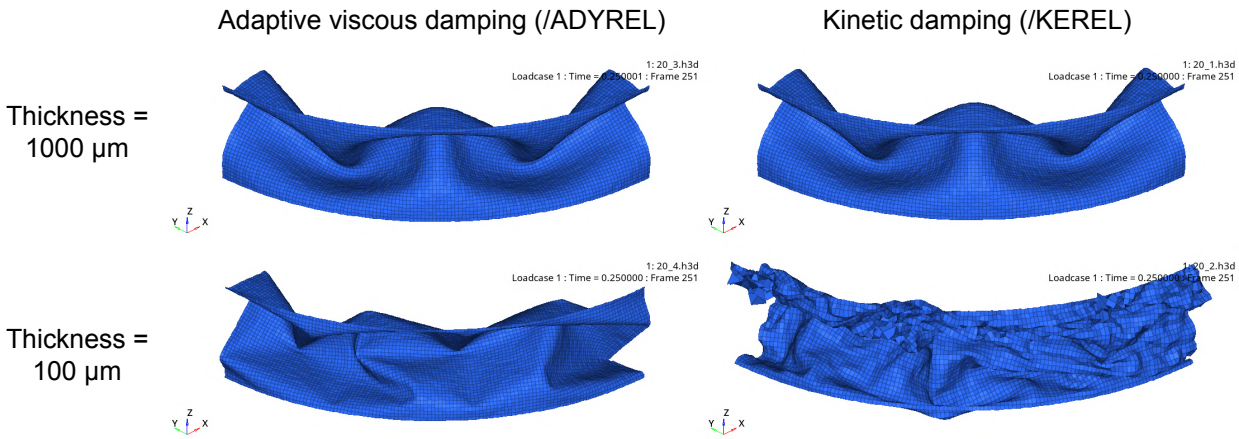

Figure A.2: Comparison between dynamic-relaxation schemes for thick (1000 µm) and thin (100 µm) shells in crumpling simulations of a cylindrical quadrant, without mass scaling.

A.2. Static stiffness extraction

A key objective of this work is to obtain a *robust* static stiffness metric directly from the explicit crumpling simulation. Ideally, the crumpling step and the subsequent stiffness evaluation could be performed in a single, automated Radioss workflow. This section reviews the experiences gathered from trying various methodologies, such as displacement- and force probing and stress removal methods.

A.2.1. Displacement- versus force-probing

The most straightforward approach to calculating stiffness is to infer it from the crumpling step itself: apply an imposed displacement and read the reported reaction force in the same direction. However, when inspecting the axial reaction forces for different overlengths (see Figure A.3b), it becomes clear that this signal is poorly suited for extracting a meaningful stiffness.

At the onset of crumpling a pronounced force peak opposite to the imposed axial motion is typically observed, associated with the first buckling event. After this initial instability, the reaction force drops as the structure becomes more compliant due to the formation of curvature and folds. With increasing deformation the force generally rises again, but *not monotonically*: discrete rearrangements of wrinkles and folds lead to sudden jumps as the morphology reorganizes. In addition, the signal contains substantial high-frequency fluctuations, which are inherent to explicit time integration as all forces are transferred via propagating sound waves of all frequencies.

As a consequence, extracting a stiffness from this curve is ill-posed. A local tangent stiffness, i.e. $k_t = \mathrm{d}F/\mathrm{d}z$, evaluated at the final position $z = 0.13\,\mathrm{m}$, can become spuriously positive or negative purely due to noise and local snap-through events. Even when switching the final increment from an explicit to an implicit linear solve (see Figure A.3a), the apparent slope remains spurious and does not show a consistent trend with increasing overlength. For some configurations, an apparent *negative local stiffness* is observed (e.g. 31% and 54% overlength in Figure A.3a), reflecting a local release of load during buckling/snap-through rather than a meaningful global stiffness of the structure.

Furthermore, the measured reaction force is not uniquely determined by the final geometry alone: it depends on the chosen numerical time scale, see Figure A.3c. In particular, the reaction force level and the average post-peak slope are sensitive to the amount of mass scaling, or equivalently the imposed loading rate. Higher mass scaling or faster loading produces larger reaction forces and a noticeably different mean force-displacement response.

These observations lead to the conclusion that reaction forces from the imposed-displacement crumpling stage are not a useful stiffness measure for the present purpose. The extracted values are dominated by (1) high-frequency numerical noise, (2) mass-scaling/loading-rate dependence, and (3) local tangent behaviour governed by intermittent buckling and fold rearrangements. In contrast, the quantity of interest is a *global, emergent stiffness* that characterises the overall resistance of the final crumpled morphology to an external load.

To obtain a more robust metric, the stiffness evaluation is reversed: instead of differentiating a noisy reaction force curve, a known axial or radial test force is applied on the top interface, and the resulting displacement is measured in the same direction. This defines an *effective (secant) stiffness* of the crumpled structure,

$$k_{\mathrm{eff}} = \frac{F_{\mathrm{probe}}}{u_{\mathrm{probe}}}, \tag{A.7}$$

which averages over local instabilities and is far less sensitive to transient fluctuations.

To further suppress the high-frequency dynamics common to explicit integration, this probing step is performed using a single-step implicit linear solve. Practically, the imposed displacement constraint on the top interface is released, the test load is applied, and the resulting quasi-static displacement is computed. This yields a stiffness measure that is directly comparable across configurations and does not require time-domain filtering and averaging of explicit reaction force histories.

However, a remaining complication is that the crumpling stage leaves the structure with significant stored elastic strain energy. If the imposed displacement on the top interface were simply released, the model would elastically spring back toward the reference configuration. This relaxation displacement

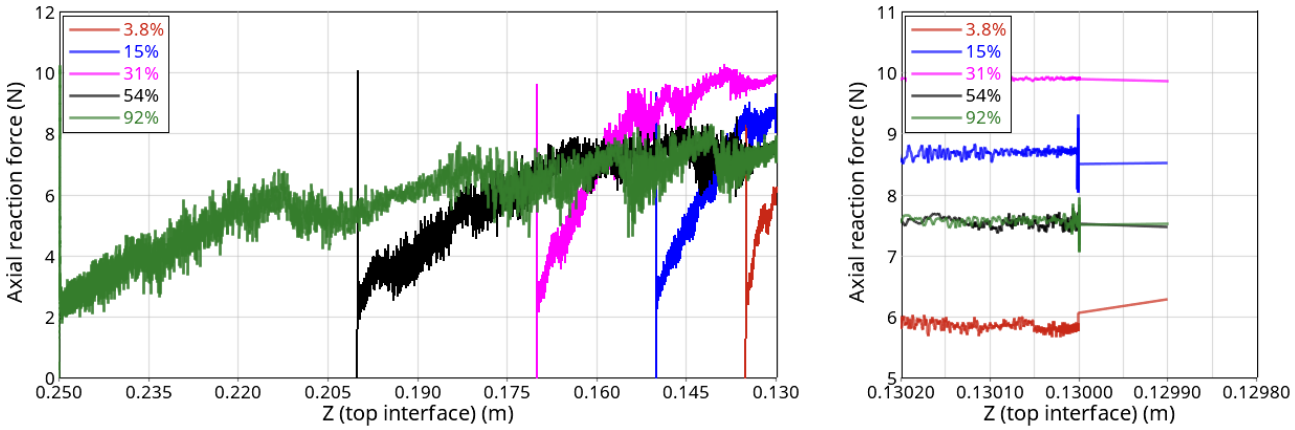

(a) Axial reaction force for decreasing Z-coordinate top interface, various overlengths (no mass-scaling, 50 µm thickness)

(b) (Zoomed on final linear implicit step)

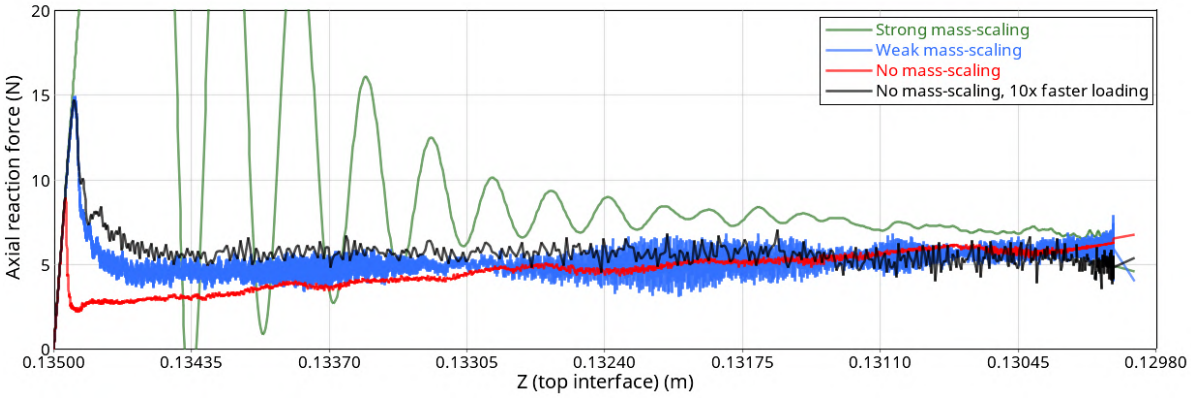

(c) Axial reaction force for decreasing Z-coordinate of top interface, using strong/weak/no advanced mass-scaling or faster loading (2 005 / 20 005 / 287 824 / 14 470 time-steps) (3.8% overlength, 50 µm thickness)

Figure A.3: Analysis of axial reaction force versus displacement as a method to measure axial stiffness. For all simulations the final step at $z = 0.13$ m was performed using a single-step linear implicit solve. This method of stiffness-measurement was found to not be robust due to (1) high-frequency dynamics causing noise, (2) dependence on mass-scaling/loading rate and (3) spuriousness of local tangent stiffness due to local buckling.

would be superimposed on the displacement caused by the test force, making it impossible to isolate the deformation attributable to the stiffness probe.

Therefore, the stiffness probe requires a stress-free reference state: internal stresses must be removed while preserving the final crumpled geometry. One option is to export the deformed mesh (e.g. from HyperView) and re-import it into HyperMesh as a new, stress-free starting configuration. In practice, this procedure is highly labourious, difficult to automate, and therefore not scalable for large parameter studies.

To enable a fully automated workflow, where crumpling is followed by automatic stiffness evaluation within a single run, an alternative approach is needed. Radioss does not provide a built-in function to reset stresses between consecutive simulation phases/engine files. For this reason, a new numerical strategy was developed that removes the internal stresses through artificial material behaviour.

A.2.2. Stress removal via strain-rate-dependent plasticity

The stress-relaxation strategy described in chapter 3 is based on an elasto-plastic material law with a strain-rate-dependent yield strength. A Johnson–Cook-type relation of the form

$$\sigma_y = \sigma_{y,0}\left[1 + c\,\ln(\dot{\varepsilon}/\dot{\varepsilon}_0)\right] \tag{A.8}$$

is used, where $\sigma_{y,0}$ is the base yield strength, c is a dimensionless strain-rate coefficient, and $\dot{\varepsilon}/\dot{\varepsilon}_0$ is the ratio between the local and reference strain rate. For brevity, the plastic-strain and temperature-dependent terms of the full material law (`/MAT/LAW2/PLAS_JOHNS`) are omitted here [29].

During the crumpling phase the strain rate is non-zero throughout the structure. By choosing c and $\dot{\varepsilon}_0$ such that even modest strain rates lead to a strong increase in σ_y, the effective yield strength remains well above the internal stresses generated by elastic buckling. As a result, the material response remains elastic in this phase and the crumpled geometry is governed by elastic instabilities rather than plastic flow.

At the end of the crumpling stage all nodal velocities are constrained to zero, forcing the strain rate to vanish. In this limit the yield strength collapses back to its base value $\sigma_{y,0}$, which is chosen to be very small. The stored elastic stresses then relax plastically towards this near-zero level, while the nodal positions remain fixed because the displacements are constrained. This procedure effectively erases the internal stress while preserving the crumpled geometry as the new reference configuration.

In practice, some trial-and-error is required to select a suitable combination of parameters. If $\sigma_{y,0}$ is chosen too low, the material may begin to yield already in the early stages of the crumpling process when the strain rate is still small, preventing the proper development of wrinkles and ridges. Conversely, if $\sigma_{y,0}$ is too high, significant residual stresses remain after the freezing step. The parameter set used in this work (Table A.1) strikes a balance: the crumpling stage remains effectively elastic, and the subsequent freezing step reduces the stresses by several orders of magnitude without noticeable geometric change. The remaining stresses do cause the frozen geometries to oscillate slightly around the new reference configuration, as seen in chapter 3, but not enough to significantly affect the measured stiffness.

Parameter name	Symbol	Value	Unit
Elastic modulus	E	650×10^6	Pa
Density	ρ	2150	kg/m^3
Poisson ratio	ν	0.4	–
Base yield strength	$\sigma_{y,0}$	1	Pa
Strain-rate coefficient	c	1×10^6	–
Reference strain rate	$\dot{\varepsilon}_0$	1×10^{-10}	s^{-1}

Table A.1: Material parameters used for buckling-cylinder simulations in chapter 3. The Johnson-Cook-type plasticity model is used according to Equation A.8 [29].

A.2.3. Stress removal via temperature-dependent plasticity

Interestingly, a similar stress-relaxation strategy can be implemented by exploiting the temperature dependence of the yield strength using a related elasto-plastic material law (`/MAT/LAW2/PLAS_ZERIL`):

$$\sigma_y = \sigma_{y,0} + C_1 \exp\big(-C_3 T + C_4 T \ln(\dot{\varepsilon}/\dot{\varepsilon}_0)\big), \tag{A.9}$$

where $\sigma_{y,0}$ is the base yield strength, C_1 is the strain-rate formulation coefficient, C_3 is the temperature-effect coefficient, and C_4 is the coefficient for the combined strain-rate and temperature effect [29]. As before, plastic-strain terms are omitted for brevity.

Using a concept analogous to the strain-rate-based relaxation, but now controlled by temperature instead of strain rate, the yield strength can be tuned even more directly. With suitably extreme parameter values (e.g. $\sigma_{y,0} = 0.1$ Pa, $C_1 = 1 \times 10^5$, $C_3 = 10$ and $C_4 = 0$), a near-zero base yield strength can be raised to a finite effective value purely by prescribing a temperature. This allows for an even smaller nominal base yield strength, since it no longer depends on the build-up of strain rate in the initial loading steps to increase σ_y, see Figure A.4. In addition, this temperature-based scheme permits a crumpling stage that does include plasticity, with the effective yield strength set directly via the chosen temperature. The strain-rate-based method cannot precisely control the local strain rates and thus cannot not be finely tuned.

This more versatile scheme has been verified for solid elements. However, Radioss does not appear to support temperature-dependent plasticity effects for shell elements, as concluded from dedicated tests. This limits its applicability to the shell-based cylinder models used in this work.

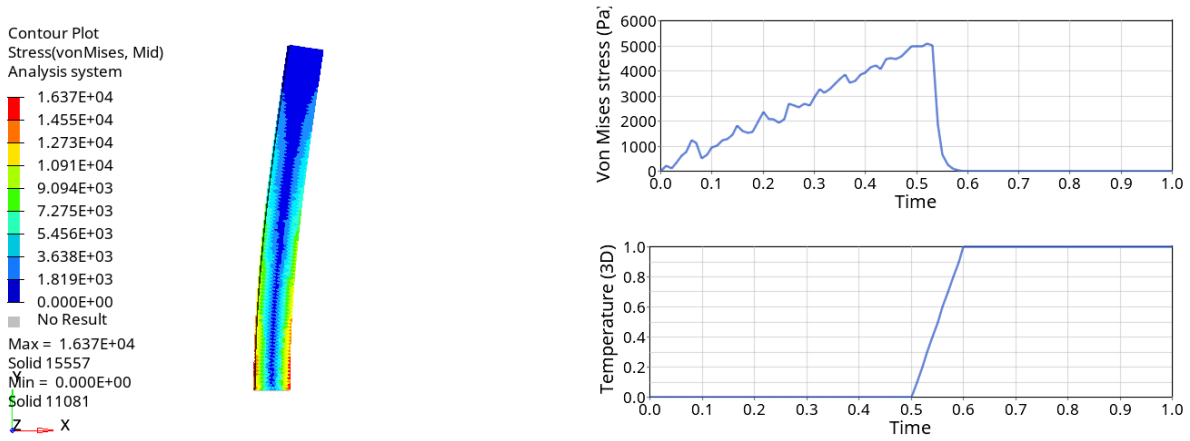

Figure A.4: Example of stress relaxation via a temperature-dependent elasto-plastic material law on a solid bending beam. By using artificial material parameters, the yield strength can be reduced to near-zero when the temperature is increased, thereby relaxing all stresses and effectively defining a new reference configuration. The contour plot shows the stress state just before the temperature increase ($t = 0.5$ s). The line plots show the time histories of stress and temperature for a representative element.

A.2.4. Post-processing

The relevant interface are stored in Radioss time-history files. These binary files are not directly readable by standard post-processing tools (besides Altair HyperView), but can be converted using an open-source Python library developed within the OpenRadioss community [46]. Once converted to a python data-frame, the displacements are related to the perturbing force to calculate the stiffness.

To cover the parameter space efficiently, each simulation run contains five cylinders with different initial heights, corresponding to five overlengths. For each thickness, the combination of overlength and random seed is varied systematically, yielding an ensemble of stiffness values that reflects both deterministic trends and stochastic variability associated with the initial imperfections.

A.3. Validation studies

The preceding sections defined how static stiffness is extracted from stress-removed crumpled configurations. In this section, we assess how robust these stiffness measurements are with respect to key numerical parameters. Specifically, we investigate how the strength of mass scaling, the assumed material stiffness, and the mesh density influence the crumpled morphology, the extracted static stiffness, and the computational cost. These parametric studies provide practical bounds on acceptable settings for the main simulations reported in chapter 3.

A.3.1. Mass-scaling strength

In practice, the systematic study of chapter 3 was carried out using time steps $\sim$750 times greater than the Courant criteria. Each simulation was carried out in 2005 steps, referred to as 'strong mass scaling' in Figure A.5 and Figure A.6. This Δt_{min} was used regardless of thickness, as it has no effect on the Courant criterium (Equation A.3). While this is quite aggressive mass-scaling, crumpling morphologies (Figure A.5a and Figure A.6a) and emergent stiffnesses (Figure A.5b and Figure A.6b) did not differ substantially compared to their expected variability, especially for higher overlengths. There are some differences in stiffness present between mass-scaling regimes in Figure A.5b and Figure A.6b, but not enough to explain the discrepancy with experiment. While Figure A.5c and Figure A.6c both show a significant increase in the internal deformation energy of the system, the kinetic energy is still a small part of the total, indicating that kinetic effects are yet to have a disproportionate effect.

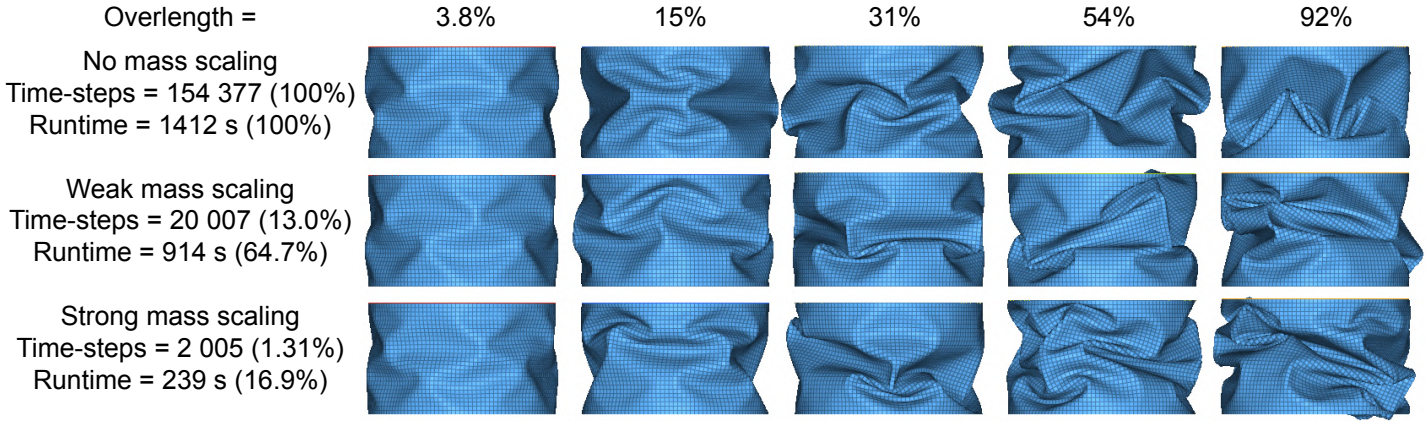

(a) Illustrative crumpling morphologies and CPU-times

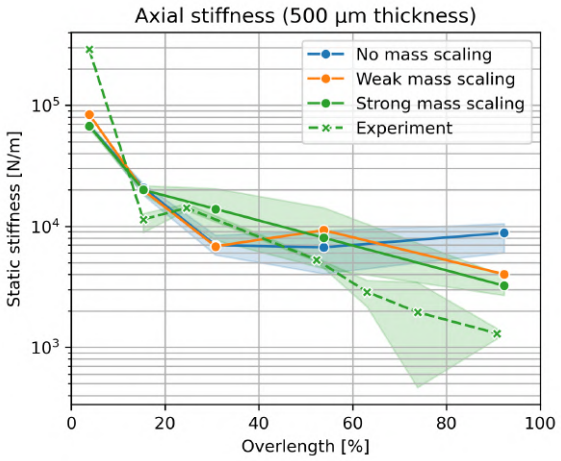

(b) Axial static stiffness vs. overlength

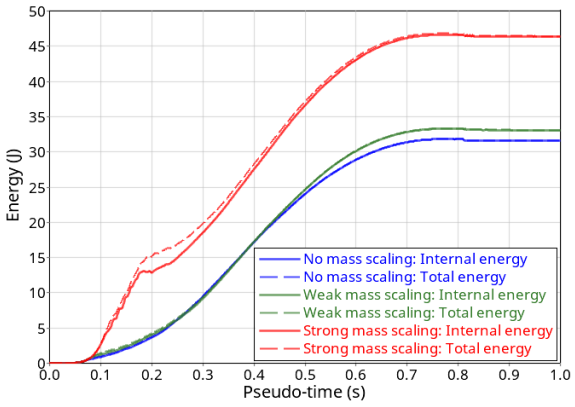

(c) Combined internal and total energy of all five crumpling cylinders

Figure A.5: Effect of advanced mass scaling on (a) morphology and CPU-time, (b) emergent axial static stiffness, and (c) internal and total energies. For all cases a 500 µm thickness is considered, using the same seed for the random perturbation. For (b) all simulations are represented via the mean and min-max spread, along with the experimental results.

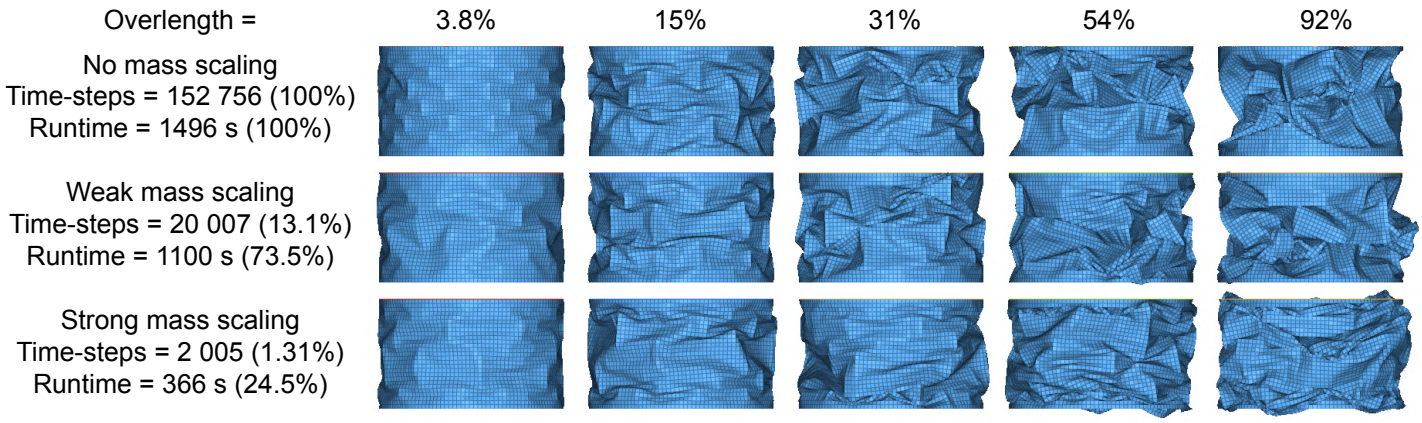

(a) Illustrative crumpling morphologies and CPU-times

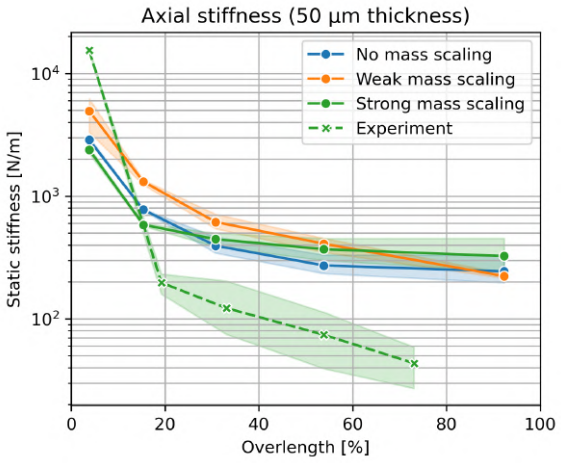

(b) Axial static stiffness vs. overlength

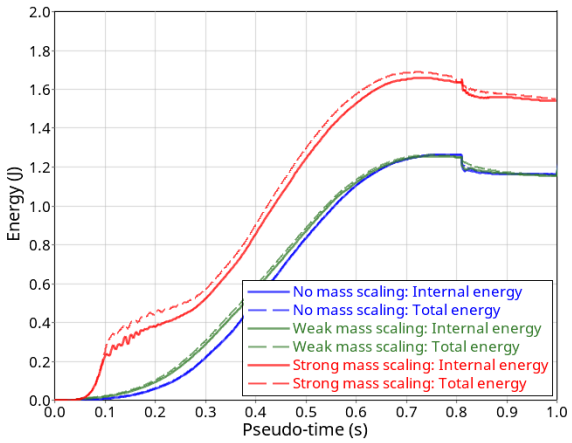

(c) Combined internal and total energy of all five crumpling cylinders

Figure A.6: Effect of advanced mass scaling on (a) morphology and CPU-time, (b) emergent axial static stiffness, and (c) internal and total energies. For all cases a 50 µm thickness is considered, using the same seed for the random perturbation. For (b) all simulations are represented via the mean and min-max spread, along with the experimental results.

A.3.2. Material dependence

If kinetic effects are negligible, the dynamic relaxation procedure should converge to a crumpled morphology that minimises the internal energy. This internal energy is the sum of in-plane (stretching) and out-of-plane (bending and twisting) deformation. The balance between stretching and bending, and thus the equilibrium shape, is controlled by the relative stiffness of these two modes.

Classical thin-plate and shell theory tells us that the in-plane (membrane) stiffness scales as $T \propto Et$, while the bending rigidity scales as $D \propto Et^3$ [47]. The ratio $D/T \propto t^2$ therefore increases with thickness: bending becomes relatively more expensive for thicker sheets. This causes the foil to take on a shape which minimizes the amount of curvature, which is consistent with the increase in average wrinkle wavelength observed in chapter 3.

Importantly, the Young's modulus E cancels out of this ratio. For a linear elastic material under displacement-controlled loading, we therefore expect that E does not affect the crumpled morphology that minimises the internal energy. In other words, changing E should rescale forces, stresses and energies, but not the geometry. It is, however, not a given that this idealised behaviour is preserved by the explicit dynamic relaxation procedure and the associated numerical settings.

To assess the robustness with respect to the material stiffness, a small parameter study was carried out for $t = 50$ µm. Simulations were repeated for several values of Young's modulus, using three different but consistent seeds for the random initial perturbation, see Figure A.7. As shown in Figure A.7a, the resulting crumpled morphologies are visually almost identical for a given seed. For small and moderate overlengths no systematic differences can be detected. Only at the largest overlengths do we observe modest deviations between the softest and stiffest materials.

The corresponding static stiffness curves are plotted in Figure A.7b. For most configurations the curves are of a similar shape, only with shifted magnitude. However, at the most extreme combinations of low E and high overlength, the robustness of the stiffness extraction deteriorates. Very compliant structures were found to exhibit numerical instabilities during the linear implicit step, and may move in the direction opposite to the applied known force. This leads to an apparent negative stiffness and causes the minimum–maximum shaded uncertainty-band to collapse towards zero in the affected regions. These cases highlight that the chosen material stiffness must remain compatible with the applied test forces and with the parameters used in the stress-removal procedure.

Finally, the dependence of emergent stiffness on Young's modulus is summarised in Figure A.7c. Here, the axial and radial stiffnesses are plotted as a function of E for different overlengths, normalised by their value at $E = 325$ MPa. For most overlengths the curves follow the expected linear trend in both directions. A notable exception is the axial stiffness at 92% overlength, where the stiffness increases more rapidly than predicted. This deviation is likely linked to the changes in crumpled morphology already observed in Figure A.7a for that extreme configuration.

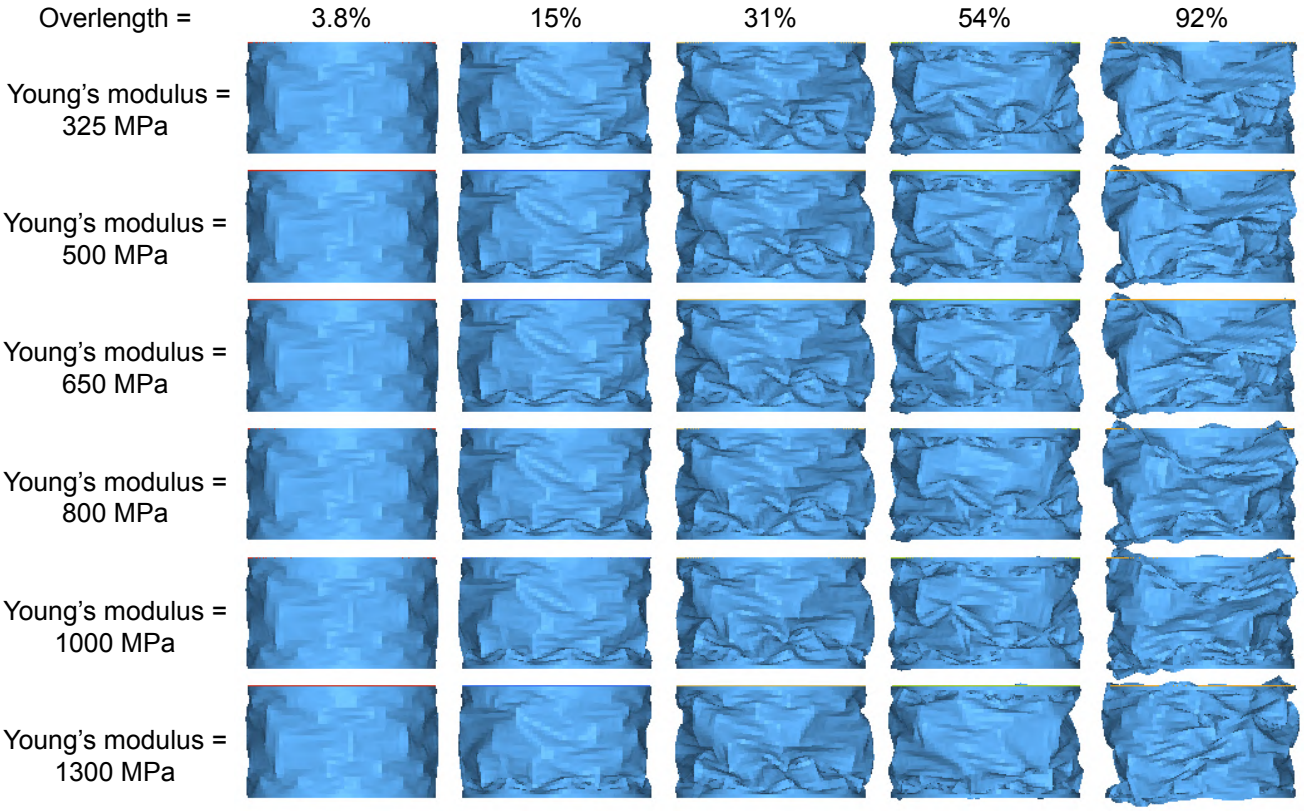

(a) Crumpled morphologies for increasing Young's modulus at different overlengths, using an identical random pertubation seed.

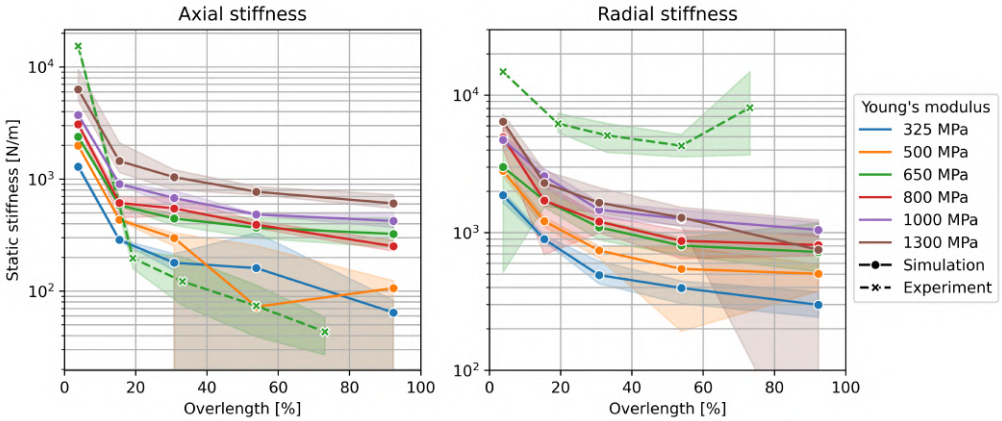

(b) Axial and radial static stiffness versus overlength for increasing Young's modulus. Markers show the mean over three random seeds; the shaded region indicates the minimum–maximum range.

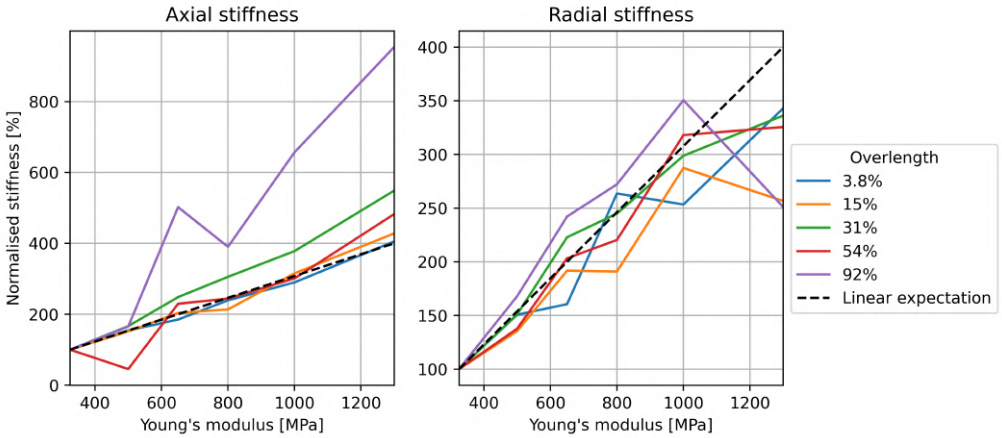

(c) Increase of mean static stiffness for increasing Young's modulus, normalised by first value.

Figure A.7: Effect of Young's modulus on the crumpled morphology and emergent stiffness for $t = 50$ µm.

A.3.3. Mesh convergence

For all finite element analyses it is important to assess the influence of mesh density. This is particularly critical in simulations of crumpling, where the mesh must be fine enough to resolve the narrow ridges and localised curvature that dominate the post-buckling response. In an explicit dynamic formulation without mass scaling, the total runtime for a two-dimensional mesh is expected to scale with the characteristic element size l_c as

$$\text{runtime} \propto (N_{\text{steps}}) \cdot (\Delta t_{\text{step}}) \propto (\Delta t_{\text{Courant}})^{-1} \cdot (N_{\text{elements}}) \propto (l_c)^{-1} \cdot (l_c)^{-2} = l_c^{-3}, \tag{A.10}$$

where $\Delta t_{\text{Courant}} \propto l_c$ is the Courant time step given by Equation A.3. This steep scaling indicates that reducing the element size rapidly becomes expensive. Nevertheless, such refinement may be required to capture the small-scale features expected for thin sheets.

To quantify this trade-off, we compare meshes for two thicknesses: $t = 500$ µm (Figure A.8) and $t = 50$ µm (Figure A.9). For the thicker shells, we consider element sizes of $l_c = 7$, 5, 4 and 2.5 mm, noting that $l_c = 5$ mm is used as the default in the remainder of this work. As illustrated in Figure A.8a, coarser meshes produce visibly smoother and less sharply defined ridges than finer meshes, although the qualitative morphology remains similar. When examining the resulting axial stiffness (Figure A.8b), the curves for the 4 and 2.5 mm meshes fall within the variability bounds of the 5 mm baseline. This suggests that a 5 mm mesh is sufficiently fine for the global stiffness response at $t = 500$ µm. In contrast, for $l_c = 7$ mm both the morphology and stiffness start to deviate: the less sharply crumpled ridges yield a stiffer, less compliant emergent response.

The measured runtimes, shown in Figure A.8c, are consistent with the expected power-law dependence. A fit of the runtime versus element size yields approximately $\text{runtime} \propto l_c^{-2.54}$. The dominant l_c^{-2} contribution can be attributed to the increasing number of elements, while the remaining $\approx l_c^{-0.54}$ reflects the residual effect of the decreased Courant time step. In these simulations all runs are constrained to a fixed number of 2005 time steps through advanced mass scaling, which partially suppresses the full l_c^{-1} dependence of the explicit time step. However, achieving this fixed step count requires stronger mass scaling for finer meshes, which in turn makes the updating and redistribution of the mass matrix more intensive. As a result, the effective scaling exponent is reduced from the expected -3 to only -2.54, but still clearly demonstrates the rapidly increasing computational cost of mesh refinement.

For the thinner bellow with $t = 50$ μm, the influence of mesh density is much more pronounced. As shown in Figure A.9a, clear morphological differences appear once the element size is reduced below $l_c = 5$ mm. For coarser meshes, the characteristic feature size is effectively limited by the mesh resolution: the ridges are overly smooth and many of the fine-scale details that are expected for such a thin sheet are suppressed. Only for the finer meshes do the narrow ridges and highly localised folds emerge clearly.

This is reflected in the axial stiffness results in Figure A.9b. In contrast to the $t = 500$ μm case, the effective stiffness continues to decrease when the element size is reduced from 5 to 4 mm, indicating that the 5 mm mesh is still not fully converged for this thinner geometry. Unfortunately, for the finest meshes with $l_c = 2.5$ and 1.25 mm the global stiffness matrices became too large and complex to complete the linear implicit step required for the stiffness evaluation, due to insufficient virtual memory on the available hardware. This also highlights an important practical distinction between simulation methodologies: the explicit crumpling phase could still be carried out successfully for these meshes because explicit integration avoids assembling and factorising large global matrices, whereas the subsequent implicit stiffness analysis is limited by memory requirements. Moreover, for $t = 50$ μm the simulations with certain mesh sizes (e.g. $l_c = 7$ and 4 mm) proved less robust, occasionally yielding non-physical negative stiffness values in the post-processing. These cases are interpreted as numerical artefacts rather than meaningful mechanical responses, further underlining the sensitivity of the thin-sheet problem to both mesh resolution and solver settings.

The corresponding runtimes are reported in Figure A.9c. A power-law fit suggests that, for this thinner bellow, the runtime scales approximately as $\text{runtime} \propto l_c^{-2.74}$, which is even steeper than the -2.54 exponent observed for the $t = 500$ μm case. This indicates that the combination of increased mesh density and stronger geometric nonlinearity makes the system more demanding to solve: the number of elements again contributes roughly an l_c^{-2} factor, while the remaining $\approx l_c^{-0.74}$ captures a combination

of the Courant time-step limitation and the additional overhead introduced by more aggressive mass scaling and more complex curvatures. Overall, these results demonstrate that for very thin sheets the mesh must be refined beyond the level acceptable for thicker configurations, but at a substantially increased computational cost.

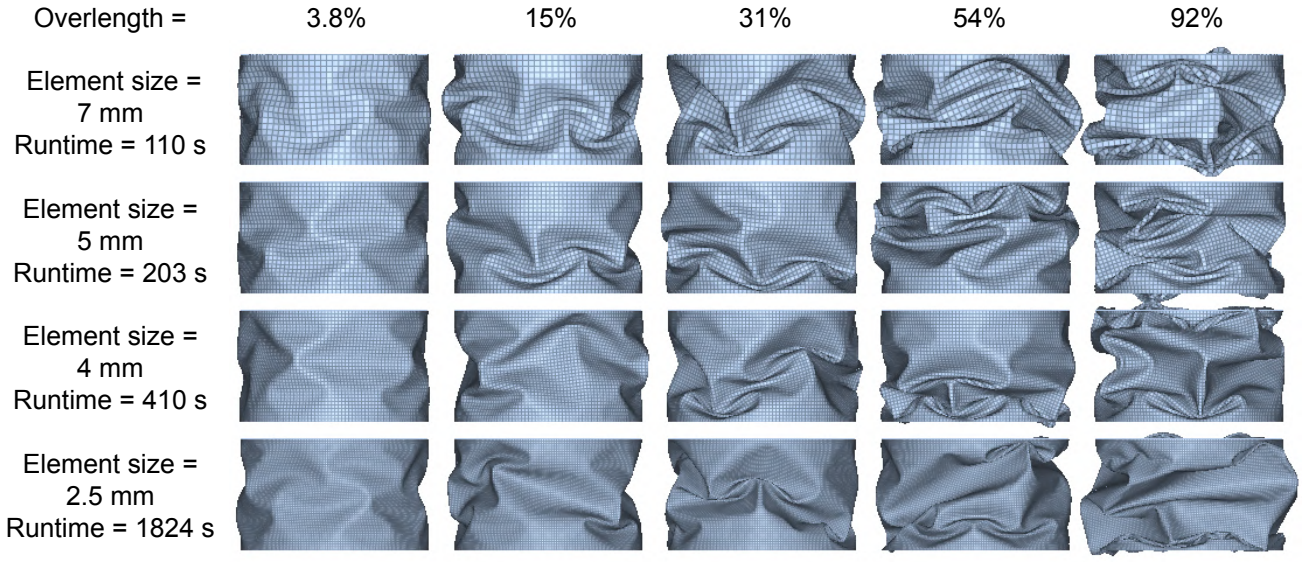

(a) Crumpled morphologies for increasing mesh densities at different overlengths, using an identical random perturbation seed.

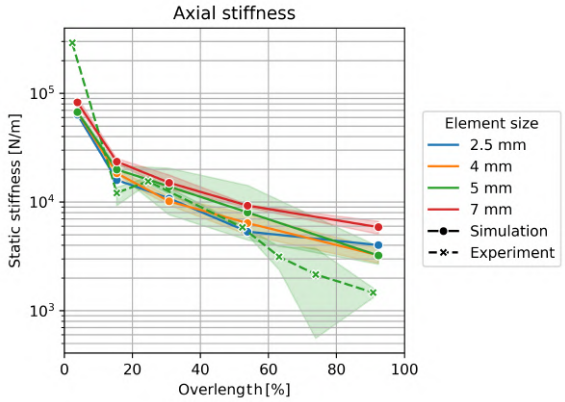

(b) Axial static stiffness vs. overlength

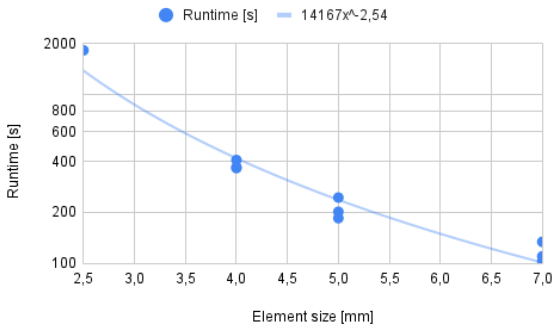

(c) Runtime comparison using power-law fit ($\mathrm{runtime} \propto l_c^{-2.54}$)

Figure A.8: Effect of element size on the crumpled morphology (a), emergent stiffness (b) and runtime (c), using $t = 500$ µm and $E = 650$ MPa. For element sizes of 4, 5 and 7 mm three simulations using different seeds were considered, while the 2.5 mm element size was only simulated once due to the extreme runtime.

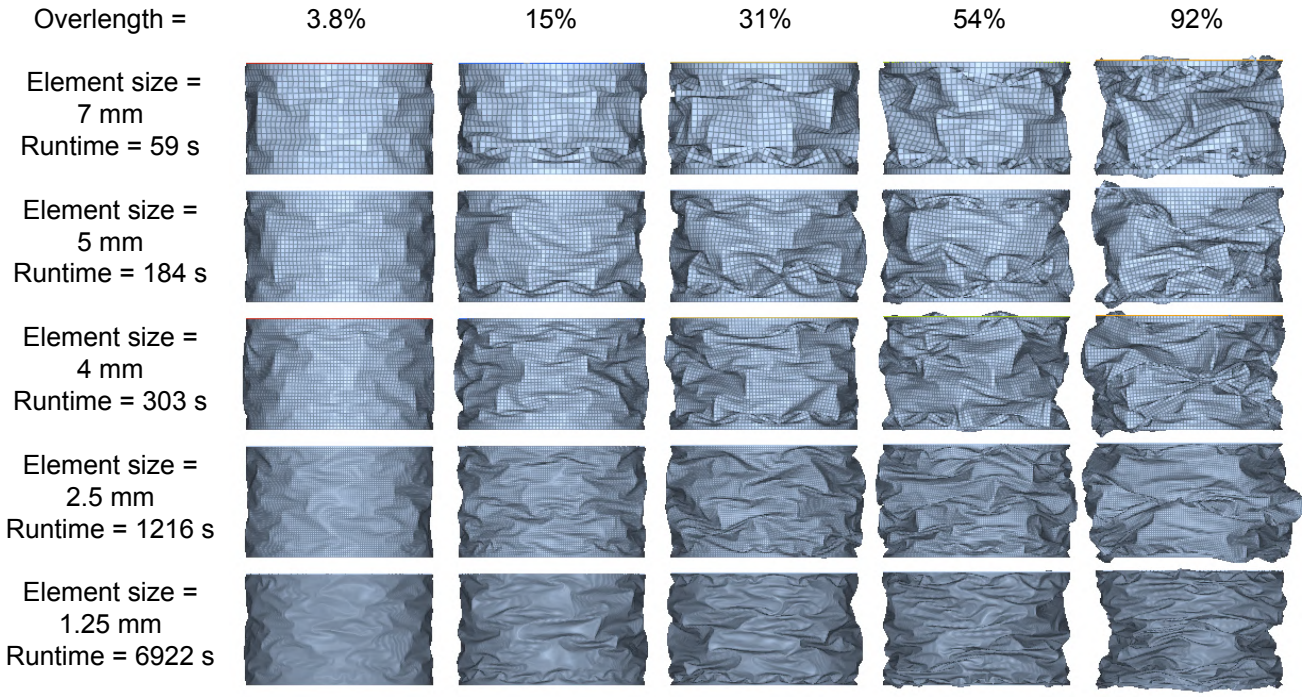

(a) Crumpled morphologies for increasing mesh densities at different overlengths, using an identical random perturbation seed.

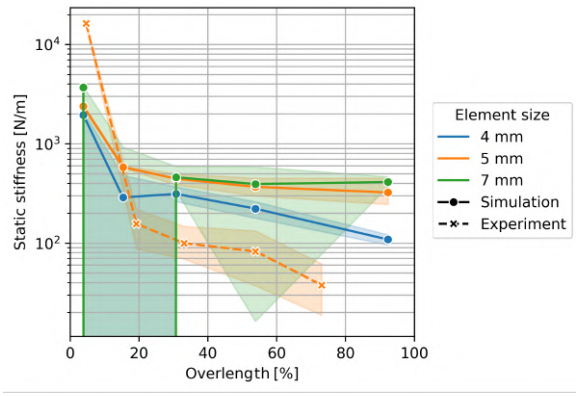

(b) Axial static stiffness vs. overlength

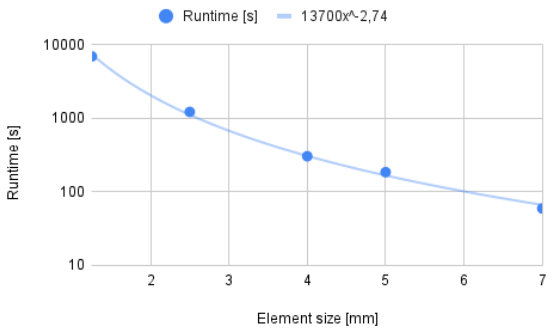

(c) Runtime comparison using power-law fit ($\text{runtime} \propto l_c^{-2.74}$)

Figure A.9: Effect of element size on the crumpled morphology (a), emergent stiffness (b) and runtime (c), using $t = 50$ µm and $E = 650$ MPa. For element sizes of 4, 5 and 7 mm three simulations using different seeds were considered, while the 2.5 and 1.25 mm element sizes were only simulated once due to the extreme runtime. The two smallest element sizes also failed the static stiffness calculation as there was insufficient virtual memory to perform the linear implicit step.

A.4. Dynamic stiffness extraction

The crumpled foil bellow investigated in this thesis is discretised with a relatively fine shell mesh in order to preserve the local curvature and ridge-like features that govern its global compliance. As a consequence, solving the full-order finite element (FE) model directly in the frequency domain for (i) many excitation directions, (ii) dense frequency grids, and (iii) a large set of geometric realisations and overlength configurations, becomes computationally prohibitive.

To make dynamic predictions feasible at this scale, the dynamic response is evaluated on a reduced-order model (ROM) obtained through *component mode synthesis* (CMS). CMS reduces the number of degrees of freedom (DoFs) by projecting the solution space onto a carefully selected basis of mode shapes, while explicitly retaining interface DoFs to preserve coupling and allow the extraction of interface-level transfer functions. By doing so, the full set of physical coordinates is reduced to a smaller set of generalized coordinates. [19, 48]

The procedure described below yields a frequency-dependent, linearised interface relation between forces/moments and relative motions of the two interfaces. This relation is subsequently used to compute transmissibility and the (6×6) dynamic stiffness matrix up to a prescribed upper frequency limit. Note that a general introduction of the method is provided here, as it was already tested and described in detail by Wijnen [19].

A.4.1. Reduced model formulation

Consider the linear, undamped FE equations of motion

$$\mathbf{M}\ddot{\mathbf{q}}(t) + \mathbf{K}\mathbf{q}(t) = \mathbf{f}(t), \tag{A.11}$$

with $\mathbf{q}, \mathbf{f} \in \mathbb{R}^n$ the physical DoFs and load vectors, and $\mathbf{M}$ and $\mathbf{K}$ the mass and stiffness matrices. In CMS the DoFs are partitioned between boundary and internal DoFs as

$$\mathbf{q}(t) = \begin{bmatrix} \mathbf{q}_B(t) \\ \mathbf{q}_I(t) \end{bmatrix}, \qquad \mathbf{q}_B \in \mathbb{R}^{n_B},\ \mathbf{q}_I \in \mathbb{R}^{n_I}, \qquad n_B \ll n_I, \tag{A.12}$$

leading to the partitioned equations for internal and interface DoFs (for the undamped case)

$$\begin{bmatrix} \mathbf{M}_{BB} & \mathbf{M}_{BI} \\ \mathbf{M}_{IB} & \mathbf{M}_{II} \end{bmatrix} \begin{bmatrix} \ddot{\mathbf{q}}_B \\ \ddot{\mathbf{q}}_I \end{bmatrix} + \begin{bmatrix} \mathbf{K}_{BB} & \mathbf{K}_{BI} \\ \mathbf{K}_{IB} & \mathbf{K}_{II} \end{bmatrix} \begin{bmatrix} \mathbf{q}_B \\ \mathbf{q}_I \end{bmatrix} = \begin{bmatrix} \mathbf{f}_B \\ \mathbf{f}_I \end{bmatrix}. \tag{A.13}$$

Centrally, CMS introduces a coordinate transformation

$$\mathbf{q}(t) \approx \mathbf{T}\mathbf{p}(t), \tag{A.14}$$

with $\mathbf{p} \in \mathbb{R}^{n_r}$ a reduced set of generalised coordinates ($n_r \ll n$). The reduced equations follow from Galerkin projection,

$$\mathbf{M}_r = \mathbf{T}^T\mathbf{M}\mathbf{T}, \qquad \mathbf{K}_r = \mathbf{T}^T\mathbf{K}\mathbf{T}, \qquad \mathbf{f}_r = \mathbf{T}^T\mathbf{f}, \tag{A.15}$$

yielding $\mathbf{M}_r\ddot{\mathbf{p}} + \mathbf{K}_r\mathbf{p} = \mathbf{f}_r$. This projection can be accomplished via various methods, each with their advantages. For example, a purely static condensation (Guyan reduction) corresponds to expressing internal DoFs solely via static constraint modes,

$$\mathbf{q}_I \approx -\mathbf{K}_{II}^{-1}\mathbf{K}_{IB}\mathbf{q}_B, \tag{A.16}$$

which is computationally attractive but neglects inertia in the reduction basis and therefore becomes inaccurate unless the frequency range of interest lies well below the first eigenfrequency of the component [19, 48].

A.4.2. Hintz-Herting reduction basis (free-free method)

In this work the *free-interface* method of Hintz-Herting is used. This method is commonly recommended when accuracy is required not only on the lowest modes but also on higher modes of the assembled structure [19]. The Hintz-Herting transformation retains all boundary DOFs and approximates the internal DOFs by a combination of (i) static constraint modes, (ii) inertia relief modes, and (iii) a truncated set of free-interface elastic modes. Following the formulation summarised by Wijnen [19], the physical displacement vector is decomposed as

$$\mathbf{q}(t) = \begin{bmatrix} \mathbf{q}_B(t) \\ \mathbf{q}_I(t) \end{bmatrix} \approx \mathbf{q}_S(t) + \mathbf{q}_R(t) + \mathbf{q}_E(t), \tag{A.17}$$

where $\mathbf{q}_S$ is the contribution of static (constraint) modes, $\mathbf{q}_R$ the contribution of inertia relief modes, and $\mathbf{q}_E$ the contribution of truncated free-interface elastic modes. The overall transformation combines these three contributions into a reduction basis, which is then used to project the original equations of motion into a reduced form. For the full mathematical formulation, see [19, 48].

Static (constraint) part. The static constraint modes approximate the deformation of internal DoFs caused by static displacements at the boundary DoFs, assuming no external loads on the internals. These ensure the reduced model provides a statically accurate response at the interfaces.

Inertia relief part. The inertia relief modes capture the rigid-body motions of an unconstrained (free) component, representing how internal DOFs deform under inertial forces from rigid-body accelerations (here 6 rigid-body modes for 3D). This avoids artificial constraints and accounts for overall rigid motion.

Free-interface elastic part. The free-interface elastic modes represent the flexible vibration modes of the unconstrained component, truncated to a subset and adjusted (residualized) for compatibility with the static constraint modes. These capture the dynamic, oscillatory behavior at higher frequencies.

The elastic mode set is truncated at a user-defined cutoff frequency. As a practical guideline for free-interface elastic modes, the cutoff is typically selected at approximately 1.5–$2.0\times$ the highest frequency of interest. [19, 48]. However, due to the high modal density for this case it was found that the response remained intact using a lower truncation frequency. For the purposes of this study results were plotted up to 800 Hz, with elastic modes being calculated up to a cut-off frequency of 1000 Hz.

A.4.3. Implementation

The workflow adopted in this thesis is as follows:

1. **Geometry export:** the crumpled equilibrium geometry obtained from the explicit crumpling simulation is exported from HyperView in Abaqus format and imported into ANSYS as an *external model*.
2. **Reconstruction of analysis model:** material properties are redefined in ANSYS for linear dynamics; the two mechanical interfaces are reconstructed as rigid bodies. Each rigid interface is represented by a master node carrying 6 DOFs (3 translations, 3 rotations), which serves as the boundary set $\mathbf{q}_B$ for the CMS formulation.
3. **Modal analysis and CMS build:** a free-free modal analysis is executed to obtain the modal ingredients required for the Hintz–Herting basis. A proprietary APDL user routine performs the Hintz–Herting reduction and exports the reduced description, namely the global mass properties along with the modal deformations of the master nodes with associated eigenfrequencies.
4. **Transfer function calculation:** Using proprietary MATLAB code a state space model is constructed with the (reduced) mass and stiffness matrices via modal superposition and 5% modal damping to compute the transfer from force to displacement defined as

$$\mathrm{H} = U_{\mathrm{top}}/F_{\mathrm{bottom}} \tag{A.18}$$

Finally, the transfer function is inverted to calculate the dynamic stiffness. In matrix form, the 6-DOF dynamic stiffness is expressed as

$$\mathbf{w}(\omega) = \mathbf{K}_{\mathrm{dyn}}(\omega)\,\Delta\mathbf{x}(\omega), \tag{A.19}$$

where $\mathbf{w} = [F_x\ F_y\ F_z\ M_x\ M_y\ M_z]^T$ is the interface wrench and $\Delta\mathbf{x} = [\Delta u_x\ \Delta u_y\ \Delta u_z\ \Delta\theta_x\ \Delta\theta_y\ \Delta\theta_z]^T$ is the relative translation/rotation between the two interface master nodes. Diagonal terms of $\mathbf{K}_{\text{dyn}}$ correspond to direct stiffness contributions, whereas off-diagonal terms represent coupling between directions (e.g. force generated by a rotational excitation). While all terms are available after the calculation, only $\Delta u_z \rightarrow F_z$ and $\Delta u_x \rightarrow F_x$ are compared to experiment to maintain conceptual clarity.

A.4.4. Limitations

The adopted approach has the following limitations:

- **Finite validity bandwidth:** the ROM is only expected to be accurate up to the chosen mode cutoff. Beyond this limit, omitted modes can contribute significantly and the predicted transmissibility and $\mathbf{K}_{\text{dyn}}(\omega)$ become unreliable. Mode-cutoff guidelines (e.g. 1.5–$2.0\times$ above the highest frequency of interest for free-interface elastic modes) provide a practical but not absolute guarantee of accuracy [19, 48].
- **Linear dynamics:** the method assumes a linearised response around the imported equilibrium geometry. Amplitude-dependent effects (contact, large-displacement nonlinearity, frictional dissipation, etc.) are not represented.
- **Loss of stress history:** importing the mesh in ANSYS as an external model reconstructs the crumpled geometry but does not transfer stress (or plastic deformation) history from the explicit crumpling simulation. Consequently, pre-stress effects on stiffness are not included.

A.4.5. Validation

Figure A.10 presents a comparison between the static stiffness obtained using CMS-based modal reduction, the Radioss-native stress-removal and probing force method, and the corresponding experimental measurements. For the 500 µm foils, both numerical approaches yield largely comparable results in terms of curve shape and stiffness magnitude. In contrast, for the 50 µm foils, a pronounced discrepancy in stiffness magnitude is observed between the two simulation methods.

Although neither numerical approach fully reproduces the absolute stiffness measured experimentally, the comparison highlights a clear thickness-dependent sensitivity of the applied force-probing methodology. This suggests that modelling assumptions and numerical treatment become increasingly critical for very thin, highly compliant structures.

CMS simulations are generally expected to provide higher fidelity results, as residual stresses are fully eliminated during the export and modal reduction procedure in ANSYS. However, this approach requires substantially greater computational resources and involves a more labour-intensive workflow. The observed discrepancies therefore indicate that the stress-removal technique based on artificial elasto-plasticity may require careful recalibration of material parameters and probing force levels when applied to significantly thinner foils.

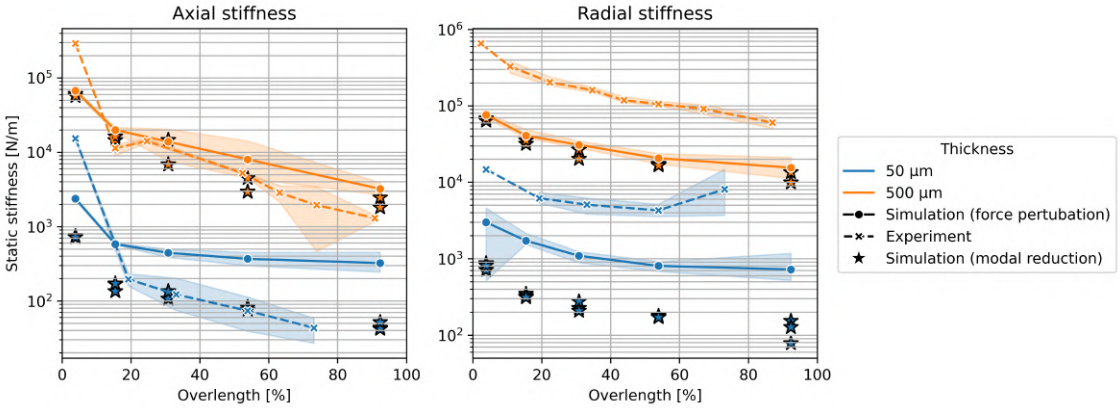

Figure A.10: Comparison of static stiffness obtained from experiments, Radioss stress-removal with force probing, and CMS-based modal reduction.

B

Experimental method

B.1. Dynamic stiffness setup

All experiments were performed on ASML's dedicated 6-DoF dynamic stiffness setup, which was originally developed by Philips Innovation Services for the qualification of air-mounts and later transferred to ASML, see Figure B.1, Figure B.2 and Figure B.3. A detailed explanation and validation of this setup, including finite-element modelling and experimental modal analysis, was already reported by Wijnen [19]. While the setup has been partly rebuilt to fit larger specimens, the general architecture of the setup has remained the same. Therefore, only a general introduction to the setup is provided here.

The setup consists of a granite anti-vibration base supporting a vertically actuated shaker table with an exchangeable interface spacer. The specimen under test is clamped between this base-frame (BF) interface and a force-cell interface connected to a cylindrical metrology frame (MF). A pneumatic bellow lifts the 500 kg mass of the MF and may thus provide a controllable gravitational static preload, allowing the operational loading conditions of in-machine vibration isolators to be mimicked. Here, the MF mass is simply lifted above its end stops as no preload is required. Vertical excitation is provided by three piezoelectric stack actuators mounted between the granite block and the shaker table; by driving these actuators in phase, an effective single vertical input is obtained. Unlike Wijnen [19] horizontal (radial) shaker vibrations are also considered in this work, using a TIRA TV 51120 (Figure B.2).

Forces transmitted through the specimen are measured by three triaxial Kistler 9027C force sensors integrated in the force cells between the specimen and the MF. Combining these three local measurements yields a global six-component force vector at the specimen interface. Motions of the BF and MF are measured by arrays of accelerometers: three 1-dimensional B&K 4381 sensors in z-direction and a single 3-dimensional PCB356B18 sensor per interface. From these measurements, global translational accelerations and rotations about the x- and y-axes are reconstructed under a rigid-body assumption for each interface, following the procedure described by Wijnen [19]. In the present study only the vertical and horizontal force and the corresponding BF–MF relative motion are used for the scalar dynamic stiffness, but the measurement chain is in principle capable of reconstructing the full 6×6 dynamic stiffness matrix.

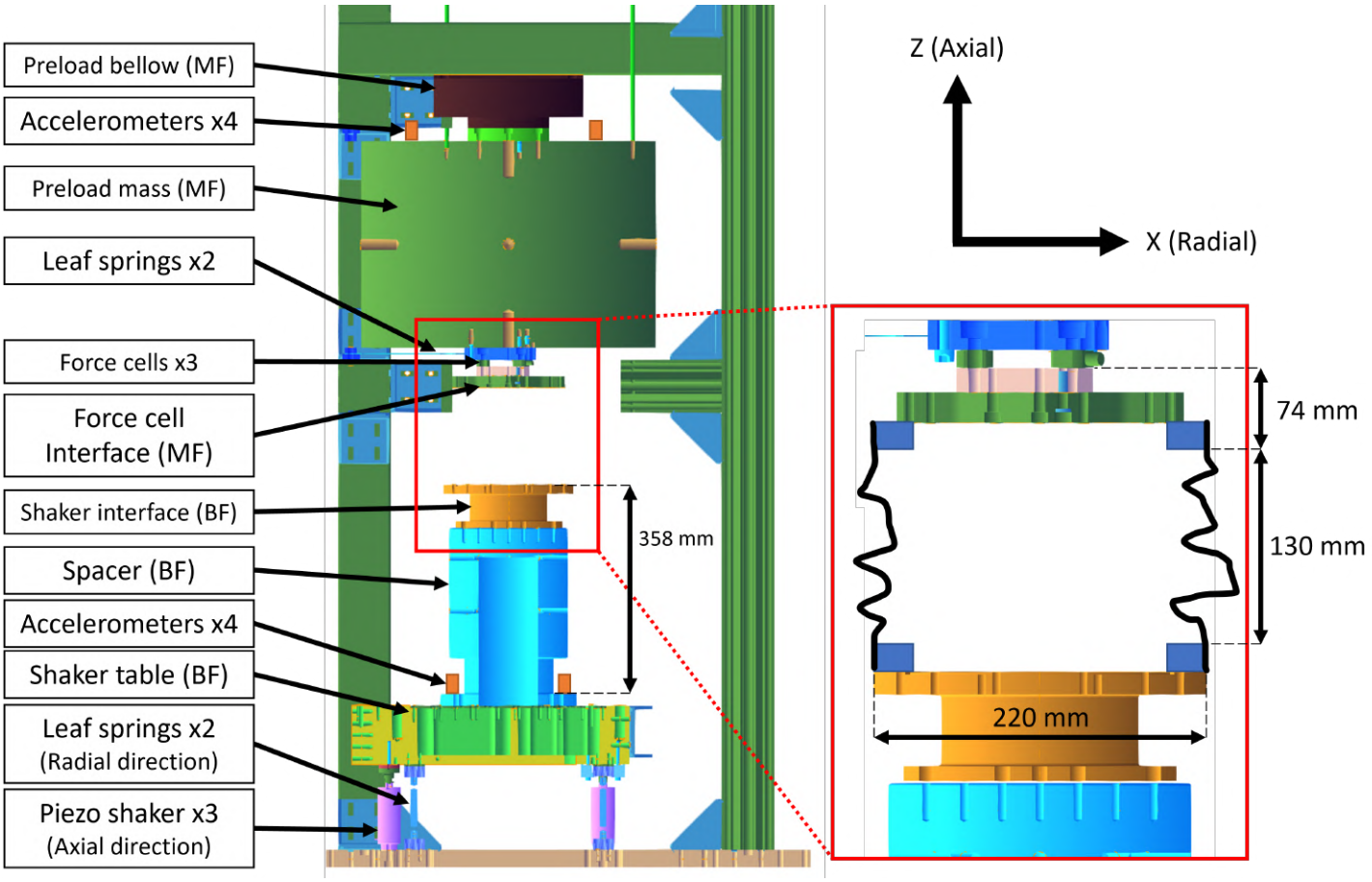

Figure B.1: Labeled schematic of ASML 6-DoF dynamic stiffness setup.

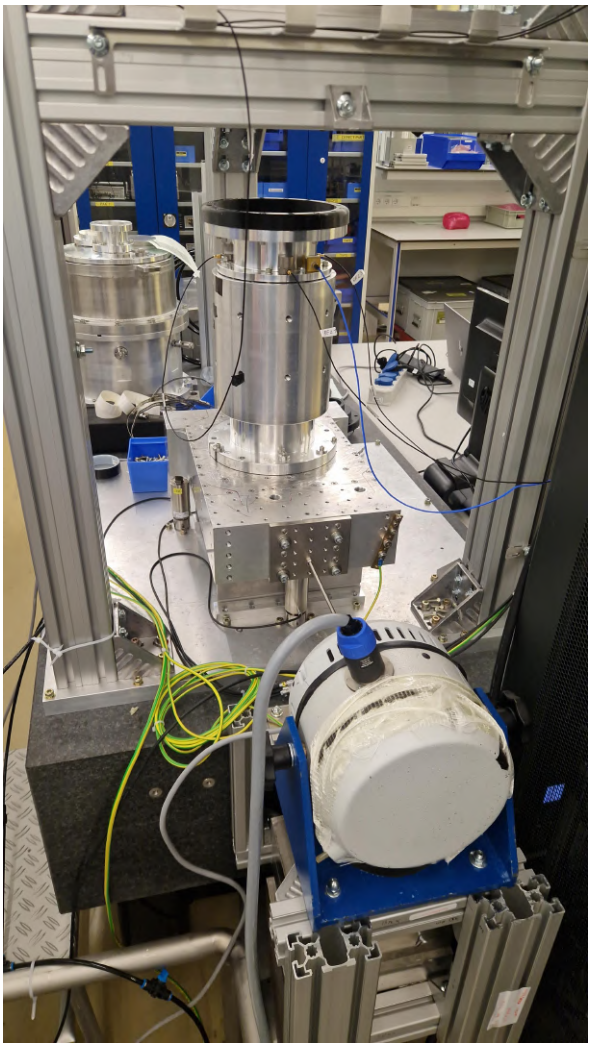

Figure B.2: Measurement setup in radial shaker configuration.

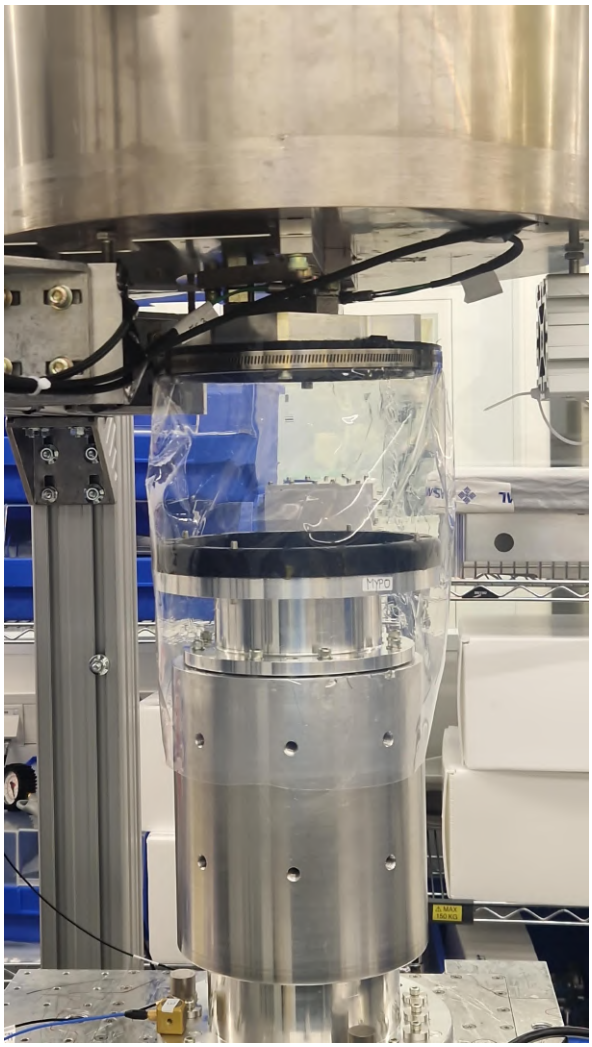

Figure B.3: Measurement setup with cylindrical bellow partly fastened using hose clamps. Accelerometers are placed in a triangle at the bottom of the BF spacer.

B.2. Specimen preperation

Foil bellows are cut from longer sheets and transformed into a cylindrical shape by using a soldering iron to create a melted seam, see Figure B.4 and Figure B.5. Figure B.6 shows the use of stickers to measure the reference cylinder height h_{ref} after each measurement session.

Figure B.4: Using a soldering iron to create a melted seam.

Figure B.5: Cylindrical bellow with completed melded seam.

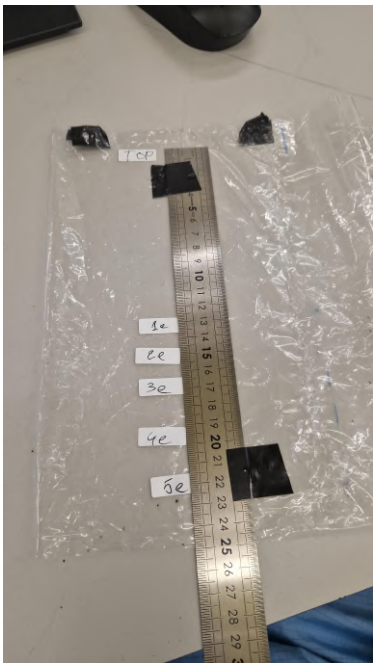

Figure B.6: Stickers used for marking reference cylinder height h_{ref} after measurements in crumpled state.

B.3. Signal processing and dynamic-stiffness definition

The definition of dynamic stiffness follows Wijnen [19]. Let $F_z(f)$ denote the global vertical force measured at the force cell and $U_{\mathrm{MF},z}(f)$ and $U_{\mathrm{BF},z}(f)$ the corresponding vertical displacements of the MF and BF interfaces in the frequency domain, obtained by double integration of the measured accelerations. The frequency-dependent vertical dynamic stiffness is then defined as

$$k_{\mathrm{dyn}}(f) = \frac{F_z(f)}{U_{\mathrm{MF},z}(f) - U_{\mathrm{BF},z}(f)}. \tag{B.1}$$

Data acquisition and basic signal processing closely follow the protocol of Wijnen [19]. Time signals are recorded with a sampling frequency of 50 kHz over measurement windows of 60 seconds. The recordings are divided into overlapping blocks of 2 seconds (50% overlap), each of which is multiplied by a Hanning window to reduce spectral leakage. Fast Fourier transforms of the windowed blocks are used to compute auto- and cross-power spectral densities, which are then averaged to suppress measurement noise. From these spectra, frequency-response functions and coherence functions are estimated and subsequently used to compute $k_{\mathrm{dyn}}(f)$ and to verify measurement quality.

B.4. Procedure and additions for the present study

The measurement sequence for the crumpled membrane links is built on the standard dynamic-stiffness protocol of Wijnen [19], with several modifications:

1. For each foil thickness and overlength, the specimen is mounted between the BF and MF interfaces, and fastened using hose clamps. The preload MF mass is lifted using the pneumatic bellow to ensure it to be floating, such that there is no preload present.
2. For low-stiffness measurements, a broadband multi-sine voltage signal is applied to the piezo actuators, exciting the setup over the frequency range 0-150 Hz or 100 - 500 Hz. Compared to the coloured noise excitation used by Wijnen [19], the multi-sine allows for a higher signal-to-noise ratio and more control over the spectral content at the cost of some additional signal design effort.
3. For each combination of thickness and overlength, three independent measurements are carried out. Between repetitions the foil is deliberately perturbed by hand so that the resulting data set samples different crumpling realizations of the same reference configuration.
4. For each run, the recorded forces and accelerations are processed as described above to obtain $k_{\mathrm{dyn}}(f)$. The three repeat measurements are then combined to estimate the mean and variability of the dynamic stiffness for that configuration.

B.4.1. Multi-sine excitation

Figure B.7 and Figure B.8 illustrate the effect of employing stitched band-limited multi-sine excitation signals on the measured dynamic stiffness and coherence. Compared to a single coloured-noise excitation, the multi-sine approach allows the input energy to be concentrated in a predefined frequency band. As a result, improved measurement coherence is obtained over the targeted frequency ranges.

Based on these observations, band-limited multi-sine excitations were adopted for the majority of measurements presented in the main body of this work. Simple coloured noise excitation was used only in cases where no significant difference in the resulting dynamic stiffness or coherence was observed. While Figure B.8 showcases how using many separate bands is ideal for the greatest measurement quality, performing such an extensive set of experiments is labour-intensive. Therefore, in this study only two different bands were used: the standard multi-sine excitation signals were generated in MATLAB by superposition of sine waves with frequency increments of 0.125 Hz over the ranges $[0 : 0.125 : 150]$ Hz and $[100 : 0.125 : 500]$ Hz. The two measurements are subsequently stitched together at 120 Hz. It should be noted that the multi-sine signal is not designed for frequency ranges >500 Hz, as doing so did not provide much clearer data. However, these higher frequencies are still partly excited due to high-frequency resonances of the shaker table.

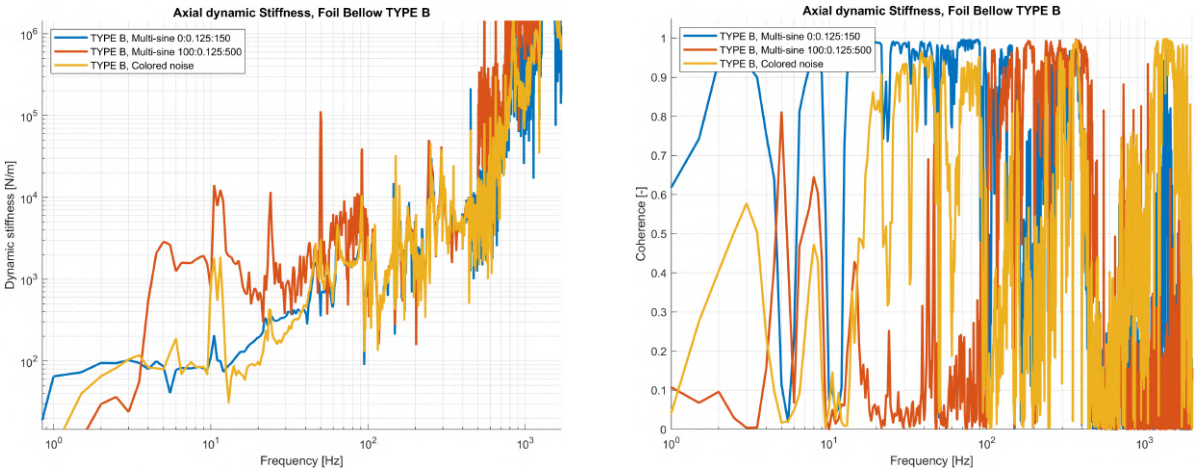

(a) Dynamic stiffness

(b) Coherence

Figure B.7: Axial dynamic stiffness measurements of ASML Foil Bellow TYPE B, comparing two separate band-limited multi-sine excitation signals (0-150 Hz and 100-500 Hz) to a broadband coloured-noise signal.

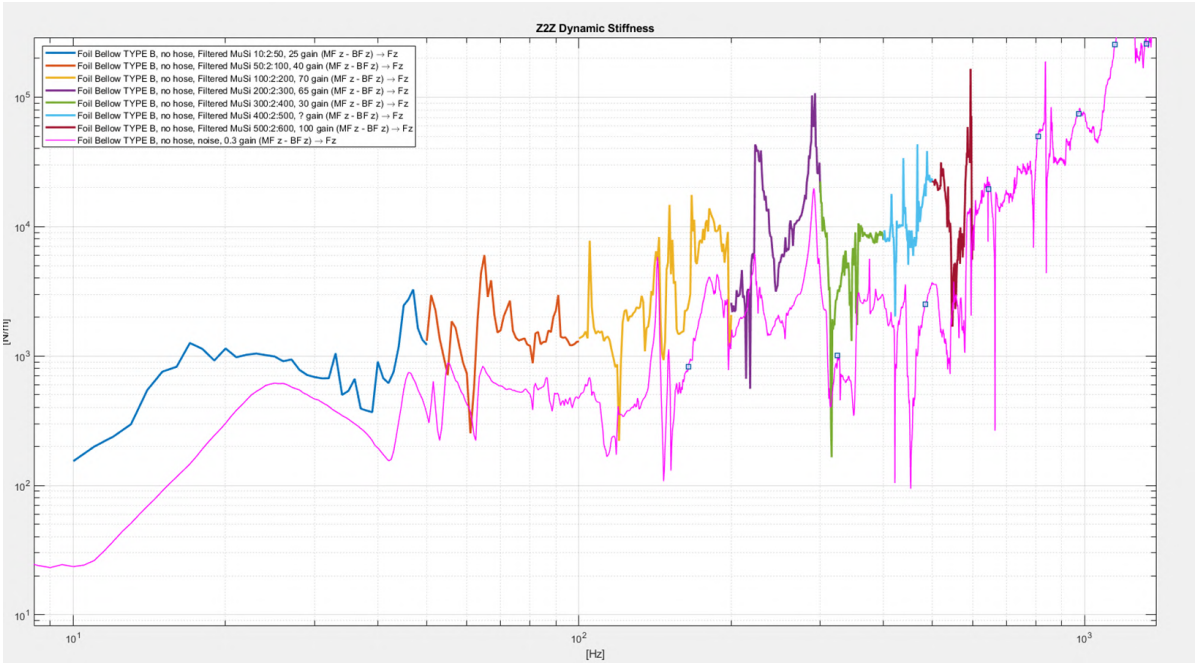

(a) Dynamic stiffness

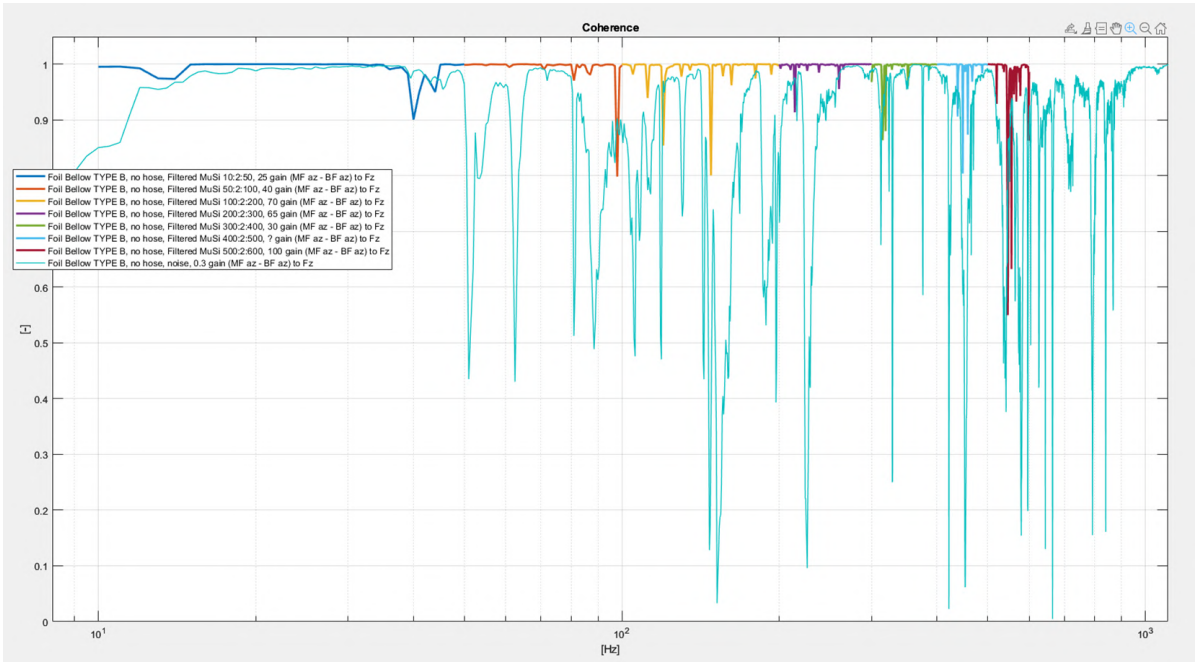

(b) Coherence

Figure B.8: Axial dynamic stiffness measurements of ASML Foil Bellow TYPE B, comparing a single coloured noise measurement (light blue) with multiple stitched-together band-limited multi-sine measurements. Note that the magnitudes in dynamic stiffness have been artificially shifted to provide a clearer picture.

B.4.2. Static stiffness extraction

For measurements involving foils with small thickness and large overlength, the signal-to-noise ratio at low frequencies is relatively poor. Consequently, the low-frequency plateau corresponding to the static stiffness in the dynamic stiffness curve is often obscured by measurement noise, complicating the identification of a clear and well-defined static region. In such cases, extracting the static stiffness from a single frequency point is unreliable, necessitating averaging over multiple points.

A simple approach, such as computing the mean over a fixed frequency interval, is insufficient in this context. The frequency range over which the stiffness remains approximately constant varies between configurations and cannot be prescribed uniformly. To address this challenge, a more robust extraction procedure was implemented.

First, the dynamic stiffness signal is smoothed using a moving average with a symmetric window of 30 Hz width. This step attenuates high-frequency fluctuations while preserving the underlying trend of the stiffness curve. The static stiffness is then defined as the mean of the smoothed stiffness within the low-frequency range from 1 to 10 Hz. Empirical evaluation across the dataset indicates that this procedure yields the most consistent and physically representative estimates of the static stiffness. Several illustrative examples are provided in Figure B.9.

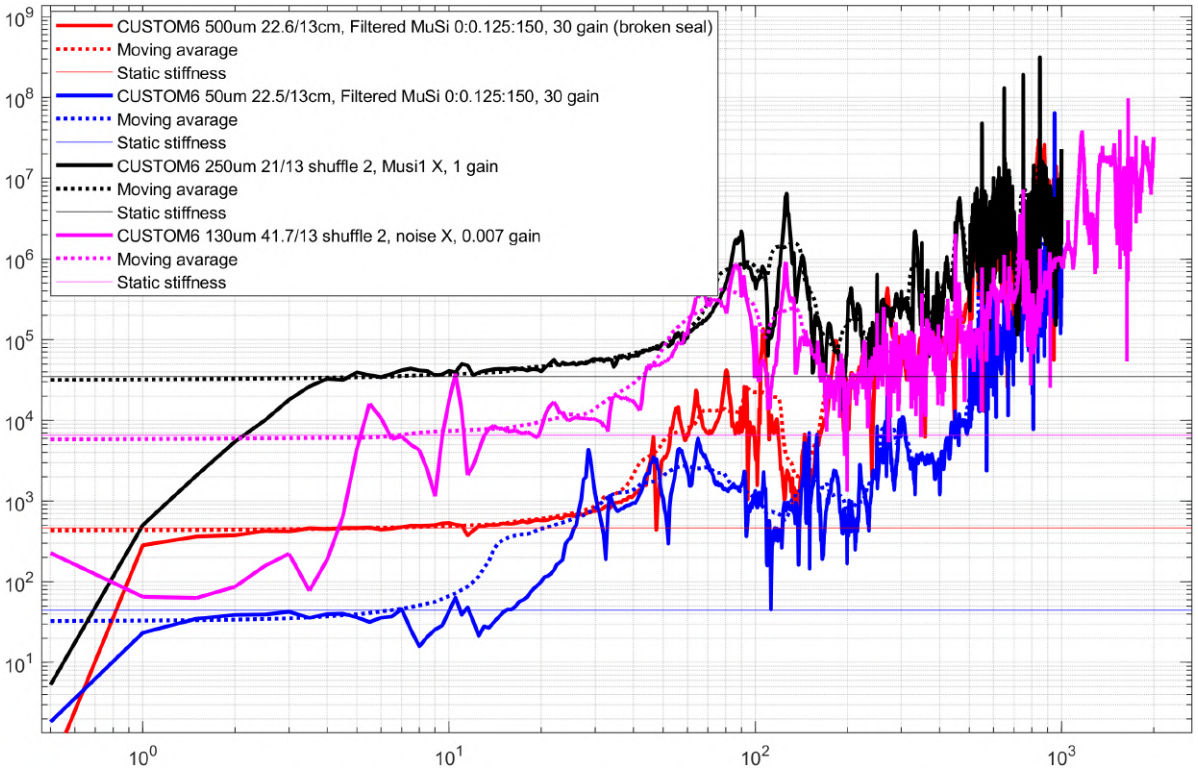

Figure B.9: Examples of static stiffness extraction from dynamic stiffness measurements. The raw signal is first smoothed using a symmetric moving average with a 30 Hz window size. The static stiffness is then calculated as the mean value of the smoothed stiffness between 1 and 10 Hz.

C

Additional results

This chapter presents supplementary findings and discussions not included in the primary text of chapter 3.

C.1. Crumpled morphology

Figure C.1 shows the crumpled morphologies obtained for all thicknesses, now inlcuding $t = 130$ µm and $t = 500$ µm. These thicknesses were not included in the main body of chapter 3, as they do not introduce qualitatively new behaviour but rather provide additional confirmation of the previously identified trend: increasing thickness results in a larger characteristic wavelength of wrinkles and an increase in the overall scale of the crumpled structures.

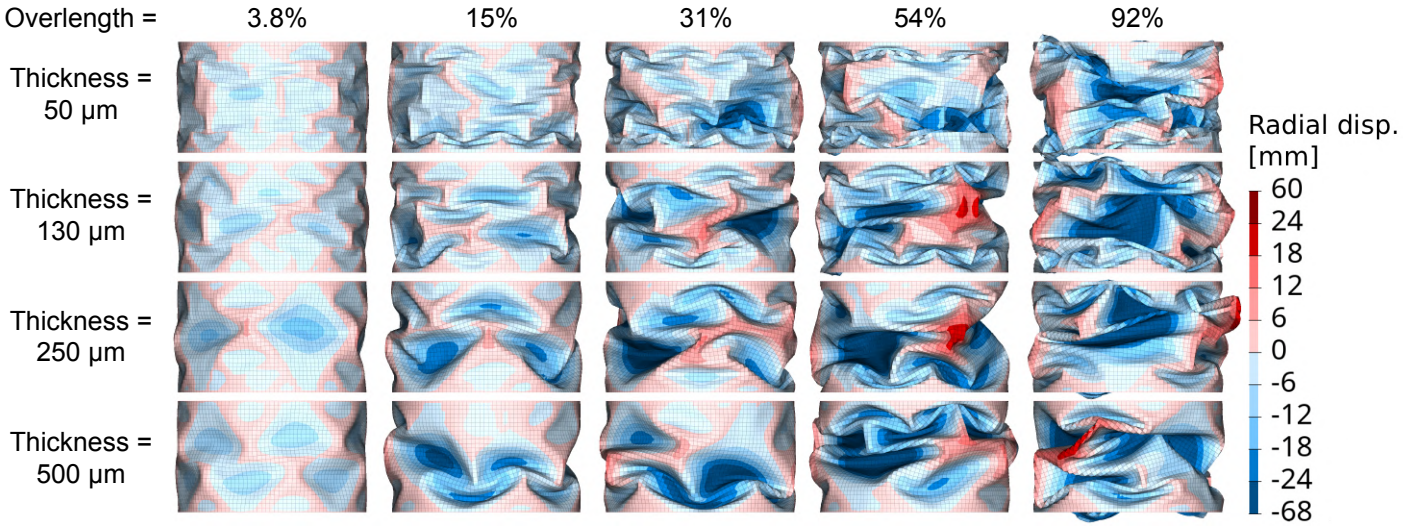

Figure C.1: Simulated crumpled geometries for increasing overlength and thickness (extended data). The results display the radial displacement relative to the cylinder centreline, with outward displacements taken as positive. The colour scale is limited to ± 24 mm to enhance the visibility of variations between small and large overlenghts. However, it should be noted that many sections display more extreme displacement, as the actual absolute range extends from -68 mm to $+60$ mm.

C.2. Static stiffness

The overlength-thickness contour plots in Figure C.2 more effectively demonstrate the power-law relationship between overlength and thickness identified in chapter 3. The analysis of the interpolated contour lines indicates a consistent trend: low stiffness values are associated with significant overlength and minimal thickness, while high stiffness is found with reduced overlength and substantial thickness. Intermediate regions display increasingly sloped diagonal lines, accurately represented by the multiplicative power-law model illustrated in blue. The axial stiffness measurements align worst with the fit due to the noisy measurement data, as reflected by the jagged interpolation and lower R^2-value for the fit.

Alternative modelling laws, such as rational polynomials, were also explored; however, none offer the same interpretability as the multiplicative power-law. Moreover, the power-law formulation is straightforward to fit, as it can be expressed in a linear form and solved via standard linear regression, an advantage not generally shared by more complex models with additional parameters.

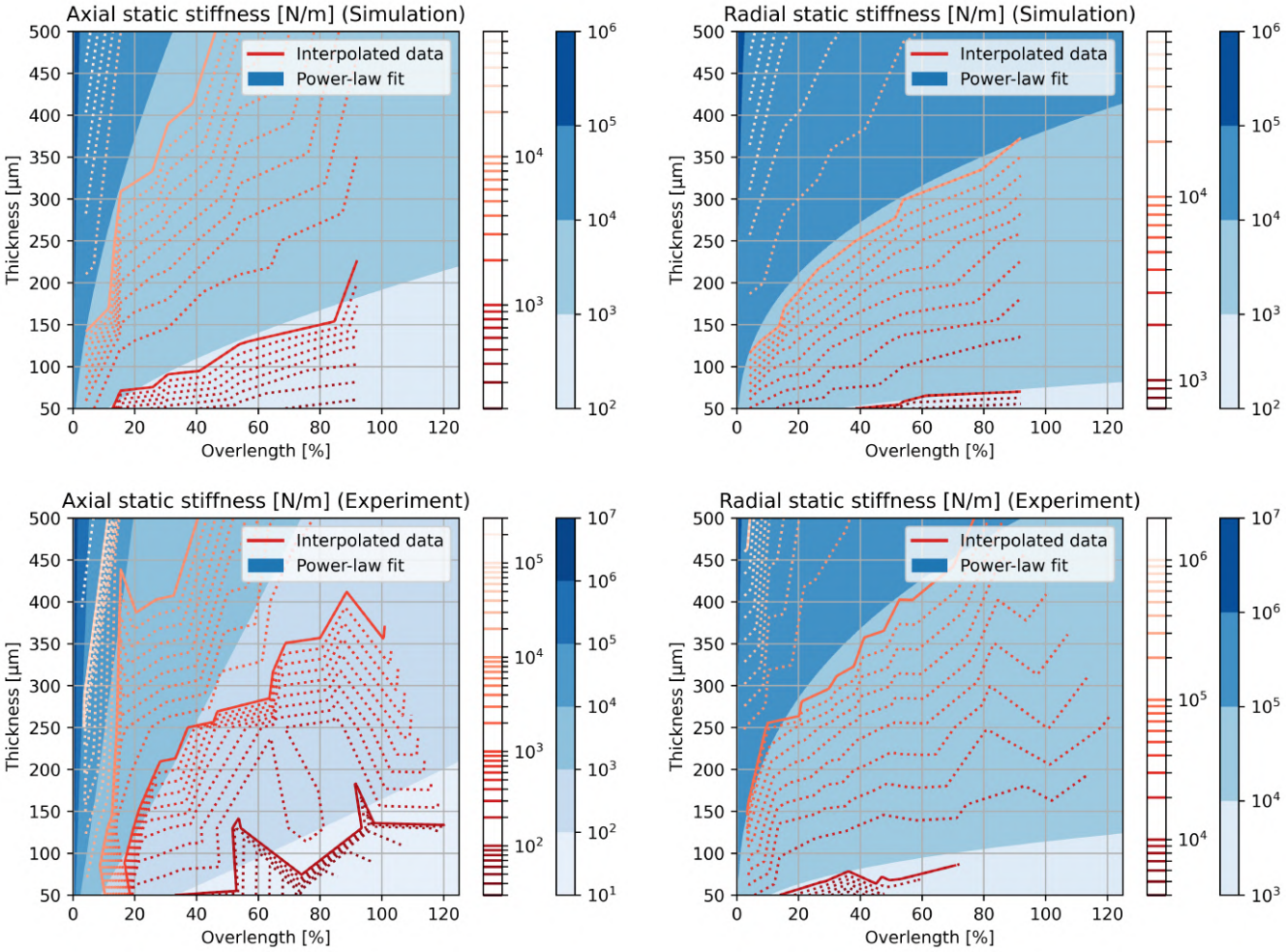

Figure C.2: Contour-plot representations of static stiffness data and subsequent power-law fit. The data from simulation or experiment is averaged per configuration and linearly interpolated to generate contour contour-lines, with solid lines indicating decades and dotted lines indicating sub-decades. It should be noted that the interpolated data does not always span the full range of overlength and thickness, and thus data is absent at these higher overlengths. The multiplicative power-law fit, with respective power-law exponents reported in chapter 3, is depicted by a blue filled contour.

Figure C.3 presents extended measurement data for the radial stiffness at $t = 130$ µm and $t = 250$ µm. Although such large overlength values are not directly relevant for the current design problem, they provide additional insight into the mechanical response of crumpled structures in this regime. As anticipated, for overlengths exceeding 100% the measured stiffness rapidly approaches a plateau, doing so faster than predicted by the power-law behaviour obtained from simulations. This observation indicates that the formation of self-contacting ridges within the structure introduces mechanical *shortcuts* and frictional interactions that mitigate the reduction in overall stiffness, see Figure C.4, Consequently, these findings further support the conclusion that practical designs should target an intermediate regime (30-60%) in which additional overlength still yields a substantial decrease in stiffness.

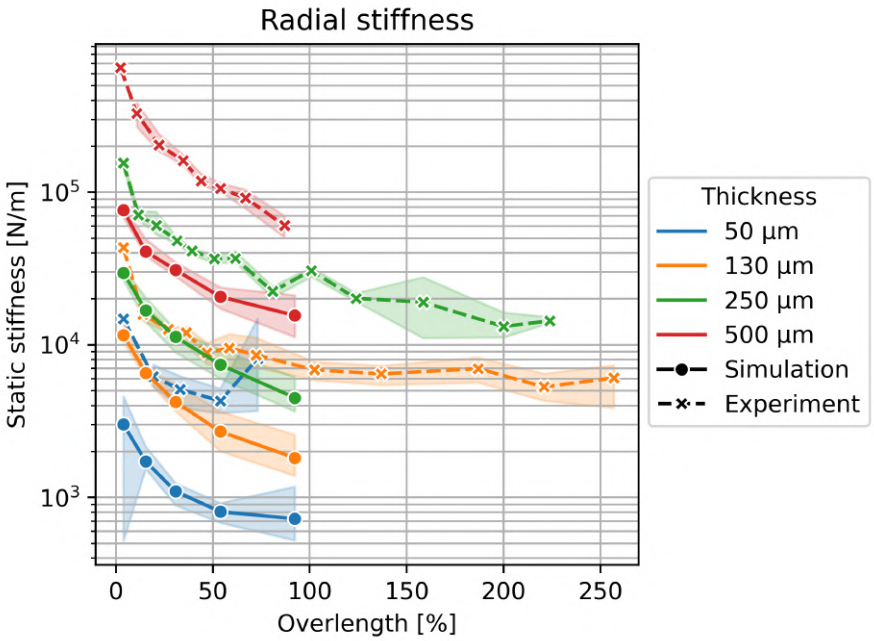

Figure C.3: Radial static stiffness results (extended data).

Figure C.4: Severely crumpled morphology demonstrating self-contacting ridges at an extreme overlength ($t = 130$ µm and overlength = 190%)

C.3. Dynamic stiffness

The following section compiles all measured and simulated dynamic stiffness data, along with coherence plots indicating measurement quality.

C.3.1. Axial stiffness measurements

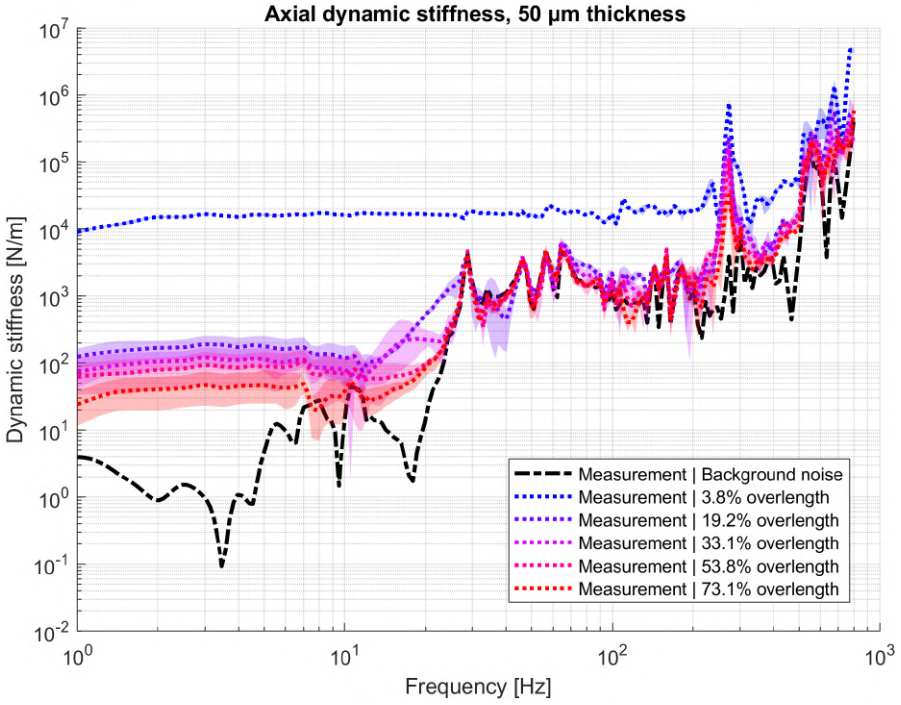

(a) Dynamic stiffness

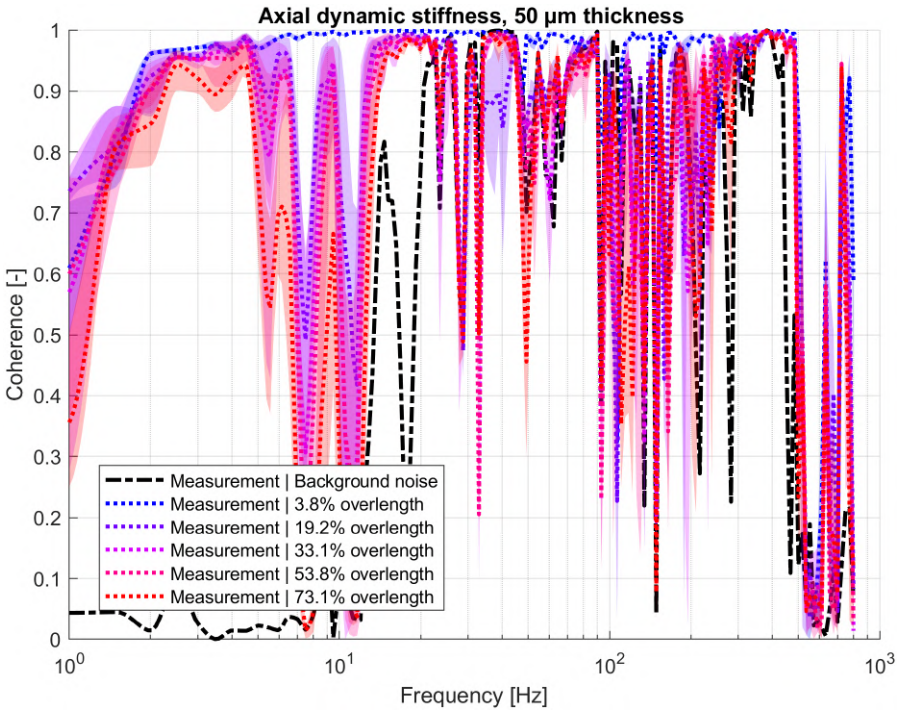

(b) Coherence

Figure C.5: Axial dynamic stiffness measurements for $t = 50$ µm, using two combined multi-sine measurements. Shade areas indicate minimum-maximum bounds for three realisations. For the smallest overlength only one realisation was measured. Background noise indicates a measurement without a bellow present.

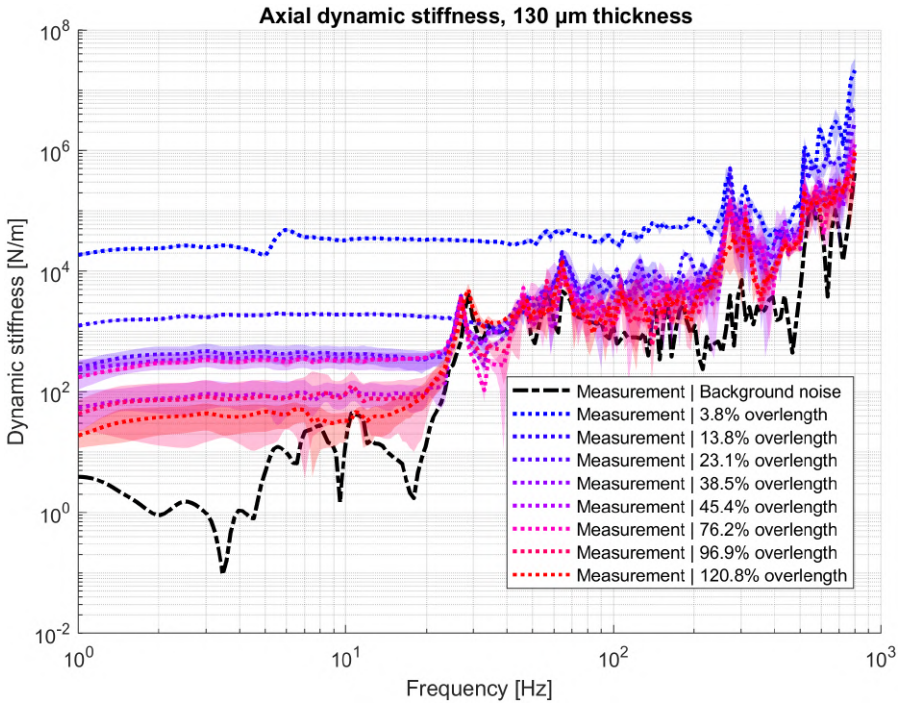

(a) Dynamic stiffness

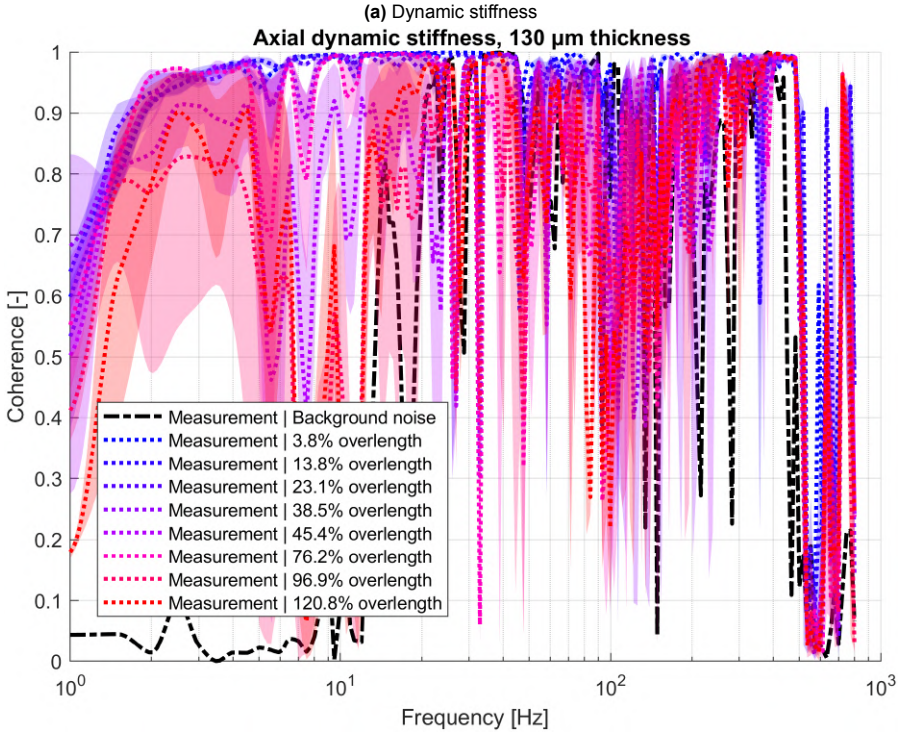

(b) Coherence

Figure C.6: Axial dynamic stiffness measurements for $t = 130$ µm, using two combined multi-sine measurements. Shade areas indicate minimum-maximum bounds for three realisations. For the smallest overlength only one realisation was measured. Background noise indicates a measurement without a bellow present.

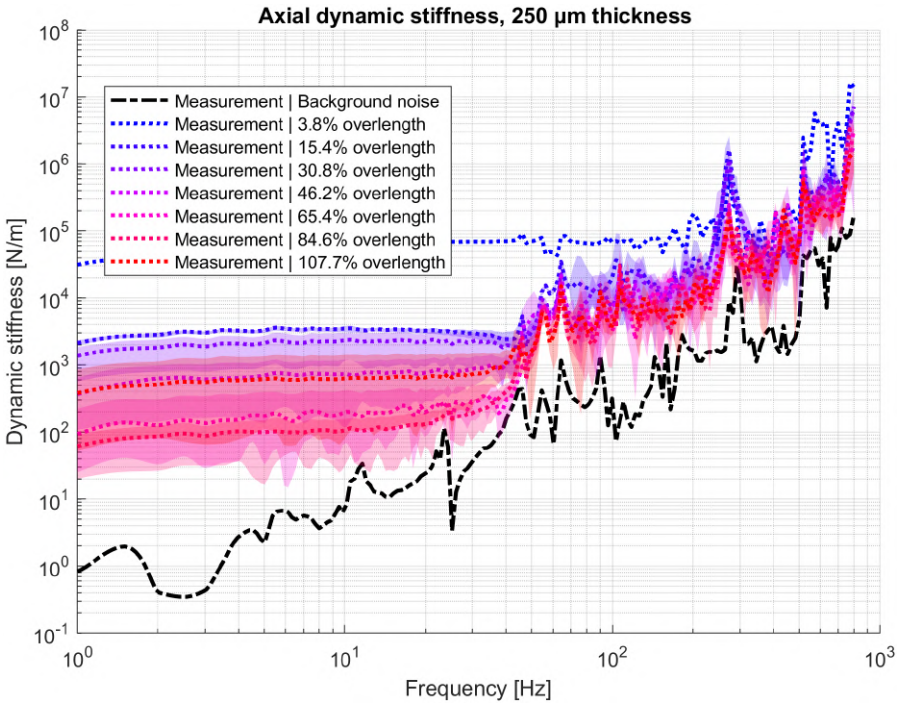

(a) Dynamic stiffness

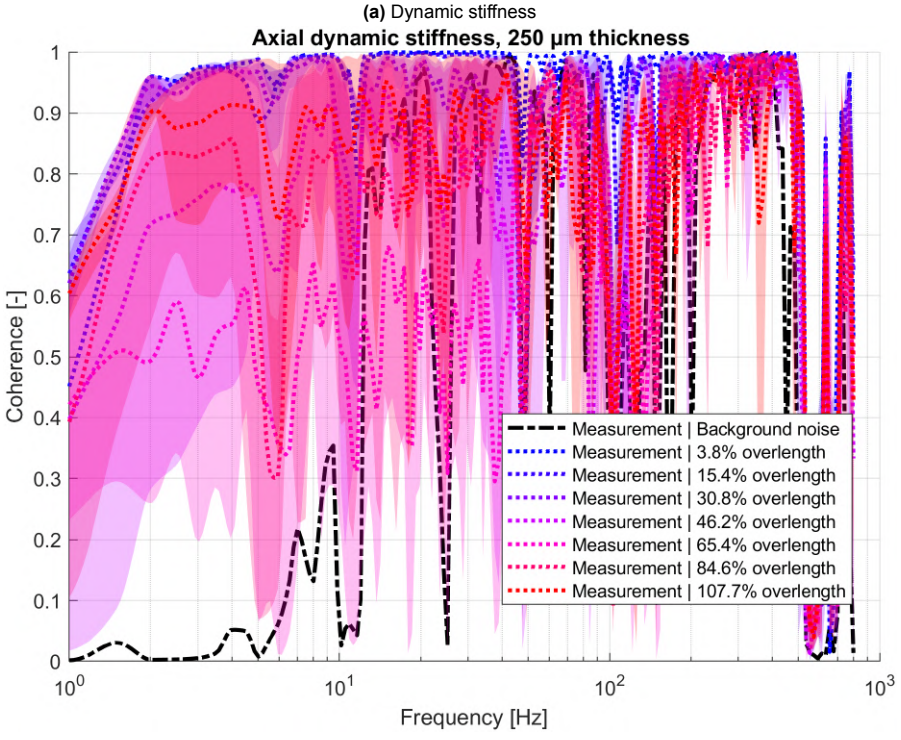

(b) Coherence

Figure C.7: Axial dynamic stiffness measurements for $t = 250$ µm, using two combined multi-sine measurements. Shade areas indicate minimum-maximum bounds for three realisations. For the smallest overlength only one realisation was measured. Background noise indicates a measurement without a bellow present.

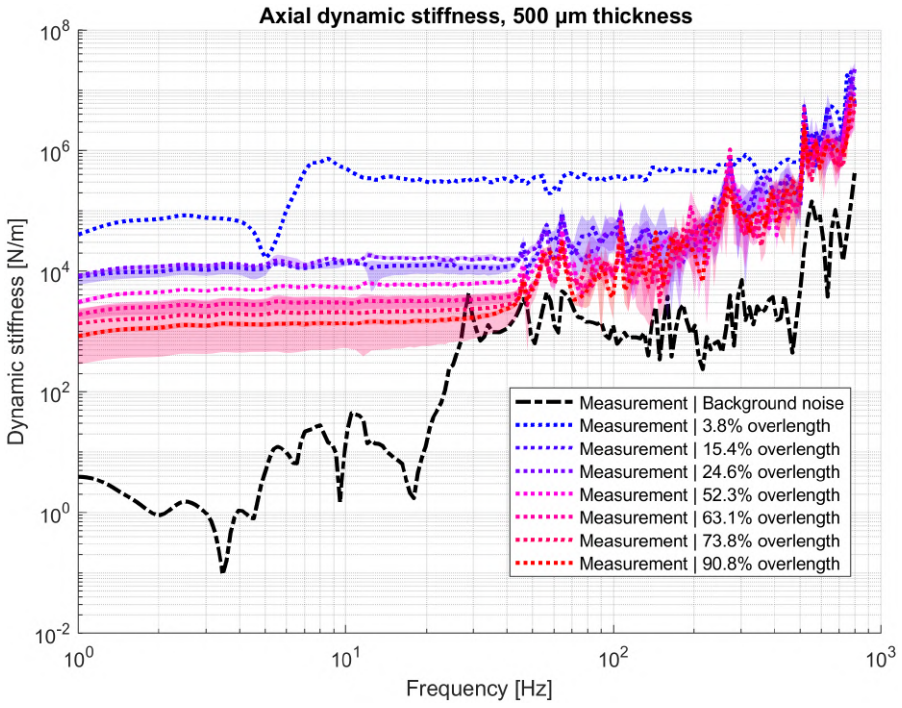

(a) Dynamic stiffness

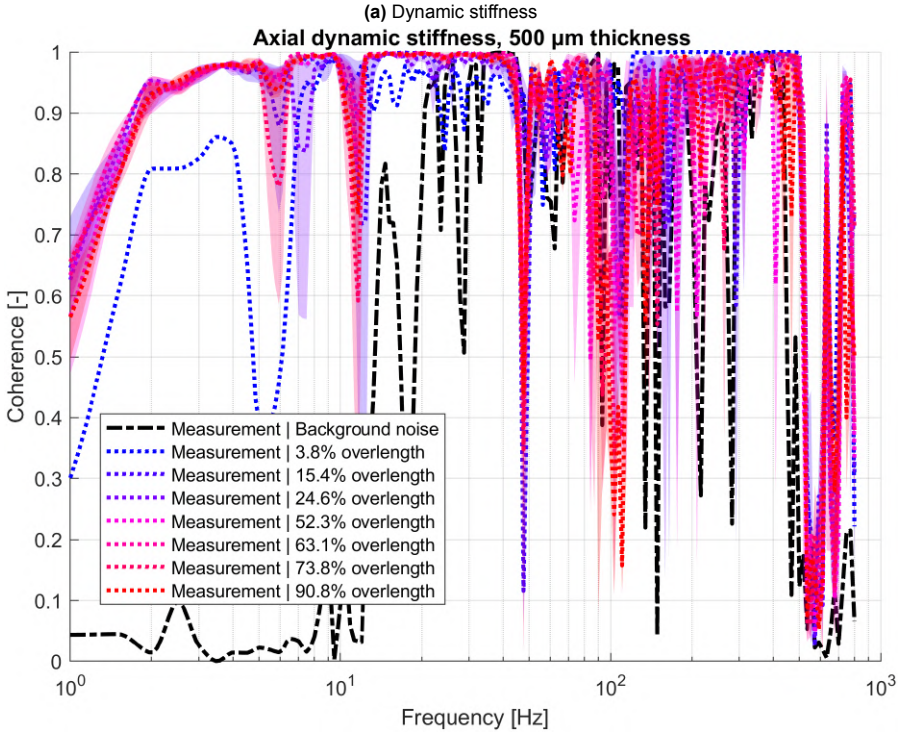

(b) Coherence

Figure C.8: Axial dynamic stiffness measurements for $t = 500$ µm, using two combined multi-sine measurements. Shade areas indicate minimum-maximum bounds for three realisations. For the smallest overlength only one realisation was measured. Background noise indicates a measurement without a bellow present.

C.3.2. Axial stiffness simulations

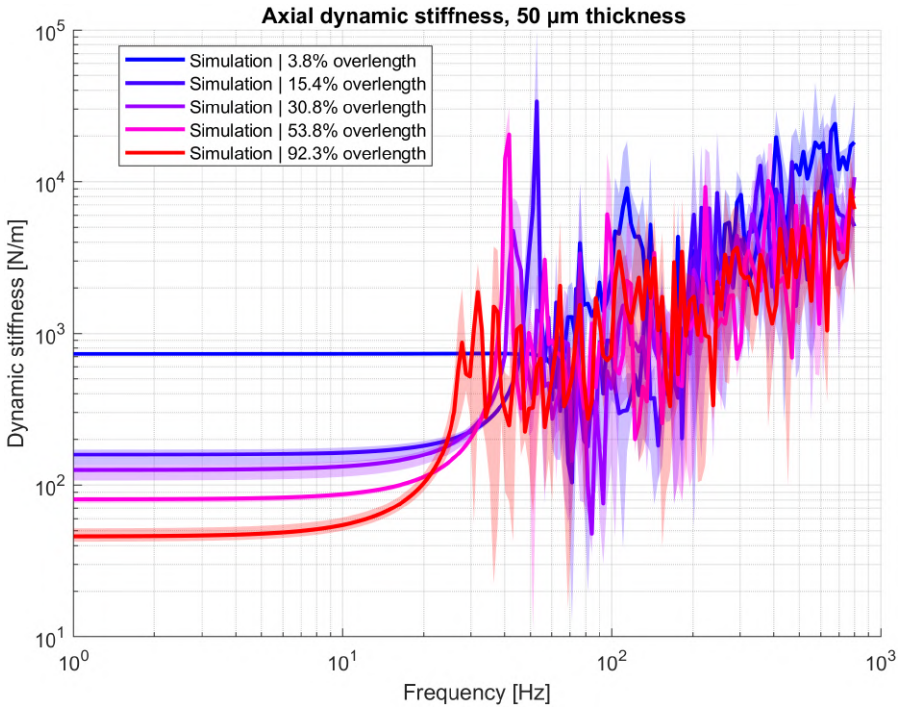

Figure C.9: Axial dynamic stiffness simulations for $t = 50$ µm, calculated using modal reduction with modes up to 1000 Hz. The shaded area indicates minimum-maximum bounds for three realisations.

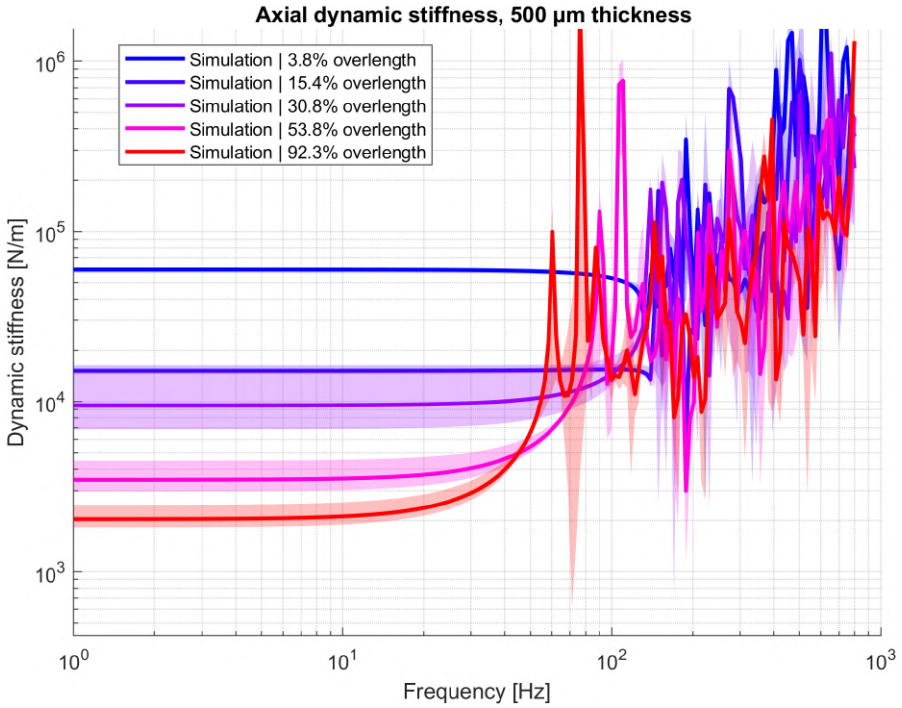

Figure C.10: Axial dynamic stiffness simulations for $t = 50$ µm, calculated using modal reduction with modes up to 1000 Hz. The shaded area indicates minimum-maximum bounds for three realisations.

C.3.3. Radial stiffness measurements

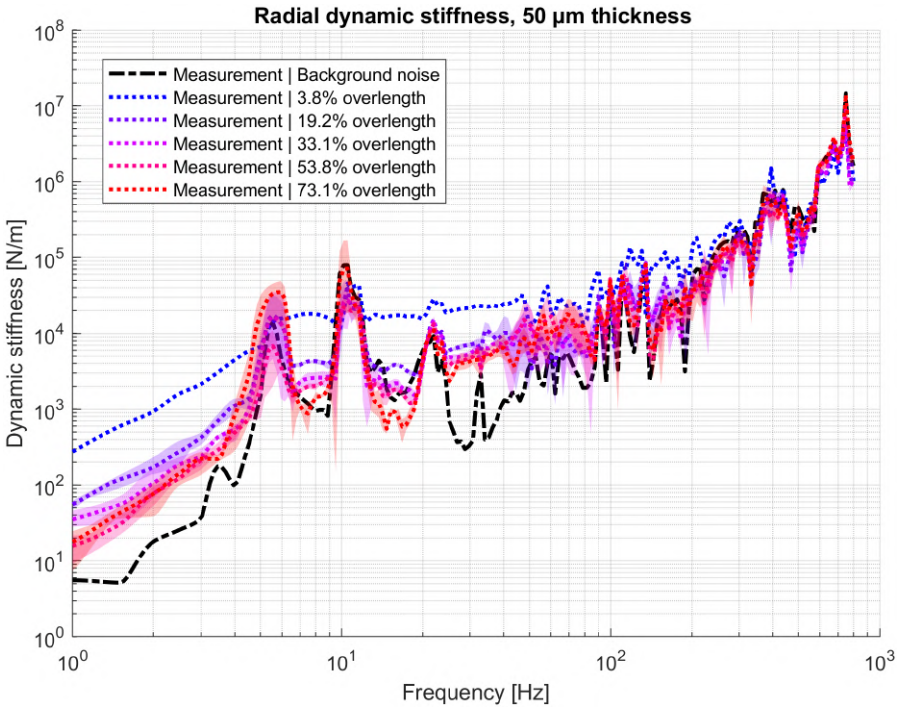

(a) Dynamic stiffness

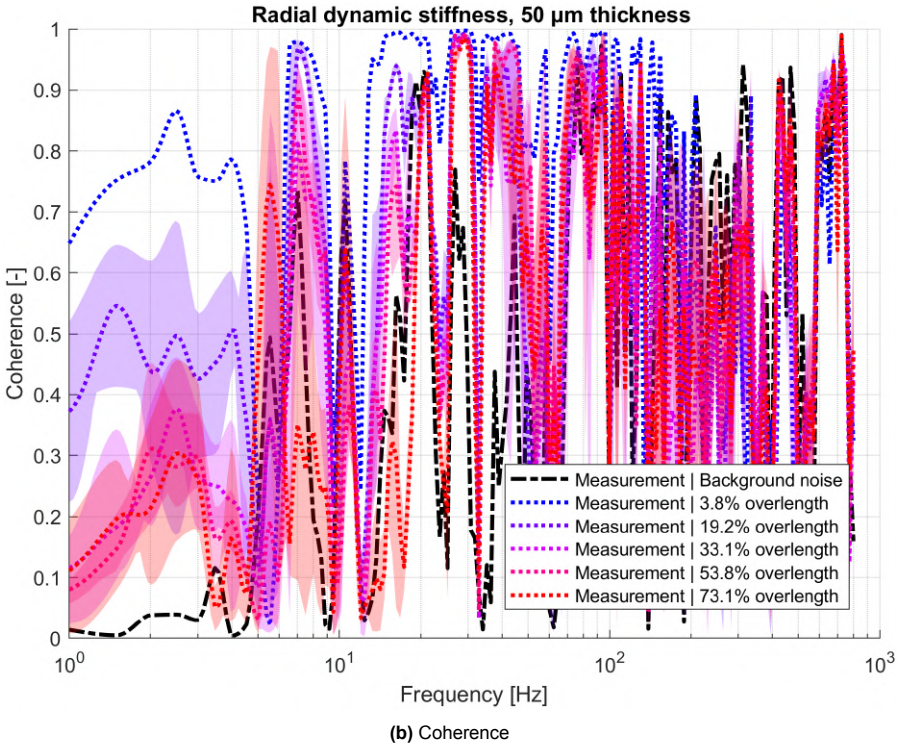

(b) Coherence

Figure C.11: Radial dynamic stiffness measurements for $t = 50$ µm, using two combined multi-sine measurements. Shade areas indicate minimum-maximum bounds for three realisations. For the smallest overlength only one realisation was measured. Background noise indicates a measurement without a bellow present.

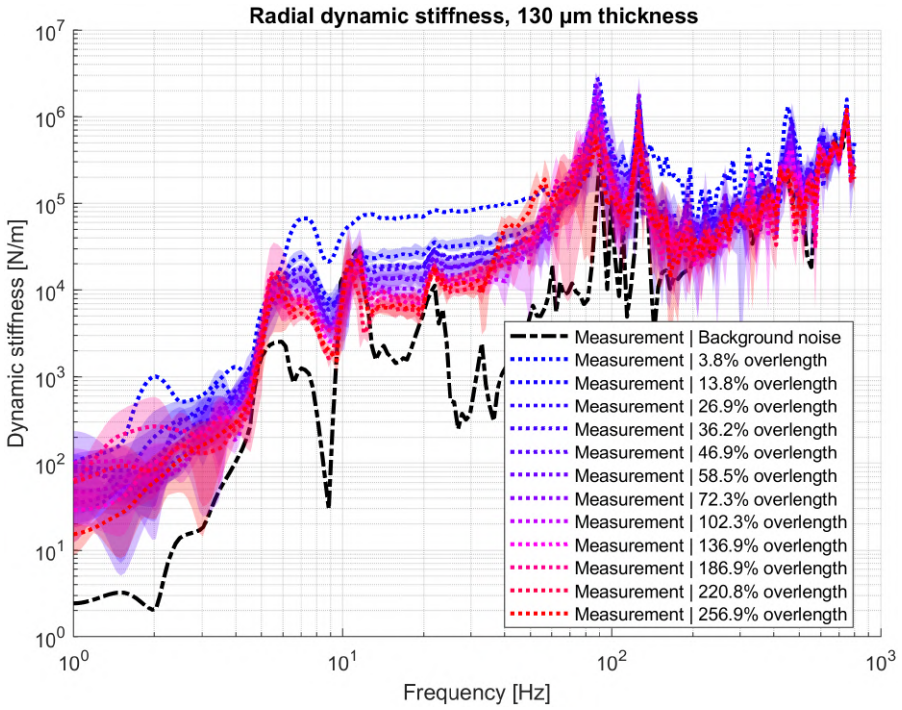

(a) Dynamic stiffness

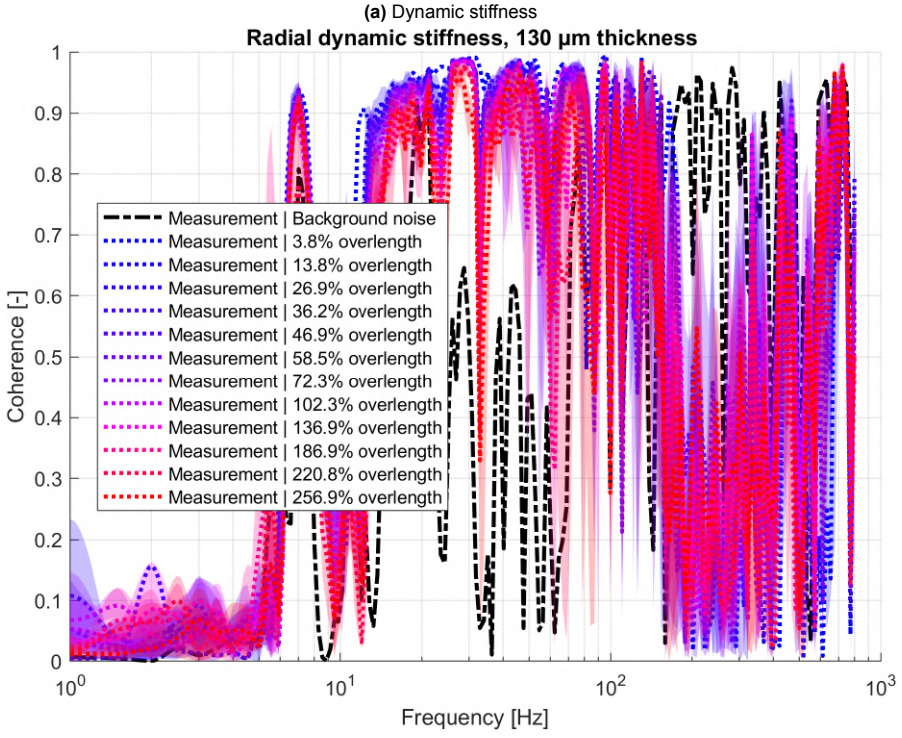

(b) Coherence

Figure C.12: Radial dynamic stiffness measurements for $t = 130$ µm, using a single noise measurement. Shade areas indicate minimum-maximum bounds for three realisations. For the smallest overlength only one realisation was measured. Background noise indicates a measurement without a bellow present.

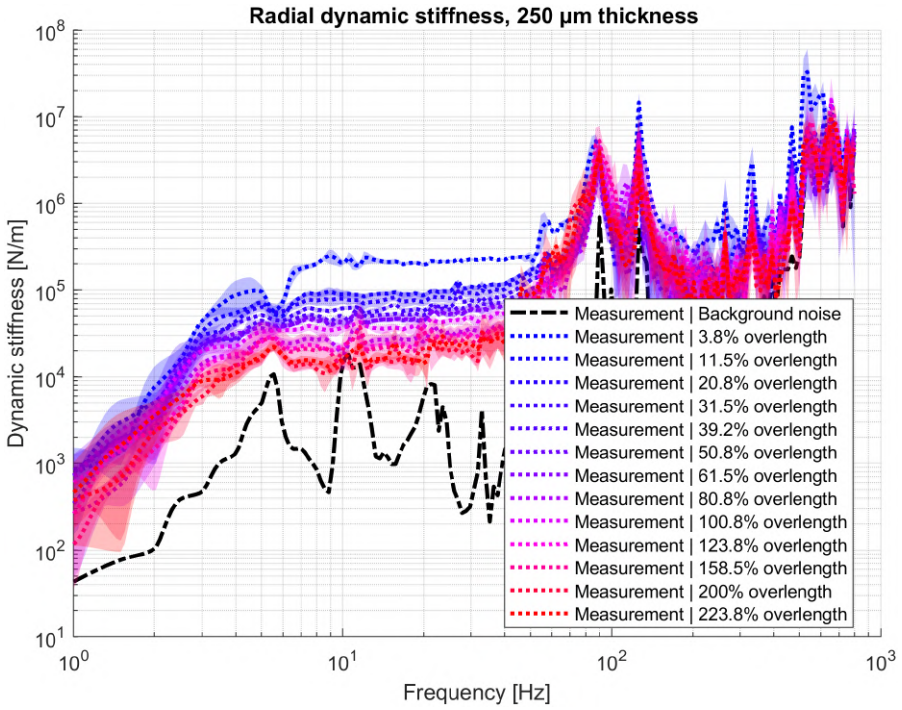

(a) Dynamic stiffness

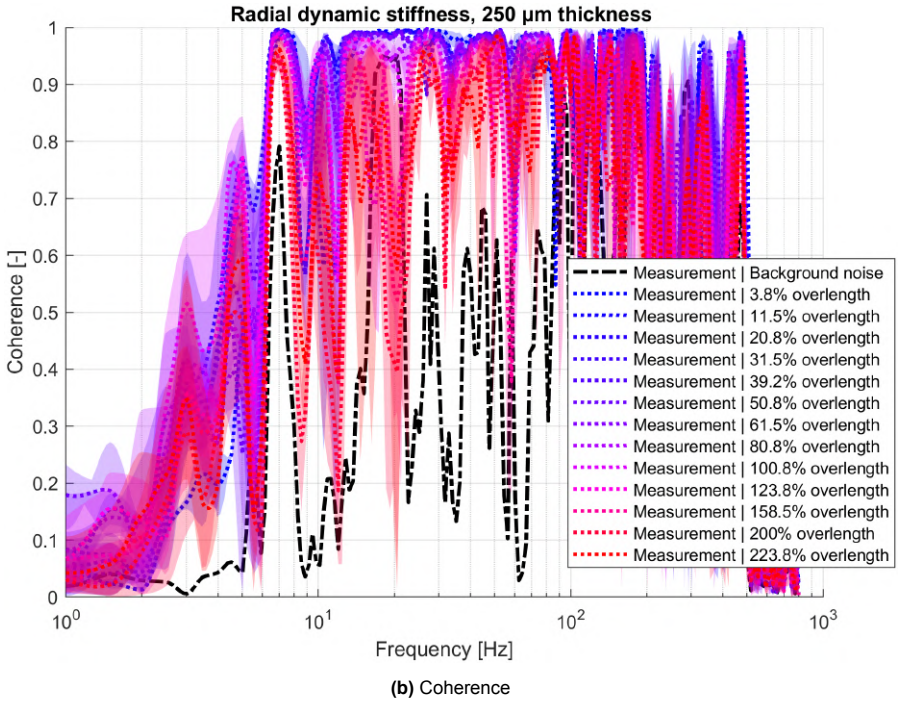

(b) Coherence

Figure C.13: Radial dynamic stiffness measurements for $t = 250$ µm, using two combined multi-sine measurements. Shade areas indicate minimum-maximum bounds for three realisations. For the smallest overlength only one realisation was measured. Background noise indicates a measurement without a bellow present.

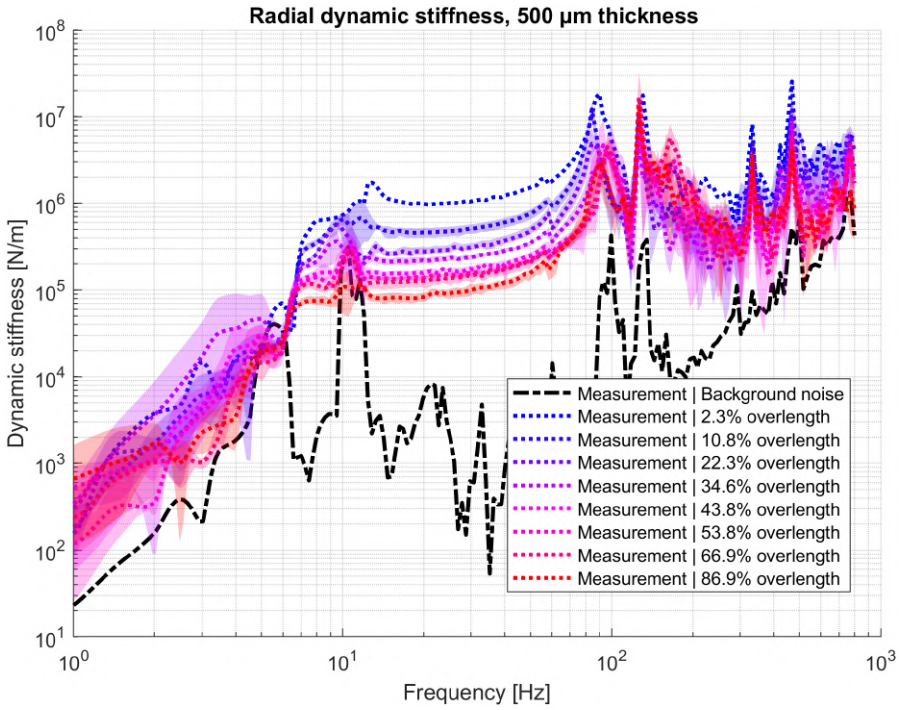

(a) Dynamic stiffness

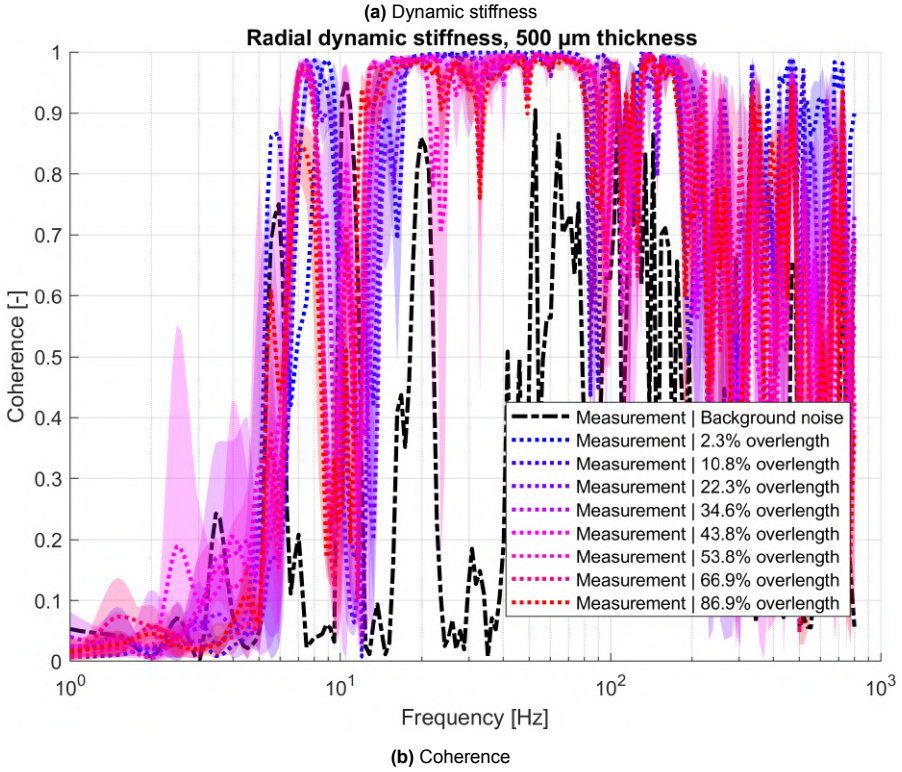

(b) Coherence

Figure C.14: Radial dynamic stiffness measurements for $t = 500$ µm, using a single noise measurement. Shade areas indicate minimum-maximum bounds for three realisations. For the smallest overlength only one realisation was measured. Background noise indicates a measurement without a bellow present.

C.3.4. Radial stiffness simulations

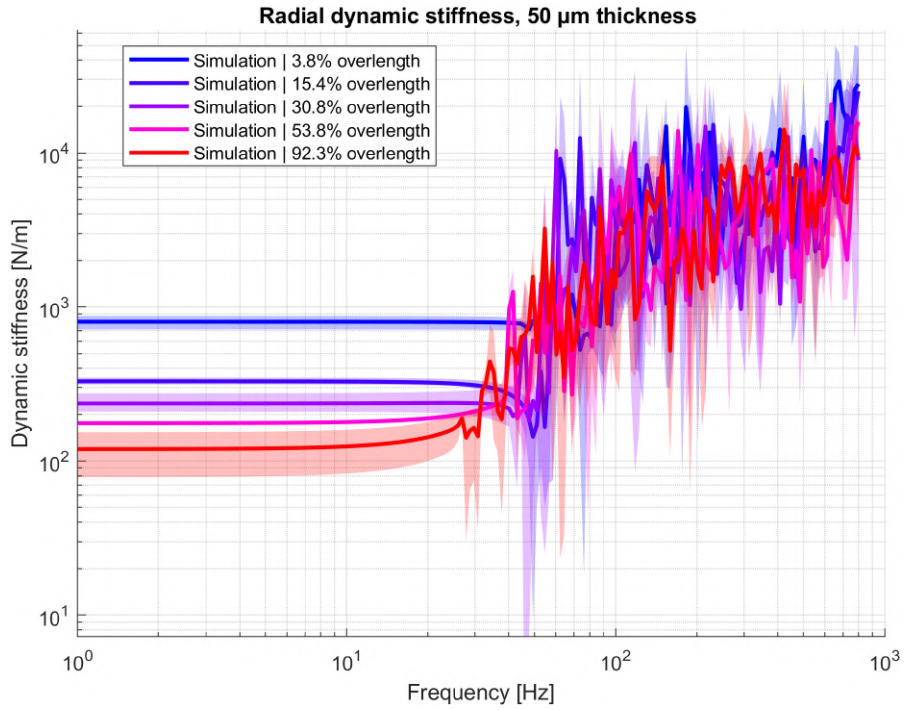

Figure C.15: Radial dynamic stiffness simulations for $t = 50$ µm, calculated using modal reduction with modes up to 1000 Hz. The shaded area indicates minimum/maximum bounds for three realisations.

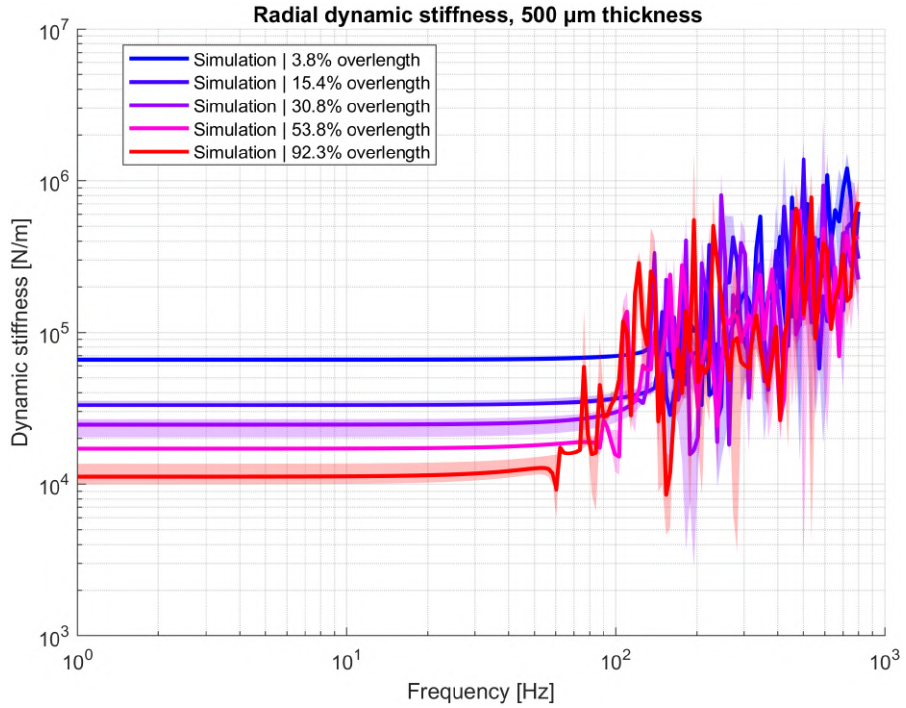

Figure C.16: Radial dynamic stiffness simulations for $t = 500$ µm, calculated using modal reduction with modes up to 1000 Hz. The shaded area indicates minimum/maximum bounds for three realisations.

C.3.5. Interpretations

The additional frequency dimension in the dynamic stiffness data complicates the identification of clear scaling relations, such as the power-law behaviour observed for static stiffness in chapter 3. Nevertheless, several consistent trends can be identified across the measurements.

For the axial dynamic stiffness measurements, the configurations with the smallest overlength (blue curves) exhibit the most pronounced static stiffness plateau. This plateau remains well above the background noise level, particularly for larger thicknesses. Only in the high-frequency regime (>300 Hz) do these stiffness curves approach the noise floor. Correspondingly, the coherence remains high (>0.9) throughout the low- and mid-frequency ranges.

However, as the overlength increases the axial static stiffness decreases rapidly. Accordingly, coherence begins to exhibit dips at progressively lower frequencies, indicating an increasing influence of background noise due to resonances originating from the measurement setup. The variability between repeated measurements also increases with overlength. This trend is consistent with the expectation that larger overlengths lead to more diverse crumpling configurations, thereby increasing configuration-dependent mechanical response.

In contrast, the radial dynamic stiffness measurements display substantially lower variability between realisations. The reduction in stiffness with increasing overlength is less pronounced, and the dynamic stiffness curves remain comparatively similar across different overlengths. This suggests that radial stiffness is governed primarily by averaged, global deformation mechanisms of the crumpled structure, rather than by the local axial bending of individual crumpled ridges, which appears to dominate the axial response.

Although the experimental results reveal fundamental differences between the axial and radial evolution with overlength, these differences are not reproduced in the numerical simulations. The discrepancy is particularly significant for axial stiffness, where the low-overlength configurations are considerably stiffer in experiment than predicted numerically. This observation supports the hypothesis that the axial stiffness is influenced by non-linear mechanisms, such as plastic deformation within bending ridges, which are not captured by the current simulation model.

Irrespective of measurement direction or method, all dynamic stiffness plots exhibit an exceptionally high modal density. This behaviour can be attributed to the omni-directional compliance inherent to crumpled structures. From a design perspective, the exact locations and shapes of individual peaks and valleys are therefore of limited relevance. Instead, the overall stiffness trends and the magnitude of deviations are of primary importance when considering these structures as dynamic links.

In this view, we observe that both experimental and numerical results demonstrate convergence of the dynamic stiffness curves at higher frequencies. Since this convergence is also observed in simulation, it cannot be attributed solely to background noise. This indicates diminishing returns when selecting extreme overlength values, as the difference between overlengths disappears in the dynamic regime. Consequently, the choice of overlength and thickness must be carefully balanced, not only to achieve sufficiently flexible stiffness characteristics, but also to mitigate practical risks such as pinhole formation and unintended mechanical shortcuts.

C.3.6. Simulated eigenfrequencies

Figure C.17 shows the dependence of the first eigenfrequency on overlength for two foil thicknesses, as generated by the modal reduction simulation. The eigenfrequencies are found to decrease via a clear power-law relation. Some of this is expected: the mass m of the total system increases linearly with h_{ref}, which would suggest the eigenfrequency should scale with $f \propto \sqrt{k/m} \propto m^{-0.5} \propto h_{\mathrm{ref}}^{-0.5}$. However, the eigenfrequencies decrease even faster due to the fall in general stiffness k, such that $f \propto h_{\mathrm{ref}}^{-2.06}$ for $t = 50$ µm and $f \propto h_{\mathrm{ref}}^{-2.42}$ for $t = 500$ µm. Thus, we see the mechanism why increasing overlength not only lowers the static stiffness, but also lowers the frequency from which the dynamic regime begins. Interestingly, for these simulations the drop-off in eigenfrequency/stiffness is slightly faster for larger thickness, an effect we have not observed in other data.

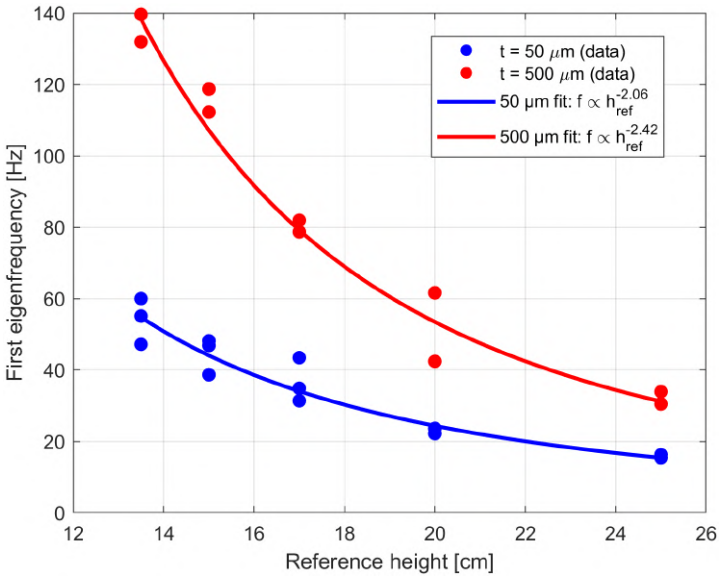

Figure C.17: First eigenfrequency of crumpled cylinder as a function of overlength for foil thicknesses of 50 µm and 500 µm. Each marker corresponds to a single simulation with a unique initial pertubation. Solid lines indicate power-law fits based on reference cylinder height h_{ref}.

Structural Dynamic Simulation of Post-Buckled Thin Sheets: a Review

Marco Bader[a]

[a]*Department of Precision and Microsystems Engineering, Faculty of Mechanical Engineering, Delft University of Technology, the Netherlands*

Abstract

We present a comprehensive review of the diverse approaches employed to model wrinkled and crumpled thin sheets, with their structural dynamics of particular interest. To get better acquainted with the problem at hand, the experimental behaviour of such sheets is discussed and the common computational challenges are presented. Notably, buckled thin sheets have been modelled using various spatial discretizations besides traditional finite element analysis, such as isogeometric analysis, tension field theory and discrete element analysis. Advanced solution procedures for buckled sheets are also examined, such as initial perturbations, dynamic relaxation, arc-length methods, modal reduction and sensitivity analysis. A general flowchart with discussion is outlined to assist the reader in traversing all these options in methods and pinpoint which are especially relevant to the user's application.

Keywords: post-buckled thin sheets, wrinkling, crumpling, isogeometric analysis, tension field theory, dynamic relaxation, arc-length methods

1. Introduction

The crumpling of a sheet of paper is an everyday phenomenon that vividly illustrates the complex post-buckling behaviour of soft thin structures. Beyond the household scale, similar instabilities emerge in flower buds, the Earth's crust, and DNA packing, all of which reveal the intricate patterns that can form through wrinkling and crumpling [1]. Until recently, engineers have often regarded these features as nuisances that negatively impact their finely designed systems. For instance, wrinkles and creases in solar sails may lead to decreased thrust force and control difficulties [1].

However, compacted crumpled sheets have also been shown to exhibit rich mechanical properties such as high energy absorption, enhanced compression resistance, and a tuneable porosity [2–4]. Together with their low weight and ease of manufacturing, these special qualities have spurred research into so-called *disordered* metamaterials [4] across a wide range of industries. Early applications include crumpled graphene for micro-scale strain and pressure sensing [5], crumpled metallic foils as lightweight alternatives to solid foams in sandwich structures [6], and controlled crumpling approaches for porous biomaterial implants [7].

Another engineering context that may show promise is where thin buckled sheets are employed to realise highly compliant joints or seals. For example, corrugated bellows common to vacuum applications illustrate how deliberately engineered ridge networks can produce flexible links with low vibrational transmissibility [8], see Figure 1. Likewise, purposefully buckled or even completely crumpled sheets might provide a simpler and more economical path to multi-directional compliance.

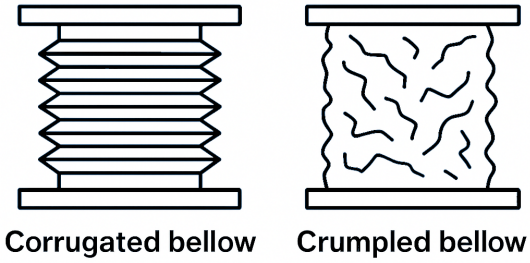

Figure 1: Schematic comparison between engineered corrugation networks and stochastic crumpled morphologies as routes to compliant thin-sheet mechanical links.

Realising this promise in design practice is hindered by the fact that the structural mechanics and dynamics of crumpled morphologies are still poorly understood. Analytical post-buckling theory is typically restricted to idealised situations close to the critical load, where deformations remain in a linearised and periodically wrinkled regime [9].

In contrast, crumpling represents the non-linear and irregular evolution of wrinkling [10]. For this regime there is no broadly applicable analytical framework. Moreover, the morphology is highly sensitive to initial imperfections and loading history, such that stochastic variability between realisations is intrinsic and many samples are needed to extract statistically meaningful trends. For engineering purposes, where one often wishes to explore parameter spaces, quantify uncertainty, and ultimately optimise designs, efficient and robust modelling strategies are therefore essential.

However, the strongly non-linear and path-dependent nature of buckled thin-sheet systems poses substantial computational challenges [11]. Even in the wrinkling regime, numerical models can rapidly lead to ill-conditioned system matrices and convergence problems, making conventional finite element approaches unstable or prohibitively expensive. Although a wide range of techniques has been proposed to address these issues [12], the literature still lacks a coherent overview that connects these computational developments to the specific task of dynamic analysis of crumpled flexible mechanical links.

To address this gap, this work aims to review how various modelling strategies can support structural-dynamic analysis for buckled thin-sheet structures. First, relevant experimental insights into the wrinkle-to-crumple transition and the dynamic behaviour of wrinkling are examined. Subsequently, common computational challenges along with the advantages of alternative spatial discretisations and advanced solution procedures are discussed. Finally, these methods are synthesised into a generalised workflow for the systematic, efficient and robust (dynamic) analysis of post-buckled thin-sheet structures.

2. Review method

Literature on the modelling of wrinkled and crumpled thin sheets was collected from the Scopus and Google Scholar databases using an iterative search strategy. A preliminary broad search was conducted using the following keyword combination:

```
("sheet" OR "membrane" OR "foil") AND
("wrinkl*" OR "crumpl*") AND ("simulat*" OR
"model*") AND NOT "bio*"
```

To efficiently screen the large number of resulting references, the AI-assisted systematic review tool *ASReview* [13] was employed. Relevant publications were first identified on the basis of their abstracts, and these labels were then used to train an active-learning model to prioritise similar documents. This procedure was repeated three times on slightly different datasets, each derived from modified search queries targeting specific subtopics, with approximately 50 references manually labelled for each run. The tool proved effective in identifying additional papers closely related to the initially selected works. However, its recommendations tended to focus on relatively narrow thematic clusters, limiting its usefulness for mapping the broader landscape of modelling approaches.

To complement this, for several key publications the web-based tool *Connected Papers* [14] was used to generate citation-based network graphs of closely related prior and derivative works. In combination with manual forward- and backward-citation tracking from these networks, this approach was found to provide a more comprehensive overview of the literature on the topic.

3. Experimental behaviour

To evaluate the accuracy and suitability of different modelling approaches, it is deemed necessary to understand the expected mechanical and dynamic behaviour of wrinkled and crumpled structures. This section therefore briefly reviews the wrinkle-to-crumple transition and its implications for structural dynamics.

3.1. Wrinkle-to-crumple transition

The formation of wrinkles, crumples, folds, and creases is a fundamental response of thin-sheet structures subjected to compressive stresses. Such stresses can arise in a wide variety of loading and geometric configurations, including sheared, stretched, pressurised, or inflated systems. Because the terminology used for these surface instabilities is not entirely standardised, the following discussion adopts pragmatic working definitions that are consistent with the cited literature.

Thin sheets are comparatively stiff in in-plane compression, and therefore tend to relieve compressive stresses by buckling out-of-plane, ultimately minimizing energy by trading membrane energy for bending energy. *Wrinkles* provide an effective mechanism for this relaxation: they are small-wavelength undulations that typically form in a spatially homogeneous manner around a slightly sheared or compressed region. Wrinkling usually remains within the elastic regime and is therefore largely reversible once the compressive load is removed. [1, 10]

When geometric confinement is increased, Timounay et al. [10] showed that *crumples* arise as the generic evolution of wrinkles. A small number of smooth wrinkles sharpen into stress-focusing ridges and vertices, while other wrinkles disappear, see Figure 2. In this process, Gaussian curvature and material stress are reduced over most of the sheet, with stresses and (optionally plastic) deformations becoming highly localised near the edges of individual crumples.

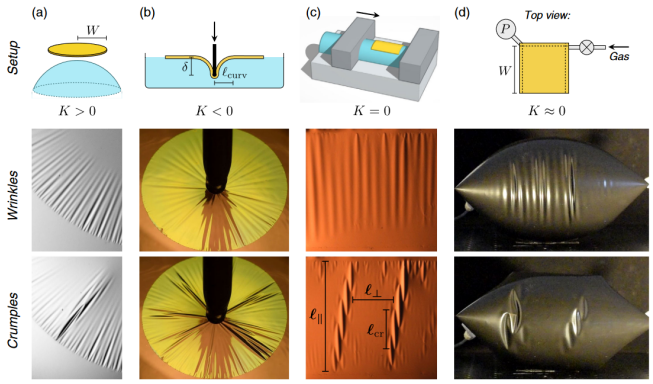

Figure 2: Wrinkle-to-crumple transition in a wide range of systems. The formation of stress-localising crumples from homogeneous wrinkles is a generic response to increasing confinement and compressive stress [10].

Folds can likewise be viewed as a further evolution of wrinkling, characterised by localised, deep surface valleys. In the extreme, *creases* are formed, characterized by self-contact and extremely sharp ridges. Although these terms are sometimes used interchangeably with crumples, the terms folds and creases are more commonly employed in the context of stiff films bonded to soft substrates or floating on liquids [11]. Various studies have attempted to predict which type of instability (wrinkling, folding, creasing, or crumpling) will emerge based on generalised system properties, with the aim of characterising the wrinkle-to-crumple transition. [10, 15]

Various variables can affect the evolution from a wrinkled to a crumpled structure. For example, the loading rate influences the ratio of elastic to plastic deformation [2]; as a fast deformation does not allow for much material relaxation, the resulting structure is more randomly folded (high entropy) with sharper plastic ridges [2]. Furthermore, for highly compacted crumpled sheets the *packing density* reaches a limit where the network of self-contact and interlocking stiffens the system, despite the fact that a significant part of the structure is still air [2]. In various situations, there exists a power-law correlation between the compaction force and this final packing density. Finally, the elasto-plastic behaviour of materials can vary; aluminium sheets are one example of a system that can be readily plastically creased [2, 4].

3.2. Structural dynamics of wrinkling

Although not available for crumpled structures, several experiments have been performed on the vibrational behaviour of wrinkled membranes compared to their unwrinkled state.

Photogrammetry is a method where multiple high-resolution cameras are used to triangulate a 3-dimensional map of a system's wrinkled configuration. These measurements have been used to compare computational findings with experimental data [16–18]. If one is also interested in the modified dynamics caused by wrinkling, *Doppler-interferometry* can be used. These studies make use of scanning laser vibrometers to capture the displacements of many points on the surface, utilising the fast Fourier transform to calculate a collection of mode shapes with corresponding eigenfrequencies [1, 19].

In general, wrinkles have been found to greatly influence the dynamics of systems in a variety of situations [16, 20]. One often encounters new low-frequency mode shapes with strong undulations localised to the wrinkled region, albeit with low modal mass. The global mode shapes with high modal mass, also present in the unwrinkled configuration, are affected as well. Depending on the interaction of a particular mode with the wrinkled region, the eigenfrequencies found are often several percent lower. This is commonly explained via the lower stiffness associated with the bent wrinkled structures [16, 20].

As performing experiments in a perfect vacuum environment is a difficult task, one should be aware of the effects the surrounding air can have on the vibrational behaviour of membranes. Kukathasan and Pellegrino [21] found that there exists a coupling between a *non-wrinkled* membrane and the surrounding layer of air, with the thickness of this layer dependent on the mode number. The air acts as an additional non-structural mass term which causes the eigenfrequencies to decrease and mode shapes to change. As more air mass is in play for the lower frequency modes, this effect is less pronounced at higher frequencies. The results found for their in-air model were subsequently backed-up by experimental data. In a follow-up study using the same in-air computational procedure on a *wrinkled* membrane, Kukathasan and Pellegrino [19] found the same decrease in eigenfrequencies. Also notable is that the vacuum modes with small modal mass, where only the wrinkles vibrate, were removed by the added mass of air.

Puzzled by the high modal damping values (3-10%) found by another experiment on a wrinkled sun-shield [22], Kukathasan and Pellegrino [19] also searched for other sources of damping besides material damping. They indeed found non-linear behaviour at larger shaker excitations where the apparent damping would increase. This was found to be caused by energy scattering into the excitation of harmonic modes at multiples of the actuation frequency. This hardening non-linearity would lead to an increased apparent damping of the system with increasing excitation amplitudes.

Hossain et al. [1] observed the dynamics of a systematically creased tensioned membrane. Here the change in eigenfrequencies compared to the pristine configuration depended on the mode and number of creases. It was argued that the mode dependence relied on the specific interaction of the crease with that mode, a feature that is also seen with wrinkles. Some modes of vibration may stretch the crease, decreasing the stiffness and thus decreasing the eigenfrequency. Other modes may bend the crease, leading to the opposite reaction.

In another study a wrinkled inflated arch was subjected to a transverse tip load by Wang et al. [20] under various internal pressures. They found the wrinkling characteristics to be sensitive to this inflation pressure, which in turn had an effect on the vibrational behaviour. As expected, for pressures leading to more wrinkling a larger decrease in eigenfrequencies was found, especially for mode shapes interacting with the wrinkled regions.

In conclusion, it may be assumed that wrinkles in any structure will have a considerable effect on the resulting mode shapes and eigenfrequencies. Although highly dependent on the system and wrinkling configuration, the reduced stiffness due to the created undulations tends to decrease the eigenfrequencies of the global modes. Unfortunately, little is known regarding the dynamics of crumpled structures, or how these buckling instabilities affect vibrational transmissibility.

4. Computational challenges

The static and dynamic simulation of post-buckled thin structures poses some particular challenges compared to stiff solids. The most pressing computational obstacles often discussed in the literature are listed, roughly in order of priority.

1. **Under-constrained buckling**
   For highly under-constrained buckling structures the solution path often becomes unstable. These systems show an extreme amount of bifurcation points associated with the many configurations in which the sheet can buckle. Each of these bifurcations marks an instability leading to a (near-)singular stiffness matrix [23]. Traditional computational methods aim to iteratively converge to the equilibrium solution of a system by implicitly solving the static or dynamic system of equations. For (geometrically) non-linear systems, these Newton-Raphson (NR) type integration schemes base their search direction on the locally linearised system stiffness matrix. By taking the inverse of this stiffness matrix, the appropriate step in the solution space can be found. However, with the use of implicit schemes this near-singular stiffness matrix can lead to instability and slow convergence. Therefore, measures must be taken to better condition the stiffness matrix, while also carefully traversing the sudden snap-throughs and snap-backs present at the bifurcation into buckling [24, 25].

2. **Small features**
   As the average size of wrinkles and crumples gets smaller with lower bending stiffness, the number of wrinkles in thin sheets can quickly become substantial. The mesh density needed to correctly capture the intricate out-of-plane geometry is roughly inversely proportional to the expected size of the wrinkles [24]. This decrease in element size will subsequently lead to an increase in computational time, even if the global out-of-plane behaviour may not be overly complicated. Therefore, measures which can lessen the need for high element densities are often sought after.

3. **Elasto-plasticity**
   The formation of folds and creases can lead to the need to consider material plasticity effects. In ridges with extreme bending, plastic deformation may relieve some bending stress by plastic yielding, leading to a softer response. The simulation of highly elasto-plastic materials such as aluminium sheets would benefit from such a non-linear material model [2]. However, it should be noted that the intended use case of the present study does not concern this extreme degree of compaction and will therefore not focus on the particular implementations of elasto-plastic materials models as seen in literature.

4. **(Self-)avoidance**
   For highly compacted crumpled structures, the self-contact of a sheet with its other faces starts to play a larger role. The physical fact that a crumpled sheet should never intersect itself is often coined *self-avoidance* in computational mechanics [4, 26, 27]. However, the computational cost to make sure these laws are respected is often substantial. Therefore, in many cases *phantom* sheets are considered where collision is neglected entirely. Nevertheless, one should make sure to mind the effects of collision of a sheet with itself or other objects, as the introduction of (self-)avoidance has shown to affect the number and length of crumpling ridges predicted [2]. Again, as the case study relevant to the present study does not entail this extreme degree of compaction, collision detection methods will also not be covered elaborately.

5. Discretization methods

The first step in the creation of any computational model is to decide on the appropriate spatial discretization method. Various techniques allow complex geometries to be segmented into smaller elements, making their collection easier to solve. The most familiar method to most engineers will be shell-based finite element analysis, but other recent methods have shown their capability in the modelling of thin sheets. Examples include spline-based isogeometric analysis, membrane-based tension field theory, and particle-based discrete element analysis. These specialised methods will be explained and compared to finite element analysis based on their characteristics relevant to the (dynamic) simulation of buckled thin sheets.

5.1. Finite element analysis

Finite element analysis (FEA) is the most traditional method for the simulation of all types of mechanical problems. Typically, buckling thin sheets are modelled using shell formulation capable of six degrees-of-freedom (DoF) in order to consider large displacements and rotations [28]. The static equilibrium can then be solved using geometrically non-linear iterative solvers, available in numerous commercial finite element software. Linearised modal analyses can be performed on the resulting buckled geometry and system matrices to obtain dynamic insights. For the purposes of this review, FEA will be used as a benchmark to compare the other discretization methods in this section to. Also, it should be assumed that referenced studies showcasing advanced solution procedures in section 6 make use of FEA unless otherwise stated.

5.2. Isogeometric analysis

In a landmark 2005 paper by Hughes et al. [29], the framework of isogeometric analysis (IGA) was proposed to bridge the gap between computer-aided design (CAD) and traditional FEA software. As is customary in CAD software, the geometry of a body in IGA is represented using *non-uniform rational B-splines* (NURBs), defined by control points [30]. This method eliminates the time needed to convert a spline-based CAD geometry to a Lagrangian node-based discretised mesh suitable for FEA. However, in practice analysis-aware geometric modelling of the part is needed to create so-called *watertight* models [31], as the boolean operations and trimming often used in CAD cannot be used directly. One needs to create the model out of several topologically rectangular *patches*, stitched together with non-smooth connections. This fact introduces the need for some additional precaution during design to make sure non-symmetric stitches do not influence results.

In many aspects, the goal of simulation stays the same as in traditional FEA: minimizing the residual between internal and external forces, but now with the solution represented as a vector of spline control-points instead of nodal displacements. As the spatial discretization is in principle decoupled from a solution procedure, the techniques of section 6 are also applicable here. Because IGA is still in its infancy compared to FEA, the preference of one method over the other is a highly debated topic between researchers. However, the spline-based structure does incur some unique advantages relevant to the simulation of thin sheets in particular.

The first difference to FEA is the allowance for simulation using exact geometries. As portrayed in Figure 3, a geometry does not suffer from discretisation errors when build using NURBs, with smooth splines connecting the geometry between *knots*. As there is no need to approximate the geometry using line-elements between nodes, performance improvements may be applicable when considering fine structures. In his introductory paper Hughes et al. [29] already notes the analysis of thin shells in particular as a field notoriously sensitive to geometric imperfection.

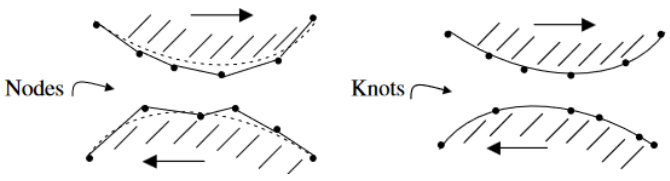

Figure 3: Approximated node-based finite element geometry (left) and exact knot-based isogeometric geometry (right). [29]

To test this notion Oesterle et al. [32] performed a buckling analysis on an axially compressed thin-shell cylinder. It was found that the correct analytical buckling mode shape was obtained using far less total DoFs using IGA compared to various FEA shell representations. For example, for the buckling cylinder the analytically predicted first buckling mode was reproduced using a mesh with one to two orders of magnitude less DoFs compared to the FEA representations. The effect seemed particularly pronounced if numerous critical buckling bifurcations appeared within a small range of load levels.

However, an accompanying analysis was performed [32] to artificially add the geometric imperfections back into the IGA model. By matching the size of the non-smooth topologically rectangular patches in IGA to the element sizes in FEA, the same approximated discretization was obtained. Interestingly, this did not seem to change the results much and the researchers concluded that the geometric exactness of IGA is not the driving force behind the apparent reduction in the required DoFs.

The second advantage of IGA may provide us the explanation for IGA's faster mesh convergence: two strategies to reach convergence in FEA are *h*-refinement, simply increasing the density of the discretized elements, and *p*-refinement, increasing the polynomial order of the basis function of elements. Using *p*-refinement allows for the representation of more complex solution fields using the same number of elements. However, in FEA the polynomial basis function will always only maintain C^0 continuity across element boundaries. A fundamentally new refinement method introduced in IGA allows the user to also increase the order of continuity between elements, at least within patches. These splines with additional smoothness due to *k*-refinement [29, 31, 32] are intuitively appealing for situations in which solutions are very smooth, such as vibrations of structures and wrinkled thin shells. This would subsequently lead to high accuracy per DoF for these applications. Another advantage of *k*-refinement is the possibility to eliminate *optical branches* in the eigenfrequency spectrum for modal analysis. These optical branches are fundamentally inaccurate spikes and outliers of eigenvalues apparent in the second half of the frequency spectrum, seen due to a side-effect of FEA's C^0 continuity [31, 33, 34].

Another benefit for thin sheets in particular is the straightforward implementation of the Kirchhoff-Love (KL) shell theory. Due to the spline's C^1 or higher continuity the curvature of the surface can be used directly to model the bending stiffness, without the need to calculate separate rotational degrees of freedom like in FEA. These KL-shells do also not suffer from the same membrane locking effect as pure displacement shell formulations due to their inter-element continuity, preventing underestimations of deformations and stress oscillations for small-thickness elements [35].

Of course, the use of IGA over FEA also carries multiple downsides. Perhaps the most pressing one is the relatively limited software available as compared to the numerous elaborate FEA packages. Nevertheless, IGA has been implemented in open-source packages such as *G+Smo* [36] or as experimental features in larger FEA software, namely *ANSYS LS-Dyna* [37] or *Altair Radioss* [38]. Performance improvements are also certainly not guaranteed, as the higher degree of conti-

nuity between elements leads to larger overlap between basis functions and thus system matrices with increased bandwidth [31]. Despite k-refinement generally allowing for reduced mesh sizes, the actual improvement in computational time highly depends on the geometry and analysis-type [39] and is not yet well-understood. For example, Li et al. [37] found FEA to be faster in principle in the case of a compressed solid cylinder, but IGA did scale better on a higher number of computational cores. Still, thin shells are considered one of the more interesting applications due to the natural implementation of Kirchhoff-Love shell theory and the smooth nature of buckling shell problems.

5.3. Tension field theory

Tension field theory (TFT) is a wrinkling approximation method often used for gossamer (extremely thin) structures in aeronautical applications, such as deployable antennas, solar sails and sun-shields [12]. First proposed by Wagner [40] in 1931 for the analysis of sheet metal girders, the theory assumes the creation of a *tension field* for membranes under shear stresses. Here, a membrane is defined as a sheet of infinitesimal thickness and therefore negligible bending stiffness. Wrinkling will therefore always be preferred to compression, leading to a structure with no compressive stresses and uni-axial tension along the wrinkle lines. Tension field theory refers to the collection of methods to replicate this behaviour by removing compressive stresses without modelling the small features of the complicated wrinkled geometry explicitly, focussing on the resulting average plane strains. [41]

The rich history of TFT begins with various analytical formulations such as the *variable Poisson's ratio* method introduced by Stein and Hedgepeth [42]. Here, the compressive stresses are released by allowing for the over-contraction of wrinkled parts of the membrane via a variable Poisson-ratio. Another influential contribution by Pipkin and Allen [43] formulated wrinkling as an energy-minimization problem: by introducing the *relaxed strain energy density* the membrane was allowed to perform a 'free' zero-energy contraction along the compression direction.

With the advent of FEA, Roddeman et al. [44] were the first to implement TFT in simulation using a modified deformation gradient tensor and membrane-elements. In order to numerically predict which elements these wrinkling modifications should be applied to, a new procedure was introduced: occasionally referred to as the *iterative membrane properties* (IMP) procedure [19], the general goal is to iteratively determine which regions of the membrane should be wrinkled via a *wrinkling criterion*, and subsequently applying a *wrinkling model* to that region. A wrinkling criterion often determines if an element should be considered to be in a taut, wrinkled or slack state based on the in-plane stresses and strains found in the previous iteration. The most accepted method looks at the major and minor principal stresses and strains, the so-called mixed (stress-strain) criterion [44, 45]:

- **Taut** ($\sigma_{min} > 0$)
  Bi-axial tension: use standard membrane element stiffness matrix.
- **Wrinkled** ($\sigma_{min} \leq 0$ and $\epsilon_{max} > 0$)
  Uni-axial tension: apply wrinkling model to modify membrane element stiffness matrix such that compressive stresses are removed, resulting in zero stiffness in the compression direction.
- **Slack** ($\epsilon_{max} \leq 0$)
  Bi-axial compression: set membrane element stiffness matrix to zero, allowing for a zero stiffness contraction as needed.

Various formulations of a wrinkling model have been implemented, such as the use of a variable Poisson's ratio or modified deformation gradient. However, most of these methods have been proven to be (mostly) mathematically equivalent by Miyazaki [46]. Alternatives to IMP methods have also been created, for example by the minimization of compression using a *penalty parameter modified material* (PPMM) method [47] or via energy-minimization using Pipkin's relaxed strain energy density model [45]. The most appropriate method often depends on the available software, as many implementations use custom user subroutines in FEA packages such as *ABAQUS* or *ANSYS*. TFT has even been demonstrated by Verhelst [31] using isogeometric analysis in G+Smo, see Figure 4. In this figure it can be seen that the general outline of a stretched and twisted thin cylinder is preserved in the TFT-approximation by predicting taut and wrinkled regions. The most important unifying feature of any wrinkling model is that the stress in the principal direction of compression, normal to the wrinkle lines, vanishes by allowing a zero-stiffness contraction.

Figure 4: Stretched and twisted thin cylinder using Neo-Hookean material in isogeometric analysis [31]. Left figure shows the full Kirchhoff-Love shell model, while the right figure shows a wrinkle approximation based on tension-field theory. The black regions denote taut sections, while grey denotes a wrinkled region where a wrinkling model is defined based on Roddeman et al. [44]. While the shape of wrinkles is not calculated using the approximation, it should be noted that the general outline of the right structure is consistent with the left case.

Some advanced techniques have been devised to help numerical stability for the use of TFT. Rossi et al. [24] use a variable penalty factor to smoothen the transition between states, such that the system does not land in a slowly converging loop by constantly switching states. Liu et al. [48] also use penalty factors in a PPMM method to allow the system to exhibit small but non-zero compressive stresses, such that the non-singularity of the stiffness matrix is retained. Miyazaki [46] notes that this also leads to a better model for a finite thickness physical sheet, as the small compressive stresses capture the real irreversible deformation around wrinkles

as they depend on the deformation path. Taylor et al. [49] decide to skip the inversion of the stiffness matrix entirely by using a dynamic relaxation procedure, to be discussed in section 6, combined with Pipkin's relaxed strain energy density.

In general, TFT has been found to be an effective alternative to full shell-based membrane models. As there is no need to pick mesh sizes small enough to model the individual small-wavelength wrinkles, significant reductions in computational effort can be achieved. Many examples have proven to provide average plane strains consistent with shell-based FEA while using only a fraction of the mesh fidelity, particularly in systems with pre-tensioned or inflated membranes [41, 44]. For example, Rossi et al. [24] showcase that the application of TFT can provide the same results for an inflated airbag as full shell simulation using only 236 instead of 4802 elements. However, it should be noted that TFT is only applicable to very thin sheets and provides us no information on the actual amplitude, wavelength, or distribution of wrinkles. Nevertheless, efforts have been made by Iwasa [17] to compare 3D photogrammetry of a wrinkled membrane to computational results to find the relation between predicted plane shrinkage and wrinkle size.

While most research into TFT focuses on the static solution of wrinkled structures, attention has been devoted into expanding these models into structural dynamics. Comparing wrinkled membrane configurations analysed with and without a TFT algorithm, Hossain et al. [47] found that the application of TFT does indeed influence the resulting eigenfrequencies found. For the shell simulation, the appearance of wrinkles decreases the eigenfrequencies compared to the unwrinkled model. With the TFT algorithm then applied eigenfrequencies increase slightly, attributed to the change in geometric stiffness due to the minimization of compressive stresses. It should be noted that this behaviour is dependent on the particular vibrational mode, as not all modes share the same modal participation factor in the wrinkled region. Hossain et al. [1] used a PPMM wrinkling model, along with a local non-linear material model to model creases, to numerically study the modal dynamics of the creased system mentioned in section 3. They found satisfactory eigenfrequencies within 10% margin of error for both the single- and double-crease case.

Another study by Johnston and Brodeur [50] found less clear correlations. Here a shell-based, TFT-based and physical scale-model of a sun-shield were compared on their vibrational modes. While the eigenfrequencies of the dominant mode were similar, the two computational models differed significantly in the total number of modes, modes shapes and effective masses. More discrepancies were found comparing with the physical model, such as the appearance of more slack regions and asymmetries than predicted in the numerical studies. As the slack regions carry no internal stresses and behave like rigid material, their deformation is highly influenced by the deformation of nearby wrinkles. TFT is often found to have difficulty replicating these slack surfaces, as the wrinkles themselves cannot be simulated [17].

5.4. Discrete element analysis

Due to an emerging interest in the use of highly compacted sheets as a new type of metamaterial [2–4], modelling techniques traditionally used in the field of computer graphics are being adapted to analysis in mechanics. The overarching strategy of discrete element analysis (DEA), also referred to as 3D mass-spring systems [51], is to model a sheet as a collection of mass particles with spring-dampers connecting them to each-other.

Similarly to the simulation of cloth in computer animation or atomic structures in molecular dynamics, a thin sheet can be discretised into a collection of small masses. These particles, often point-masses or rigid triangles, connect to their neighbours via virtual springs and dampers. Andrejevic and Rycroft [27] performed such a simulation of an elasto-plastic thin sheet using a discretization of point-mass nodes, see Figure 5. By translating traditional elasticity models from continuum to discrete strain energy densities, the appropriate parameters can be found for the in-plane spring-dampers connecting these nodes. Bending stiffness was applied using a penalty function on the misalignment of the normal vectors of adjacent triangles, again aiming to imitate continuum bending rigidity. Plasticity can be replicated by adding a constant value to this bending penalty function to specify a non-flat shape as the resting angle.

Contact-detection and self-avoidance is a particularly well-developed subject in computer animation for fabrics and cloth. The detection method used by Andrejevic and Rycroft [27] assigns all nodes into blocks. During simulation all nodes in the blocks within the local search space of a particular node are checked for possible contact. If contact is detected, one method is to correct the position and velocity of the interacting nodes according to conservation of momentum. However, this method can become problematic if multiple contacts are present at once, as considering one contact may cause further self-intersection. Another method relies on penalty functions to separate the particles with stiff local springs, which proved more robust for the researcher's purpose.

Andrejevic and Rycroft [27] note the disparity in time scales between the slower large-scale deformations as opposed to the sudden localised buckling and snap-through events. They implemented a hybrid integration scheme to adaptively switch between an implicit quasi-static formulation and a fully explicit dynamic formulation. In the quasi-static formulation accelerations of nodes are approximated to zero, and the subsequent differential-algebraic system of equations is implicitly solved via a version of Newton's method. If large changes in local velocity are detected, for example during rearrangement of ridges and vertices by buckling or during abrupt self-contact, the solver switches to the fully dynamic formulation. The buckling is now explicitly solved

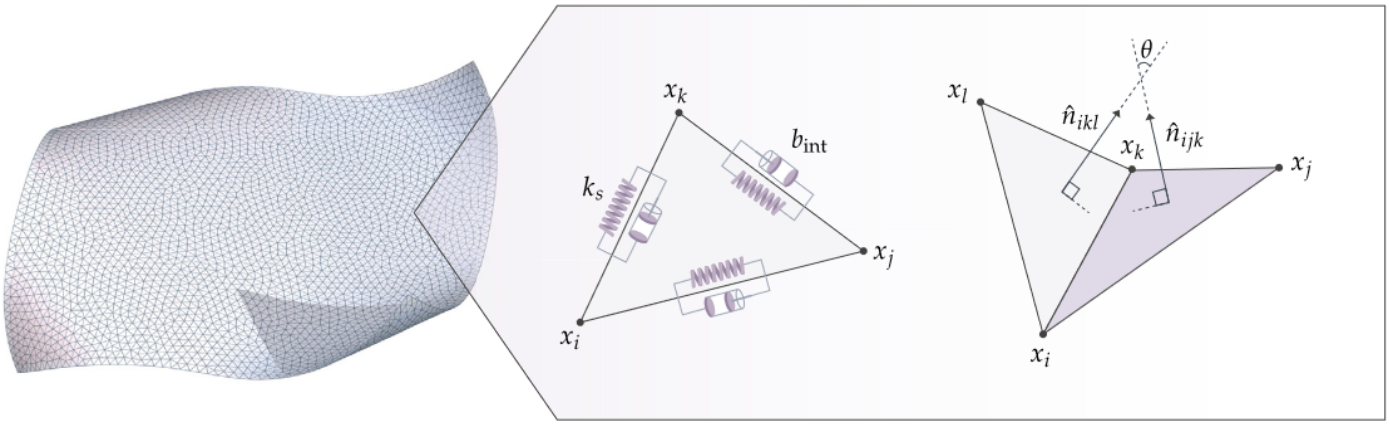

Figure 5: Microscopic model of a discretised sheet defined by point-masses in discrete element analysis [27]. In-plane stretching is governed by spring-dampers between neighbouring nodes. Bending stiffness is defined via a penalty factor on the misalignment of normal vectors between adjacent triangles.

using a Runge-Kutta integration method with adaptive step-control. Using this method the researchers were successful in the simulation of highly compacted sheets, finding the same logarithmic crease length growth as found in experiments [2, 4].

A common concern in DEA literature on stiff thin sheets is the issue of *bending locking* [52]. As bending can only occur along the vertices of adjacent triangles, sharp bends not perfectly aligned with these directions can only be achieved via the bending of multiple other ridges. When using a coarser mesh this fact leads to an artificial stiffness to bending and unrealistic bending behaviour. Narain et al. [52] used an adaptive re-meshing procedure to iteratively refine their triangle-based discretization to create edges aligning with bending. For stiff thin shells they found that jittering would occur when simply refining the mesh by splitting the existing triangles. For this reason, a dynamic projection method was introduced to interpolate node forces instead of node positions, such that the dynamic equilibrium before and after re-meshing is preserved. The researchers found adaptive re-meshing to be an effective way to reduce mesh density while being able to resolve fine features and large flat regions simultaneously.

Another way to prevent bending locking is by simply decreasing the stiffness of the bending springs (penalty factors). However, this would make the material appear softer than may be desired. Jin et al. [53] replaced the equality constraint on the triangle edge lengths with an inequality constraint to allow some element compression, such that this slight compression can function as a surrogate model for bending modes that would otherwise not be representable by the mesh. The inequality constraint was implemented using a penalty function (barrier method) and an optimization algorithm using Newton steps and line searches to solve for the equilibrium shape. This is an example of how form-finding problems in DEA are often formulated as optimization problems, with an energy function consisting of bending energies and penalty parameters to be minimized [54].

The discretised nature of DEA leaves one major drawback: many concepts found in continuous models that are often used in dynamic analyses are absent. Lacking any form of traditional system matrices, the inability to perform eigenvalue analysis rules out any modal and harmonic analyses. This only leaves explicit time-domain simulation to be used for structural dynamics. Due to the need for minuscule time-steps at higher frequencies, this would be costly to simulate and has not been attempted to the best of the author's knowledge. Common tools in computer graphics are also not designed for strict accuracy in the prediction of stresses and strains, as they are mainly designed for efficiency and visual realism. Only more recent studies provide any basic comparison to FEA in mechanical accuracy on simple problems [51]. Due to these two factors, DEA is not (yet) considered a complete tool for the structural dynamic analysis of thin sheets, and will be subsequently disregarded in following discussion.

6. Solution procedures

When a spatial discretization method and other model definitions have been established, the residual between external and internal forces can be calculated. Regardless of the discretization used, this residual and the corresponding solution vector can be used in a generalized non-linear solution procedure in order to integrate the residual to zero and find equilibrium. In this section, the most commonly used advanced numerical solution procedures relevant to buckled thin sheets will be covered, namely the introduction of initial perturbations, dynamic relaxation, arc-length methods, modal reduction and sensitivity analysis.

6.1. Initial perturbation

Initial perturbations are often applied to sheets in order to nudge the element nodes from their *perfect* initial condition, such that the initiation of buckling becomes easier. Without these perturbations, the structure would not prefer any one way to buckle and would slowly approach a buckling bifurcation with increasing load [55]. These buckling bifurcations are associated with singularities in the system stiffness matrix, which in turn contribute to stability problems for traditional implicit solvers. By applying small perturbations the perfect bifurcations can be smoothed and thus more easily passed without full singularities forming [55].

In general two methods exist to apply initial perturbations. The pseudo-random *direct turbulence* method uses randomly assigned force perturbations on the nodes, setting the net force on the total body equal to zero in order not to influence the system behaviour [16, 56]. A more commonly used method is to perform a linear buckling analysis on the initial configuration in order to calculate the first (few) buckling mode(s) [57, 58]. This *scaled buckling modes* method uses a scaled superposition of these modes to subsequently perturb the nodes. This buckling mode version of perturbation would theoretically cause the structure to buckle via the 'ideal' buckling path and is therefore repeatable. However, one could argue that the turbulence method is more accurate to the imperfect systems we find in reality, and could also be made repeatable by starting the random number generator with a consistent seed. In either case, the perturbations are removed shortly after the initial buckling in order not to influence the final result by too much. Liu and Cai [57] suggest a perturbation of 1%-100% of the membrane thickness as a middle-ground for not making the initial stage of buckling too slow while not influencing results.

6.2. Dynamic relaxation method

The dynamic relaxation method (DRM) is an explicit iterative algorithm for the static analysis of structures. The method avoids the calculation of a near-singular stiffness matrix by the use of an explicit scheme. First given this name by Day [59], the static solution is considered as the limit or steady-state part to the transient response of the system. To illustrate this, the static solution can be written as the solution of the system of differential equations

$$\mathbf{f}(\mathbf{u}, \dot{\mathbf{u}}) = \mathbf{p}, \tag{1}$$

with $\mathbf{f}$ being a generally non-linear vector function representing the internal forces, dependent on the nodal displacements $\mathbf{u}$ and its time derivative $\dot{\mathbf{u}}$, and $\mathbf{p}$ being the external forces. Note that Equation 1 can be written in a linear form where the left-hand side is converted to a product between the stiffness matrix K and displacement vector $\mathbf{u}$, to be solved algebraically. However, in the general non-linear case the solution can be iteratively solved for by integrating the solution via an implicit Newton-Raphson (NR) type method using the inverse of the locally linearized stiffness matrix K [60].

Alternatively, in DRM the equation is expanded by turning it into the damped dynamic equation

$$\mathrm{M'}\ddot{\mathbf{u}} + \mathrm{C'}\dot{\mathbf{u}} + \mathbf{f}(\mathbf{u}, \dot{\mathbf{u}}) = \mathbf{p}, \tag{2}$$

with M' and C' respectively the fictitious mass and damping matrices. This is a problem in the *pseudo-time* domain, which can be integrated using central finite difference methods [55, 60].

Note that in the absence of any nodal velocities $\dot{\mathbf{u}}$ or accelerations $\ddot{\mathbf{u}}$, Equation 2 reduces into the same form as Equation 1. Thus it can be seen that the static solution may indeed be regarded as the limit of the damped dynamic response. As the fictitious mass and damping matrices play no role in this final solution, they can be artificially chosen based on heuristic rules with the purpose of a fast but stable convergence. While various methods to construct the mass matrix exist, a popular way introduced by Underwood [61] is to choose a diagonal mass matrix based on Gershgorin's circle theorem. The diagonal mass elements are based on the corresponding entries in the effective stiffness matrix, and may be updated multiple times during iteration via the equation

$$m_i = \frac{\lambda \Delta t'^2}{2} \sum_j |\mathrm{K}_{ij}|, \tag{3}$$

where m_i is the mass at node i, $\Delta t'$ is the fictitious time-step and λ an adjustable parameter used to improve stability. The sum is taken over the absolute entries of the local tangent stiffness matrix in all Cartesian directions j. The use of (a version of) Gershgorin's theorem ensures an optimum ratio between the minimum and maximum eigenfrequencies of the system [58, 62, 63].

For the fastest convergence possible, the fictitious damping term should lead to a perfectly damped system. In practice, *viscous* damping like in Equation 2 is usually avoided as a trial analysis is needed to estimate the lowest eigenvalue via Rayleigh's principle [62]. Instead, *kinetic* damping is regularly used [58, 60, 64]: setting C' = 0 in Equation 2, the damping behaviour is instead artificially replicated by studying the systems total potential and kinetic energies. For a conservative mechanical system, these two energy types alternate in their magnitudes. When the kinetic energy is at its maximum, the potential energy will be at its minimum, with this minimum corresponding to the state most resembling equilibrium. When using kinetic damping, the geometry of the system is frozen at this peak of kinetic energy. By constantly resetting the velocities to zero and restarting dynamic simulation from this frozen geometry, a simple yet efficient artificial damping behaviour is introduced, see Figure 6 [65].

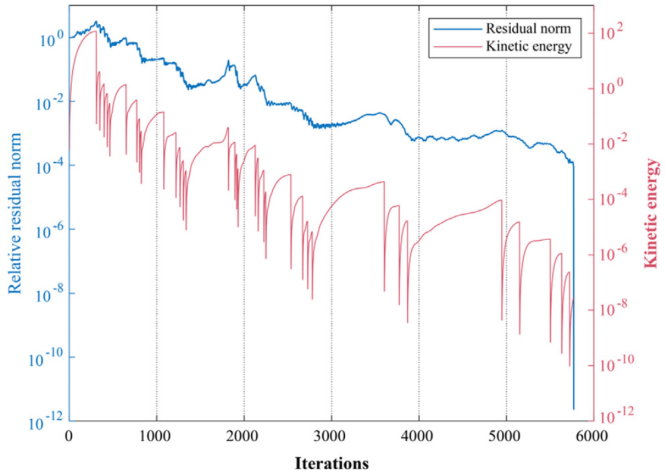

Figure 6: Typical histories of relative residual norm and kinetic energy of a system with kinetic damping. At every peak in kinetic energy the nodal velocities are reset to zero, leading to a damping effect without the need for viscous terms. The residual norm can be seen to decrease, with a sharp decline when the dynamic relaxation scheme switches to implicit Newton-Raphson integration in its final iterations [65].

DRM is particularly well suited to buckled thin sheets, as there is no need for an inversion of the often near-singular stiffness matrix due to its explicit nature. Since all quantities can be treated as vectors, the DRM is easily programmable and has low storage requirements, while also being ideal for systems with highly non-linear geometric and material behaviour [25].

Lee and Youn [63] successfully used viscously damped DRM together with a TFT-based discretization to simulate a twisted annulus and an inflated airbag. These results were used as benchmarks by Nakashino et al. [65] for their expanded model based on IGA and kinetic damping. Interestingly, both studies also perform some implicit NR-integration after their DRM procedure to make the final steps towards equilibrium, see Figure 6. This showcases the effectiveness of using DRM for the general form-finding for buckled structures, which may be combined with implicit solvers for the final steps to reach greater precision.

6.3. Arc-length method

Incremental NR-procedures are often adopted for problems with highly non-linear boundary conditions which lead to large forces and deformations. In these quasi-static methods the forces or displacements are slowly increased from zero to their final value, while equilibrium is continuously calculated. Depending on the independent variable in these procedures this procedure is respectively referred to as *load-controlled* or *displacement-controlled* time-stepping. For post-buckling analysis in particular these methods are essential to traverse the highly non-linear and unstable behaviour near buckling bifurcations, and thus also of importance to the simulation of crumpled sheets.

Buckling bifurcations lead to the creation of multiple stable and unstable branches. Referring to Figure 7 [66], this fact may lead to one of the most difficult issues for either load-control or displacement-control to solve: the creation of each additional wrinkle or crumple corresponds to a bifurcation where localised *snap-through* (BD in Figure 7) or *snap-back* (GI in Figure 7) may occur. the buckling path is illustrated as a non-linear relation between loading and displacement. It can be observed that the stable branch after a bifurcation point may lead to a (temporary) reduction in either load or displacement. Load-control and displacement-control cannot handle these bifurcations effectively and will suddenly snap to another part of the branch, or even not find any continuation at all [67]. It should be noted that Figure 7 is only a 2D simplification of the multidimensional load-deflection space.

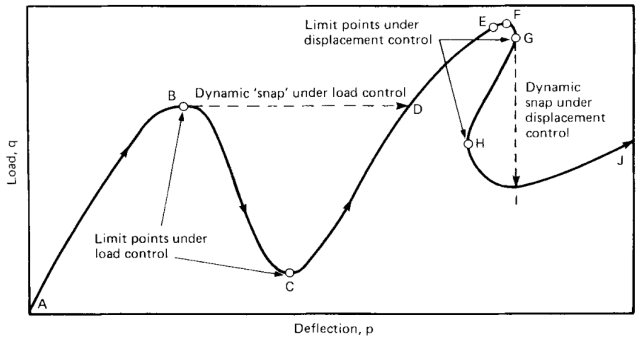

Figure 7: Buckling path plotted as non-linear function of load and displacement [66]. Snap-through (line BD) and snap-back (line GI) events can cause large jumps in the solution for traditional load-controlled or displacement-controlled time-stepping.

The solution for this problem is to combine the two paradigms of load-control and displacement-control in so-called *arc-length methods* (ALM). The main two methods were introduced by Riks [68] and Crisfield [67], both based on the addition of a constraint on the displacement and load increments to stay inside a defined hypersphere of certain arc-length [69]. For both methods a prediction step of this arc-length is taken tangent to the current position on the buckling path, see point A in Figure 8. From this predicted solution (B in Figure 8) the Riks method defines a hyper-plane (BC in Figure 8) normal to the prediction tangent, to be traversed via NR-iterations. Alternatively, Crisfield's method constrains the NR-iterations to the hyper-sphere (BD in Figure 8) or the hyper-cylinder tangent to the loading parameter (BE in Figure 8).

The Crisfield method is considered to be somewhat more robust, but for ever more non-linear buckling paths, a related but less popular method based on the *normal flow* algorithm could also be considered [69]. Here, the NR-iterations are forced along a path normal to the so-called Davidenko flow curves. These curves can be seen as the contour curves of constant perturbation ($\mathbf{f}(\lambda, d) = \delta$), positioned along the solution curve ($\mathbf{f}(\lambda, d) = 0$). This ensures the fasted possible path from the prediction point to the actual buckling path.

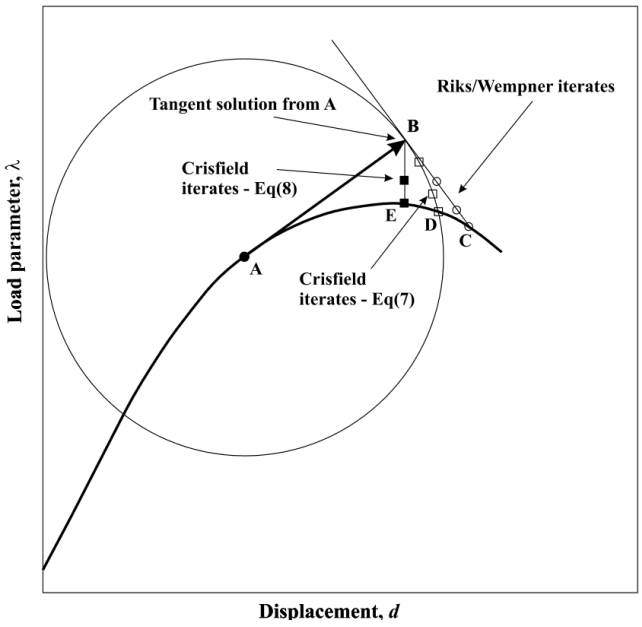

Figure 8: Arc-length method based on Riks' [68] and Crisfield's [67] methods. A prediction increment of certain arc-length is taken along the buckling path tangent. From there Newton-Raphson iterations are taken to find the real equilibrium point on the buckling path, either by walking normal to the prediction tangent (Riks) or along the hypersphere defined by the arc-length (Crisfield). [69]

In most cases DRM and ALM are used as two alternative methods for solving highly non-linear systems. For example, the analysis by Liu and Cai [57] shows ALM to come to a similar result as DRM for a tensioned membrane. However, Lee et al. [64] demonstrated an explicit ALM using dynamic relaxation with kinetic damping. Here, the representation of the external forces $\mathbf{p}$ in Equation 2 is expanded using an incrementally increasing loading parameter $\lambda^{t+\Delta t}\mathbf{p}_0$ (note that C'= 0 as kinetic damping is used). The loading parameters $\lambda^{t+\Delta t}$ can be subsequently constrained via Crisfield's hyper-cylindrical arc-length constraint. A *total displacement* constraint was also tested, where the arc-length is calculated centred around the initial configuration instead of the current configuration. Here, step increments are not taken tangent to the current position on the buckling curve, but in the direction through the origin to the current position. For both methods the researchers found good agreement with non-linear verification examples, although direct comparison to traditional implicit NR-methods in efficiency is lacking.

Verhelst et al. [23] used ALM to simulate a simple buckling beam via an isogeometric representation in *G+Smo*, but now without using initial perturbations. The ALM allowed for a slow approach near to the bifurcation point. At a small distance from this limit point the first buckling mode was extracted and applied to the system as a perturbation. In this way, it was made possible to skip past the bifurcation and safely switch to the buckling branch past it, without needing 'random' initial perturbations which could influence results.

6.4. Modal reduction

Assuming one has been able to calculate the static crumpled configuration of a thin sheet using one of the aforementioned procedures, various methods exist to get information on the dynamic behaviour. Traditionally, these structural dynamic problems are tackled via frequency domain representations, namely modal analysis [70]. By solving an eigenvalue problem for the mass and stiffness matrices, one quickly finds the relevant eigenmodes and natural frequencies of vibration.

For large interconnected mechanical systems engineers are often interested in the combined dynamics of a large number of subsystems. As modal analyses of the whole system are too large and complex, *dynamic substructuring* (DS) is often applied to compartmentalize the problem [70, 71]. DS aims to decompose a large structure into subcomponents and calculate the dynamics behaviour on component-basis, to be combined later. This recombination may be performed using *frequency-based substructuring* (FSB), which also allows for integration of simulated and experimental data in the form of frequency response functions. However, recombination via *component-mode synthesis* (CMS) in the modal domain proves more flexible and allows for the extraction of mode shapes and time-domain behaviour. Here, *modal reduction* is used to rewrite the equations of motion of a simulated component into a basis of modal vectors [71, 72]. By only considering modes up to a frequency of interest, the full set of physical coordinates can be reduced to a smaller set of generalised coordinates. Examples of popular methods to perform this matrix projection into reduced modal coordinates are the Guyan, Craig-Bampton and Hintz-Herting techniques [71], which differ in how they handle the interfaces and reactions between different components [70, 71].

It should be noted that standard modal analysis and CMS assume linear system behaviour, and will thus be inaccurate for non-linear material behaviour, self-contact, or large vibrations with dynamic buckling [71]. To address the problem for large vibrations, Weeger [34] proposed a nonlinear vibration analysis based on the harmonic balancing method, in which the equations of motion are approximated in the frequency domain using Fourier expansions. However, this approach significantly increases the system size and computational cost. To make the method feasible, a nonlinear-compatible model reduction is required. Weeger [34] introduces a reduction based on *modal derivatives*, which extends the linear modal basis to account for nonlinear deformation effects. This approach enables accurate prediction of nonlinear frequency responses while keeping the computational effort manageable.

6.5. *Uncertainty analysis*

Noting a lack of insight into uncertainty effects associated with system imperfections, Luo et al. [73] performed experiments and simulations to establish the sensitivity of wrinkling amplitude to the non-uniformity of thickness for a stretched Kapton film. Twelve sheets of varying thicknesses were examined, and a substantial spread was found in the location of wrinkles and the extremes in wrinkling amplitudes, see Figure 9. Interestingly, post-buckling simulations of 'perfect' membranes with uniform nominal thickness were consistently found to show less wrinkling than experiment would suggest, indicating the important role uncertain initial conditions play in the initiation of buckling.

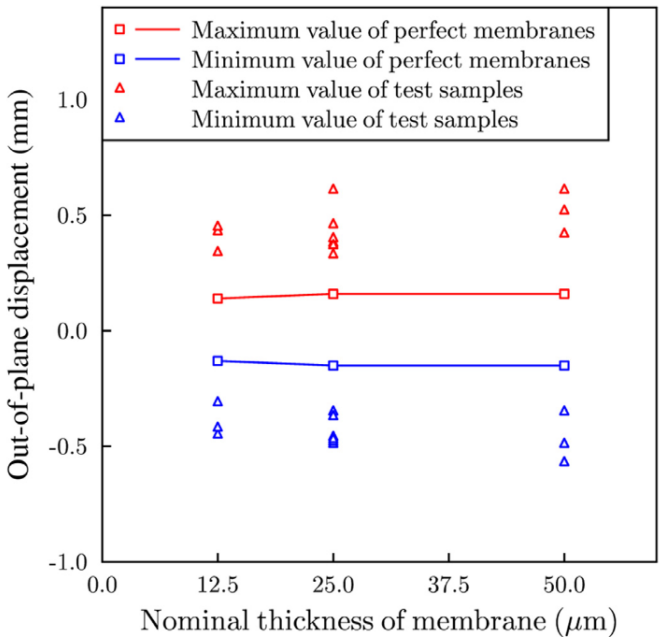

Figure 9: Maximum and minimum out-of-plane wrinkling amplitudes of stretched Kapton membranes from test samples and perfect simulated membranes with uniform nominal thickness [73]. The imperfect test samples consistently showed larger wrinkles than simulation would suggest. The spread between experimental values indicates the importance of accounting for imperfections in experiment.

As experimental data will always be limited by sample size, Luo et al. [73] set out to perform a probabilistic computational analysis of the problem. It should be noted that for most applications it is difficult to get an exact measure of the non-uniform thickness profile, therefore an uncertain field model with *bounded-field* description was used based on the nominal thickness and tolerance provided by the manufacturer. A probabilistic function determined a continuous thickness field within the aforementioned bounds, utilising a spatial correlation parameter to determine smoothness. The resulting total out-of-plane displacement was calculated for numerous models in order to construct a surrogate model to predict input-output behaviour. The initial sampling points were determined via orthogonal-maximin Latin hypercube design, with subsequent sampling points efficiently added to maximise the expected value of a so-called improvement function. The method was able to efficiently compute the expected upper and lower bounds for the total out-of-plane displacement for an increasing thickness tolerance bound, see Figure 10. These bounds were proven to be consistent with the results from 10,000 Monte Carlo realisations.

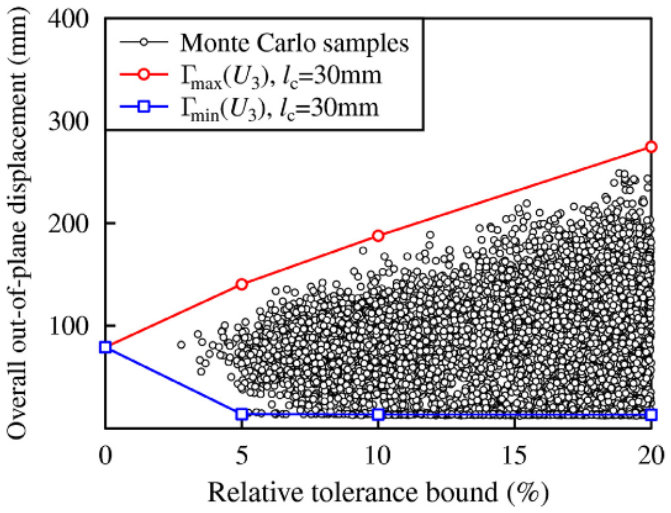

Figure 10: Relationship between overall out-of-plane displacement and relative tolerance bound for rectangular Kapton membrane simulations. The spread for 10,000 Monte Carlo realizations is shown to be consistent with the predictions for the upper (Γ_{max}) and lower (Γ_{min}) bounds made by a trained surrogate model. [73]

A generalization of the uncertainty analysis procedure was presented by Vu-Bac et al. [74] in the form of a *MATLAB* toolbox. The unified framework can be used to generate random samples, build surrogate models to approximate the real system, and perform sensitivity analysis. Again, sampling is performed via the Latin hypercube method in order to get a representative variety of data-points. Surrogate models can be trained via multi-variable polynomial regression, taking overfitting in mind by using cross-validation to assess the validity of the model by performing a priori predictions for a subset of the training data. The surrogate model can then be used to estimate the sensitivity indices of the model with correlated parameters, allowing for a variance-based sensitivity estimation for interdependent variables.

7. Discussion

A great variety of techniques to model the mechanics and dynamics of buckling thin sheets has been presented. We have developed a generalised flowchart to help the reader navigate the relevant choices for themselves, see Figure 11. Many alternative techniques are possible for the discretisation method, material model, perturbation method and the specifics of the post-buckling solver. The aim is to guide the user in finding a suitable collection of methods for their application, discussing (dis)advantages of the different options along the way.

7.1. Preprocessing

As concluded in section 5, DEA is out of the question for structural dynamics due to the impossibility for eigenvalue analysis, and thus the competition falls between FEA and IGA. IGA has proven to have high accuracy per DoF, particularly for thin sheets. The higher degree of continuity associated with the spline-based meshes allow for fast k-refinement, while also making KL-shells easily implementable. Another advantage is the subsequent lack of inaccurate optical branches in the eigenfrequency analysis, relevant to the structural dynamics. However, the efficiency improvements of IGA are not yet well-understood and may depend on the use-case. Along with the relative lack of available software negatively impacting the ease-of-use, FEA is still the best option for most engineering proposes. However, IGA is a quickly developing field which may be of interest to certain specialised applications.

Regardless of the spatial discretization, a TFT algorithm may be used to greatly reduce mesh density. However, it should be noted that TFT can only be applied to small-deformation elastic wrinkling, and not crumpling. Furthermore, TFT may only be applicable in situations of shearing, stretching and inflation, as the slack regions present in compression cannot

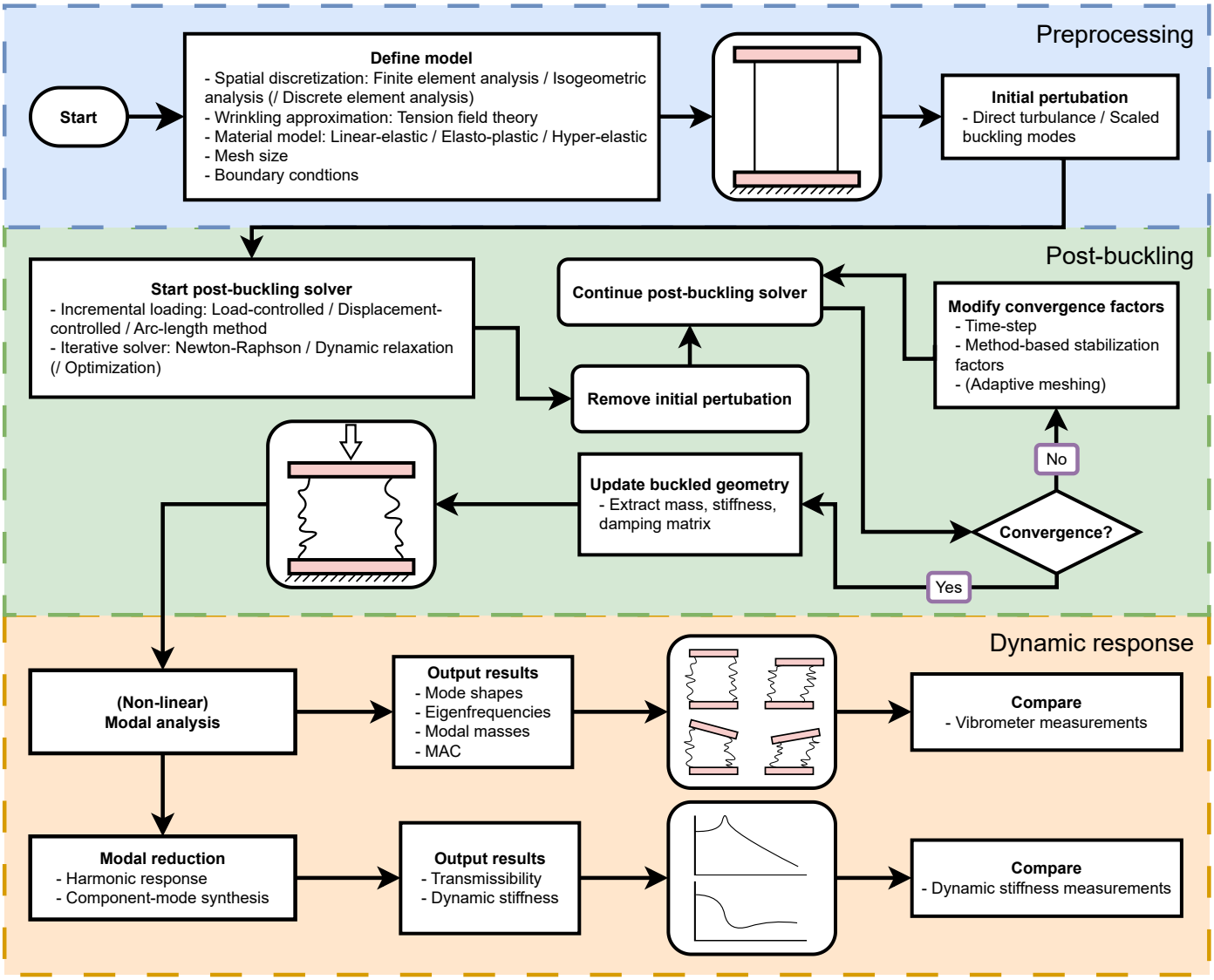

Figure 11: Flowchart for a general structural dynamic analysis of buckled thin sheets structures, developed with the aim to help the reader traverse the diverse options in numerical methods. Sketches indicate the stage in the simulation process, inspired by the cylindrical bellow case study mentioned in the section 1.

be captured accurately. Another disadvantage is the lack of information on the wrinkling geometry itself, which may also negatively impact the accuracy of subsequent modal analysis.

Materials models have not been covered explicitly in this review. However, it should be noted that non-linear material models may be needed in case of extreme compaction (elasto-plastic) or stretching (hyper-elastic).

Regarding initial perturbations, scaled buckling modes may be used to induce the preferred way of buckling for a certain 'perfect' structure. However, in practice no structure is perfect and a more easily implemented random direct turbulence perturbation is probably sufficient. To make results repeatable a consistent seed can be used for the random number generator. It may also be interesting to perform sensitivity analysis on this random perturbation to establish how much we expect experimental data to differ between tests.

7.2. Post-buckling solver

For the non-linear post-buckling solver there exist multiple ways to increment the loading for large deformations. In problems with snap-through and snap-back buckling, load-controlled and displacement-controlled time-stepping may become unstable. ALM offers a combination of the two to create a more stable method, ensuring that the buckling path is not lost at bifurcation points, at the cost of more complicated implementation.

Dynamic relaxation is also a useful method to ensure stability despite the near-singular stiffness matrices found in buckling. DRM with kinetic damping is easily implemented via vector-representations and convergence can be intuitively understood. However, convergence may still not be as fast as the quadratic convergence of implicit Newton-Raphson integration. For this reason some NR-iterations are preferred after a DRM procedure to make the last steps toward equilibrium. As modal analysis requires the calculations of the system matrices either way, the implementation of implicit NR-integration should not incur much more effort.

After a few iterations of the non-linear solver the initial perturbations should be removed in order to not influence the final results. If convergence cannot be reached after more iterations, the relevant convergence factors may be modified. Besides simply reducing the time-step, specific methods allow for the adjustment of their stabilization factors. Examples include the fictitious mass matrix and kinetic damping criteria in DRM, the arc-length in ALM, or the compression-minimizing penalty factors in TFT. Adaptive meshing could also be considered in order to more finely describe the mesh around crumple lines, although thus far such methods have only been tested in DEA.

7.3. Dynamic response

After the static post-buckling form-finding problem has been solved, the buckled geometry can be updated and the system matrices extracted. Mode shapes, eigenfrequencies and modal masses can be calculated by solving the eigenvalue problem on the updated mass and stiffness matrices. As most engineering problems consider small-amplitude vibrations, non-linear modal analysis is not required. A *modal assurance criterion* (MAC) may be used to know what mode shapes to compare between slightly different simulation by computing their correlation in displacement [72]. Mode shapes and eigenfrequencies may also be checked against vibrometer measurements, allowing for the verification and improvement of the modelling method. In the same vein, modal reduction using component-mode synthesis may be used to calculate the harmonic response for vibrational transmissibility between specified interface nodes. The resulting transmissibility or dynamic stiffness frequency response may again be compared against measurements.

Depending on the perceived spread between measurement results, it may be of interest to perform uncertainty analysis on the problem by building a surrogate model. Many variables are expected to impact buckling behaviour, such as sheet dimensions, non-uniform thicknesses or the random initial perturbations.

8. Conclusion

We have presented a generalised framework for the dynamic simulation of buckled thin sheets, highlighting a range of methods found in the literature. Both advanced discretization and solver techniques are addressed, including comparisons between isogeometric and discrete element analysis versus traditional finite element approaches. Tension field theory is discussed as an effective tool for reducing mesh size, though it must be applied with care. To handle the near-singular stiffness matrices typical of buckled systems, advanced iterative solvers such as dynamic relaxation and the arc-length method are considered. Finally, we propose performing dynamic analysis of buckled sheets through modal reduction, complemented by uncertainty analysis methods to improve the predictive reliability of these complex systems.

References

[1] N. Hossain, K. Woo, C. Jenkins, Dynamic Response of Systematically Creased Membranes, in: 48th AIAA/ASME/ASCE/AHS/ASC Structures, Structural Dynamics, and Materials Conference, American Institute of Aeronautics and Astronautics, 2007. doi:10.2514/6.2007-1806.

[2] M. C. Fokker, S. Janbaz, A. A. Zadpoor, Crumpling of thin sheets as a basis for creating mechanical metamaterials, RSC Advances 9 (2019) 5174. doi:10.1039/c8ra07565d.

[3] J. Kwon, O. Bouaziz, H. S. Kim, Y. Estrin, Finite Element Modeling of Crumpling of Metallic Thin Foil, Advanced Engineering Materials 25 (2023) 2300063. doi:10.1002/adem.202300063.

[4] G. Giménez-Ribes, M. Motaghian, E. van der Linden, M. Habibi, Crumpled structures as robust disordered mechanical metamaterials, Materials & Design 232 (2023) 112159. doi:10.1016/j.matdes.2023.112159.

[5] S. Kundu, R. Sriramdas, K. R. Amin, A. Bid, R. Pratap, N. Ravishankar, Crumpled sheets of reduced graphene oxide as a highly sensitive, robust and versatile strain/pressure sensor, Nanoscale 9 (2017) 9581–9588. doi:10.1039/C7NR02415K.

[6] O. Bouaziz, R. Bouafif, R. Massion, Sandwich materials with a crumpled aluminium core, Metallurgical Research & Technology 118 (2021) 320. doi:10.1051/metal/2021014.

[7] M. Ganjian, S. Janbaz, T. van Manen, N. Tümer, K. Modaresifar, M. Minneboo, L. E. Fratila-Apachitei, A. A. Zadpoor, Controlled metal crumpling as an alternative to folding for the fabrication of nanopatterned meta-biomaterials, Materials & Design 220 (2022) 110844. doi:10.1016/j.matdes.2022.110844.

[8] C. A. Maas, B. Thibault, New Generation of Flexible Elastomer Exhaust Decouplers: LINKEO™ System, Technical Report 2005-01-1153, SAE Technical Paper, 2005. doi:10.4271/2005-01-1153.

[9] N. Yamaki, Elastic Stability of Circular Cylindrical Shells, North-Holland Series in Applied Mathematics and Mechanics; Vol. 27, North-Holland, Amsterdam, 1984.

[10] Y. Timounay, R. De, J. L. Stelzel, Z. S. Schrecengost, M. M. Ripp, J. D. Paulsen, Crumples as a Generic Stress-Focusing Instability in Confined Sheets, Physical Review X 10 (2020) 021008. doi:10.1103/PhysRevX.10.021008.

[11] B. Li, Y.-P. Cao, X.-Q. Feng, H. Gao, Mechanics of morphological instabilities and surface wrinkling in soft materials: A review, Soft Matter 8 (2012) 5728–5745. doi:10.1039/C2SM00011C.

[12] A. Chandraul, M. V, S. Kumar, A review on dynamic analysis of membrane based space structures, Advances in Space Research 74 (2024) 740–763. doi:10.1016/j.asr.2024.03.082.

[13] ASReview - Active learning for Systematic Reviews, https://asreview.nl/, 2025.

[14] Connected Papers | Find and explore academic papers, https://www.connectedpapers.com/, 2025.

[15] H. King, R. D. Schroll, B. Davidovitch, N. Menon, Elastic sheet on a liquid drop reveals wrinkling and crumpling as distinct symmetry-breaking instabilities, Proceedings of the National Academy of Sciences 109 (2012) 9716–9720. doi:10.1073/pnas.1201201109.

[16] Y.-L. Li, M.-Y. Lu, H.-F. Tan, Y.-Q. Tan, A study on wrinkling characteristics and dynamic mechanical behavior of membrane, Acta Mechanica Sinica 28 (2012) 201–210. doi:10.1007/s10409-011-0512-2.

[17] T. Iwasa, Experimental verification on wrinkling behavior given by wrinkling analysis using the tension field theory, International Journal of Solids and Structures 136–137 (2018) 1–12. doi:10.1016/j.ijsolstr.2017.11.028.

[18] C. G. Wang, X. W. Du, H. F. Tan, X. D. He, A new computational method for wrinkling analysis of gossamer space structures, International Journal of Solids and Structures 46 (2009) 1516–1526. doi:10.1016/j.ijsolstr.2008.11.018.

[19] S. Kukathasan, S. Pellegrino, Nonlinear Vibration of Wrinkled Membranes, in: 44th AIAA/ASME/ASCE/AHS/ASC Structures, Structural Dynamics, and Materials Conference, Structures, Structural Dynamics, and Materials and Co-located Conferences, American Institute of Aeronautics and Astronautics, 2003. doi:10.2514/6.2003-1747.

[20] C. G. Wang, J. Xie, H. F. Tan, Vibration Simulations of a Wrinkled Membrane-Inflated Arch, Journal of Aerospace Engineering 27 (2014) 414–422. doi:10.1061/(ASCE)AS.1943-5525.0000260.

[21] S. Kukathasan, S. Pellegrino, Vibration of Prestressed Membrane Structures in Air, volume 2, 2002. doi:10.2514/6.2002-1368.

[22] S. Lienard, J. Johnston, B. Ross, Dynamic testing of a subscale sunshield for the Next Generation Space Telescope (NGST), 19th AIAA Applied Aerodynamics Conference (2001). doi:10.2514/6.2001-1268.

[23] H. M. Verhelst, M. Möller, J. H. D. Besten, F. J. Vermolen, M. L. Kaminski, Equilibrium Path Analysis Including Bifurcations with an Arc-Length Method Avoiding A Priori Perturbations, in: F. J. Vermolen, C. Vuik (Eds.), Numerical Mathematics and Advanced Applications ENUMATH 2019, Springer International Publishing, Cham, 2021, pp. 1109–1117. doi:10.1007/978-3-030-55874-1_110.

[24] R. Rossi, R. Vitaliani, E. Oñate, FE Analysis of membrane systems including wrinkling and coupling (2005). doi:10.1007/1-4020-3317-6_6.

[25] Haseganu, M. Eliza, Analytical Investigation of Tension Fields in Lightweight Membrane Structures, Ph.D. thesis, University of Alberta, 1994.

[26] T. Tallinen, J. A. Åström, J. Timonen, Discrete element simulations of crumpling of thin sheets, Computer Physics Communications 180 (2009) 512–516. doi:10.1016/j.cpc.2008.12.036.

[27] J. Andrejevic, C. H. Rycroft, Simulation of crumpled sheets via alternating quasistatic and dynamic representations, Journal of Computational Physics 471 (2022) 111607. doi:10.1016/j.jcp.2022.111607.

[28] W. Changguo, L. Yunliang, D. Xingwen, H. Xiaodong, S. Guozhi, Simulation Analysis of Vibration Characteristics of Wrinkled Membrane Space Structure, International Journal of Space Structures 22 (2007) 239–246. doi:10.1260/026635107783133825.

[29] T. J. R. Hughes, J. A. Cottrell, Y. Bazilevs, Isogeometric analysis: CAD, finite elements, NURBS, exact geometry and mesh refinement, Computer Methods in Applied Mechanics and Engineering 194 (2005) 4135–4195. doi:10.1016/j.cma.2004.10.008.

[30] R. Cardoso, O. Adetoro, D. Adan, Contact Modelling in Isogeometric Analysis: Application to Sheet Metal Forming Processes, Journal of Physics: Conference Series 734 (2016) 032123. doi:10.1088/1742-6596/734/3/032123.

[31] H. M. Verhelst, Isogeometric Analysis of Wrinkling (2024). doi:10.4233/0e4c3644-31a4-4157-983d-bd001d91b8ca.

[32] B. Oesterle, F. Geiger, D. Forster, M. Fröhlich, M. Bischoff, A study on the approximation power of NURBS and the significance of exact geometry in isogeometric pre-buckling analyses of shells, Computer Methods in Applied Mechanics and Engineering 397 (2022) 115144. doi:10.1016/j.cma.2022.115144.

[33] J. A. Cottrell, A. Reali, Y. Bazilevs, T. J. R. Hughes, Isogeometric analysis of structural vibrations, Computer Methods in Applied Mechanics and Engineering 195 (2006) 5257–5296. doi:10.1016/j.cma.2005.09.027.

[34] O. Weeger, Isogeometric Finite Element Analysis of Nonlinear Structural Vibrations, Ph.D. thesis, 2015.

[35] H. M. Verhelst, M. Möller, J. H. D. Besten, A Wrinkling Model for General Hyperelastic Materials based on Tension Field Theory, 2024. doi:10.48550/arXiv.2410.16990. arXiv:2410.16990.

[36] G+Smo, https://gismo.github.io/, 2025.

[37] L. Li, D. Benson, A. Nagy, M. Montanari, N. Petrinic, S. Hartmann, Recent Developments in Isogeometric Analysis with Solid Elements in LS-DYNA, in: 15th International LS-DYNA Users Conference, ANSYS, 2018.

[38] M. Occelli, T. Elguedj, S. Bouabdallah, L. Morançay, LR B-Splines implementation in the Altair RadiossTM solver for explicit dynamics IsoGeometric Analysis, Advances in Engineering Software 131 (2019) 166–185. doi:10.1016/j.advengsoft.2019.01.002.

[39] J. Bocko, P. Pleško, I. Delyová, P. Sivák, Comparison of Structural Analysis of Thin-Walled Structures Accomplished by Isogeometric Analysis and the Finite Element Method, Materials 15 (2022) 6516. doi:10.3390/ma15196516.

[40] H. Wagner, Flat sheet metal girders with very thin metal web. Part I : General theories and assumptions, 1931.

[41] C. Mseikeh, Wrinkling of Membranes, Plates, and Shells, Canadian Theses, McGill University Libraries, 1997.

[42] M. Stein, J. Hedgepeth, Analysis of partly wrinkled membranes, 1961.

[43] Pipkin, C. Allen, The Relaxed Energy Density for Isotropic Elastic Membranes, IMA Journal of Applied Mathematics 36 (1986) 85–99. doi:10.1093/imamat/36.1.85.

[44] D. G. Roddeman, J. Drukker, C. W. J. Oomens, J. D. Janssen, The Wrin-

kling of Thin Membranes: Part II—Numerical Analysis, Journal of Applied Mechanics 54 (1987) 888–892. doi:10.1115/1.3173134.
[45] X. F. Wang, Q. S. Yang, S.-s. Law, Wrinkled membrane element based on the wrinkling potential, International Journal of Solids and Structures 51 (2014) 3532–3548. doi:10.1016/j.ijsolstr.2014.06.004.
[46] Y. Miyazaki, Wrinkle/slack model and finite element dynamics of membrane, International Journal for Numerical Methods in Engineering 66 (2006) 1179–1209. doi:10.1002/nme.1588.
[47] A. Hossain, C. H. Jenkins, K. Woo, H. Igawa, Transverse Vibration Analysis for Partly Wrinkled Membranes, Journal of Spacecraft and Rockets 43 (2006) 626–637. doi:10.2514/1.11327.
[48] X. Liu, C. H. Jenkins, W. W. Schur, Large deflection analysis of pneumatic envelopes using a penalty parameter modified material model, Finite Elements in Analysis and Design 37 (2001) 233–251. doi:10.1016/S0168-874X(00)00040-8.
[49] M. Taylor, K. Bertoldi, D. J. Steigmann, Spatial resolution of wrinkle patterns in thin elastic sheets at finite strain, Journal of the Mechanics and Physics of Solids 62 (2014) 163–180. doi:10.1016/j.jmps.2013.09.024.
[50] J. Johnston, S. Brodeur, Finite Element Analysis of Wrinkled Membrane Structures for Sunshield Applications (2002).
[51] S. Tudruj, K. Kurec, J. Piechna, K. Kamieniecki, Mass-Spring System (MSS) 3D simulation of a thin flexible membrane with a new model of the elasticity parameters, Archive of Mechanical Engineering vol. 70 (2023) 199–218. doi:10.24425/ame.2023.144817.
[52] R. Narain, T. Pfaff, J. F. O'Brien, Folding and crumpling adaptive sheets, ACM Trans. Graph. 32 (2013) 51:1–51:8. doi:10.1145/2461912.2462010.
[53] N. Jin, W. Lu, Z. Geng, R. P. Fedkiw, Inequality cloth, in: Proceedings of the ACM SIGGRAPH / Eurographics Symposium on Computer Animation, SCA '17, Association for Computing Machinery, New York, NY, USA, 2017, pp. 1–10. doi:10.1145/3099564.3099568.
[54] J. Montes, B. Thomaszewski, S. Mudur, T. Popa, Computational design of skintight clothing, ACM Trans. Graph. 39 (2020) 105:105:1–105:105:12. doi:10.1145/3386569.3392477.
[55] Altair Engineering Inc., Altair Radioss User Documentation, Software Documentation Radioss 2025.1, 2025.
[56] A. Tessler, D. Sleight, J. Wang, Effective Modeling and Nonlinear Shell Analysis of Thin Membranes Exhibiting Structural Wrinkling, Journal of Spacecraft and Rockets - J SPACECRAFT ROCKET 42 (2005) 287–298. doi:10.2514/1.3915.
[57] X. Liu, G. Cai, Nonlinear dynamic analysis of wrinkled membrane structure, Engineering Computations 40 (2022) 41–61. doi:10.1108/EC-02-2022-0083.
[58] H. Le Meitour, G. Rio, H. Laurent, A. Lectez, P. Guigue, Analysis of wrinkled membrane structures using a Plane Stress projection procedure and the Dynamic Relaxation method, International Journal of Solids and Structures 208–209 (2021) 194–213. doi:10.1016/j.ijsolstr.2020.10.026.
[59] AS. Day, An introduction to dynamic relaxation, The engineer 219 (1965) 218–221.
[60] J. Rombouts, G. Lombaert, L. De Laet, M. Schevenels, On the equivalence of dynamic relaxation and the Newton-Raphson method, International Journal for Numerical Methods in Engineering 113 (2017). doi:10.1002/nme.5707.
[61] P. Underwood, Dynamic relaxation, Computational method for transient analysis, Elsevier (1983) 245–65.
[62] M. Rezaiee-Pajand, H. Estiri, Finding buckling points for nonlinear structures by dynamic relaxation scheme, Frontiers of Structural and Civil Engineering 14 (2020) 23–61. doi:10.1007/s11709-019-0549-z.
[63] E.-S. Lee, S.-K. Youn, Finite element analysis of wrinkling membrane structures with large deformations, Finite Elements in Analysis and Design 42 (2006) 780–791. doi:10.1016/j.finel.2006.01.004.
[64] K. Lee, S. Han., T. Park, A simple explicit arc-length method using the dynamic relaxation method with kinetic damping, Computers & Structures 89 (2011) 216–233. doi:10.1016/j.compstruc.2010.09.006.
[65] K. Nakashino, A. Nordmark, A. Eriksson, Geometrically nonlinear isogeometric analysis of a partly wrinkled membrane structure, Computers & Structures 239 (2020) 106302. doi:10.1016/j.compstruc.2020.106302.
[66] M. A. Crisfield, Snap-through and snap-back response in concrete structures and the dangers of under-integration, International Journal for Numerical Methods in Engineering 22 (1986) 751–767. doi:10.1002/nme.1620220314.
[67] M. A. Crisfield, A fast incremental/iterative solution procedure that handles "snap-through", Computers & Structures 13 (1981) 55–62. doi:10.1016/0045-7949(81)90108-5.
[68] E. Riks, An incremental approach to the solution of snapping and buckling problems, International Journal of Solids and Structures 15 (1979) 529–551. doi:10.1016/0020-7683(79)90081-7.
[69] S. A. Ragon, Z. Gürdal, L. T. Watson, A comparison of three algorithms for tracing nonlinear equilibrium paths of structural systems, International Journal of Solids and Structures 39 (2002) 689–698. doi:10.1016/S0020-7683(01)00195-0.
[70] D. Rixen, S. Voormeeren, General Framework for Dynamic Substructuring: History, Review, and Classification of Techniques, Aiaa Journal - AIAA J 46 (2008) 1169–1181. doi:10.2514/1.33274.
[71] J. van Steen, Comparison of Model Order Reduction Techniques for Interface Dynamics, Master's thesis, Eindhoven University of Technology, Eindhoven, 2020.
[72] R. Wijnen, Validation and Improvement of a Dynamic Stiffness Measurement Setup, Master's thesis, Eindhoven University of Technology, 2019.
[73] Y. Luo, J. Xing, Z. Kang, J. Zhan, M. Li, Uncertainty of membrane wrinkling behaviors considering initial thickness imperfections, International Journal of Solids and Structures 191–192 (2020) 264–277. doi:10.1016/j.ijsolstr.2020.01.022.
[74] N. Vu-Bac, T. Lahmer, X. Zhuang, T. Rabczuk, A software framework for probabilistic sensitivity analysis for computationally expensive models, Advances in Engineering Software 100 (2016) 19–31. doi:10.1016/j.advengsoft.2016.06.005.

Numerical and experimental analysis of structural dynamics of crumpled cylindrical foils

Marco Bader[a]

[a]Department of Precision and Microsystems Engineering, Faculty of Mechanical Engineering, Delft University of Technology, the Netherlands

Abstract

We investigate the structural mechanics and dynamics of crumpled cylindrical foils as ultra-compliant links for mechatronic systems. A systematic and computationally efficient finite element framework is developed to quantify how sheet thickness and degree of crumpling govern the emergent static and dynamic stiffness. Realistic crumpled morphologies are generated using explicit dynamic relaxation in Radioss, after which stress removal and modal reduction are employed to extract stiffness behaviour for direct comparison with shaker experiments. The results reveal a clear morphological transition from periodic wrinkling to stress-focusing crumpled ridge network, accompanied by new power-law scaling laws of stiffness with thickness and crumpling degree. Variability between measurements increases at higher crumpling levels, reflecting the intrinsic stochastic nature of ridge formation. Remaining discrepancies between simulations and experiments expose the critical influence of non-linear effects, particularly plasticity and self-contact, underscoring the need to incorporate these mechanisms to achieve fully predictive models of crumpled structures.

Keywords:
post-buckled thin sheets, crumpling, crumpling morphology, structural dynamics, dynamic relaxation, dynamic stiffness

1. Introduction

Anyone who has ever put on a freshly ironed shirt or dress is familiar with the frustrations caused by unwanted wrinkles and crumples. Likewise, in engineering contexts such buckling instabilities can compromise the performance of carefully designed structures. For instance, in aerospace applications such as solar sails, wrinkles and creases can reduce thrust and complicate control [1]. From a structural dynamics perspective, wrinkles have been shown to significantly influence system behaviour by reducing local stiffness and eigenfrequencies [1–5].

These challenges have motivated the development of numerous analytical and numerical methods to better understand wrinkling phenomena. One prominent approach is tension field theory (TFT), in which compressive stresses are relieved by approximating out-of-plane wrinkling patterns by equivalent in-plane membrane shortening [1, 4, 6–20]. While traditionally implemented in finite element analysis (FEA) software, TFT has also been applied to isogeometric analysis (IGA), which represents geometry using continuous splines rather than nodal discretizations [15, 21–28]. This approach is particularly advantageous for wrinkled sheets, as the higher inter-element continuity allows complex curved geometries to be captured with fewer degrees-of-freedom (DoFs).

Despite these advances, thin-sheet buckling remains challenging to model due to the under-constrained nature of the instability, which can induce matrix inversion instabilities in implicit solvers. Arc-length methods (ALM) mitigate this by following highly non-linear deformation paths using combined load-displacement increments [29–34]. Alternatively, explicit dynamic relaxation can bypass matrix inversions altogether, computing the static buckled geometry as the long-term limit of a damped dynamic system [35–43].

Still, most studies to date focus on the periodically wrinkled regime. In contrast, crumpling represents a generic evolution of wrinkling [44], in which periodic undulations give way to a limited number of stress-focusing ridges. While full FEA or IGA becomes impractical for highly crumpled and compacted sheets, discrete element analysis (DEA) has been shown capable of simulating such structures efficiently [41, 45–49]. DEA constructs sheets as networks of discrete mass elements connected by springs and dampers, allowing efficient self-contact handling. However, these methods have primarily been developed for computer graphics and remain limited with respect to engineering-oriented structural mechanics and dynamics studies.

Despite these challenges, the study of crumpled sheets holds promise for novel engineering applications. One such application is the design of ultra-compliant mechanical links between vibrationally isolated frames in vacuum mechatronic systems. Instead of engineered corrugated pipes or bellows, crumpled sheets naturally form multiple ridges and creases that function as flexible hinges, see Figure 1. For these links, accurate prediction of frequency-dependent vibrational transmissibility or dynamic stiffness is critical, as internal dynamics can cause apparent stiffening at higher frequencies [50].

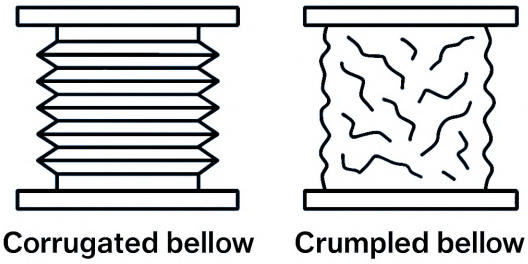

Figure 1: Comparison of engineered corrugation networks and stochastic crumpled morphologies as routes to compliant thin-sheet mechanical links.

However, to date literature on the structural dynamics of post-buckled sheets is limited to modal analyses in the wrinkled regime. Therefore, the present work aims to develop a systematic, robust, and computationally efficient numerical methodology for investigating the static and dynamic stiffness of crumpled structures. This involves generating crumpled morphologies, modelling their static and dynamic behaviour, and validating the models experimentally. Collectively, these efforts seek to establish a foundation for understanding how crumples govern emergent system stiffness, and ultimately leveraging this insight in the design of highly compliant mechanical links.

The remainder of this paper is organized as follows. Section 2 introduces the case study and outlines the numerical and experimental methodologies. Section 3 presents the results, first describing crumpling morphologies and then comparing simulated and experimental stiffness data, including emergent power-law scaling and variability trends. Section 4 discusses the implications and discrepancies between simulations and experiments. Finally, Section 5 summarizes the main contributions, with additional background provided in the Appendices.

2. Method

To demonstrate the feasibility of the proposed modelling approach a representative case study is employed, allowing direct validation of the numerical results against experimental measurements. The following sections first define the specifics of the case study, followed by a summary of the numerical and experimental methodologies.

2.1. Case study definitions

The present case study is motivated by a novel application of crumpling for the creation of flexible dynamic links in vacuum mechatronic systems [51]. Traditionally, corrugated bellows are used to connect vacuum regions requiring flexible joints, such as between two vibrationally isolated frames. These bellows illustrate how deliberately engineered ridge networks can provide compliant, low-transmissibility connections [52]. In an analogous manner, intentionally crumpled foils may offer a simpler and more cost-effective approach to achieving multi-directional compliance, provided their stiffness characteristics can be accurately predicted and controlled.

Figure 2 presents a schematic of the system under consideration. A cylindrical thin polymer sheet in its reference configuration (left) is axially crumpled and fixed between a top and bottom interface in the deformed configuration (right). In this study, the dynamic stiffness, defined as the frequency-dependent transfer function between a small excitation ($<$ 1 mm) applied to the bottom interface and the resulting force on the top interface, is used to quantify vibrational transmissibility. The introduction of crumpling ridges is expected to substantially reduce the dynamic stiffness in all directions, as these ridges act as natural flexible hinges.

The degree of crumpling is characterized by the cylinder overlength, defined as the ratio between the axial height of the cylinder in the reference (h_{ref}) and deformed (h_{def}) configurations:

$$\text{Overlength} = \frac{h_{\text{ref}} - h_{\text{def}}}{h_{\text{def}}} \cdot 100\%. \tag{1}$$

In this study, overlength is varied by increasing h_{ref}. Additionally, multiple sheet thicknesses are considered: 50, 130, 250, and 500 µm. All other system parameters are held constant, with a cylinder diameter $D = 0.2$ m and deformed height $h_{\text{def}} = 0.13$ m. The sheet material is fluorinated ethylene propylene (FEP), with a density $\rho = 2150$ kg/m^3, elastic modulus $E = 650$ MPa, and Poissons ratio $\nu = 0.4$ [53].

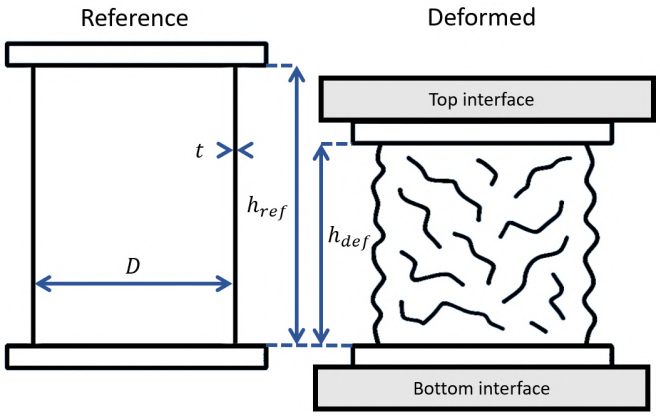

Figure 2: Case study: axially crumpled cylindrical foils as an alternative to corrugated bellow joints. The top interface is lowered towards the bottom interface to induce crumpling. Crumpling overlength is defined as the ratio between the axial heights of the reference (h_{ref}) and deformed (h_{def}) configurations. Overlength is varied via h_{ref}, together with sheet thickness t. Cylinder diameter D and deformed height h_{def} are kept constant across all tests.

2.2. Numerical method

A computational methodology was developed with an emphasis on efficiency and user-friendliness. The workflow is divided into four stages: (i) model definition, (ii) post-buckling simulation to generate crumpled geometries, and calculation of the (iii) static and (iv) dynamic responses. The key modeling decisions are outlined below, with additional details provided in Appendix A.

2.2.1. Model definition

Finite element analysis (FEA) remains the standard approach for structural mechanics and dynamics problems. However, for buckling thin shells the choice of discretisation method requires more careful consideration: discrete element analysis (DEA) and isogeometric analysis (IGA) offer potential advantages but also significant limitations in the present context.

DEA has been used successfully to simulate highly compacted sheets with plastic creasing and extensive self-contact [47]. However, existing DEA implementations are primarily developed for computer graphics and lack support for frequency-domain calculations due to their discretised nature [46]. IGA, by contrast, has already been applied to modal buckling of cylindrical shells [23] and typically requires fewer total DoFs than conventional FEA. Nevertheless, the resulting system matrices are considerably less sparse, which can offset computational gains [15]. Due to the limited availability of mature DEA and IGA software, a conventional finite-element approach was selected for this proof-of-concept study.

Drawing inspiration from automotive crashworthiness studies [54–56], two FEA solvers capable of handling highly geometrically nonlinear phenomena were considered: Ansys LS-Dyna and Altair Radioss. Radioss was selected for its clear input syntax, extensive documentation [57], and availability as the free stand-alone solver OpenRadioss, which benefits from an active user community and supporting tools [58].

Cylindrical shell models with five reference heights (h_{ref} = 0.135, 0.15, 0.17, 0.20, and 0.25 m) were created in Altair HyperMesh. Preliminary simulations and a mesh convergence study (Appendix A) determined that 5 mm square shell elements provided sufficient resolution for ridge formation. Following Radioss recommendations [57], the reduced-integration QEPH shell formulation (Quadrilateral Elasto-Plastic Physical Hourglass Control) was employed. This choice reduces computational cost and avoids shear locking compared with fully integrated elements, while the spurious zero-energy hourglass modes caused by the reduced integration are stabilised effectively.

Unlike traditional crashworthiness studies [54–56], where accurate plastic energy absorption and reaction forces play a central role, the present simulations aim solely to generate realistic crumpled geometries as quickly as possible. Consequently, linear-elastic material behaviour was adopted and self-contact was omitted, as the considered overlengths remain moderate.

Geometric imperfections were introduced using the `/RANDOM` keyword, superimposing Gaussian noise with an amplitude of 10 µm on the nodal coordinates. This is consistent with recommendations that imperfection amplitudes should range between 1% and 100% of the shell thickness [32]. To capture sensitivity to initial conditions, each thickness-overlength combination was simulated six times using reproducible random seeds.

2.2.2. Post-buckling simulation

The crumpling of thin cylinders is characterised by many local instabilities and snap-through events, which renders conventional incremental stepping procedures using implicit solvers fragile [16, 34, 42]. The implicit stepping can be improved by using an arc-length method to more closely follow the non-linear loading paths found in snap-through buckling. [29–31]. However, as for this work only the final crumpled morphology is of interest, the dynamic relaxation method (DRM) [35–40, 42] provides a more robust alternative: the desired static equilibrium is obtained as the long-time limit of a near-perfectly damped dynamic system, integrated explicitly in pseudo-time. This method is especially powerful for this form-finding application as it can easily deal with the under-constrained buckling present here, as there is no need to invert near-singular stiffness matrices in the explicit scheme.

Crumpling is induced by fixing all nodes at the bottom interface while imposing a downward displacement on the top interface. To minimize inertial effects and allow rapid convergence to steady state, the displacement follows a smooth sigmoid function over pseudo-time, producing small initial and final velocities and reducing high-frequency oscillations. Advanced mass scaling (`DT/AMS`) increases the stable time step without significantly affecting low-frequency response [57, 59, 60]. Additionally, adaptive viscous nodal damping (`/ADYREL`) [57] suppresses residual oscillations, yielding an effectively damped system.

Combined, these strategies allow efficient simulation of crumpling in under five minutes on a standard laptop. Further theoretical background and performance validation are provided in Appendix A.

2.2.3. Static response

To characterize the dependence of stiffness on overlength and thickness, an effective measure of axial and radial link stiffness is required. Direct tangent stiffness estimation from reaction forces ($k = \mathrm{d}F/\mathrm{d}z$) during crumpling is unreliable due to high-frequency fluctuations, sensitivity to loading rate and mass scaling, and local snap-through events, see Appendix A. Instead, a secant stiffness is computed by applying a known probing force F_{probe} = 100 N to the top interface and measuring the resulting displacement u_{probe} via a single linear-implicit step:

$$k_{\text{static}} = \frac{F_{\text{probe}}}{u_{\text{probe}}}. \tag{2}$$

This approach provides a global metric of morphology compliance, unaffected by transient dynamics.

However, if this probing force was applied with elastic stresses still present in the crumpled geometry, the cylinder would spring-back to its original shape, which would be indistinguishable from the deformation caused by the probing force. Thus, a key challenge was to remove stored elastic stresses post-deformation to establish a new crumpled but stress-free

reference geometry. As Radioss does not offer a function to automatically remove stresses in a single-run process, a novel stress-removal strategy was adopted using an elasto-plastic Johnson-Cook material law with strain-rate-dependent yield strength σ_y [57]:

$$\sigma_y = \sigma_{y,0}\left[1 + c\ln\left(\frac{\dot{\varepsilon}}{\dot{\varepsilon}_0}\right)\right], \tag{3}$$

where $\sigma_{y,0}$ is the base yield strength, c is a dimensionless strain-rate coefficient, and $\dot{\varepsilon}/\dot{\varepsilon}_0$ is the ratio between the local and reference strain rate. Parameters were artificially set ($\sigma_{y,0} = 1$ Pa, $c = 1 \times 10^6$, $\dot{\varepsilon}_0 = 1 \times 10^{-10}$ s^{-1}) to ensure linear-elastic behaviour during crumpling (high effective σ_y at non-zero $\dot{\varepsilon}$). At the end of the deformation, nodal velocities are frozen ($\dot{\varepsilon} \to 0$), collapsing σ_y to near-zero and plastically relaxing stresses while preserving geometry. While this method does not completely eliminate residual stresses, the equilibrium reached after unfreezing all nodes and relaxing is close to the desired crumpled shape.

To post-process the simulation results, the deformation u_{probe} resulting from the probing force is automatically acquired by extracting interface displacements from Radioss time-history files, converted to a Python dataframe using the OpenRadioss community library Vortex-Radioss [58].

2.2.4. Dynamic response

The dynamic behaviour of the crumpled foil is evaluated using a modal reduction approach to reduce computational cost while retaining essential interface dynamics. The full system is projected onto a basis of rigid-body and elastic eigenmodes up to 1000 Hz, following the Hintz-Herting methodology [50, 61]. This captures dynamic behaviour up to approximately 800 Hz without the need for computing the full system response, see Appendix A.

In practice, the crumpled geometry from Radioss is manually imported into an ANSYS modal analysis study. Interface nodes are rigidly connected to master nodes, and a free-free (no boundary conditions) modal analysis is performed. The resulting modes form the basis for the Hintz-Herting reduction, and the reduced-order model is exported using a proprietary user routine. In MATLAB, modal superposition using 5% modal damping is used to compute transfer functions from interface forces to displacements, which are then inverted to obtain the 6-DoF, frequency-dependent dynamic stiffness matrix [50].

This method captures the principal dynamic characteristics within the frequency range of interest but is limited to linearized behaviour and thus does not account for contact or prestress effects. Due to the high modal density of these compliant structures, generating the reduction basis is still computationally intensive. This underscores the advantage of the static secant stiffness calculation via stress-removal, which can be performed efficiently in a single Radioss run without repeated geometry export and import.

2.3. Experimental method

Experiments were performed using a 6-DoF dynamic stiffness measurement system originally developed for air-mount qualification and validated by Wijnen [50]. A schematic cross-section and photograph of the setup are shown in Figure 3. A specimen is clamped between a base frame (BF) and a metrology frame (MF). Vertical axial excitation (<1 mm amplitude) is applied to the BF using three in-phase piezoelectric stack actuators. Alternatively, radial excitation can be introduced via a horizontal shaker. The MF consists of a 500 kg mass that can be suspended using a preload bellow to apply gravitational preload. In this study, no preload was applied; the MF was lifted to float freely above its end stops.

Transmitted forces and moments are measured using three triaxial force sensors mounted on the MF. Interface motions of BF and MF are reconstructed from accelerometer arrays assuming rigid-body kinematics. Although the system measures all six force and moment components, the present study considers only axial (Z) and radial (X) forces and the corresponding relative displacements. Dynamic stiffness is defined in the frequency domain as the transfer function between relative displacement (MF-BF) and transmitted force at the MF.

Time signals were recorded at 50 kHz over 60 s intervals. Spectral estimation employed periodic block processing with 2 s blocks, Hanning windowing, and 50% overlap, yielding a frequency resolution of 0.5 Hz. Signal power and coherence functions were obtained from averaged spectra to verify data quality, see Appendix B and C. To maximize measurement coherence for highly compliant configurations (small thickness, large overlength), excitation was applied using two band-limited multi-sine signals (0-150 Hz and 100-500 Hz) instead of a single broadband coloured-noise signal as used by Wijnen [50]. Concentrating signal power within narrower frequency bands proved essential, as transmitted axial forces were small and easily masked by parasitic MF vibrations arising from shaker reaction paths, see Appendix B

For each combination of foil thickness and overlength, three independent measurements were conducted. Between repetitions, the sheet was manually perturbed to generate distinct crumpled geometries. This procedure enables quantification of both mean dynamic stiffness and variability arising from the stochastic crumpling process.

Static stiffness is extracted from the low-frequency region of the dynamic stiffness curves. However, for thin sheets with large overlength limited signal-to-noise ratios obscure a clear stiffness plateau. To obtain robust estimates, the dynamic stiffness is first smoothed using a symmetric moving-average filter (30 Hz bandwidth). Static stiffness is then defined as the mean smoothed stiffness between 1 and 10 Hz. This procedure provided the most consistent and physically representative values across all tested configurations and crumpling realizations, see Appendix B.

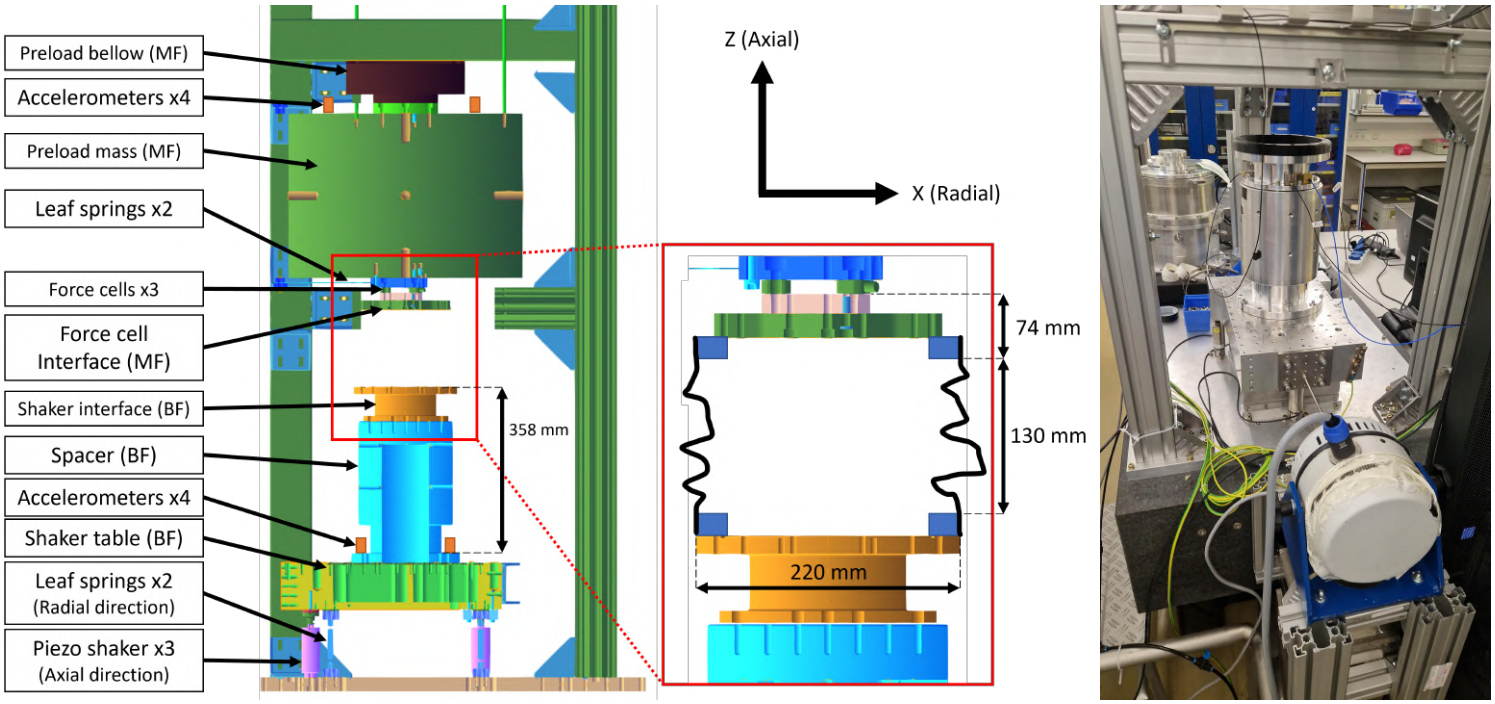

Figure 3: Schematic cross-section and photograph of the 6-DoF dynamic stiffness setup. The BF is excited using three vertical or one horizontal piezoelectric actuator(s). Three triaxial force sensors on the MF measure transmitted forces and moments, while accelerometers reconstruct BF and MF motions. The MF (500 kg) can apply gravitational preload via a preload bellow; no preload was used in this study.

3. Results

This section covers the results of the applied numerical and experimental methods, focusing on shared trends and discrepancies found in the crumpled morphologies and static and dynamic stiffnesses.

3.1. Crumpling morphology

Figure 4 compares simulated and experimental configurations for increasing overlength and thickness. While post-buckling states are inherently imperfection-sensitive and therefore not expected to match exactly between simulation and experiment, both approaches reveal the same underlying mechanical progression.

For small overlengths, the response is governed by classical shell buckling. The deformation field closely resembles the diamond-shaped modes predicted for cylindrical shells by Yamaki [62], indicating that the structure remains in a near-linear post-buckling regime. The surface pattern consists of spatially periodic wrinkles with well-defined wavelength and amplitude. Increasing thickness increases bending stiffness, which energetically penalizes curvature and therefore drives a coarsening of the wrinkle pattern: both wavelength and amplitude increase, consistent with established membrane bending scaling arguments [16].

As overlength increases, the deformation mechanism changes qualitatively. The structure transitions from distributed wrinkling to localized crumpling. Rather than maintaining a periodic mode, the shell minimizes its elastic energy by concentrating Gaussian curvature into sharp ridges and vertices, forming a network of stress-focusing ridges and vertices [44]. This localization reduces the energetically expensive bending over large areas by confining curvature to narrow regions. In this regime, a single characteristic wavelength is no longer meaningful. Instead, the morphology is defined by ridge density and ridge amplitude.

Again, thickness continues to act as the dominant mechanical control parameter. Higher bending stiffness suppresses fine-scale localization, resulting in fewer but more pronounced ridges. This reflects a stiffness-controlled length scale selection: as bending energy becomes more costly, the system favours larger structural features to balance membrane and bending contributions.

The experiments exhibit the same mechanics-driven transition from periodic wrinkling to ridge-dominated crumpling. Although boundary imperfections introduced by hose clamps reduce wrinkle regularity, the governing trend remains similar. In both simulation and experiment, increasing thickness leads to systematic coarsening of surface features, confirming that bending stiffness dictates the morphological length scale across regimes.

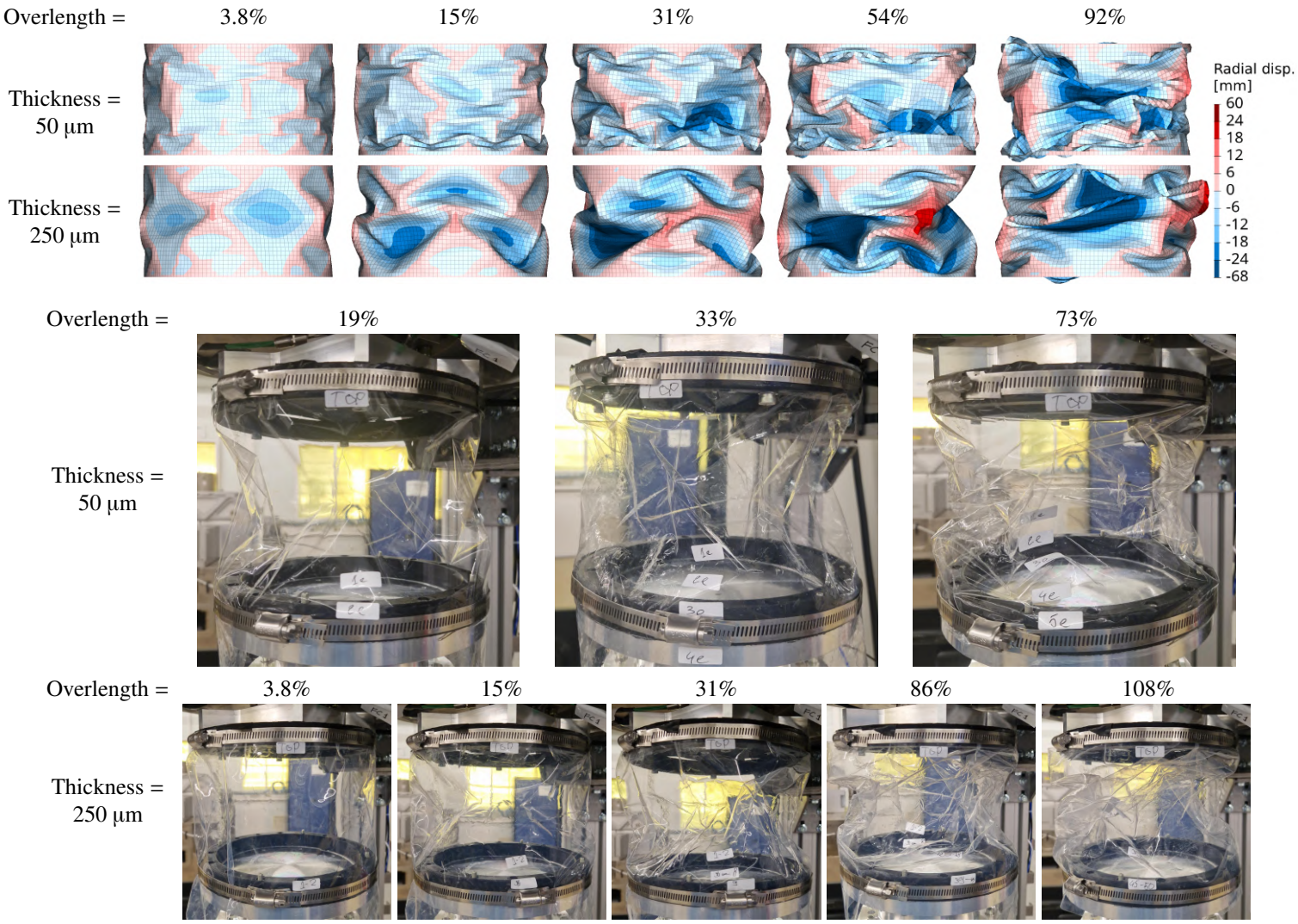

Figure 4: Simulated and experimental crumpled morphologies for increasing overlength and thickness. Simulations show radial displacement relative to the cylinder centreline (outward positive). The colour scale is limited to ±24 mm to enhance contrast between configurations; the full displacement range spans −68 mm to +60 mm.

3.2. *Static stiffness*

Figure 5 shows the evolution of the von Mises stress in a random element over pseudo-time, along with the axial height of five cylinders with different overlength. It can be seen that the cylinders are axially compressed to a final common height along a sigmoid function (0–0.8 s). Thereafter, all nodal velocities are frozen in order to remove stresses using non-physical plastic yielding (0.8 s), with a drop in von Mises stress as a result. With the sheet now relieved of most stresses, the cylinders are allowed to find a new (crumpled) equilibrium (0.8–1.0 s). Finally, a linear-implicit step is used (1.0–2.0 s) to apply a probing force F_{probe} on the top interface of each stress-free crumpled cylinder in axial or radial direction, with the magnitude of deformation u_{probe} indicating the effective stiffness k_{static} in that direction. As expected, the cylinders with largest overlength deform most and thus have the lowest stiffness.

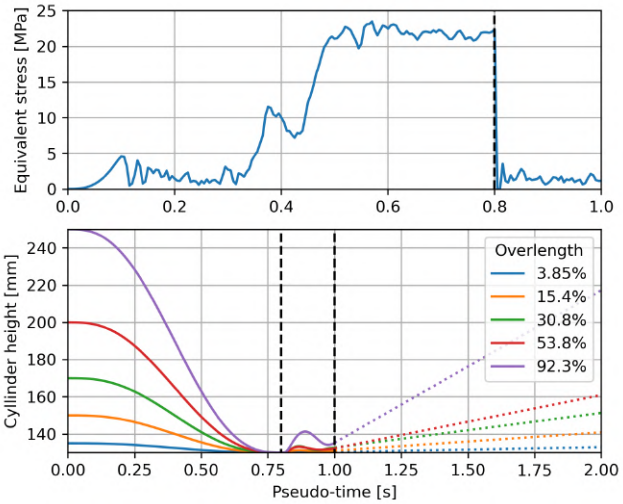

Figure 5: Evolution of von Mises stress and axial height for five cylinders with different overlengths, probed for effective stiffness in the axial direction.

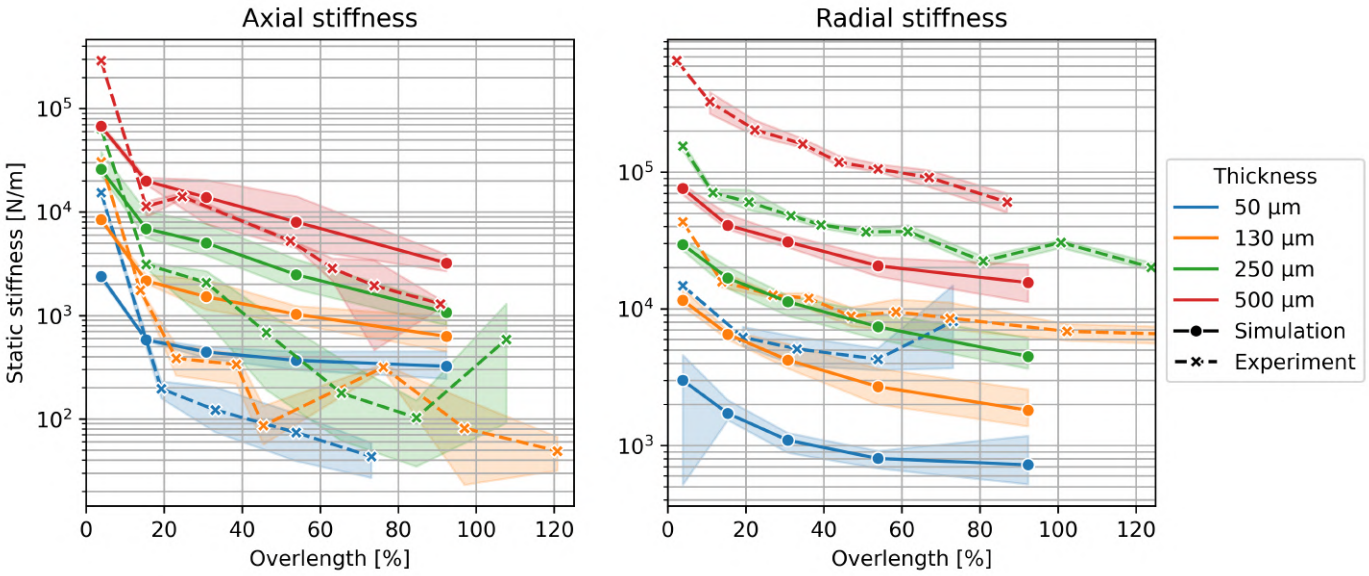

Figure 6: Simulated and experimental responses of axial and radial static stiffness as a function of overlength and thickness. For each configuration, the mean value of multiple realizations with different initial conditions is shown (six for simulations and three for measurements). Shaded regions indicate the absolute minimum and maximum bounds for each configuration.

Figure 6 presents the axial and radial static stiffness as a function of overlength, obtained from both simulation and experiment. For each thickness, the mean stiffness is shown together with shaded bands indicating the observed minimum and maximum values. Several systematic trends emerge: first, all configurations exhibit a fast exponential decay of stiffness with increasing overlength, indicating that even modest overlength already substantially diminishes the effective structural stiffness. Second, stiffness increases monotonically with thickness, reflecting the increased bending rigidity of the shell. Notably, the overall shape of the stiffness-overlength curves remains largely invariant across thicknesses, while their absolute magnitude shifts. This suggests that the effects of overlength and thickness act predominantly independently.

Despite the qualitative agreement in trends, clear quantitative discrepancies are observed between simulation and experiment. In particular, the experimentally measured axial stiffness exhibits a significantly steeper decay with overlength. This stronger sensitivity is not observed in the radial direction, where simulation and experiment display closer agreement, aside from a systematic offset in magnitude.

Motivated by the apparent independence of thickness and overlength effects (see Appendix C), the static stiffness k_{static} was modelled using a decoupled power-law relation,

$$k_{\text{static}} = \exp(\alpha) \cdot (\text{Overlength})^{\beta} \cdot (\text{Thickness})^{\gamma}, \tag{4}$$

with α, β, and γ as fitting parameters obtained using least-squares regression. To perform this fit, the model is linearized by taking the logarithm of both sides, yielding:

$$\ln(k_{\text{static}}) = \alpha + \beta \cdot \ln(\text{Overlength}) + \gamma \cdot \ln(\text{Thickness}). \tag{5}$$

This transformation ensures that relative variations are weighted uniformly across the data range, preventing configurations with large absolute stiffness values from dominating the fit.

The resulting parameters are summarized in Table 1. The high R^2-values indicate that the decoupled power-law relation captures the dominant trends in the data. The lowest coefficient of determination ($R^2 = 0.856$) corresponds to the experimental axial stiffness, consistent with its larger scatter and less smooth behaviour in Figure 6.

A marked discrepancy is observed in the overlength exponent β for axial stiffness: the experimentally obtained value ($\beta = -1.8$) is significantly more negative than the simulated value ($\beta = -0.85$), reflecting the steeper decay observed experimentally. In contrast, the radial stiffness exponents for overlength agree within uncertainty bounds, indicating consistent scaling behaviour between simulation and experiment in that direction.

The thickness exponent γ remains remarkably consistent across all cases ($1.4 \leq \gamma \leq 1.6$), suggesting that the influence of bending rigidity on stiffness follows a natural scaling law largely independent of loading direction.

Finally, systematic differences in absolute magnitude are reflected in the parameter α. For radial stiffness, where β and γ are nearly identical between simulation and experiment, the difference in α corresponds to a multiplicative factor of approximately $\exp(4.5 - 3.2) = 3.7$. It should be noted that the absolute value of α is unit-dependent and therefore does not carry independent physical meaning beyond this global scaling offset.

	Axial stiffness		Radial stiffness	
	Simulation	Experiment	Simulation	Experiment
R^2	0.960	0.856	0.963	0.939
α	3.5 ± 0.2	4.6 ± 0.8	3.2 ± 0.2	4.5 ± 0.3
β	-0.85 ± 0.03	-1.8 ± 0.1	-0.52 ± 0.02	-0.55 ± 0.04
γ	1.40 ± 0.04	1.6 ± 0.1	1.42 ± 0.03	1.48 ± 0.05

Table 1: Fitted parameters of the log-linear regression model in Equation 5, for axial and radial static stiffness. Reported uncertainties represent standard deviations obtained from the least-squares fit. The coefficient of determination R^2 quantifies the goodness of fit.

The variability of static stiffness measurements across repeated simulations and experiments is quantified in Figure 7 using the coefficient of variation (standard deviation normalized by the mean) for each overlength. As no systematic trend with sheet thickness was observed, data from all thicknesses are grouped together. It should be noted that the limited number of experimental repetitions renders the standard deviation sensitive to outliers, particularly at high overlength.

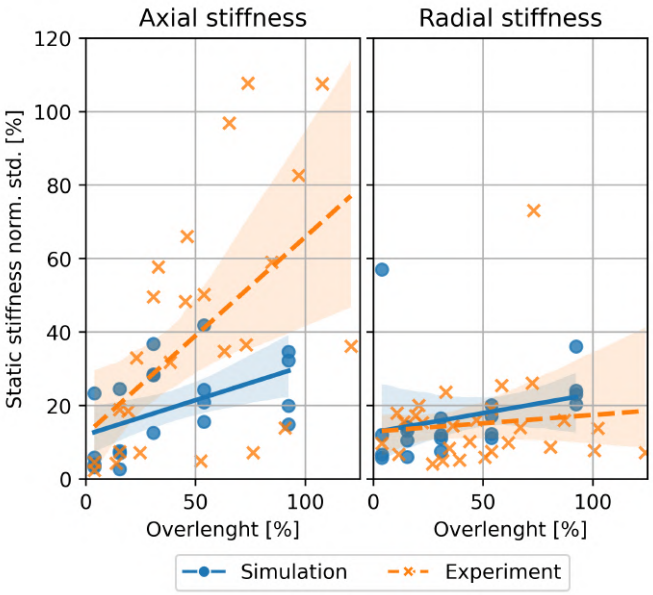

R^2-value	Axial stiffness	Radial stiffness
Simulation	0.305	0.079
Experiment	0.297	0.012

Figure 7: Scatter plot of normalised standard deviations (coefficient of variation) per overlength-thickness configuration, with all thicknesses grouped. A linear regression indicates the general trend, along with a shaded 95% confidence interval of the regression. The strength of correlation in the data is represented by R^2-values.

A weak positive correlation between stiffness variability and overlength is apparent for both axial and radial directions in simulations and experiments. This trend is consistent with the expected increase in morphological divergence at higher overlengths as cylinders transition from regular wrinkling patterns to irregular, stress-focused crumpled states. At minimal overlength, all realizations closely resemble the periodic diamond-shaped wrinkle pattern, yielding nearly identical stiffness values. With increasing overlength, deviations between realizations grow due to the amplification of local snap-through events and ridge localization, see Figure 8.

Experimental measurements display a more pronounced increase in variability compared to simulations, reflecting additional sources of uncertainty such as imperfect boundary conditions, clamping irregularities, and intrinsic noise of the measurement system. Moreover, low-stiffness configurations at high overlength approach the noise floor of the experimental setup, further enhancing relative variability.

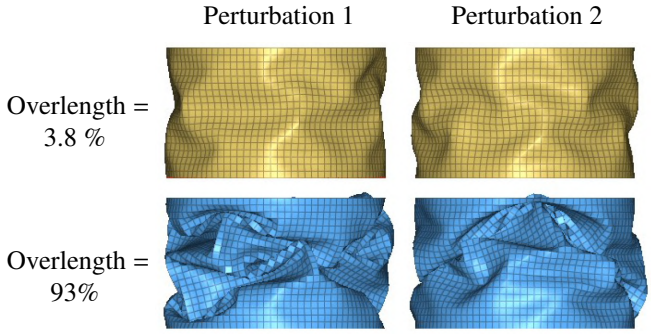

Figure 8: Comparison of crumpled morphologies for the same thickness (t = 500 µm) but different seeds for the initial perturbation.

3.3. Dynamic stiffness

The dynamic response of the crumpled cylinders, expressed as frequency–dependent dynamic stiffness, is shown in Figure 9. The shaded minimum-maximum bounds illustrate variability across different realizations, reflecting the pronounced sensitivity of resonance peak positions to small initial geometric perturbations which are amplified during crumpling. Background noise measurements, obtained without a bellow fixed between the interfaces, are also included to represent force cell disturbances caused by parasitic shaker vibrations propagating through the springsuspension of the metrology frame. These reference measurements indicate the effective noise floor of the setup and highlight the intrinsic challenge of testing ultra-compliant links. It should be noted that only a representative subset of configurations is presented here; the complete dataset, including coherence plots and additional realizations, is provided in Appendix C.

Simulated results exhibit the expected characteristics of flexible dynamic links. At low frequencies, the dynamic stiffness coincides with the static stiffness, forming a flat baseline that reflects quasi-static geometric compliance. The onset of the dynamic regime occurs at the first structural resonance, beyond which stiffness increases with frequency due to the cumulative contribution of multiple vibration modes. Configurations with lower static stiffness enter this dynamic regime at lower frequencies, as their reduced structural rigidity leads to lower natural frequencies. Consequently, the dynamic stiffness

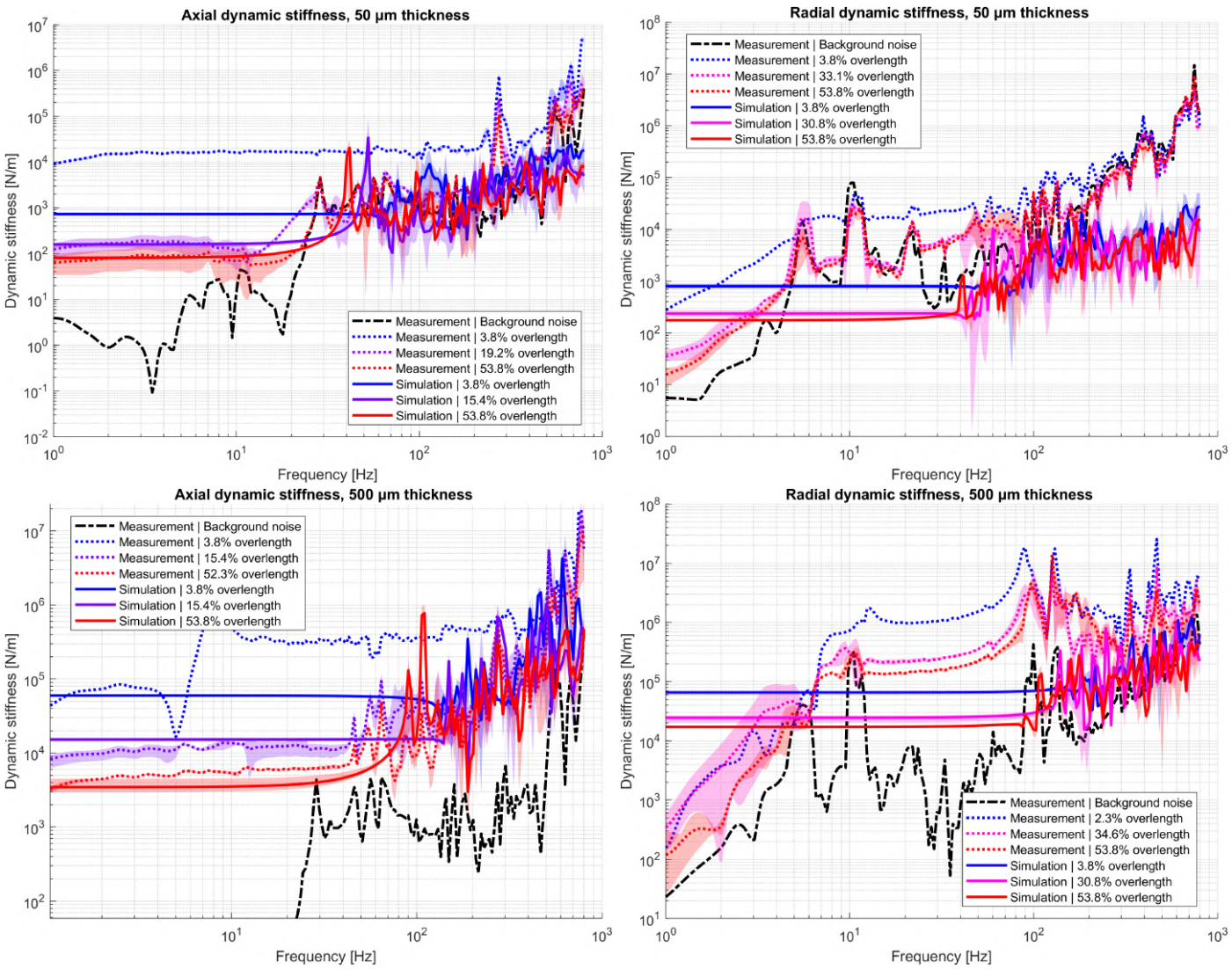

Figure 9: Dynamic stiffness transfer functions in axial and radial directions, for $t = 50$ µm and $t = 500$ µm and various overlengths. Shaded areas indicate minimum and maximum bounds between three realisations. Measurements without any specimen present are indicated as background noise, resulting from force cell disturbances due to reaction path vibrations.

curves progressively converge at higher frequencies. This convergence suggests that while static response is governed primarily by geometric factors such as ridge curvature and fold topology, the high-frequency behaviour becomes increasingly influenced by distributed mass participation, which is similar across configurations of equal thickness.

The exceptionally high modal density observed in all configurations is consistent with the presence of a hierarchical ridge network, in which local bending and folding elements introduce numerous low-mass, low-stiffness substructures. Each ridge segment effectively behaves as a local oscillator, weakly coupled to the global deformation field. The resulting dynamic behaviour is therefore not dominated by a few well-separated global modes, but rather emerges from the superposition of many interacting local modes spanning a broad frequency range. In such stochastic systems, small geometric variations shift individual resonance frequencies without fundamentally altering the overall response envelope. This underscores the importance of interpreting general stiffness trends rather than attempting peak-to-peak comparisons, which are inherently non-repeatable and of limited physical significance.

For experimental measurements, configurations with small thickness and high overlength are strongly influenced by background noise transmitted through the shaker reaction path. As specimen stiffness approaches the compliance of the measurement frame, their dynamics become increasingly coupled. While the low-frequency static region remains distinguishable, the onset of the dynamic regime is partially contaminated by setup resonances, reducing the reliability of individual peaks. These measurements must therefore be interpreted with caution, as some apparent resonances may originate from the measurement system rather than the specimen itself.

For thicker sheets, the signal-to-noise ratio improves significantly, and the transition from static to dynamic stiffness is more clearly resolved. In these cases, both simulations and experiments indicate that the dynamic regime begins around 100 Hz. Although resonance peaks shift in frequency with overlength and between realizations, their overall shape and spacing remain qualitatively similar, suggesting that the global deformation mechanisms of the crumpled cylinders are preserved despite geometric variability. Nevertheless, individual peaks remain difficult to isolate unequivocally from background contributions and should not be interpreted literally; instead, the global evolution of the dynamic stiffness envelope is of primary importance.

Overall, the dynamic behaviour of crumpled cylinders appears to be governed by a transition from geometry-dominated compliance at low frequencies to increasingly inertia-dominated response at higher frequencies, superimposed with a dense spectrum of locally activated ridge modes. This dual character explains both the sensitivity to initial crumpling configuration and the eventual convergence of stiffness curves in the dynamic regime. It also provides a consistent framework for interpreting discrepancies between experiment and simulation, particularly in directions where non-linear ridge mechanics or plastic deformation may enhance stiffness beyond that predicted by the current elastic numerical model.

4. Discussion

The results presented in this study demonstrate that crumpling fundamentally transforms both the static and dynamic stiffness of thin sheets. Increasing overlength initially produces a pronounced reduction in static stiffness, marking the transition from a membrane-dominated response to one governed by a sparse network of bending ridges and vertices. In this regime, load transfer is concentrated in a limited number of hinge–like features, allowing substantial compliance through localized bending. However, as overlength increases further, the stiffness reduction exhibits clear diminishing returns. Beyond moderate overlengths, the static stiffness approaches an apparent lower bound (see Appendix C), indicating that additional geometric complexity does not translate into proportional gains in compliance.

This saturation can be understood as a structural evolution of the crumpled network. As the configuration densifies, ridge-ridge interactions and self–contact become increasingly frequent [63]. The structure gradually transitions from a hinge-dominated system toward a contact–stabilized network with finite residual stiffness. In this regime, further crumpling may even induce local stiffening through mechanical shortcuts with other parts of the machine, such that direct frictional contacts bypass compliant bending ridges and provide unintended load transfer paths. The effective stiffness is therefore governed not only by geometric freedom, but also by contact topology.

These mechanisms introduce an important engineering trade-off. Larger overlengths (and small thicknesses) reduce quasi-static stiffness and may be attractive for designing ultra-compliant links. However, excessive crumpling increases the risk of pinhole formation due to extreme local curvature, as well as the likelihood of contact–induced stiffening and mechanical shortcuts. From a reliability perspective, highly densified configurations may therefore compromise structural integrity or long-term durability. The results suggest that stiffness reduction through crumpling is beneficial only within a finite window: beyond that window, gains in compliance are marginal.

Interestingly, a consistent anisotropy is observed between axial and radial loading directions in both static and dynamic responses. Axial stiffness is generally lower and exhibits greater variability, reflecting the dominant role of a limited number of ridge structures in accommodating axial deformation. Under axial loading, deformation energy is concentrated in a small subset of highly stressed ridges, rendering the global response sensitive to crumpling history and ridge orientation. Radial stiffness, by contrast, is distributed over a larger ensemble of circumferential load paths, resulting in a stiffer and more repeatable response. This directional dependence highlights that crumpled sheets cannot be described by a single effective stiffness parameter; rather, they exhibit intrinsically anisotropic and configuration–dependent behaviour.

The comparison between simulations and experiments further underscores the importance of material and contact nonlinearities. Although the numerical model captures the overall stiffness trends and the convergence behaviour in the dynamic regime, discrepancies in the axial response remain. The simulations do not fully reproduce the experimentally observed faster softening at large overlengths. A plausible explanation is the absence of material plasticity in the current model: Stress–focusing ridges with extreme curvature are likely to undergo local yielding, permanently weakening hinge stiffness. Incorporating plastic deformation in future models is therefore essential for quantitatively accurate prediction of crumpled-sheet mechanics.

In the dynamic domain, all configurations exhibit a transition from geometry-dominated compliance at low frequencies to inertia–dominated behaviour at higher frequencies, accompanied by a dense spectrum of locally compliant ridge modes. Importantly, the dynamic stiffness curves converge at higher frequencies, irrespective of overlength. This convergence indicates that increasing overlength primarily affects quasi-static compliance, while offering limited benefit for high–frequency dynamic isolation. From a design perspective, this suggests diminishing returns when selecting extreme overlength values: improvements in static flexibility do not proportionally enhance dynamic performance.

Taken together, these findings indicate that crumpling is a powerful but bounded strategy for stiffness reduction. An optimal crumpling state likely exists in which static compliance is significantly enhanced, dynamic behaviour remains predictable, and risks associated with self–contact, plastic damage, and pinhole formation are minimized. The combined static and dynamic characterization framework developed in this study provides a basis for identifying this balance and for guiding the engineering design of crumpled sheet structures as compliant dynamic links.

5. Conclusion

In this study, we have developed a systematic, robust, and computationally efficient numerical framework for analysing the static and dynamic stiffness of crumpled structures. Dynamic relaxation methods were used to quickly generate representative crumpled morphologies, while stress–removal techniques and modal reduction approaches were applied to extract the static and dynamic stiffness of these deformed configurations. The numerical results were validated against experimental measurements of dynamic stiffness, obtained using multi-sine shaker excitation to enhance the signal-to-noise ratio. From these analyses, new power-law relationships were identified to characterize the influence of crumpling on the emergent stiffness of the structures. Observed discrepancies in the scaling parameters highlight limitations of the current simulation workflow, particularly the absence of plasticity and self-contact effects, which should be addressed in future developments to improve predictive accuracy. However, this work still marks a strong foundation for the understanding of crumpling in the engineering context of structural mechanics and the design of ultra-flexible dynamic links.

References

[1] N. Hossain, K. Woo, C. Jenkins, Dynamic Response of Systematically Creased Membranes, in: 48th AIAA/ASME/ASCE/AHS/ASC Structures, Structural Dynamics, and Materials Conference, American Institute of Aeronautics and Astronautics, 2007. doi:10.2514/6.2007-1806.

[2] Y.-L. Li, M.-Y. Lu, H.-F. Tan, Y.-Q. Tan, A study on wrinkling characteristics and dynamic mechanical behavior of membrane, Acta Mechanica Sinica 28 (2012) 201–210. doi:10.1007/s10409-011-0512-2.

[3] C. G. Wang, J. Xie, H. F. Tan, Vibration Simulations of a Wrinkled Membrane-Inflated Arch, Journal of Aerospace Engineering 27 (2014) 414–422. doi:10.1061/(ASCE)AS.1943-5525.0000260.

[4] S. Kukathasan, S. Pellegrino, Nonlinear Vibration of Wrinkled Membranes, in: 44th AIAA/ASME/ASCE/AHS/ASC Structures, Structural Dynamics, and Materials Conference, Structures, Structural Dynamics, and Materials and Co-located Conferences, American Institute of Aeronautics and Astronautics, 2003. doi:10.2514/6.2003-1747.

[5] S. Lienard, J. Johnston, B. Ross, Dynamic testing of a subscale sunshield for the Next Generation Space Telescope (NGST), 19th AIAA Applied Aerodynamics Conference (2001). doi:10.2514/6.2001-1268.

[6] A. Chandraul, M. V, S. Kumar, A review on dynamic analysis of membrane based space structures, Advances in Space Research 74 (2024) 740–763. doi:10.1016/j.asr.2024.03.082.

[7] H. Wagner, Flat sheet metal girders with very thin metal web. Part I : General theories and assumptions, 1931.

[8] C. Mseikeh, Wrinkling of Membranes, Plates, and Shells, Canadian Theses, McGill University Libraries, 1997.

[9] M. Stein, J. Hedgepeth, Analysis of partly wrinkled membranes, 1961.

[10] Pipkin, C. Allen, The Relaxed Energy Density for Isotropic Elastic Membranes, IMA Journal of Applied Mathematics 36 (1986) 85–99. doi:10.1093/imamat/36.1.85.

[11] D. G. Roddeman, J. Drukker, C. W. J. Oomens, J. D. Janssen, The Wrinkling of Thin Membranes: Part II—Numerical Analysis, Journal of Applied Mechanics 54 (1987) 888–892. doi:10.1115/1.3173134.

[12] X. F. Wang, Q. S. Yang, S.-s. Law, Wrinkled membrane element based on the wrinkling potential, International Journal of Solids and Structures 51 (2014) 3532–3548. doi:10.1016/j.ijsolstr.2014.06.004.

[13] Y. Miyazaki, Wrinkle/slack model and finite element dynamics of membrane, International Journal for Numerical Methods in Engineering 66 (2006) 1179–1209. doi:10.1002/nme.1588.

[14] A. Hossain, C. H. Jenkins, K. Woo, H. Igawa, Transverse Vibration Analysis for Partly Wrinkled Membranes, Journal of Spacecraft and Rockets 43 (2006) 626–637. doi:10.2514/1.11327.

[15] H. M. Verhelst, Isogeometric Analysis of Wrinkling (2024). doi:10.4233/0e4c3644-31a4-4157-983d-bd001d91b8ca.

[16] R. Rossi, R. Vitaliani, E. Oñate, FE Analysis of membrane systems including wrinkling and coupling (2005). doi:10.1007/1-4020-3317-6_6.

[17] X. Liu, C. H. Jenkins, W. W. Schur, Large deflection analysis of pneumatic envelopes using a penalty parameter modified material model, Finite Elements in Analysis and Design 37 (2001) 233–251. doi:10.1016/S0168-874X(00)00040-8.

[18] M. Taylor, K. Bertoldi, D. J. Steigmann, Spatial resolution of wrinkle patterns in thin elastic sheets at finite strain, Journal of the Mechanics and Physics of Solids 62 (2014) 163–180. doi:10.1016/j.jmps.2013.09.024.

[19] J. Johnston, S. Brodeur, Finite Element Analysis of Wrinkled Membrane Structures for Sunshield Applications (2002).

[20] T. Iwasa, Experimental verification on wrinkling behavior given by wrinkling analysis using the tension field theory, International Journal of Solids and Structures 136–137 (2018) 1–12. doi:10.1016/j.ijsolstr.2017.11.028.

[21] T. J. R. Hughes, J. A. Cottrell, Y. Bazilevs, Isogeometric analysis: CAD, finite elements, NURBS, exact geometry and mesh refinement, Computer Methods in Applied Mechanics and Engineering 194 (2005) 4135–4195. doi:10.1016/j.cma.2004.10.008.

[22] R. Cardoso, O. Adetoro, D. Adan, Contact Modelling in Isogeometric Analysis: Application to Sheet Metal Forming Processes, Journal of Physics: Conference Series 734 (2016) 032123. doi:10.1088/1742-6596/734/3/032123.

[23] B. Oesterle, F. Geiger, D. Forster, M. Fröhlich, M. Bischoff, A study on the approximation power of NURBS and the significance of exact geometry in isogeometric pre-buckling analyses of shells, Computer Methods in Applied Mechanics and Engineering 397 (2022) 115144. doi:10.1016/j.cma.2022.115144.

[24] J. A. Cottrell, A. Reali, Y. Bazilevs, T. J. R. Hughes, Isogeometric analysis of structural vibrations, Computer Methods in Applied Mechanics and Engineering 195 (2006) 5257–5296. doi:10.1016/j.cma.2005.09.027.

[25] O. Weeger, Isogeometric Finite Element Analysis of Nonlinear Structural Vibrations, Ph.D. thesis, 2015.

[26] H. M. Verhelst, M. Möller, J. H. D. Besten, A Wrinkling Model for General Hyperelastic Materials based on Tension Field Theory, 2024. doi:10.48550/arXiv.2410.16990. arXiv:2410.16990.

[27] L. Li, D. Benson, A. Nagy, M. Montanari, N. Petrinic, S. Hartmann, Recent Developments in Isogeometric Analysis with Solid Elements in LS-DYNA, in: 15th International LS-DYNA Users Conference, ANSYS, 2018.

[28] J. Bocko, P. Pleško, I. Delyová, P. Sivák, Comparison of Structural Analysis of Thin-Walled Structures Accomplished by Isogeometric Analysis and the Finite Element Method, Materials 15 (2022) 6516. doi:10.3390/ma15196516.

[29] M. A. Crisfield, A fast incremental/iterative solution procedure that handles "snap-through", Computers & Structures 13 (1981) 55–62. doi:10.1016/0045-7949(81)90108-5.

[30] E. Riks, An incremental approach to the solution of snapping and buckling problems, International Journal of Solids and Structures 15 (1979) 529–551. doi:10.1016/0020-7683(79)90081-7.

[31] S. A. Ragon, Z. Gürdal, L. T. Watson, A comparison of three algorithms for tracing nonlinear equilibrium paths of structural systems, International Journal of Solids and Structures 39 (2002) 689–698. doi:10.1016/S0020-7683(01)00195-0.

[32] X. Liu, G. Cai, Nonlinear dynamic analysis of wrinkled membrane structure, Engineering Computations 40 (2022) 41–61. doi:10.1108/EC-02-2022-0083.

[33] K. Lee, S. Han., T. Park, A simple explicit arc-length method using the dynamic relaxation method with kinetic damping, Computers & Structures 89 (2011) 216–233. doi:10.1016/j.compstruc.2010.09.006.

[34] H. M. Verhelst, M. Möller, J. H. D. Besten, F. J. Vermolen, M. L. Kaminski, Equilibrium Path Analysis Including Bifurcations with an Arc-Length Method Avoiding A Priori Perturbations, in: F. J. Vermolen, C. Vuik (Eds.), Numerical Mathematics and Advanced Applications ENUMATH 2019, Springer International Publishing, Cham, 2021, pp. 1109–1117. doi:10.1007/978-3-030-55874-1_110.

[35] AS. Day, An introduction to dynamic relaxation, The engineer 219 (1965) 218–221.

[36] J. Rombouts, G. Lombaert, L. De Laet, M. Schevenels, On the equivalence of dynamic relaxation and the Newton-Raphson method, International Journal for Numerical Methods in Engineering 113 (2017). doi:10.1002/nme.5707.

[37] P. Underwood, Dynamic relaxation, Computational method for transient analysis, Elsevier (1983) 245–65.

[38] H. Le Meitour, G. Rio, H. Laurent, A. Lectez, P. Guigue, Analysis of wrinkled membrane structures using a Plane Stress projection procedure and the Dynamic Relaxation method, International Journal of Solids and Structures 208–209 (2021) 194–213. doi:10.1016/j.ijsolstr.2020.10.026.

[39] M. Rezaiee-Pajand, H. Estiri, Finding buckling points for nonlinear structures by dynamic relaxation scheme, Frontiers of Structural and Civil Engineering 14 (2020) 23–61. doi:10.1007/s11709-019-0549-z.

[40] E.-S. Lee, S.-K. Youn, Finite element analysis of wrinkling membrane structures with large deformations, Finite Elements in Analysis and Design 42 (2006) 780–791. doi:10.1016/j.finel.2006.01.004.

[41] J. Montes, B. Thomaszewski, S. Mudur, T. Popa, Computational design of skintight clothing, ACM Trans. Graph. 39 (2020) 105:105:1–105:105:12. doi:10.1145/3386569.3392477.

[42] Haseganu, M. Eliza, Analytical Investigation of Tension Fields in Lightweight Membrane Structures, Ph.D. thesis, University of Alberta, 1994.

[43] K. Nakashino, A. Nordmark, A. Eriksson, Geometrically nonlinear isogeometric analysis of a partly wrinkled membrane structure, Computers & Structures 239 (2020) 106302. doi:10.1016/j.compstruc.2020.106302.

[44] Y. Timounay, R. De, J. L. Stelzel, Z. S. Schrecengost, M. M. Ripp, J. D. Paulsen, Crumples as a Generic Stress-Focusing Instability in Confined Sheets, Physical Review X 10 (2020) 021008. doi:10.1103/PhysRevX.10.021008.

[45] J. Kwon, O. Bouaziz, H. S. Kim, Y. Estrin, Finite Element Modeling of Crumpling of Metallic Thin Foil, Advanced Engineering Materials 25 (2023) 2300063. doi:10.1002/adem.202300063.

[46] S. Tudruj, K. Kurec, J. Piechna, K. Kamieniecki, Mass-Spring System (MSS) 3D simulation of a thin flexible membrane with a new model of the elasticity parameters, Archive of Mechanical Engineering vol. 70 (2023) 199–218. doi:10.24425/ame.2023.144817.

[47] J. Andrejevic, C. H. Rycroft, Simulation of crumpled sheets via alternating quasistatic and dynamic representations, Journal of Computational Physics 471 (2022) 111607. doi:10.1016/j.jcp.2022.111607.

[48] R. Narain, T. Pfaff, J. F. O'Brien, Folding and crumpling adaptive sheets, ACM Trans. Graph. 32 (2013) 51:1–51:8. doi:10.1145/2461912.2462010.

[49] N. Jin, W. Lu, Z. Geng, R. P. Fedkiw, Inequality cloth, in: Proceedings of the ACM SIGGRAPH / Eurographics Symposium on Computer Animation, SCA '17, Association for Computing Machinery, New York, NY, USA, 2017, pp. 1–10. doi:10.1145/3099564.3099568.

[50] R. Wijnen, Validation and Improvement of a Dynamic Stiffness Measurement Setup, Master's thesis, Eindhoven University of Technology, 2019.

[51] M. Hoogerkamp, R. R. Waiboer, R. G. K. M. Aarts, Modeling of flexible non-linear dynamic links in Nano-Positioning Motion Systems, in: ECCOMAS Multibody Dynamics 2013, 1-4 July, 2013, University of Zagreb, Croatia, University of Zagreb, 2013, pp. 287–296.

[52] C. A. Maas, B. Thibault, New Generation of Flexible Elastomer Exhaust Decouplers: LINKEO System, Technical Report 2005-01-1153, SAE Technical Paper, 2005. doi:10.4271/2005-01-1153.

[53] Polyfluor Plastics B.V., Material Datasheet: FEP (Fluorinated Ethylene Propylene), Material Datasheet, Polyfluor Plastics B.V., 2026.

[54] A. Othman, A. Jailani, M. Hamzah, S. Applanaidu, Finite Element Modeling of Radial Corrugated Tubular Composite Structure under Axial Loading, 2012.

[55] A. Rossi, Z. Fawaz, K. Behdinan, Numerical simulation of the axial collapse of thin-walled polygonal section tubes, Thin-Walled Structures 43 (2005) 1646–1661. doi:10.1016/j.tws.2005.03.001.

[56] Z. Liu, W. Hao, J. Xie, J. Lu, R. Huang, Z. Wang, Axial-impact buckling modes and energy absorption properties of thin-walled corrugated tubes with sinusoidal patterns, Thin-Walled Structures 94 (2015) 410–423. doi:10.1016/j.tws.2015.05.002.

[57] Altair Engineering Inc., Altair Radioss User Documentation, Software Documentation Radioss 2025.1, 2025.

[58] Vortex CAE, Vortex-Radioss, Vortex Engineering Group Ltd, 9-9-25.

[59] DYNAmore GmbH, LS-DYNA User's Guide, https://www.dynasupport.com/tutorial/ls-dyna-users-guide, 2026.

[60] L. Morancay, G. Winkelmuller, Dynamic condensation and selective mass scaling in RADIOSS® Explicit (2009).

[61] J. van Steen, Comparison of Model Order Reduction Techniques for Interface Dynamics, Master's thesis, Eindhoven University of Technology, Eindhoven, 2020.

[62] N. Yamaki, Elastic Stability of Circular Cylindrical Shells, North-Holland Series in Applied Mathematics and Mechanics; Vol. 27, North-Holland, Amsterdam, 1984.

[63] M. C. Fokker, S. Janbaz, A. A. Zadpoor, Crumpling of thin sheets as a basis for creating mechanical metamaterials, RSC Advances 9 (2019) 5174. doi:10.1039/c8ra07565d.